Advanced Integration of GNSS and External Sensors for Autonomous Mobility Applications

Doctoral Dissertation

Doctoral Program in Electrical, Electronic and Communications Engineering (31.th cycle)

Advanced Integration of GNSS and External Sensors for Autonomous Mobility Applications

Calogero Cristodaro

* * * * * *

Supervisors

Prof. Fabio Dovis, Supervisor

Doctoral Examination Committee:

Prof. Rafael Toledo, Referee, Universidad Politecnica de Cartagena

Prof. Ling Pei, Referee, Shanghai Jiao Tong University

Prof. Laura Ruotsalainen, University of Helsinki

Prof. Roberto Garello, Politecnico di Torino

Dr. Sophie Damy, Joint Research Centre

Politecnico di Torino

2019

I hereby declare that, the contents and organisation of this dissertation constitute my own original work and does not compromise in any way the rights of third parties, including those relating to the security of personal data.

. . . . . .

Calogero Cristodaro

Turin, 2019

Acknowledgements

First of all, I would like to express my sincere gratitude to my supervisor, Professor Fabio Dovis, for his mentorship, constant support, guidance and encouragement during these years. Thank you very much for your trust and for believing in me since the first day of my journey within this academic world. Thank you also for giving me the possibility to travel abroad having the privilege to meet so many nice and interesting people. Nevertheless, I would like to thank all the members of the NavSAS group who contributed with their advice and their friendship to my work. I learnt so much from you all and I am really grateful for that. In particular, I would like to express my appreciation to Gianluca Falco, his endless support and vast knowledge strongly contributed to my work. Many thanks to the people (who became also friends) making the working environment very pleasant: Nicola, Alex, bomber Mattia, Esteban, Rodrigo, Luciano, Sabrina, Andrea, Neil, Hieu, Caner, Wenjan, Rayan and all the others.

I would like to thank professor Laura Ruotsalainen, who supervised the period of six months I spent at the Finnish Geospatial Research Institute in Finland. Your precious support, enthusiasm and passion for science guided my research activities into new and unexplored topics. I would like to extend my gratitude also to the researchers from the Department of Navigation and Positioning at FGI who made my period in Finland very pleasant.

Magneti Marelli S.p.A is gratefully acknowledged for financially supporting the research topic addressed within this thesis, which is part of the research activities carried out in collaboration with Magneti Marelli S.p.A., in the framework of the navigation in the ITS domain.

Warm thanks to my friends from my hometown with whom I grew up as well as with the ones I met during these years in Torino. Thanks Mattia, Vincenzo, Domenico and all the others.

I would like to thank my parents Giovanni and Concetta as well as my sister Gandyna, Akira and my loves Leon and Ayla. They have all believed in me since the first day I started my studies and have been a precious support and guidance during these years. All what I am now is thanks to them. You are an example and a model.

Last, but definitely not least, I would like to thank my unconditioned love and wife Marianna who has fully supported me in this process. This thesis would never have finished without her precious support, patience and understanding. I left the last special thank for my little boy Amos, who is the hugest source of happiness in my life. Thank you for filling my days with such happiness.

Abstract

The need of accurate and reliable positioning, not only is essential for the autonomous mobility, but it is of paramount importance with the advent of new services and means for transportation systems. The more accurate and reliable the positioning information, the more stringent service it can support. Within this picture, Global Navigation Satellite Systems (GNSSs) are considered as the superior system able to provide accurate and global position, velocity and time. However, GNSS technology experiences its limitation due to the physical principle of satellite based position determination that highly depends on the conditions it is used in. As an example, urban areas are typical environments where the GNSS signals are attenuated, blocked or reflected by high buildings and other objects in the line of sight between the user and the satellite. Therefore, in order to meet the requirements demanded by Intelligent Transport System (ITS) services in such areas, more complex navigation unit must be adopted with the aim to enhances the performance in terms of positioning accuracy, reliability and continuity of the position. Coupling sensors that have complementary characteristics, consistently enhances the performance of the navigation system, limiting, at the same time, the weaknesses of each individual sensor.

In this context, this thesis aims at assessing the performance of multi-sensor navigation system, mainly addressing two different architectures of the hybridized receiver, i.e. tight and ultra tight integration. Data fusion is achieved integrating GNSS, Inertial Navigation System (INS), visual sensor and odometer. The performance of the navigation system is assessed in different scenarios, with the aim to demonstrate its effectiveness as well as its feasibility with respect to different classes of ITS services.

Contents

List of Tables

List of Figures

List of acronyms

A/D	Analog-to-Digital
ADC	Analog-to-Digital Converter
AGC	Automatic Gain Control
AI	Artificial Intelligence
AoA	Angle of Arrival
AR	Auto-Regressive
AV	Allan Variance
AWGN	Additive White Gaussian Noise
BOC	Binary Offset Carrier
BPSK	Binary Phase Shift Keying
CAF	Cross Ambiguity Function
CBOC	Composite Binary Offset Carrier
CDF	Cumulative Distribution Function
CDMA	Code Division Multiple Access
C/N_0	Carrier-to-Noise density power ratio

CoO	Cell of Origin
CS	Commercial Service
CW	Continuous Wave
CWI	Continuous Wave Interference
DAC	Digital-Analog Converter
DC	Deeply Coupled
DCM	Direction Cosine Matrix
DLL	Delay Lock Loop
DSP	Digital Signal Processors
ECEF	Earth-Centered Earth-Fixed
ECI	Earth-Centered Inertial
EKF	Extended Kalman Filter
FLL	Frequency Lock Loop
FPGA	Field Programmable Gate Array
GBPT	GNSS-Based Positioning Terminal
GLONASS	GLobal NAvigation Satellite System
GM	Gauss-Markov
GNSS	Global Navigation Satellite System
GPP	General Purpose Processor
GPS	Global Positioning System
GSA	Global Navigation Satellite Systems Agency

HOW	Hand-over word
HPE	Horizontal Positioning Accuracy
HW	Hardware
IF	Intermediate Frequency
IMU	Inertial Measurement Unit
INS	Inertial Navigation System
IVS	In-Vehicle Systems
ISMR	Ionospheric Scintillation Monitoring Receivers
ITS	Intelligent Transport System
KF	Kalman Filter
LC	Loosely Coupled
LDOP	Line Dilution Of Precision
LiDAR	Light Detection and Ranging System
LNA	Low Noise Amplifier
LO	Local Oscillator
LS	Least Square
MBOC	Multiplexed BOC
MEMS	Micro Electro-Mechanical System
ML	Maximum Likelihood
NBI	Narrow Band Interference
NCO	Numerical Controlled Oscillator

NED	North-East-Down
OS	Open Service
PC	Personal Computer
PLL	Phase Lock Loop
PND	Personal Navigation Device
PNT	Position Navigation Time
PRN	Pseudo-Random Noise
PRS	Public Regulated Service
PSD	Power Spectral Density
PVT	Position, Velocity and Time
RADAR	RAdio Detection And Ranging
R&R	Record and Replay
RF	Radio Frequency
RFE	Radio Front-End
RFCS	Radio-Frequency Constellation Simulators
RFI	Radio-Frequency Interference
RMS	Root Mean Square
RSSI	Receives Signal Straight Indicator
RTMeS	Reference Trajectory Measurement System
RFCS	Radio Frequency Constellation Simulators
RTK	Real Time Kinematic

SDR	Software Defined Radio
SIS	Signal-In-Space
SIFT	Scale Invariant Feature Transform
SLAM	Simultaneous Localization And Mapping
SNR	Signal-to-Noise Ratio
SoL	Safety-of-Life
SAR	Search-and-Rescue
SV	Satellite Vehicle
SW	Software
TC	Tightly Coupled
TLM	Telemetry word
TDoA	Time Difference of Arrival
ToA	Time of Arrival
ToF	Time of Flight
TOW	Time of Week
UKF	Unscented Kalman Filter
USB	Universal Serial Bus
USRP	Universal Software Radio Peripheral
U-TC	Ultra-Tightly Coupled
UWB	Ultra Wide Band
VDLL	Vector Delay Lock Loop

VERT	Vehicle for Experimental Research on Trajectories
VFLL	Vector Frequency Lock Loop
VO	Visual Odometry
VSG	Vector Signal Generator
WB	Wide-Band
WBI	Wide-Band Interference
WLAN	Wireless Local Area Network
WSS	Wheel Speed Sensor

Chapter 1

Introduction

Millions of people every day benefit from new services and applications related to the Intelligent Transport System (ITS) domain. Smart mobility applications are emerging and concerns about safety and liability are being debated, with also impact on the still unclear regulatory domain. Nevertheless, autonomous driving is becoming a reality thanks to the fast evolution of the technology and the users expectations for greener and safer mobility. Considering the plethora of fast evolution of existing applications or the introduction of new ones in the ITS domain, as well as the variety of operational scenarios, the technical user requirements, as well as the key performance parameters, vary significantly. It is clear that autonomous driving requires high accuracy, availability, integrity of the position in all the scenarios and that these requirements are less stringent for other kind of applications, such as a dynamic route guidance, as an example.

Given this picture, it is clear that the availability of a specific ITS service heavily depends on the reliability and on the accuracy that its positioning system can provide. As far as the ITS domain is concerned, such a positioning system is not anymore a simple Global Navigation Satellite System (GNSS) receiver, in charge of estimating the user position, but it is a more complex system that might be denoted as a *positioning-based system for road ITS*. A possible architecture of such a smart and connected unit is shown in Figure 1.1, where it is possible to distinguish two main sub-systems such as the *positioning system* (left) and the *application module* (right). Basically, the former

estimates the positioning quantities, that are used by the latter to provide the user with the required service.

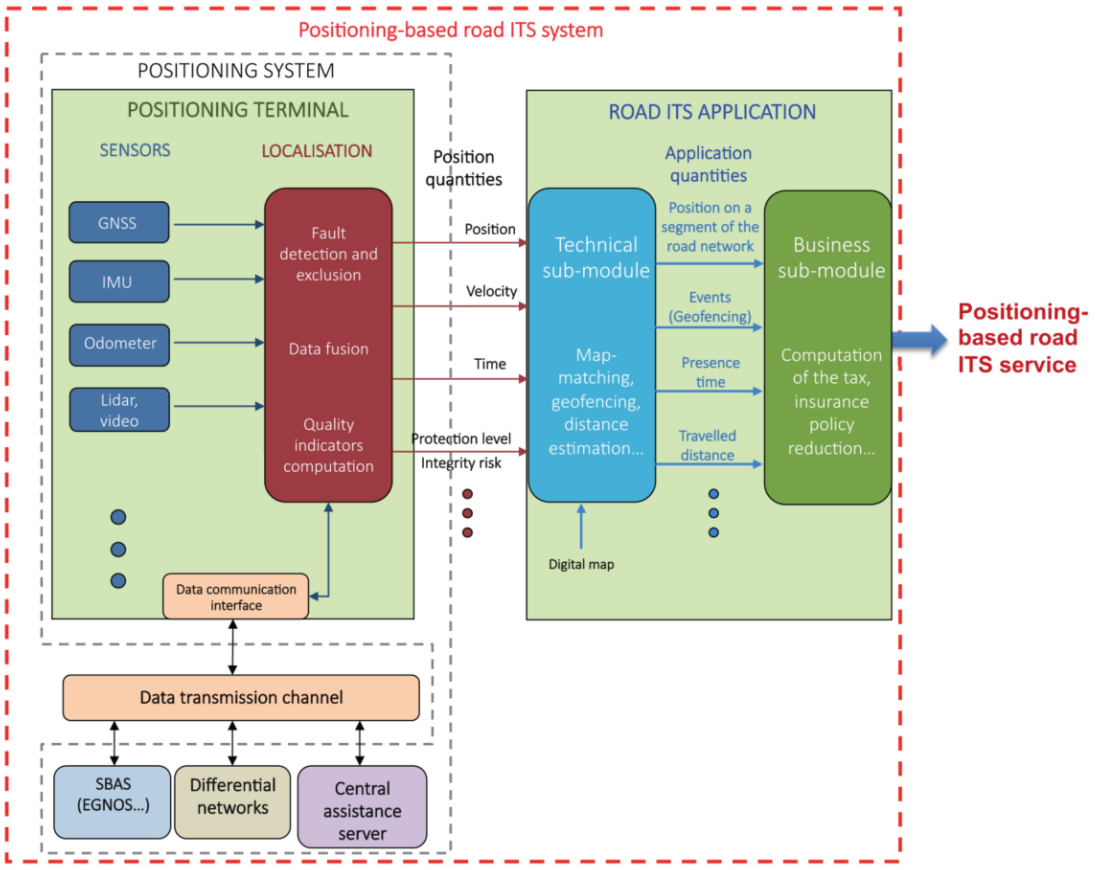

Figure 1.1: Reference architecture of a positioning-based road ITS system. Modified from [175].

Within this architecture, the core of the *positioning system* is the *positioning terminal*, which is in charge of estimating the user position quantities. It is based on specific architectural and design implementation choices, in fact it might optionally communicate with other modules, located elsewhere, through a data transmission channel, obtaining corrections from differential networks, e.g. Real Time Kinematic (RTK). As GNSS is able to provide accurate and global position, velocity and time, it can be considered the dominant technology within the *positioning terminal*. In fact, the latter can be identified through the term GNSS-Based Positioning Terminal (GBPT). However, it is well known that GNSS experiences its limitation depending on the conditions it is used in. As an

example, urban areas are typical environments where the GNSS signals are attenuated, blocked or reflected by high buildings and other objects in the line of sight between the user and the satellite. Moreover, GNSS is vulnerable to a range of threats, since the signals are received with an extremely low power after traveling from the satellite transmitter to the user receiver antenna on the Earth making GNSS prone to unintended and malicious Radio-Frequency Interference (RFI).

One possible strategy to overcome these weaknesses is given by the integration of measurements from multiple sensors with complementary characteristics. The intelligent integration of heterogeneous data not only enhances the performance of the GBPT but, at the same time, limits the weaknesses of each individual sensor. Such a data fusion concept is exploited within the GBPT reported as reference in Figure 1.1, embedding sensors such as Inertial Measurement Unit (IMU), odometer, Light Detection and Ranging System (LiDAR), that are coupled with GNSS through the data fusion module.

Once the positioning quantities are estimated by the *positioning system*, they are fed to the *application module*, that eventually provides the final service to the user. Although it is hard to define a common architecture for the *application module*, due to different choices addressed during the design phase, it can be typically divided into sub-modules, since operations of different nature have to be computed (e.g. technical and business-related). In particular, with respect to the system reported in Figure 1.1, the *technical sub-module* uses the digital map to perform operations such as map matching, geo-fencing, distance estimation. On the other hand, the *business sub-module* uses these application quantities to perform the computation of tax, insurance policy, eventually providing the required ITS service for the user.

Research objectives

Given the fundamental role of the navigation unit in ITS applications [16], [17], the objective of this thesis is the development of innovative algorithms that aim at enhancing its performance. Since these algorithms are bounded within the *positioning terminal*, with respect to the architecture in Figure 1.1, it comes out that the operations carried out

within the whole *positioning-based ITS system* (addressing operations performed to refine the position estimation, such as the communication with differential network through a dedicated data communication channel, or the map matching performed in the technical sub-module) are beyond the scope of this work and thus not considered in the thesis.

Multi-sensor systems are then considered, addressing hybrid architectures of the GBPT where GNSS, which is the essential and dominant component, is coupled with other sensors, referred in this thesis as *external sensors*. In particular, Inertial Navigation System (INS), visual sensors and odometer have been chosen as the external sensors to be coupled with GNSS, according to two integration strategies: Tightly Coupled (TC) and Ultra-Tightly Coupled (U-TC). These integration strategies are characterized by different level of integration between GNSS and the external sensors. In particular, in TC integration, the sensors provide their basic measurements to generate the navigation solution whereas in U-TC integration, the GNSS tracking module is embedded within the navigation filter fusing the measurements. While TC is quite consolidated in the scientific literature, the benefits of U-TC, especially in presence of different sensors with different features, have still to be investigated.

In this work, the performance of the TC and U-TC integration algorithms has been assessed in meaningful scenarios, chosen to be representative of different operational environments. The choice of meaningful scenarios was dictated by the complexity of having an exhaustive and fair performance assessment in all the possible conditions, due the variability of many parameters such as the environmental conditions (satellite visibility, presence of multipath, etc.), the different number of sensors involved within the integrated system, the architecture of the GNSS module, to cite only few of them. Meaningful scenarios have been then chosen performing relative comparisons.

The aim of such a performance assessment is to show the feasibility and applicability of the developed integration algorithms, with respect to different classes of ITS services. This study assumes high importance since the analysis, the development and the assessment of innovative algorithms, which are able to retrieve higher position accuracy and reliability, is the key for enabling ITS services.

Main contributions

The main contributions of the thesis can be summarized as follows:

- Analysis, development and performance assessment of TC and U-TC integration algorithms performing the hybridization of the GNSS receiver with inertial sensors, monocular camera and odometer. Performance assessment carried out in meaningful scenarios, characterized by different GNSS signal conditions, representative of different operational environments.
- Analysis of the feasibility and applicability of TC and U-TC integration algorithms in different classes of ITS services and applications.
- Evaluation of the performance improvements associated by using multi-sensor systems with respect to the classical GNSS/INS integrated systems, in case of both TC and U-TC integration algorithms.
- Analysis and real implementation of the R&R approach for the creation of synthetic but realistic scenarios. Implementation carried out by capturing real world signal environments, eventually (and faithfully) replayed in a lab controlled environment injecting impairments, such as RFI, to the recorded GNSS signals.
- Analysis and real implementation of the R&R approach for the assessment of GNSS receiver performance in lightly and heavily signal degraded environments, in the frame of the road application.

The work presented in this thesis was presented in peer-reviewed journal papers [45] and in different international conferences of worldwide renown in the GNSS community [47], [49], [46]. Some contributions were included in the techincal report [31]. Furthermore, side works related to the design of software receivers, and hybrid architectures led to the publications [48], [155], [117], [116], [118], [128] and [129].

Outline of the remainder of this thesis

Chapter 2 gives an overview about GNSS, first describing the principles of satellite navigation, and then providing details about the main characteristics of GPS and Galileo signals, available today and foreseen in the future. The frequency bands currently allocated for the different GNSSs are also discussed. Eventually, it gives an overview about the vulnerabilities affecting GNSS, briefly introducing the intentional attacks, and therefore describing two general classes of Radio Frequency (RF) channel impairments, such as interference and ionospheric scintillations.

Chapter 3 first describes the architecture of a classical GNSS receiver and then it introduces a more complex structure, called vector tracking. The two architectures are compared and the main differences highlighted. Eventually, implementations of the receiver by a software defined and fully software architectures are discussed introducing the concept of Software Defined Radio (SDR)-based GNSS receivers.

Chapter 4 first provides a review of the most commonly used coordinate frames used in navigation, together with their relationship, which is essential to define the framework for fusing the information to reliable estimates on position, velocity, and attitude. Afterwards, it gives an overview about the use of multiple sensors for positioning together with a literature review about the use of these technologies for navigation purposes. Eventually, it provides the fundamental concepts of INS, visual sensor and odometer as the subset of sensors considered within this thesis, to be coupled with GNSS.

Chapter 5 describes the most commonly used filters to combine information from sensors of different nature and, eventually, it gives an overview about the different strategies that can be used for the data fusion. Loose, tight and ultra-tight integration strategies are thus presented and the general principles discussed. The equations of the navigation filter, implemented according to an Extended Kalman Filter (EKF) scheme, and used for each integration strategy, are presented.

Chapter 6 describes the concept of R&R discussing the advantages offered by the recording and the replay of the raw samples of the GNSS signal. The results of real data replay are then presented for two cases: first, for the performance assessment of a

GNSS receiver and then for evaluating the impact of interfering signals on GNSS signals affected by ionospheric scintillations recorded in equatorial region.

Chapter 7 includes the performance assessment of the multi-sensor TC and U-TC integration algorithms developed within this thesis. The methodologies, adopted to assess the performance of the integration algorithms, are also discussed.

Chapter 8 aims at assessing the performance of the multi-sensor TC and U-TC integration algorithms, in scenarios characterized by the presence of jamming. An overview about the generation of the scenarios chosen for the performance assessment is also given.

Chapter 9 finally provides a summary of the research presented within this thesis and discusses some future works.

Chapter 2

Global Navigation Satellite Systems

GNSS is the term used for satellite systems providing positioning and timing information with global coverage of stationary or moving objects by means of the RF electromagnetic signals transmitted by a constellation of satellites. This technology is used nowadays for many types of applications, covering the mass market, professional and safety-critical applications. GPS was the first satellite navigation system enabling users to determine precisely position in global coordinate frame. It is the most popular among today's GNSS. However, several countries are independently investing into the development of the own GNSS, such as Europe (Galileo) and China (BeiDou). Also the Russian federation is modernizing and upgrading its own system GLobal NAvigation Satellite System (GLONASS).

A general overview about GNSS is given in this Chapter, which presents the principles of satellite navigation using ToAs estimation of signals received from a set of satellites. As far as the signal broadcast by the satellites is concerned, it provides details about the main characteristics of GPS and Galileo signals, available today and foreseen in the future. The frequency bands currently allocated for the different GNSSs are also discussed. Finally, it gives an overview about the vulnerabilities affecting GNSS, briefly introducing the intentional attacks, and therefore describing two general classes of RF channel impairments, such as interference and ionospheric scintillations.

2.1 Principles of satellite navigation

GNSS allows the users to estimate their Position, Velocity and Time (PVT) with respect to a reference frame in the space and time domains. GNSS relies on the ToA concept to determine the user position, which consists of measuring the propagation time of the signal from a set of satellites, at a known locations, to the GNSS receiver. This time difference is transformed into a range information, by multiplying it by the speed of light in the vacuum. The satellites, equipped with very accurate atomic clocks, are finely synchronized to a common scale. Assuming that the j-th satellite transmits a pulse at time t_0, and it is received at time $t_0 + \tau$, the distance R_j between the transmitter (j-th satellite) and the receiver can be estimated as

$$R_j = c \cdot \tau \tag{2.1}$$

where c is the speed of light. In three-dimensional space, every distance R_j defines a spherical surface whose center is the position of the j-th satellite. The intersection of at least three of these spheres, retrieve the user position. The second point where the spheres intersects can be easily discarded as it is located in deep space. However, since the clock of GNSS receivers is not synchronized with the transmitter clock, the measure of the distance suffers of a bias ε, common to each satellite. As a result, the measurement performed by the receiver thus become a pseudorange ρ_j, defined as

$$\rho_j = R_j + \varepsilon = c(\tau + \delta t_u) \tag{2.2}$$

where δt_u is the clock bias. The effect of the receiver clock offset on the ToA measurements is shown in Figure 2.1.

The generic j-th pseudorange ρ_j can be written as:

$$\rho_j = \sqrt{\left(x_{sj} - x_u\right)^2 + \left(y_{sj} - y_u\right)^2 + \left(z_{sj} - z_u\right)^2} + b_{ut} \tag{2.3}$$

where x_u, y_u, z_u are the user coordinates, x_{sj}, y_{sj}, z_{sj} are the coordinates of the j-th satellite,

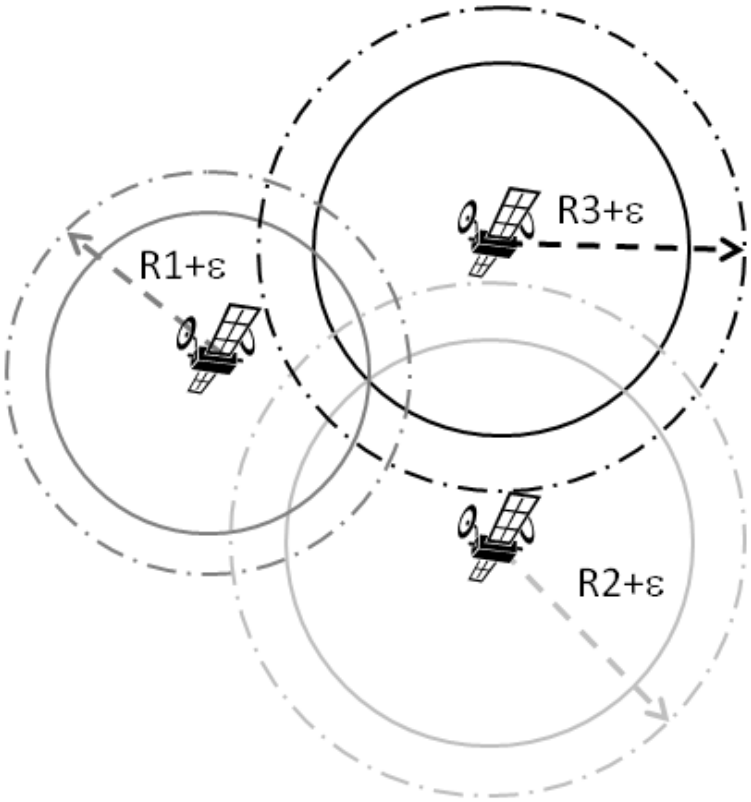

Figure 2.1: Effect of Receiver Clock Offset on ToA Measurements. Taken from [58].

and $b_{ut} = c \cdot \delta t_u$ is the clock bias term. It is worth noting that the receiver must have at least four satellites in view in order to estimate its position and the clock bias terms. Better estimation can be obtained if a larger number of available satellites is available. In fact, this approach is used by the modern receivers combining signals from multiple GNSSs.

2.2 Signal structure

The signal broadcast by the navigation satellites is usually denoted as Signal-In-Space (SIS). This signal has been designed to allow the user estimating his distance from the satellite, the so-called *pseudorange*. It must also be robust to the transmission through the atmosphere as well as to intentional and unintentional interference, multipath

and other type of errors and disturbances. Nevertheless, it must be identified in a unique way and, at the same time, carry data containing useful information about the satellite position, velocity and time. The Code Division Multiple Access (CDMA) technique, used to multiplex the transmission channel, is able to accomplish these requirements provided that the signal transmitted by each satellite is modulated by a unique PRN code. Since all of the PRN sequences are nearly uncorrelated with respect to each other, the correlation between the received data and properly shifted local replica of the spreading codes, allows the receiver to separate and detect the signals broadcast by different Satellite Vehicle (SV). This scheme is used by GPS, Galileo and Beidou to broadcast its own navigation signal.

2.2.1 GNSS frequency plan

GNSSs transmit the signal in two or more frequencies in L band. Since multiple services and users coexist in the same range, the allocation of frequency bands is a complex process. A summary of the different frequency bands used by the European Galileo, the American GPS, the Russian GLONASS, the Chinese BeiDou, the Japanese QZSS and the Indian IRNSS are depicted in Figure 2.2. It is worth noting that not all of these signals are transmitted at the time of writing, but they are on the plans of the modernization of the different GNSS.

2.2.2 The GNSS transmitted signal

The payload of a GNSS satellite generates all the components that are needed to create the SIS broadcast to the users. For example, in the case of Galileo $E5$ signal, 4 channels $E5a\text{-}I$, $E5a\text{-}Q$, $E5b\text{-}I$ and $E5b\text{-}Q$ are transmitted in two adjacent sidebands $E5a$ and $E5b$, as shown in Figure 2.2. The most general form of a GNSS signal, transmitted by a GNSS satellite j, can be represented as

$$s_{RF}(t) = \sum_{i=1}^{L} x_{RF,i}(t) \tag{2.4}$$

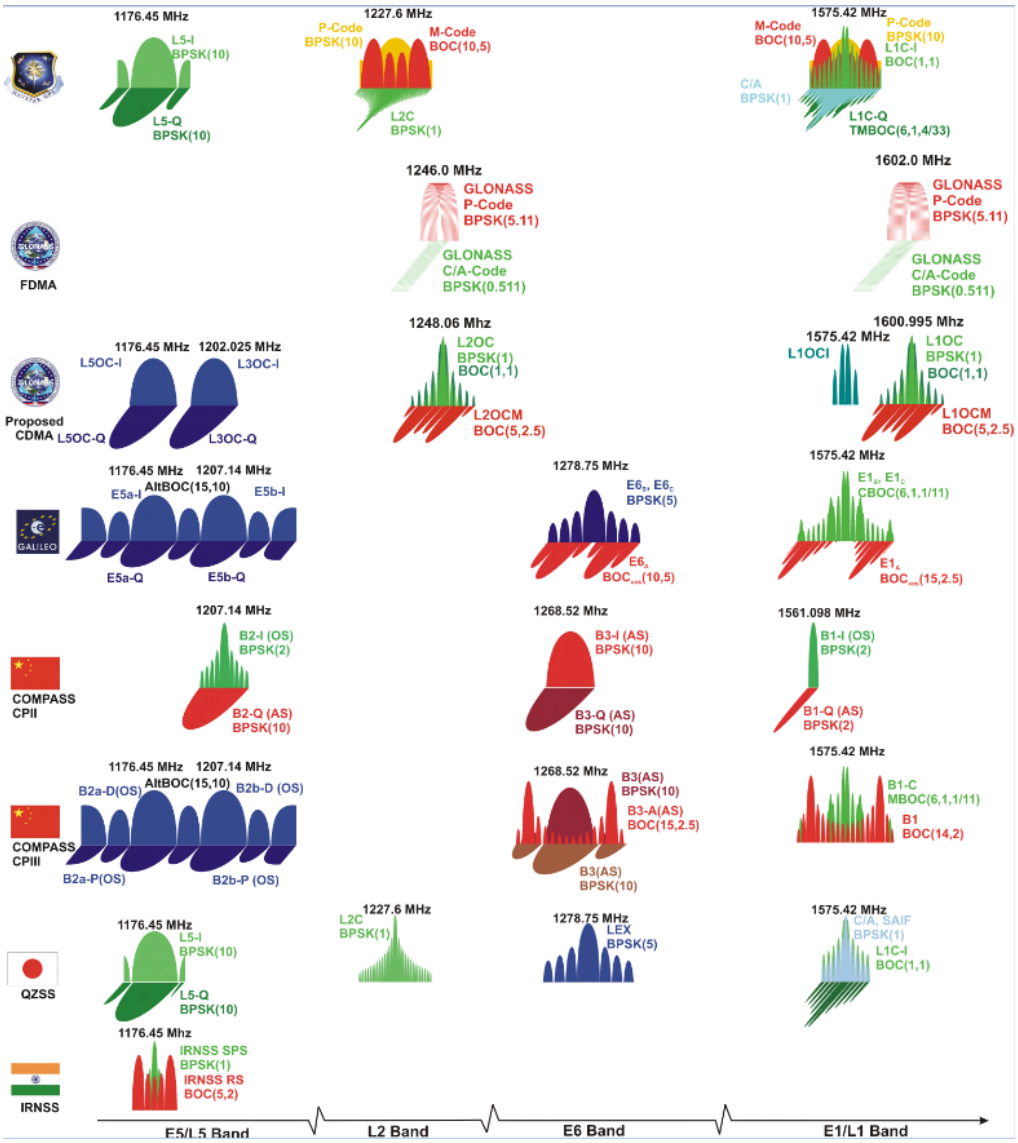

Figure 2.2: GNSS frequency bands [1].

where $x_{RF,i}(t)$ are the different signal components and L is the number of transmitted channels, equal to 4 in case of Galileo $E5$ signal. Each signal component consists of three different terms:

- *carrier*, which is a RF sinusoidal signal at a certain frequency,
- *spreading code*, which is a PRN code,
- *navigation message*, which is a sequence of bit containing useful information about

the satellite position, velocity, time and other complementary information.

The three components are shown respectively in the top, middle and bottom part of Figure 2.3, in case of the GPS $L1$ and $L2$ signals. From the figure it is possible to appreciate the substantial difference among the rates of each component. For instance, considering the $L1$ signal, they have a length of about 19 cm, 300 m and 6000 km, respectively.

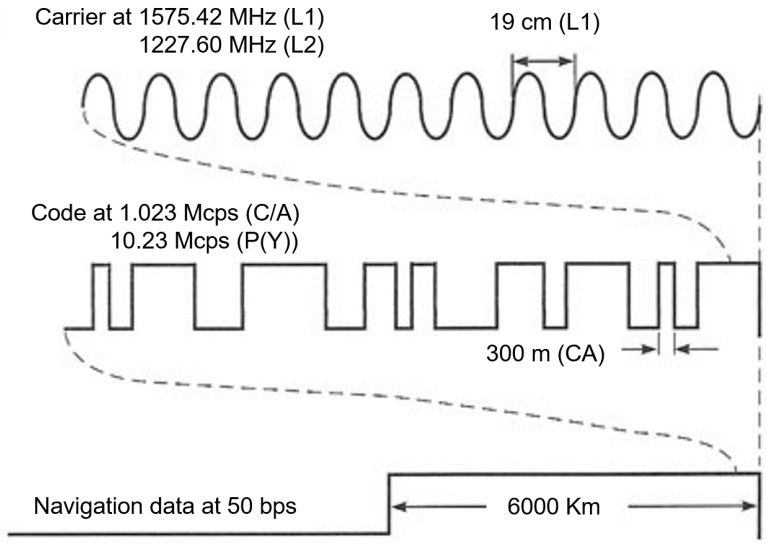

Figure 2.3: GPS signals, containing carrier (top), code (middle) and navigation data (bottom) [130].

Each component $x_{RF,i}(t)$ can be modeled as

$$x_{RF,i}(t) = \sqrt{2P_T}c_i(t)\bar{c}_i(t)d_i(t)\cos(2\pi f_{RF,i}t) \tag{2.5}$$

where:

- P_T is the power associated to the channel,
- $c_i(t)$ is the spreading code,
- $\bar{c}_i(t)$ is the secondary code, present in most recent GNSS signals. If it is not present, then $\bar{c}(t) = 1\ \forall t$,

- $d_i(t)$ is the navigation message, which could not be present in some channels, conventionally denoted as *pilot channels*,
- $\cos(2\pi f_{RF,i}t)$ is the carrier at the centre frequency f_{RF}.

2.2.3 GPS L1 signal

At the time of writing (March 2019), GPS satellites transmit three signals in the L1 band: C/A Code, P(Y) Code and M-Code. An additional new civil signal, known as L1C, will also be transmitted in a few years by the modern and fully renovated satellite named GPS III.

C/A code and the P code are known as the legacy signals and are broadcast by all the available GPS satellites. C/A code is nowadays used for civilian applications in any kind of receiver. It is a bi-phase modulated signal using a 1023 chips long PRN periodic sequence with chipping rate equal to 1.023 MHz, then 1023 chips last 1 ms. The GPS C/A signal belongs to a family of PRN codes, known as Gold codes, and chosen for their good correlation properties.

The Protected (P) code is the precision signal and it is bi-phase modulated at 10.23 Mchip/s; therefore, the main lobe of the spectrum is 20.46 MHz wide from null to null. The PRN P-code is a ranging code, 7 days long. The Y-Code is used in place of the P-code whenever the Anti-Spoofing (AS) mode of operation is activated as described in the [74].

The C/A and P(Y) signals for the i-th satellite in the L1 frequency are in quadrature and they can be written as

$$s_{L1}(t) = Ap_i(t)d_i(t)\cos(2\pi f_{L1}t + \theta_1) + \sqrt{2}Ac_i(t)d_i(t)\sin(2\pi f_{L1}t + \theta_1) \tag{2.6}$$

where $s_{L1}(t)$ is the band-pass signal at L1 frequency; A is the amplitude of the P code; $p_i(t)$ and $c_i(t)$ represent the phase of the P code and C/A code, respectively; $d_i(t)$ represents the data code; f_{L1} is the L1 frequency; and θ_1 is the initial phase. The P(Y), C/A, and the carrier frequencies are all phase locked together. Each data stream (C/A or P(Y))

employs Binary Phase Shift Keying (BPSK) modulation.

Table 2.1 provides an overview of the present and future GPS signals and their characteristics.

Band	**Service**	**Type (*)**	**Modulation scheme**	**Spect. occup. (**)**	**Code rate**		**Navig. data rate**	**Min. Rx Power**	**Status (***)**
				MHz	**chip/s**		**bit/s**	**dBW**	
L1	C/A	C	BPSK(1)	2.046	1.023e6		50	-158.5	T
L1/L2	P	M	BPSK(10)	20.46	10.23e6		50	-161.5	T
L1	L1C	C	TMBOC(6,1,4/33) BOC(1,1)	4.092 4.092	CP CD	1.023e6 1.023e6	no data 50	-158.25 -163	F
L2	L2C	C	BPSK(1)	2.046	CM CL	511.5e3 511.5e3	25 no data	-158.5	P
L1/L2	M	M	BOC(10,5)	30.69	5.115e6		N/A	N/A	T
L5	L5	C	QPSK(10)	20.46	I5 Q5	10.23e6 10.23e6	50 no data	-157 -157	P

REMARKS:

(*)	C = civil signal M = military signal
(**)	null-to-null bandwidth For BOC modulations, only the two main spectral lobes are considered
(***)	T = transmitted (full operation capability); P = pre-operational broadcast; F = foreseen signal.

Table 2.1: Current and modernized GPS signals [75], [76], [74]. Taken from [58].

2.2.4 Galileo E1 signal

The whole transmitted Galileo E1 signal consists of the multiplexing of the three following components: the E1 Open Service (OS) Data channel $e_{E1-B}(t)$, the E1 OS Pilot channel $e_{E1-C}(t)$ and the E1 Public Regulated Service (PRS) channel $e_{E1-A}(t)$.

As far as the OS is concerned, the E1 modulation receives the name of Composite Binary Offset Carrier (CBOC) and is a particular implementation of MBOC [28]. MBOC(6,1,1/11) is the result of multiplexing a wideband signal, BOC(6,1), with a narrowband signal, BOC(1,1), in such a way that 1/11 of the power is allocated, in average, to the high frequency component

$$G_{MBOC}(f) = \frac{10}{11} G_{BOC(1,1)}(f) + \frac{1}{11} G_{BOC(6,1)}(f) \tag{2.7}$$

where $G_{BOC(1,1)}(f)$ is the unit power spectral density of a sine-phased BOC(1,1) modulation and $G_{MBOC}(f)$ is the resulting MBOC power spectral density. The spreading modulation design include the BOC(6,1) component in order to place a small amount of additional power at higher frequencies. The comparison among the PSDs of the BOC(1,1) and the MBOC(6,1,1/11) is represented in Figure 2.4.

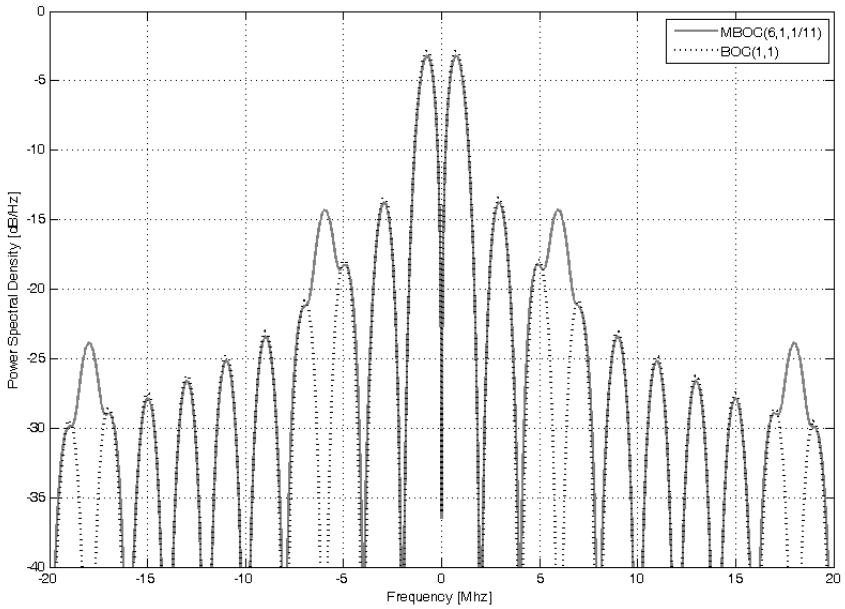

Figure 2.4: Unit PSD comparison of BOC(1,1) and MBOC(6,1,1/11) [58].

The data signal $e_{E1-B}(t)$ in the time domain is given by

$$e_{E1-B}(t) = d_{E1-B}(t) c_{E1-B}(t) s_{CBOC}(t) \tag{2.8}$$

and a pilot component given by

$$e_{E1-C}(t) = c_{E1-C}(t)s_{CBOC}(t) \tag{2.9}$$

where $d_{E1-B}(t)$ is the navigation binary signal, $c_{E1-B}(t)/c_{E1-C}(t)$ are the spreading codes and $s_{CBOC}(t)$ are the CBOC (6,1,1/11). The BOC modulation applies a squared subcarrier to a BPSK signal so that the maximum of the power spectrum is shifted with respect to the center frequency. The generic view of the E1 OS signal generation is depicted in Figure 2.5.

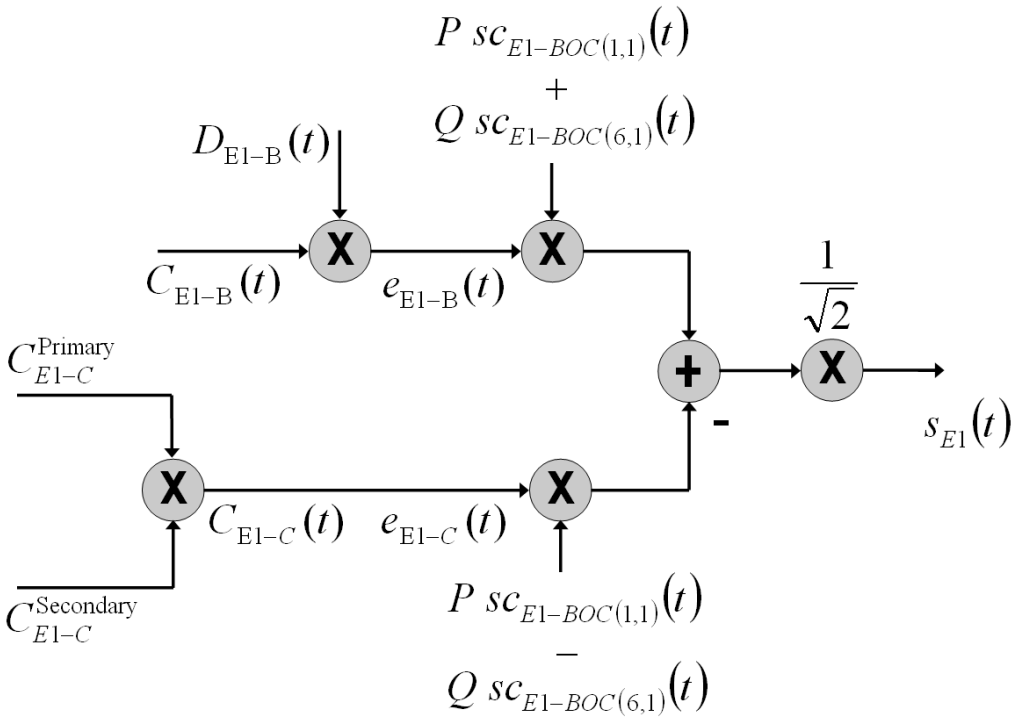

Figure 2.5: Modulation Scheme for the Galileo E1 OS Signals [28].

The services to be provided by Galileo are the OS, the Safety-of-Life (SoL) Service, the Commercial Service (CS), the PRS, the Search-and-Rescue (SAR) Service. They were initially planned to be available to users of the Galileo system through 10 different navigation signals transmitted in E1, E6 and E5 frequency bands. Table 2.2 summarizes the Galileo signals and their characteristics.

Band	Service	Channel	Modulation scheme	Spectral occup. (*)	Subcarrier freq.	Code rate	Sec. code rate	Nav. data	Multiplex. tech.	Min. Rx power	Status(**)
				MHz	MHz	Mchip/s	chip/s	symb/s		dBW	
E1	PRS	A	BOCcos(15,2.5)	35.805	15.345	2.5575	-	N/A	Const. env.	N/A	T
	OS	B	CBOC(6,1,1/11)	14.322	1.023 / 6.138	1.023	-	250		-157 (B+C)	T
	Pilot	C	CBOC(6,1,1/11)	14.322	1.023 / 6.138	1.023	250	no data			T
E6	PRS	A	BOCcos(10,5)	30.69	10.23	5.115	-	N/A	Const. env.	N/A	T
	CS	B	BPSK(5)	10.23	-	5.115	-	1000		-155 (B+C)	V
	Pilot	C	BPSK(5)	10.23	-	5.115	1000	no data			V
E5a	OS	I	BPSK(10)	20.46	15.345	10.23	1000	50	AltBOC(15,10)	-155 (I+Q)	T
	Pilot	Q	BPSK(10)	20.46	15.345	10.23	1000	no data			T
E5b	OS	I	BPSK(10)	20.46	15.345	10.23	1000	250		-155 (I+Q)	T
	Pilot	Q	BPSK(10)	20.46	15.345	10.23	1000	no data			T

REMARKS:

(*) null-to-null bandwidth
For BOC modulations, only the two main spectral lobes are considered

(**) T = transmitted (initial services);
V = under test and validation.

Table 2.2: Current Galileo signals [61], [62], [63]. Taken from [58].

2.3 GNSS vulnerabilities

Although GNSS can provide accurate position, velocity and time in a global frame, it is high vulnerable to a range of threats. In particular, the power weakness of GNSS signals makes it vulnerable to intentional and unintentional RFI. Furthermore, GNSS threats include intentional attacks with the objective to disrupt the target receiver. An overview about these vulnerabilities is given in this Section, first briefly introducing the intentional attacks and, eventually, describing two general classes of RF channel impairments. The first class is the *interference*, and the second class is *ionospheric scintillation*. The reason of considering only these two classes of signal impairments, is due to the fact that these threats have been considered within the experimental work of this thesis, as it will be explained in Chapter 6 and in Chapter 8.

2.3.1 Intentional attacks

The risk of intentional attackers willing to disrupt the GNSS receiver functions, has been recently highlighted by many works [20], [78], [178]. This phenomenon has been boosted also by the proliferation of programmable simulators and SDR systems, capable to generate counterfeit attacks [151].

The intentional attacks on GNSS receivers can act at two different levels: *(a)* directly on the receiver. It typically includes the alteration of the position reported by the receiver to a control center or a service provider. *(b)* at the GNSS signal level. It is conventionally characterized in three different forms [57], [179]:

- *Jamming*: intentional emission of electromagnetic radiation by masking GNSS signals.
- *Meaconing*: rebroadcasting of recorded and delayed GNSS signals with a power higher than the satellite signal in order to make the receiver track the transmitted signal and obtain a position solution at the position of the attacker.
- *Spoofing*: broadcast of a GNSS-like signals, with the intent to take control of the receiver. The spoofer can slowly modify the position solution of the victim without

the receiver noticing any inconsistency or jumps in the solution, thus without disrupting GNSS operations.

2.3.2 Interference

RFI is one of the most dangerous threat for a GNSS receiver. It is due to the extremely low power of the signal that reaches the antenna of the user receiver. It is possible to identify RFI as the presence of spurious anthropogenic signals over the GNSS bandwidths [57, 59], that might be unintentional or intentionally generated to disrupt the GNSS operations in an area. Depending on the nature, on the power and on the spectral characteristics of the interfering signal, RFI can degrade the quality of the received signals, resulting in a reduced navigation accuracy or, in severe cases, in a total receiver outage.

Events of unintentional RFI are generally unpredictable. The presence of interfering power can be due to several reasons, but the main effects can be recognized to be caused by harmonics or spurious components generated by intermodulation products in the communication transmitter. Although GNSS bandwidths are protected and no transmission is allowed, it is likely that some out-of-band energy from signal frequencies located nearby the GNSS bands could interfere, due to secondary harmonics or power leakages [135]. Such effects, which are normally negligible for communication systems, are in fact threatening for a navigation receiver, because of the extremely low received power.

On the other hand, jamming refers to intentional transmission of RF energy by masking GNSS signals with noise. These disruptive signals overlap a large part of the targeted GNSS frequency band thus preventing the operation of GNSS receivers in estimating their position. Although the use of *jammers* is not legal, their rapid diffusion is becoming a serious threat to satellite navigation.

Classification of interfering sources

The classification of the interfering sources for GNSS receivers takes into account heterogeneous aspects [57]. According to the source, it is possible to distinguish between intentional and unintentional, as discussed in Section 2.3.2. Another classification can be done according to the frequency domain characteristics of the interfering signal thus evaluating its B_{int} with respect to the bandwidth of the GNSS signals B_{GNSS}. According to this principle, the interference can be classified as:

- *Narrow Band Interference (NBI)* when the spectral occupation is smaller with respect to the GNSS signal bandwidth ($B_{int} << B_{GNSS}$)
- *Wide-Band Interference (WBI)* when the spectral occupation is comparable with respect to the GNSS signal bandwidth ($B_{int} \approx B_{GNSS}$)
- *Continuous Wave Interference (CWI)* which represents the ultimate limit in NBI and appears as a single tone in the frequency domain ($B_{int} \rightarrow 0$)

It is worth mentioning that the interfering signals might have frequency-varying characteristics. As an example, the chirp signal, which is typically generated by jammers, is characterized by a linear variation in time of the instantaneous frequency, thus appearing as WBI.

Furthermore, interfering signals can be classified based on their spectral characteristics, as:

- *Out of band interference*, when the carrier frequency of the interference signal f_{int} is located near to the targeted GNSS frequency band f_{GNSS}. In this case $f_{int} < f_{GNSS} - B_{GNSS}/2$ or $f_{int} > f_{GNSS} + B_{GNSS}/2$
- *In band interference*, when the carrier frequency of the interference signal falls within the GNSS frequency band. In this case $f_{GNSS} - B_{GNSS}/2 < f_{int} < f_{GNSS} + B_{GNSS}/2$.

Interfering sources might be also classified based on their characteristics in the time domain. According to this criterion, an interfering signal may be either non-pulsed

(continuous) or pulsed. Pulsed interfering signals are characterized by on-off status of short duration in the order of μs, which alternate in the time domain.

Impact of RFI on GNSS receivers

Strong interference can cause GNSS receivers to lose lock on satellite signals and stop working. However, in many cases the presence of interference power is only strong enough to decrease the receiver performance but not to blind it completely. Such intermediate power values turn out to be the most dangerous since sometimes they cannot be detected. They lead to an increased error in pseudoranges and phase measurements, thus decreasing the accuracy of the position solution. Interference has different impact at each stage of the GNSS receiver [57], [103]. However, the impact assessment of interference on the different stages of the receiver (front-end, acquisition and tracking), is beyond the scope of this thesis and then it is not reported here. Interested readers can find this performance assessment in [57].

2.3.3 Ionospheric scintillations

As GNSS signals propagate through Earth's upper atmosphere, they undergo severe propagation nuisances, such as phase shifts, group delays and amplitude variations. In particular, the upper atmosphere of the Earth is known as ionosphere and it presents a region particularly rich of free electrons. The atmosphere of low and high-latitude regions is particularly prone to irregular electron density concentrations, as well as geomagnetic storms and strong space weather events, which induce rapid fluctuations in signal intensity (*amplitude scintillation*) and phase jittering (*phase scintillation*). Ionospheric scintillations may be defined as rapid fluctuations of the signal amplitude and phase, and are originated from a scattering effect in the ionosphere due to zones with irregular electron concentration [105]. A graphical representation of such a phenomenon is given in Figure 2.6.

Ionospheric scintillations occurrence is determined by several factors: geographic location, solar and geomagnetic activity, season and local time [98]. Scintillation of GNSS

signals are generated by diffraction and refraction of the electromagnetic signal as it passes through small-scale spatial irregularities (plasma bubbles) in the ionospheric electron density. This leads to rapid fluctuations in signal intensity (amplitude scintillation) and phase jittering (phase scintillation). Differently from what happens at equatorial region, where ionospheric scintillations are likely to happen during post-sunset hours, at high latitudes the occurrence may take place also during the day or night. Moreover, as the electron density in the E-layer is low, the irregularities usually do not result in amplitude scintillations, and as a consequence GNSS users mostly experience phase scintillations.

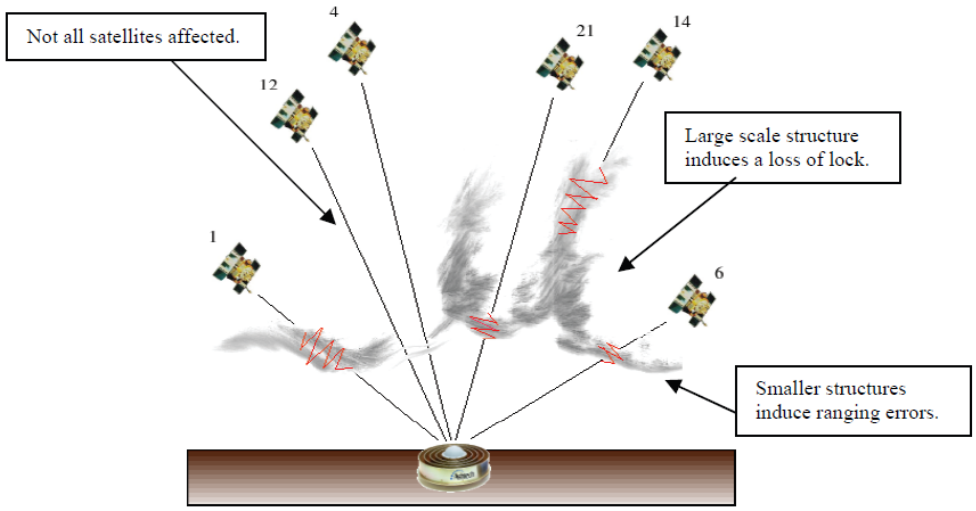

Figure 2.6: Schematic of the varying effects of scintillation on GNSS signals [80].

Measuring ionospheric scintillations with GNSS receivers

GNSS receivers are able to measure the amount of scintillation affecting a satellite signal in both amplitude and phase, by making use of 50 Hz rate data from the tracking processing blocks. The traditional way in monitoring nuisances due to ionospheric propagation envisages the use of professional commercial hardware receivers such as Ionospheric Scintillation Monitoring Receiverss (ISMRs) [177]. Nonetheless, some recent works consider SDR as a valuable, competitive and cost-effective alternative for the design of monitoring stations [115], [48], [116], [117].

Two indices, computed over an observation interval of 1 minute, are employed for this end. Amplitude scintillation is monitored by computing the S_4 index, which is the standard deviation of the received power as computed from the prompt correlator samples normalized by its mean value. Phase scintillation monitoring is achieved by computing the σ_ϕ index, which is the standard deviation of the detrended carrier phase measurements. The most widely used σ_ϕ index is the Phi60, which is calculated over the same 60 seconds interval as the S_4 [177].

$$S_4 = \sqrt{\left(\frac{\langle I^2 \rangle - \langle I \rangle^2}{\langle I \rangle^2}\right)} \tag{2.10}$$

$$\sigma_\phi = \sqrt{\langle \varphi^2 \rangle - \langle \varphi \rangle^2} \tag{2.11}$$

where I is intensity, $\langle\ \rangle$ denotes averaging usually over a period of 60 seconds, σ_ϕ is carrier phase in radians.

Impact of ionoshperic scintillations on GNSS receivers

This kind of nuisances cannot be empirically modeled and can have a serious impact on the receiver tracking performance, inducing cycle slips, phase errors and increased carrier Doppler jitter, and resulting in disruptive impact on sub-meter navigation and precise positioning. The receiver measurements can thus be heavily corrupted, resulting in positioning errors of tens of meters or, in the most severe cases, in complete outages due to loss of lock.

Chapter 3

GNSS receivers

GNSS receivers are part of the GNSS ground segment. They process the received GNSS signals that, propagating through space, arrive to the earth with an extremely low power. Thus, the role of a GNSS receiver is to capture this tiny signal and extract the useful information to provide the user with coordinate and time. In order to perform this task, the receiver must properly estimate the propagation delay and the Doppler shift of the incoming signal, that quantify the misalignment between the incoming signal and the locally generated one. This stage is usually divided into code acquisition and tracking. The acquisition stage roughly estimates these values reducing the code epoch and Doppler shift uncertainties to limited intervals. The tracking stage performs continuous fine delay estimation. The architecture of a conventional GNSS receiver is presented in this Chapter and it is compared with a more complex structure called vector tracking receiver. Implementations of the receiver by a software defined and fully software architectures are discussed in the last part of the Chapter.

3.1 Received signal

The antenna is the first element of the receiving chain. It is used to capture the GNSS signal inducing a voltage from the incident radio waves. In a real receiver, the received signal $y_{RF}(t)$ includes the contribution of the various signals transmitted in a

given bandwidth from all the satellites in view. Therefore, it is given by the superposition of K useful signals of the form of (2.4) and a noise term; K denotes the number of satellites in view. Each useful signal, $s_{RF,j}(t)$ (2.4), passes through a communication channel that modifies it introducing delay, Doppler and noise. The received signal, usually denoted SIS, can be modeled as:

$$y_{RF}(t) = \sum_{j=1}^{K} \tilde{s}_{RF,j}(t) + \eta(t) \tag{3.1}$$

where $\tilde{s}_{RF,j}(t)$ denotes the signal received by the j-th satellite and $\eta(t)$ is the non-filtered noise contribution. It can either come from the outside environment and be captured by the antenna (interference), or being generated by the electronic devices inside generated by the electronic devices inside the receiver (thermal noise).

The noise $\eta(t)$ results in a random process that is usually modeled as an Additive White Gaussian Noise (AWGN), with a flat power spectral density equal to $N_0/2\ W/Hz$. So the noise term η is a white sequence, distributed according to a Gaussian process with zero mean and variance equal to σ^2

$$\eta(t) \sim \mathcal{N}(0, \sigma^2) \tag{3.2}$$

Each signal $\tilde{s}_{RF,j}(t)$ in (3.6) is the linear combinations of H useful components $\tilde{x}_{R,ij}(t)$, and can be written as

$$\tilde{s}_{RF,j}(t) = \sum_{i=1}^{H} \tilde{x}_{RF,ij}(t) \tag{3.3}$$

where each signal component, $\tilde{x}_{R,ij}(t)$ can be modeled as

$$\tilde{x}_{RF,ij}(t) = \sqrt{2P_{ij}} c_{ij}(t - \tau_{ij}) \bar{c}_{ij}(t - \tau_{ij}) d_{ij}(t - \tau_{ij}) \cos(2\pi(f_{RF,ij} + f_{d_{ij}})t + \varphi_{ij}) \tag{3.4}$$

where P_{ij} is the received signal power of the i-th component of the signal broadcast by the j-th satellite, τ_{ij} is is the code delay, $f_{d_{ij}}$ is the Doppler frequency shift, φ_{ij} is the phase of the carrier.

The propagation delay τ depends on the distance D (called range) between the antennas

of the satellite and the user terminal, that is

$$\tau = \frac{D}{c} \tag{3.5}$$

where c is the speed of light. Considering only one component of the signal i and only one satellite j, the received signal (3.6) can be written as

$$y_{RF}(t) = \sqrt{2P_R}c(t-\tau)\bar{c}(t-\tau)d(t-\tau)\cos(2\pi(f_{RF}+f_d)t+\varphi) \tag{3.6}$$

3.2 Front end

A radio receiver usually consists of two main parts: the analog and the digital part. The analog part includes the antenna and the RFE and it is placed before the digital part, which is in charge of implementing all the processing needed to extract the information from the received signal with the final goal to compute the position, velocity and time.

Within this structure, the analog part of the receiver is considered in this Section and its main operations are described. The first operation performed by the RFE is to condition the signal so that it is suitable for signal processing. Since the received signal at the antenna output is extremely weak, it needs to be amplified. Due to the low level of received GNSS signal power, the overall gain is computed considering only the noise power as there were no signals at the antenna. Typically, Low Noise Amplifiers (LNAs) are used for this purpose, as shown by the typical architecture of a RFE in Figure 3.1. LNA effectively sets the noise figure of the receiver [103]. The signal is finally filtered by a band-pass filter to minimize out-of-band contributions and ready to be down-converted to Intermediate Frequency (IF).

The amplified and filtered signal $y_{RF}(t)$ (3.6) is then down-converted to an IF using signal mixing frequencies from Local Oscillators (LOs). The mixer simply multiplies the incoming signal by a sinusoidal tone locally generated by the LO. Neglecting the Doppler frequency shift f_d and the code delay τ, then the signal $s_{mix}(t)$ at the mixer output can be

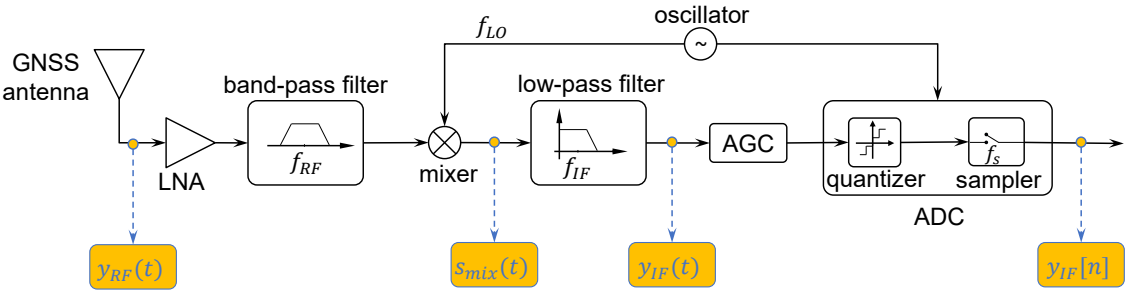

Figure 3.1: GNSS RFE architecture.

written as

$$\begin{aligned} s_{mix}(t) &= \underbrace{y_{RF}(t)}_{\text{RF signal}} \cdot \underbrace{2\cos(2\pi f_{LO} t)}_{\text{LO}} \\ &= \sqrt{2P_R}c(t)\bar{c}(t)d(t)\cos(2\pi \underbrace{(f_{RF} - f_{LO})}_{\text{IF}} t + \varphi) + \\ &\quad \sqrt{2P_R}c(t)\bar{c}(t)d(t)\cos(2\pi(f_{RF} + f_{LO})t + \varphi) + \eta(t) \end{aligned} \tag{3.7}$$

where f_{LO} term is the local oscillator frequency, which depends on the overall frequency plan and on the desired IF. It is chosen to obtain $(f_{IF} = f_{RF} - f_{LO})$.

The signal $s_{mix}(t)$ (3.7) contains two different terms with: one with frequency centered at $(f_{RF} - f_{LO} = f_{IF})$ and the other one with frequency centered at $(f_{RF} + f_{LO})$. Since only the term at IF is desired, the higher order harmonics are filtered out. At the end of the filtering process, the component $y_{IF}(t)$ can be written as:

$$y_{IF}(t) = \sqrt{2P_R}c^{(b)}(t)\bar{c}^{(b)}(t)d(t)\cos(2\pi f_{IF} t + \varphi) + \eta_{IF}(t) \tag{3.8}$$

where $c^{(b)}(t)$ represent the filtered version of the in-phase transmitted PRN code, $\bar{c}^{(b)}(t)$ represent the filtered version of the subcarrier, η_{IF} is the filtered noise at the output of the IF filter which is still a white Gaussian noise with the same variance. The subscript (b) on the code and the subcarrier denote the fact that the pulses could be actually be modified by the IF filtering. On the other hand, the data are almost unaffected by the filtering effect due to their very low rate in GNSS systems.

Finally, the frequency down-conversion allows the Analog-to-Digital Converter (ADC), which is the last component of RFE shown in Figure 3.1, to acquire the signal at a suitable rate. ADC conversion allows to convert the analog signal to a digital format and it is made of two steps: the discrete time conversion of the signal (sampling) and the quantization. An Automatic Gain Control (AGC) can be used to automatically adjust the signal dynamics.

The digital signal $y_{IF}(nT_s)$ after the ADC converter can be written as

$$y_{IF}(nT_s) = \sqrt{2P_R}c^{(b)}(nT_s)\bar{c}^{(b)}(nT_s)d(nT_s)\cos(2\pi f_{IF}(nT_s) + \varphi) + \eta_{IF}(nT_s) \tag{3.9}$$

Note that, in the following, the notation $y[n] = y(nT_s)$ will indicate a discrete-time sequence $y[n]$, obtained by sampling a continuous-time signal $y(t)$ with a sampling frequency $f_s = 1/T_s$. The digital signal $y_{IF}[n]$ finally becomes:

$$y_{IF}[n] = \sqrt{2P_R}c^{(b)}[n]\bar{c}^{(b)}[n]d[n]\cos(2\pi f_{IF}[n] + \varphi) + \eta_{IF}[n] \tag{3.10}$$

3.3 Acquisition

The acquisition strategy is adopted by GNSS receivers to estimate the arrival time τ (which contains the information required for computing user position and clock offset) and the Doppler frequency f_d (which contains the information required for computing the user velocity and the clock frequency). Therefore, acquisition is exploited, after signal conditioning, to first detect which satellites are in view and estimate approximate value of τ and f_d. These values are therefore passed to the tracking block, that performs a local search for their accurate estimates. In this stage also the estimation of the carrier phase may be included. The acquisition system is made of a number of functional blocks that conceptually operate independently.

According to the estimation theory, it is possible to show that the Maximum Likelihood (ML) estimate of the vector $p = (\tau, f_d)$, whose elements are two unknowns of $y_{IF}[n]$, is

obtained by maximizing the function

$$\hat{\mathbf{p}}_{ML} = \arg\max_{\bar{\mathbf{p}}} \left| \frac{1}{L} \sum_{n=0}^{L-1} y_{IF}[n] \hat{r}_{IF}[n] \right|^2 \tag{3.11}$$

where L is the number he number of samples used to process the incoming signal $y_{IF}[n]$, $\hat{\mathbf{p}} = (\hat{\tau}, \hat{f}_d)$ is a vector of test variables $\hat{\tau}$, and $\hat{f}_d = f_c + \hat{f}_{d,v}$ is the estimate of the true Doppler $\hat{f}_{d,v}$ plus the frequency shift f_c, defined in a proper support D_p which contains all the possible values which can be assumed by the elements of $p = (\tau, f_d)$. $\hat{r}_{IF}[n]$ is a locally generated signal

$$\hat{r}_{IF}[n] = c[n - \hat{\tau}] \exp(j2\pi(f_{IF} + \hat{f}_d)n) \tag{3.12}$$

where $c[n-\tau]$ is the local replica producing the PRN code, the subcarrier and potentially the secondary code.

The inner product of (3.11) is the CAF which basically is a two-dimensional cross-correlation function between the incoming code and a local replica of the desired signal to acquire. Therefore the CAF can be defined in the discrete time as

$$R(\hat{\tau}, \hat{f}_d) = \sum_{n=0}^{N-1} y_{IF}[n]\, c[n - \hat{\tau}] \exp(j2\pi(f_{IF} + \hat{f}_d)n) \tag{3.13}$$

where $y_{IF}[n]$ (3.10) is the received signal and $\hat{r}_{IF}[n]$ (3.12) is the local generated signal.

In order to decide if a specific satellite is in view or not, detection is usually performed on the squared envelop of the CAF. This choice is adopted in order to be insensitive to the phase of the incoming signal and also to the sign of the bits in case a data channel is acquired

$$S(\hat{\tau}, \hat{f}_d) = |R(\hat{\tau}, \hat{f}_d)|^2 \tag{3.14}$$

S is compared with a predetermined threshold (V) in order to decide which hypothesis between H_0 ($S < V$) and H_1 ($S > V$) is true, where H_0 and H_1 respectively represent the absence or presence of the desired peak. Once the decision s taken, the parameters $\hat{\tau}$ and

$\hat{f}_d$ are taken. Such parameters are estimated within a grid of point called *search space*, as shown in Figure 3.2. The resolution of the code search is usually a 0.5 chip interval. On the other hand, the Doppler frequency typically ranges from 5 to 10 kHz. In the specific case of a GPS receivers, the Doppler frequency range is estimated in the range ±5 kHz, with respect to the carrier L1.

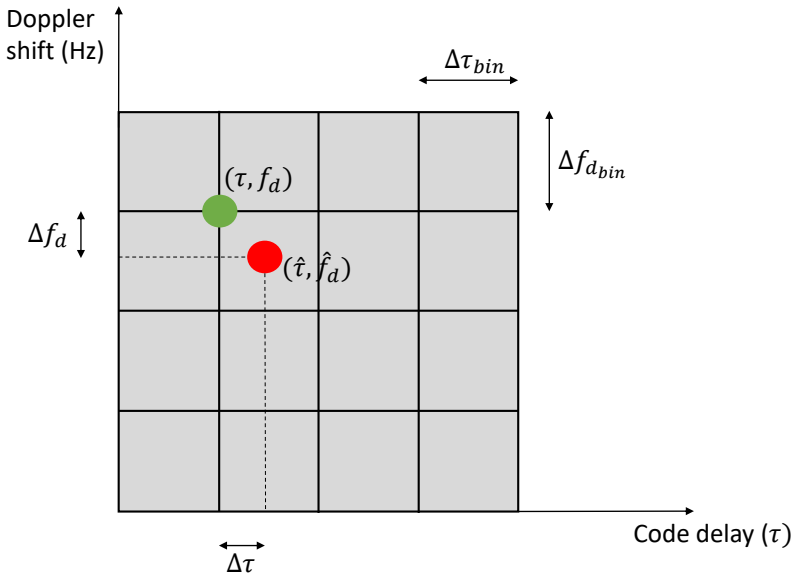

Figure 3.2: Example of search space.

In order to remain in a 0.5 chip delay range, it is possible to compute the frequency step, as suggested in [103], as

$$\Delta f_0 = \frac{2}{3T} \tag{3.15}$$

where Δf_0 is the frequency bin width, expressed in Hz, and T coherent integration time, expressed in seconds. As an example, the CAFs evaluated over the search space on a Galileo PRN12 and PRN21 real signal are reported in Figure 3.3. The figure shows how the signal was acquired for PRN12 (left) and not acquired for PRN21 (right) as only noise was present.

There are several acquisition techniques reported in literature, that implement different types of searches and in general have a trade-off between the complexity of the search and the numbers of operations: two examples are the *serial search* and the *parallel search*.

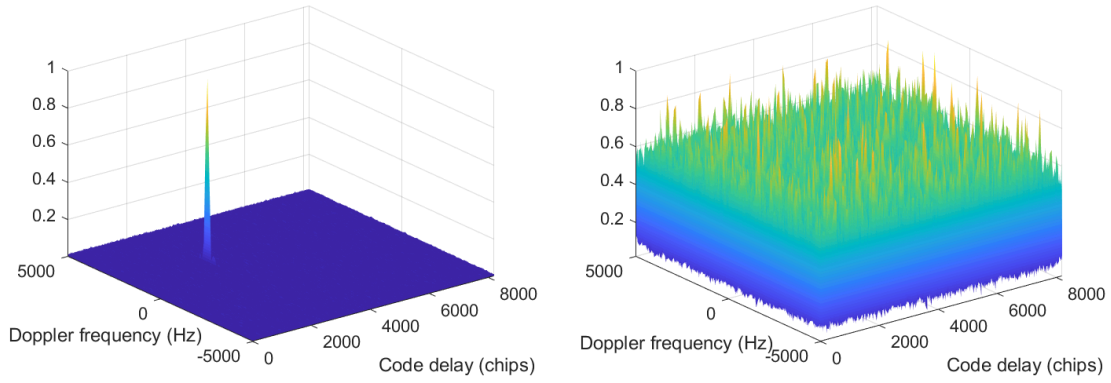

Figure 3.3: Example of CAF over the search space evaluated on a Galileo PRN12 (left) and for PRN21 (right) realistic signal.

More details about these acquisition strategies can be found in [34] as well as in many books such as [103] and [130].

3.4 Tracking

The tracking stage is responsible of refining the code delay and Doppler shift estimates from the acquisition. It has to continuously maintain and correct the best possible alignment between the two codes by means of closed loop operations.

The coupled loops required to maintain the best possible alignment between the two codes, are DLL for the code and a PLL for the carrier. The DLL continuously adjusts the local code replica to keep it aligned with the code of the incoming signal. When the two codes are perfectly aligned, the PRN code is removed from the signal (*code wipe-off*), leaving just the carrier modulated by the navigation messages. This signal is the input of the PLL, which estimates the carrier frequency (*carrier wipe-off*). After *carrier wipe-off* the DLL can synchronize the local carrier and the incoming carrier. This process continuously goes on during the receiver operations [103]. The generic tracking loop (DLL/PLL) architecture is shown in Figure 3.4. The two loops are initialized by the outputs of the acquisition phase ($\hat{\tau}^A$, $\hat{f}_d{}^A$).

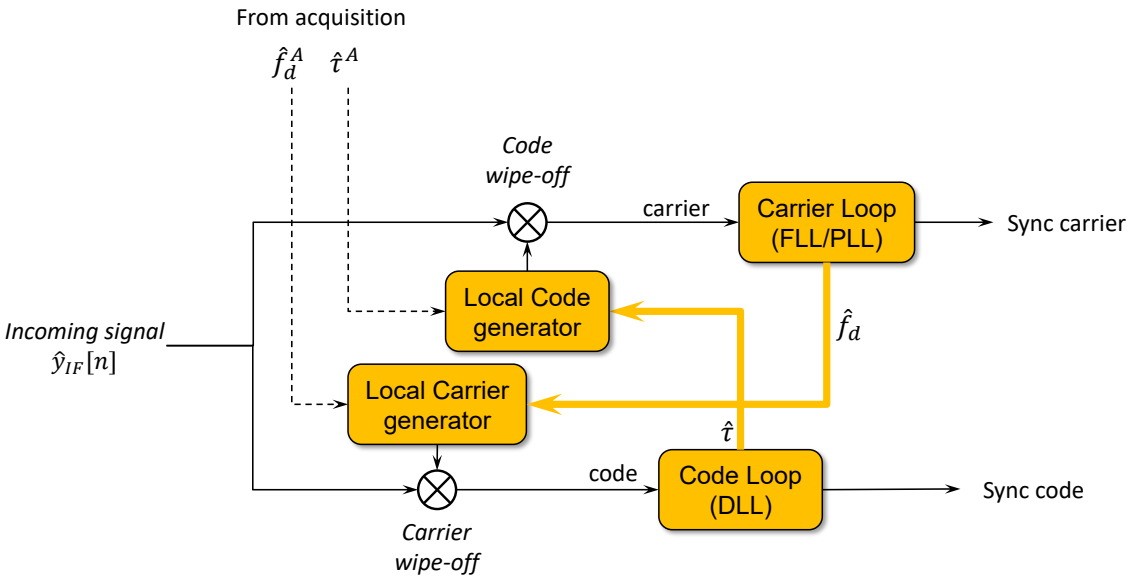

Figure 3.4: Generic tracking loop (DLL/PLL) architecture.

3.4.1 Code tracking loops

The code tracking loop is a feedback loop able to finely estimate the residual code delay by means of a DLL. Since the information about the relative delay between the incoming and the local code is contained in the correlation peak, the goal of DLL is to finely estimate the correlation value. However, GNSS receivers do not search the maximum of the correlation peak since it is not an effective approach and it would be dependent on the absolute peak value. They adopt a strategy insensitive to the absolute peak value, based of a discrimination function that is null only when the incoming and the local codes are synchronized (*null-seeker*).

Figure 3.5 shows the block diagram of a tracking system commonly used in digital GNSS receivers. It is possible to distinguish the code and the carrier tracking loops. Focusing for the moment on the code tracking loop, it is characterized by the design of the components of the loop, such as predetection integrators, code loop discriminator and code loop filter [103]. The first operation to be performed is the correlation between the incoming signal and different local code replicas, each characterized by a different delay. They are denoted as prompt (P), early (E) and late (L) versions. These correlation values are integrated to produce an output which is subsequently used by the discriminator

function, denoted also *S-curve*. This discrimination function is unambiguous with respect to the delay, contrary to the normal correlation function. It is proportional to the difference of the values of the early and late correlators. A comprehensive description about the most common discriminator functions can be found in [103]. The output of the discriminator is given to the code loop filter, which combines the present and past values of the error signal. It generates corrections to the locally generated code in order to maintain the discriminator function output around zero, according to the null seeker principle. The *E*, *P* and *L* replica codes can be synthesized by the code generator, a shift register and the code Numerical Controlled Oscillator (NCO) which generates an accurate code replica of the incoming signal.

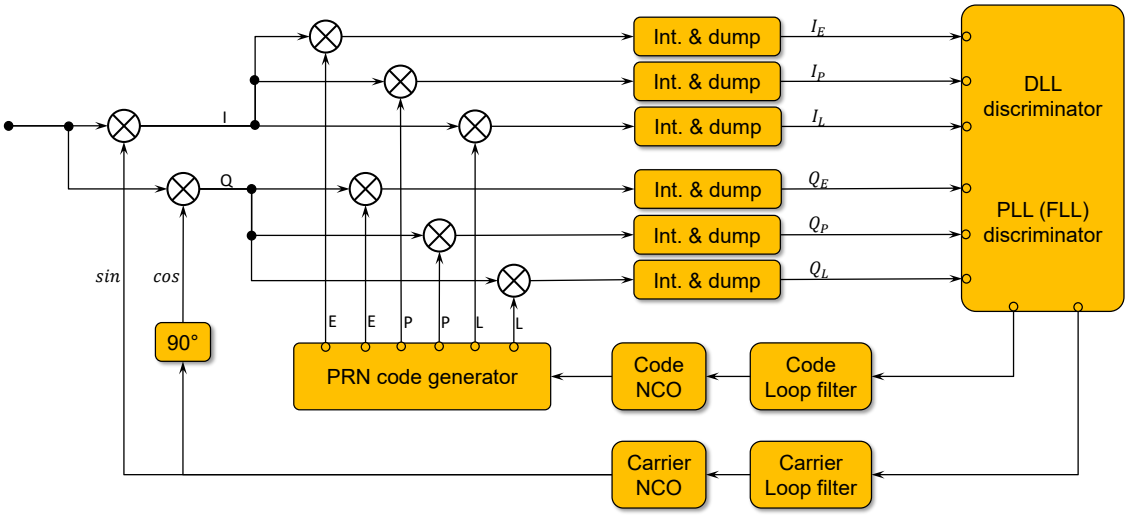

Figure 3.5: Architecture of a generic code and carrier tracking loop block diagram for GNSS receivers.

The process performed by the DLL can be seen in Figure 3.6 where the incoming signal is correlated with the three replicas of the locally generated signal. When the replica code is aligned, the discriminator does not generate any error since early and late envelopes are equal in amplitude. On the other hand, if the replica code is misaligned, the early and late envelopes are unequal by an amount that is proportional to the amount of code phase error between the replica and the incoming signal [103].

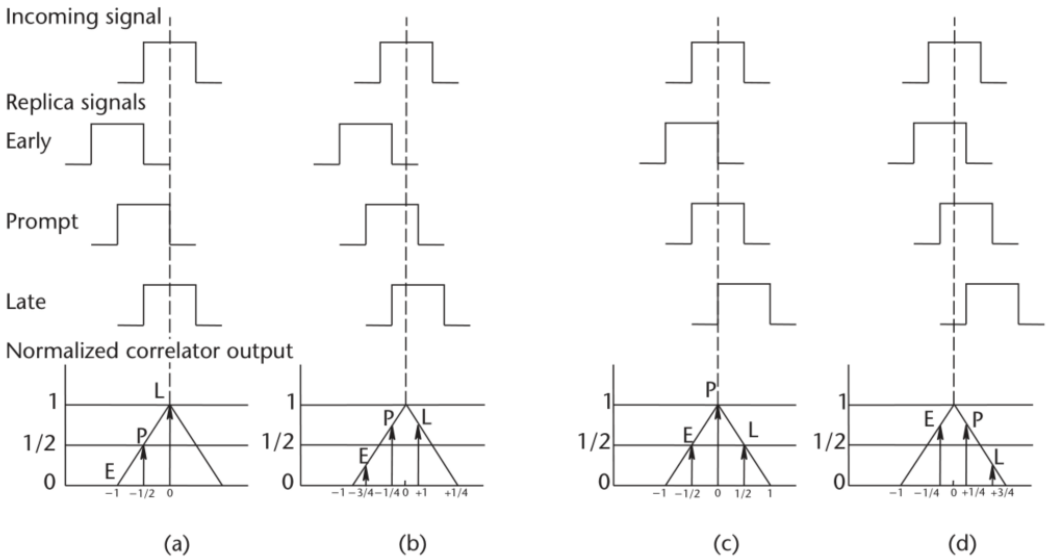

Figure 3.6: Example of code correlation phases: (a) replica code 1/2-chip early, (b) replica code 1/4-chip early, (c) replica code aligned, and (d) replica code 1/4-chip late. Figure taken from [103].

3.4.2 Carrier tracking loops

The carrier tracking loop is a feedback loop able to finely estimate the frequency of a noisy sinusoidal wave and to track the frequency changes while the satellite is moving. In the GNSS community, one of the most used scheme is the PLL. It is able to adjust the frequency of a local oscillator to match the frequency of an input signal. Also the phase of the received signal is estimated. It is worth noting that, if the receiver is tracking a data channel, after the code wipe-off has been performed, the PLL would receive a continuous wave signal still modulated by the navigation data. Therefore, a PLL insensitive to phase transitions has to be adopted. Costas loop is one of the most used in the GNSS community. It tolerates the presence of data modulation on the received signal and then provides a carrier phase reference. Note that if data is not present in the signal, a pure PLL could be used. Another carrier tracking loop is the Frequency Lock Loop (FLL) which is able to track the frequency of the signal, ignoring the phase. In this case, PLL could be used to refine the value of the frequency provided by the FLL. Excellent references about the theory of PLL, FLL and Costas loops, that can be used in GNSS receives, is provided in

many textbooks [103], [144] and [130].

The block diagram of a generic carrier tracking loop is shown in Figure 3.5. The principle of PLL is similar as the one of DLL. The local generator generates two sinusoidal signals, a sine and a cosine, in the two branches of the loop, called In-Phase (I) and Quadrature (Q) components. The role of the PLL is to align the instantaneous phase of the I component with the phase of the incoming signal. After the effect of the noise is mitigated by the integrators, the discriminator extracts the phase difference between the incoming signal and the local one. A loop filter can be included to further reduce the effect of noise. Once the phase difference is approximately zero, the PLL reaches a steady-state condition and the local waveform results aligned with the incoming carrier which is needed for the recovery of the code delay by the DLL.

After code wipe-off has been performed, assuming an unitary amplitude, the incoming signal is

$$y(t) = d(t-\tau)\cos(2\pi(f_{IF} + f_d)t + \varphi) \tag{3.16}$$

Costas loop contains two multiplications. The input signal is multiplied by the local carrier wave as well as by its phase-shifted version by 90°, obtaining two different expressions for I and Q. After low-pass filtering, the two terms with the double intermediate frequency are eliminated and the following two signals remain

$$I = \frac{1}{2}d(t-\tau)\cos(\varphi) \tag{3.17}$$

$$Q = \frac{1}{2}d(t-\tau)\sin(\varphi) \tag{3.18}$$

The phase error of the local carrier phase replica can be found as

$$\frac{Q}{I} = \tan(\varphi) \tag{3.19}$$

By using this discriminator, it can be seen how the phase error is minimized when the correlation in the quadrature-phase arm is zero and the correlation value in the in-phase arm is maximum. Therefore, it is clear that the goal of the Costas loop is to try to keep all

energy in the I (in-phase) arm. According to [103], which also describes other possible Costas discriminators the, the *arctan* discriminator in (3.19) is the most precise of the Costas discriminators, but it is also the most time-consuming.

The characteristics of a PLL can be seen in Figure 3.7. The phasor A is represented by the vector sum of I_P and Q_P. It tends to remain aligned with the I-axis. If a navigation bit transition occurs, it switches 180°. Costas loop is therefore capable to detect the bits in the data message, despite there is a phase ambiguity of 180°.

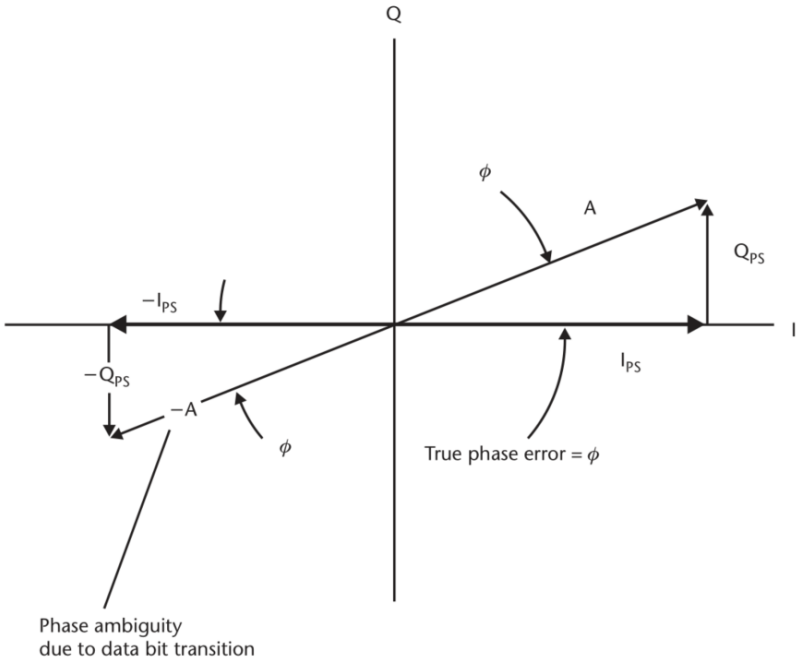

Figure 3.7: I, Q phasor diagram. Figure taken from [103]

3.4.3 Kalman filter-based tracking

One alternative to the traditional tracking loop architectures, is given by the use of a KF to drive the code and carrier NCOs. Replacing scalar loop filters by a KF provides a more adaptive estimation algorithm. This property is embedded within the adaptive nature of KF as the estimation is based on the prediction model, the observation model and the associated statistics. In fact, the benefits of using KF for signal tracking are more evident for receivers operating under changing conditions [138]. Moreover, the

use of KF allows smoother code and carrier error estimation, as demonstrated in [150], which presents smoother-based signal tracking to improve the accuracy of the receiver's estimates code and carrier phase errors.

The measurements of the dynamic process under consideration can be either the GNSS accumulated correlator outputs I and Q or the output of the discriminators. The first model, known as *coherent approach*, results in a "pure" Kalman filter since the measurement noise is non-Gaussian. Therefore, as the discriminators are not involved, there is the advantage of not introducing unmodelled non-linearities in the measurement inputs to the Kalman filter. As a result, it allows the use of higher gains in the Kalman filter as the assumed measurement noise covariance. Unfortunately, this approach presents the high complexity of accurately modeling the mean and variance of the measurement noise processes as well as of having an accurate process model. As a result, it is feasible only under circumstances where the GNSS signal is received with high C/N_0 in order to be able to track the carrier phase variations. On the other hand, the second model is known as *non-coherent approach* and it is characterized by a non-linear relationship between the measurements and the KF states. The use of non coherent integration is the optimum integration architecture in case of weak signal-to-noise environments since the code discriminator function is independent of the carrier phase and then the estimation of precise carrier phase measurements is not required. A comprehensive overview about coherent and non-coherent approaches is given in [82].

The block scheme of the two architectures is shown in Figure 3.8 for coherent (left) and non-coherent (right).

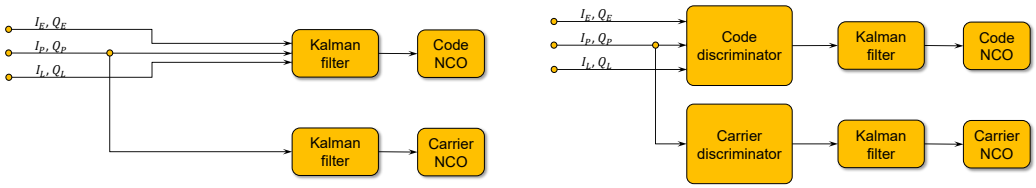

Figure 3.8: Coherent (left) and non-coherent (right) KF-based tracking.

3.5 Navigation solution

When both code and carrier tracking loops are locked, they provide estimate of apparent transmit time and carrier phase of the received signal. These measurements are used to generate the so-called pseudoranges and the carrier phase measurements which, in turn, enable the navigation module to solve the navigation equations.

In order to estimate the pseudoranges, pieces of information gathered both from the tracking module (output from DLL) and from the decoding of the navigation message are used.

Such a navigation message consists of a number of frames and subframes. For instance, in case of GPS C/A signal, a counter named Z-count measures the number of 1.5 seconds since the starting zero time reference. Recalling the structure of the GPS navigation message, it is organized in pages, each containing 5 subframes, and each subframe contains 10 words of 30 bits each. Therefore, in order to estimate the satellite clock time, the Z-count in the current subframe has to be determined plus the time elapsed since the beginning of the subframe. This elapsed time can be measured counting the whole number of navigation data bits transmitted since the beginning of the subframe, plus the whole number of code periods since the beginning of the current navigation data bit, plus the number of chips elapsed in the current code cycle, plus the fraction of the current chip [130]. The last two terms are computed by the DLL and given to the navigation module which, on its own, compute the number of navigation data bits and the number of code periods. This time calculation, in addition to the satellites position extracted from decoding the navigation message, are used to obtain the pseudoranges ρ.

The receiver, in order to determine its spatial coordinates, has to solve a system of equations containing the pseudoranges ρ from at least four satellites in view, with known coordinates. The satellites positions can be computed from the ephemeris and the time of transmission, which are embedded in the navigation message. The fourth equation is needed because of the unknown bias between the user's clock and the satellite time scale. One of the simplest algorithm and one of the most used for estimating the position is the Least Square (LS) method. However, other methods can be adopted, such as

Kalman filter. The latter takes into consideration the previous states of the system and the evolution of the solution and then it is able to smooth the LS solutions.

Estimation using Least squares

The LS method is the most used for solving the set of equations containing the pseudoranges. The generic j-th pseudorange ρ was defined in (2.3) and reported here for clarity

$$\rho_j = \sqrt{\left(x_{sj} - x_u\right)^2 + \left(y_{sj} - y_u\right)^2 + \left(z_{sj} - z_u\right)^2} + b_{ut} \tag{3.20}$$

where x_u, y_u, z_u are the user coordinates, x_{sj}, y_{sj}, z_{sj} are the coordinates of the j-th satellite, and $b_{ut} = c \cdot \delta t_u$ is the clock bias term. The intersection of four spheres from four satellites is then given by the following system of equations

$$\begin{cases} \rho_1 &= \sqrt{(x_{s1} - x_u)^2 + (y_{s1} - y_u)^2 + (z_{s1} - z_u)^2} + b_{ut} \\ \rho_2 &= \sqrt{(x_{s2} - x_u)^2 + (y_{s2} - y_u)^2 + (z_{s2} - z_u)^2} + b_{ut} \\ \rho_3 &= \sqrt{(x_{s3} - x_u)^2 + (y_{s3} - y_u)^2 + (z_{s3} - z_u)^2} + b_{ut} \\ \rho_4 &= \sqrt{(x_{s4} - x_u)^2 + (y_{s4} - y_u)^2 + (z_{s4} - z_u)^2} + b_{ut} \end{cases} \tag{3.21}$$

The solution of (3.21) gives the user location and the value of δt_u, allowing the user to synchronize its own receiver to the GNSS time scale.

Knowing an approximation of the true position and bias $\left(\hat{x}_u, \hat{y}_u, \hat{z}_u, \hat{b}_{ut}\right)$, and expanding (2.3) in a Taylor series centered in $\left(\hat{x}_u, \hat{y}_u, \hat{z}_u, \hat{b}_{ut}\right)$ it is possible to obtain the position offset $(\Delta x_u, \Delta y_u, \Delta z_u, \Delta b_{ut})$ as a linear function of the known coordinates and of the pseudorange measurements. The delta-pseudorange $\Delta\rho_j = \hat{\rho}_j - \rho_j$ can be written as

$$\Delta\rho_j = a_{xj}\Delta x_u + a_{yj}\Delta y_u + a_{zj}\Delta z_u - \Delta b_{ut} \tag{3.22}$$

Putting these equations in matrix form, the following system can be obtained:

$$\Delta\boldsymbol{\rho} = \mathbf{H} \cdot \Delta\mathbf{x} \tag{3.23}$$

where

1. $\Delta\boldsymbol{\rho} = (\Delta\rho_1 \ \Delta\rho_2 \ \ldots \ \Delta\rho_n)^T$ as the vector offset of the error-free pseudorange values corresponding to the user's actual position and the pseudorange values corresponding to the linearization point;

2. $\Delta\mathbf{x} = (\Delta x_u \ \Delta y_u \ \Delta z_u \ -\Delta b_{ut})^T$ as the vector offset from the position linearization point;

3. $\mathbf{H}$ as the geometrical matrix containing, in the first 3 columns, the unit vectors pointing from the linearization point to each j-th satellite

$$\mathbf{H} = \begin{pmatrix} a_{x1} & a_{y1} & a_{z1} & -1 \\ a_{x2} & a_{y2} & a_{z2} & -1 \\ \ldots & \ldots & \ldots & \ldots \\ a_{xn} & a_{yn} & a_{zn} & -1 \end{pmatrix} \tag{3.24}$$

The system (3.22) has solution:

$$\Delta\mathbf{x} = \mathbf{H}^{-1}\Delta\boldsymbol{\rho} \tag{3.25}$$

When more than 4 pseudorange measurements are available, the method of LS can be used to calculate the displacement $\Delta\mathbf{x}$.

Then, starting from the general representation of (A.7), and neglecting the weighting matrix W, the solution becomes:

$$\Delta\mathbf{x} = (\mathbf{H}^T\mathbf{H})^{-1}\mathbf{H}^T\Delta\boldsymbol{\rho} \tag{3.26}$$

3.6 Vector tracking GNSS receivers

Conventional GNSS receivers use a decentralized architecture separating the tracking module from the navigation module. Within this scheme, each channels' measurements are incorporated into the navigation filter to estimate the PVT solution. As a consequence, if one channel is corrupted – based on the intelligence of the navigation filter – can be

ignored and not corrupting the other ones. This structure, denoted as scalar tracking, shows relatively ease of implementation and it can be considered as the *standard* GNSS receiver. However, it is not able to cope with signals with low C/N_0 since the possibility for one channel to aid another one, cannot be exploited.

On the contrary, vector tracking receivers are characterized by a deep level of integration between signal processing and the navigation processor. The main difference with respect to scalar tracking, is that the channels are not tracked individually and independently anymore but they are aided from the navigation filter. Within this approach, once a good PVT solution is available, satellite signals can be continuously tracked even under weak signal conditions.

Vector tracking was first proposed by [168] where the authors addressed a Vector Delay Lock Loop (VDLL) processing for GPS signals. The architecture of a VDLL-based receiver was described as well as the potential advantages in improving noise performance. Afterwards, several authors investigated the potentiality of such an implementation discussing the benefits and the weaknesses under different conditions. In [142] [141], the authors extended the analysis to Vector Frequency Lock Loop (VFLL) showing the benefits of a VDLL/VFLL based receiver and its capability to track signals with extremely low C/N_0. Also, the perforamnce of vector tracking based receiver were assessed under weak signal conditions in [111], [166] and under the presence of different threats, such as jamming [139], [85], [32] and ionospheric scintillations [55]. Moreover, various methods of implementing a vector-tracking receiver were discussed in [148], with focus on the carrier phase tracking performance of the receiver.

The architecture of a vector-based tracking GNSS receiver is reported in Figure 3.9. The navigation filter is the core of the vector-tracking receiver and it is often implemented according to an EKF scheme. Following the discussion about coherent and non-coherent KF tracking-based architectures in Section 3.4.3, it can be applied also to the vector tracking structure. Recalling the main principles of both architectures, non-coherent vector tracking use the output of the discriminators as measurements vector for the navigation filter. Despite they introduce non-linear modeling errors, they can sustain tracking with low C/N_0 provided that the estimation of precise carrier phase

measurements is not required. On the other hand, coherent approaches use directly the correlators outputs as measurements vector for the navigation filter. Non-coherent architecture is adopted within the block scheme of the vector tracking receiver reported in Figure 3.9. The tracking errors for a specific channel are estimated by the *channel filter*. Such a filter includes either DLL and PLL loop filters in case of scalar-based tracking or a KF in case of KF-based tracking. The advantaged and disadvantages of using the two approaches were discussed in Section 3.4.3.

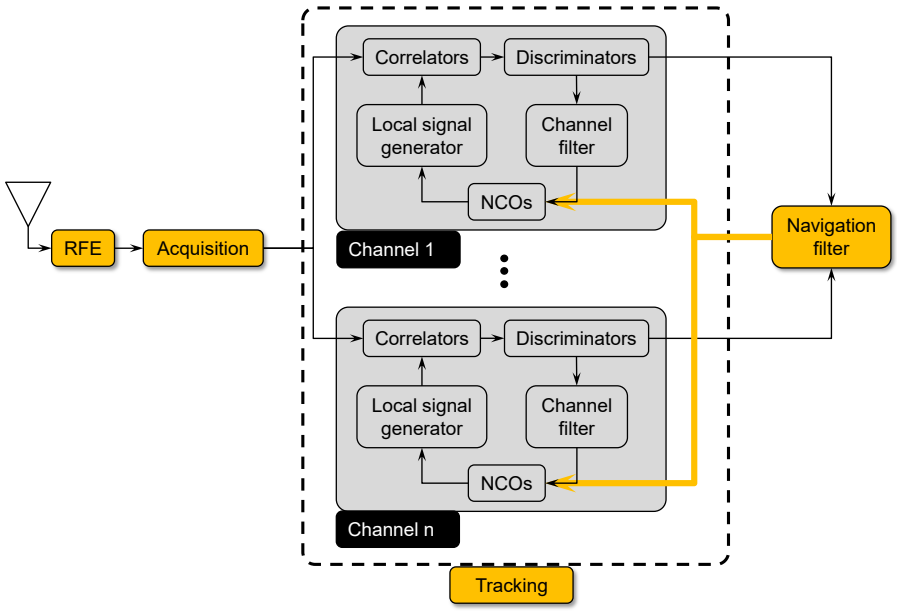

Figure 3.9: Architecture of a non-coherent vector-based tracking GNSS receiver.

The deep level of integration characterized by the vector-tracking receivers, with respect to the conventional receivers, is represented by the feedback from the navigation filter to the NCOs. According to a non-coherent approach, the incremental observations (pseudorange and pseudorange rate residuals) are generated from the code and carrier discriminators, while the feedbacks to the NCOs are computed from the prediction of the code rate and Doppler frequency derived from the EKF. In this way the satellite signal processing channels are coupled together through the common feedback from the filter states. Since the KF generates optimum estimates of signal parameters of each satellite, based on the correlation outputs from all channels, the noise is therefore reduced

in all channels. In order to keep a stable and reactive tracking process, the feedback must be generated at 'correlation rate' (i.e., between 50 Hz and 1 kHz), which may be a challenging requisite for the centralized filter.

In particular, the code frequency can be computed in the discrete time domain as [159]:

$$\hat{\mathbf{f}}_{code}[n] = \left[f_{code} - \frac{f_{code}}{c} \frac{\Delta\hat{\boldsymbol{\rho}}[n]}{T_c} \right]^T \in \mathbb{R}^{N_{sat},1} \tag{3.27}$$

where f_{code} is the code frequency, expressed in Hz; c is the speed of light, expressed in m/s; T_c is the sampling interval, expressed in s; $\Delta\hat{\boldsymbol{\rho}}[n] = \hat{\boldsymbol{\rho}}[n] - \hat{\boldsymbol{\rho}}[n-1]$ is vector of the difference between the pseudoranges, estimated by the navigation filter at instant n and n-1, expressed in m.

On the other hand, the carrier frequency can be computed as:

$$\hat{\mathbf{f}}_{carr}[n] = \left[f_{IF} - \frac{f_{carr}}{c} \frac{\hat{\boldsymbol{r}}[n]}{T_c} + \frac{f_{carr}}{c} \Delta v_\tau[n] \right]^T \in \mathbb{R}^{N_{sat},1} \tag{3.28}$$

where f_{IF} is the intermediate frequency of the signal, expressed in Hz; f_{carr} is the carrier frequency of the signal, expressed in Hz; $\hat{\boldsymbol{r}}[n]$ is the vector of the pseudorange rates, estimated by the navigation filter at instant n, expressed in m/s; $\Delta v_\tau[n]$ is the receiver clock drift, expresses in m/s.

3.7 SDR-based GNSS receivers

The increasing success of satellite based navigation applications is boosting the development of improved technologies for navigation receivers. Although GNSS receivers must adopt more and more complex signal processing techniques, to meet such high requirements, when compared with communication receivers, they deal with much lower data-rates, thus making them appealing for SDR implementations. The concept of SDR was introduced by [131] for the implementation of communication transceivers and the implementation of GNSS receivers according to this paradigm, thus represents a specific implementation case. It consists of replacing some hardware components with

software-based signal-processing techniques enabling reconfigurable radio communication architectures. It then provides a useful simulation and testing environment and opens to the prototyping of new architectures. Although the application to the whole set of GNSS signals is limited by the processing capabilities of the hardware architectures, SDR technology has steadily evolved over the last decades in the field of satellite navigation receivers. The opportunities opened by SDR in the field of GNSS receivers are discussed in [119]. A brief history of GNSS software receivers, the opportunities and practical engineering challenges that they pose for manufacturers, and the state of the art and related applications of them are discussed in [180].

SDR GNSS receivers are usually implemented either in mixed Hardware (HW)/Software (SW) modules or according to a fully software approach.

HW/SW mixed solutions implement dedicated and optimized hardware blocks to efficiently perform tasks in a parallel manner. Recent improvements on the technology of Field Programmable Gate Array (FPGA), make this technology very attractive for SDR-targeted receivers implemented according to a reconfigurable logic. Within this configuration, the HW/SW partitioning dominates the overall performance of the receiver and its degree of flexibility. Design rules foresee the use of HW modules to compute the intensive tasks, such the implementation of the acquisition unit as well as the correlators of the tracking loops. On the other hand, algorithms that need to be configured and upgraded such as the generation of the pseudoranges and PVT computation, are embedded in SW routines. As an example, the design of a GNSS receivers according to an HW/SW approach are described in [170] and [96].

On the other hand, fully SW SDR GNSS receivers feature a digital processor based on a General Purpose Processor (GPP). Within this architecture, the core of the receiver is implemented in SW running on a GPP, e.g. a Personal Computer (PC), which is in charge of receiver the digitized data collected by a front-end. They are interfaced either via a Universal Serial Bus (USB) communication port or Ethernet connections. Although fully SW receivers allow high reconfigurability, flexibility and independence from the HW platform, their cost, size and power dissipation make the commercial diffusion quite improbable in the short term. In fact, this kind of receivers are mostly used for research

and development purposes becoming very popular in universities and research centers. The first implementation of a fully SW SDR GNSS was proposed in the dissertation of [19] addressing the GPS $L1$ C/A signal. The Matlab version of the receiver was then documented as a book [35]. Other implementations can be found in [133] and [164].

The adoption of new processing platforms and their associated processing techniques, is pushing toward the concept of cloud-GNSS which consists of migrating the heavy tasks required by the receiver signal processing stages from local into a distribute, scalable and high-performance computing platform. [51] gives an overview about the different receiver topology by means of traditional and cloud-based architectures. In [123] the authors relied on a cloud-based GNSS approach to migrate the signal processing modules – acquisition, tracking and PVT blocks – to the cloud platform whereas the GNSS sensor consisted of the RFE only. They also discussed the energy consumption and the economic aspects of migrating the GNSS signal processing in the cloud.

Chapter 4

Sensors for positioning

Multiple positioning technologies and sensors are available nowadays. Based on the own different nature, each sensor can provide absolute or relative positioning. Within this context, GNSS provides the user with accurate estimates of his own position and velocity in a global frame and with errors bounded in any instant. In fact, GNSS is considered as the dominant technology as already in use in an infinite number of navigation units performing outdoor. Unfortunately, due to the physical principle of satellite based position determination, GNSS is highly environmental dependent. Environments characterized by the presence of high buildings and other objects in the line of sight between the user and the satellite, might attenuate, block or reflect the weak signal traveling from the satellite to the Earth. These effects may be limited relying upon other sensors, that can be coupled with satellite navigation receivers, to enhance the performance of the whole navigation system. Such an integration combines the advantages of the different technologies, limiting, at the same time, the weaknesses of each individual sensor.

Nowadays there is a plethora of positioning technologies available, that can be coupled with GNSS, to reach a robust and reliable navigation solution. They have been already exploited by the scientific community, as reported by the literature review given in this Chapter, and aim at guaranteeing the user requirements in term of accuracy, cost, coverage, date rate, integrity and more. Considering this broad number of sensors, a cost-effective solution is the one proposed in this work which includes INS, visual

sensor and odometer, in addition to GNSS. These technologies offer several advantages with respect to other well spread navigation solution (Simultaneous Localization And Mapping (SLAM), LiDAR-based, short range RAdio Detection And Ranging (RADAR), etc.) in particular considering the cost of the sensors, the computational complexity of the fusion filter, and the simplicity of on-board implementation. It is obvious that other subset of sensors might be considered, based on the user requirements and on their relevance in the ITS domain.

This Chapter first provides a review of the most commonly used coordinate systems, together with their relationship, which is essential to define the framework for fusing the information to reliable estimates on position, velocity, and attitude. Afterwards, an overview about the use of multiple sensors for positioning is given, together with a literature review about the use of these technologies for navigation purposes. Eventually, the fundamental concepts of INS, visual sensor and odometer are given in the remainder of this Chapter.

4.1 Coordinate frames

The concept of a coordinate frame is used to define the position and orientation of an object and it is essential to define the framework for fusing the information to reliable estimates on position, velocity, and attitude. GNSS measures the position with respect to a constellation whereas other sensors, such as INS or visual sensors, measure the motion with respect to an initial frame. Since typically a generic user wants to know its position with respect to the Earth, it is very important to define the main coordinate frames used in navigation and their relationship.

Earth-Centered Inertial frame

Earth-Centered Inertial (ECI) frame is known also as a i-frame. The origin of the ECI coordinates is at the center of the mass center of the Earth. The z-axis always points along the Earth's axis of rotation from the center to the true (and not magnetic) north pole. The x-y plane spans the equator and the x-axis point towards the vernal equinox,

which is the spring equinox in the northern hemisphere.

Within this coordinate frame, the axes do not rotate with the Earth. The *y*-axis always lies 90 degrees ahead of the *x*-axis in the direction of rotation. Such a frame is important in navigation because inertial sensors measure motion with respect to an inertial frame.

Earth-Centered Earth Fixed frame

Similarly to the ECI frame, an Earth-Centered Earth-Fixed (ECEF) frame has the origin at the mass center of the earth. ECEF frame is known also as a *e*-frame. The difference is that the coordinates rotate with the Earth and the *x*-axis is defined as going through the Greenwich meridian. The *y*-axis completes the right-handed orthogonal set, pointing from the center to the intersection of the equator with the 90-degree east meridian.

GNSS coordinates and user position are natively expressed in ECEF frame. It is important in navigation since it gives the position relative to the Earth.

Navigation frame

The coordinate of a navigation frame, known also as a *n*-frame, serve as local reference directions for representing the vehicle attitude and velocity. A common orientation is the North-East-Down (NED) frame where the *x*-axis points towards true north, the *y*-axis points east and the z-axis points toward the centre of the earth.

The local navigation frame is important in navigation because the user wants to know their attitude relative to the north, east, and down directions. For position and velocity, it provides a convenient set of resolving axes, but is not used as a reference frame.

Body frame

The origin of the body frame coincides with that of the local navigation frame, but the axes remain fixed with respect to the body. For angular motion, the *x*-axis is the *roll* axis, the *y*-axis is the *pitch* axis, and the *z*-axis is the *yaw* axis. Hence, the axes of the body frame are sometimes known as *roll*, *pitch*, and *yaw*. This concept, widely used within the

remainder of the dissertation, is depicted in Figure 4.1.

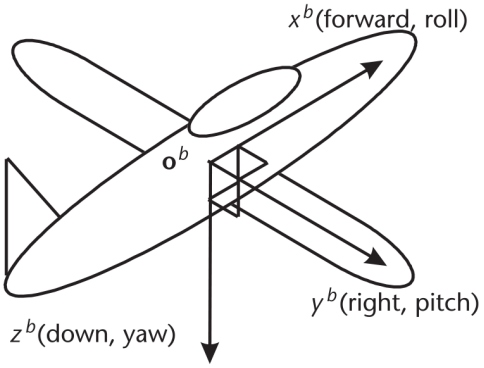

Figure 4.1: Body frame axes. Figure from [81].

Coordinate transformations

Coordinate transformations allow to represent a vector into different coordinate systems. One technique that can be used to perform the transformation, is the application of a Direction Cosine Matrix (DCM). The derivation of C can be found in several textbooks [81]. Here only the final expression is given. The DCM from the e-frame to the n-frame is:

$$C_e^n = \begin{bmatrix} -\sin\varphi\cos\lambda & -\sin\varphi\sin\lambda & \cos\varphi \\ -\sin\lambda & \cos\lambda & 0 \\ -\cos\varphi\cos\lambda & -\cos\varphi\sin\lambda & -\sin\varphi \end{bmatrix} \tag{4.1}$$

where φ and λ are the geodetic latitude and geodetic longitude, respectively.

The DCM from the b-frame to the n-frame is:

$$C_b^n = \begin{bmatrix} c\theta c\psi & -c\phi s\psi + s\phi s\theta c\psi & s\phi s\psi + c\phi s\theta c\psi \\ c\theta s\psi & c\phi c\psi + s\phi s\theta s\psi & -s\phi c\psi + c\phi s\theta s\psi \\ -s\theta & s\phi c\theta & c\phi c\theta \end{bmatrix} \tag{4.2}$$

where θ, ψ and ϕ are the roll, pitch and yaw, respectively. s and c indicates *sin* and *cos*, respectively.

The Euler angles can be determined from the DCM C_b^n with the following equations

$$\phi = \arctan 2 \left(C_b^n[3,2], C_b^n[3,3] \right) \tag{4.3}$$

$$\theta = -\arcsin \left(C_b^n[3,1] \right) \tag{4.4}$$

$$\psi = \arctan 2 \left(C_b^n[2,1], C_b^n[3,1] \right) \tag{4.5}$$

where $\arctan 2(y, x)$ is a four quadrant inverse tangent function.

4.2 Sensors' overview and related works

Nowadays a vast number of positioning technologies is available. Based on the own different nature, each sensor can provide absolute or relative positioning, as shown in Figure 4.2. Moreover, they can exploit different physical principles, such as inertial measurements (accelerometers and gyroscopes), mechanical waves (audible and ultrasound), RF (Ultra Wide Band (UWB), bluetooth, Wi-Fi) and visible light (imaging sensors, infrared sensors). A deep survey on positioning systems is given in [126], [54].

Among these technologies, INSs are certainly the most widely used complementary technologies to GNSS. INSs are self-contained sensors and include accelerometers and gyroscopes measuring the measures specific force and the angular rate, respectively. They provide relative position independently from the environment but, unfortunately, the are affected by unbounded errors. The complementary error characteristics of GNSS and INS thereby significantly improve the integrated navigation solution. In fact, sensor fusion between GNSS and INS has been studied extensively in the last decade addressing different level of integration, depending on the final application [146], [64], [92], [65], [165].

Mobile laser scanners, known as LiDARs, are ranging technologies for rapid spatial data collection and 3D point cloud generation. They are composed by a rotating beam which measures distances and polar angles between the sensor and the surrounding spaces,

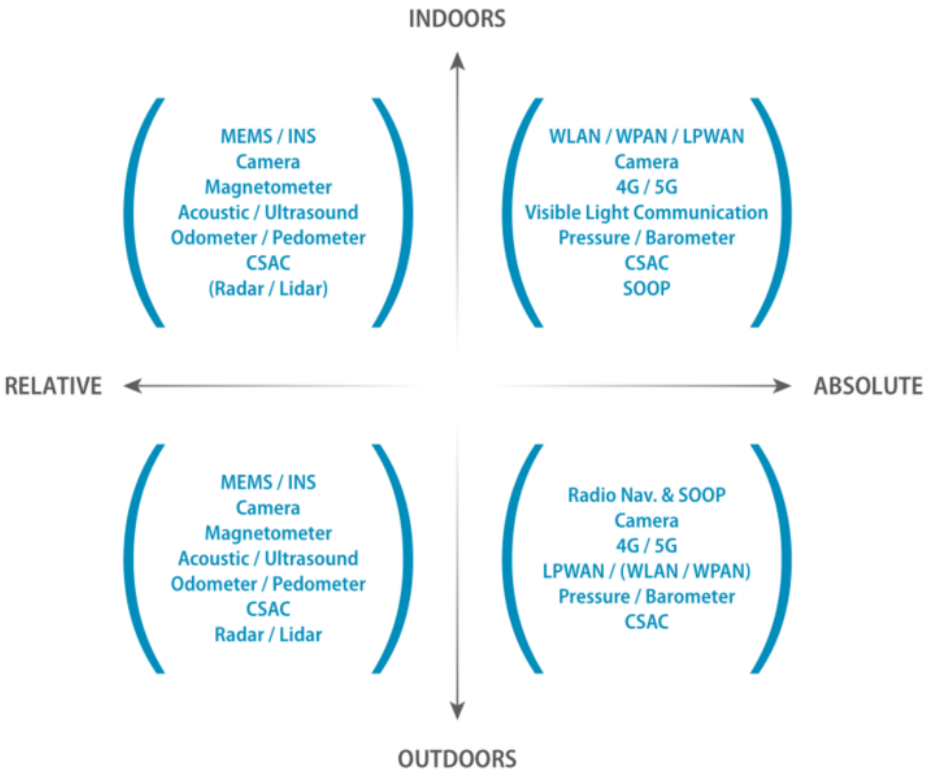

Figure 4.2: Complementary technologies to GNSS [17].

through a light laser. The distances can be estimated by Time of Flight (ToF) measurements or phase measurements. The 3D information provided by this system can be used to perform navigation. The environmental map is usually used in autonomous navigation systems as aiding information for enhancing the accuracy of the positioning engine as well as for obstacle avoidance or context sensing [104]. In order to geo-referencing the environmental 3D model, accurate pose of the scanner is required. Typically, this information is provided by GNSS and INS. However, when these sensors are not available, SLAM method could be exploited for the pose estimation. In fact, SLAM consists on solving the problem of creating a map of an unknown environment while simultaneously maintaining a location within that map [36], [70], [122]. As an iterative estimation problem, SLAM starts with a known condition (location and pose of the user) which is propagated using a prediction model based on the body motion. SLAM is usually implemented using statistical techniques, such as Kalman or particle filters.

Imaging sensors (RGB cameras and/or infrared cameras) are widely used for navigation due to the possibility to extract not only spatial information, simulating human perception, but also geometric relations between the camera and the real world. The process of estimating the ego-motion of a body using the information contained in the images acquired by a camera, is known as Visual Odometry (VO). In particular, VO incrementally estimates the camera pose by observing the changes that motion induces on the images, i.e. correspondent features. This motion is represented by a three-dimensional rigid transformation between subsequent frames, which is composed by rotation and translation. This relation is equivalent up to a scale factor, which means solving the distance between the camera center and the 3D object scene. Usually, this is computed by using two cameras (stereo-camera), provided that their baseline is known [99], [27]. However, the distance between the two cameras affects the accuracy of the motion estimation obtained from images. The farther the two cameras are from each other the better the accuracy [94]. Monocular camera might also be exploited to retrieve information about the distance of the objects being photographed. It consists on extracting this distance from external information, like an a-priori 3D model or an active ranging sensor. On the other hand, if context information is not provided, the distance between the camera center and the object point can be estimated by geometrical relations. For instance, when the camera is pointing down to the ground, the distance is constant and equals the height of the camera. The method utilizing the downward-pointing camera has been used in the applications of vehicle navigation [137], [107] and in pedestrian navigation [91].

In autonomous navigation, a wide spread image-based method is the visual SLAM. In addition to the VO, it not only provides navigation but it also constantly builds and updates a map based on the visual information. The map is built associating visual features to location landmarks. As the estimated location of the landmark is highly correlated with the estimated position of the user, it is necessary to estimate both the user pose and landmarks position simultaneously [183], [163], [112], [60], [30].

Another technology that can be used for positioning includes ultra-sound systems. This kind of systems, that are based on mechanical waves, measure oscillations or pressure transmitted through a medium. Within this context, the most simple configuration foresees

the use of two devices for range estimation using ToA of received pulses. In contrast to RF-based systems, they operate in short ranges, typically under 10 meters. Locating several devices (beacons) within the environment, it is possible to estimate the receiver (listener) position by multi-lateration. As in the case of other RF signals, Time Difference of Arrival (TDoA) method are typically used to avoid issues related to time synchronization. Application of positioning system based on ultra-sound have been investigated in [108], [24].

Wireless Local Area Network (WLAN), also known as Wi-Fi, can be used to estimate the position of a device lying within the network. Since WLAN signals are available in many indoor environments, they can be easily exploited to perform indoor but also outdoor positioning, to certain extent. Positioning estimation methods are based on ToA, Angle of Arrival (AoA), although the most popular method is to make use of Receives Signal Straight Indicator (RSSI), which is particularly easy to extract from the access point. Other strategies consist on propagation modeling, Cell of Origin (CoO), multi-lateration and fingerprinting. A compltete overview about these methods is provided in [109]. However, the main disadvantage of these systems concerns security and privacy as some cyber-attacks might capture transmitted packets and retrieve the user position. The use of this technology for navigation has been already exploited in several works [113], [18], [68].

UWB positioning systems are RF-based technologies for communication and radar applications. The band allocated to this technology is 7.5 GHz wide, enormously grater with respect to any other communication channels. In order to cover this huge bandwidth, very short pulses, narrow in the time-domain, are used. This signal characteristics provide several advantages in positioning estimation. In fact, the short duration of a pulse allows very little uncertainty in time measurements at the antenna receivers. Knowing signal reception time with little uncertainty means estimating distances with high accuracy. By combining the distances estimated by multiple anchors spread within a network, it is possible to use multi-lateration to estimate the position of a receiver. Several implementations of UWB for positioning and navigation can be found in [93], [52], [124], [43], [77].

A magnetic compass provides absolute angle information of the user with respect to magnetic north by measuring the intensity of Earth's magnetic field [42]. In the most common implementation, it is hybridized with an inertial platform which provides the motion direction. It can be used as a standalone system, provided that it belongs to a network of magnetometers. In general, the magnetic positioning systems have high accuracy and do not suffer from non-line-of-sight errors between sensors and tracked objects. However, the limited coverage and the interference produced by steel and metal structures can affect the performance of the systems. These issues can be ovecame by using multiple magnetometers in array configuration. The use of magnetic systems for navigation has been exploited by several works [15], [42].

RADAR is a technique to estimate the range and the angle of incidence to an object. It is based on the basic concept that the distance is linearly related to the ToF. This time can be measured observing the tiny part of wave's energy that return to the transmitter antenna after bouncing back from a passive surface. More recent implementations consist in multiple devices composed by transceivers which actively receive and transmit the signal used in multi-lateration approaches. Several research have been made to provide positioning estimation using continuous or modulated waves radar [169], [134].

The use of the odometer in navigation, which provides information about the curvilinear distance traveled by a vehicle, has been extensively exploited by the GNSS community as coupled with GNSS and other sensors to enhance the performance of the integrated system [176], [72] [88], [69], [167]. In fact, although some other technologies may be used for the estimates along the longitudinal axis of the vehicle, it is the most widely spread approach [175].

INS, visual sensor and odometer have been chosen in this thesis to be integrated with GNSS. They are described in detail in the remainder of this Chapter.

4.3 Inertial Navigation Systems

Inertial sensors comprise accelerometers and gyroscopes. Accelerometers are sensors for measuring inertial acceleration and provide position and velocity. On the other hand,

gyroscopes are sensors for measuring rotation and measure rotation rate. Inertial sensors thus retrieve relative measurements, that can be used to compute position, velocity and attitude with respect to an initial condition and with respect to an initial frame. The different coordinate frames involved in the navigation domain, together with their relationship, must properly defined since GNSS and INS measure their quantities with respect to different frames.

INSs exhibit small short-term errors, they can output the own measurements with very high rate and they are insensitive to environmental condition as well as to external sources of errors. Moreover, they are self-contained sensors, in the sense that no external infrastructures are required for operation. However, they exhibit unbounded errors that rapidly degrade, i.e. drifts. The principle of inertial sensors and inertial technology can be found in [81] and [79].

A detailed description of INS is given in the remainder of this Section describing the system of equations used to compute the position, velocity and attitude, i.e. *mechanization*, as well as the characterization of the noise affecting inertial sensors. The term IMU is also introduced, which is represented by the ensemble of sensors for the INS, that are typically placed in a single enclosure.

4.3.1 Structure of INS

The ensemble of inertial sensors, rigidly mounted to a common base, is called inertial sensor assembly and it is illustrated in Figure 4.3. In particular, an accelerometer measures specific force and a gyroscope measures angular rate. Multiple accelerometers and gyroscopes, usually three per each, are combined by an IMU. The IMU coupled with a computational unit form the INS. IMU can be categorized based on their accuracy (or grade). According to [81], they can be grouped into five broad performance categories, such as: *marine-grade*, *aviation (or navigation)-grade*, *intermediate-grade*, *tactical-grade* and *automotive-grade*. Low-cost Micro Electro-Mechanical System (MEMS)-IMU can be included into the *automotive-grade*. In the mass-market sector, current inertial sensor development is focused on MEMS technology, which are small sensors able to

realize low-performance IMU.

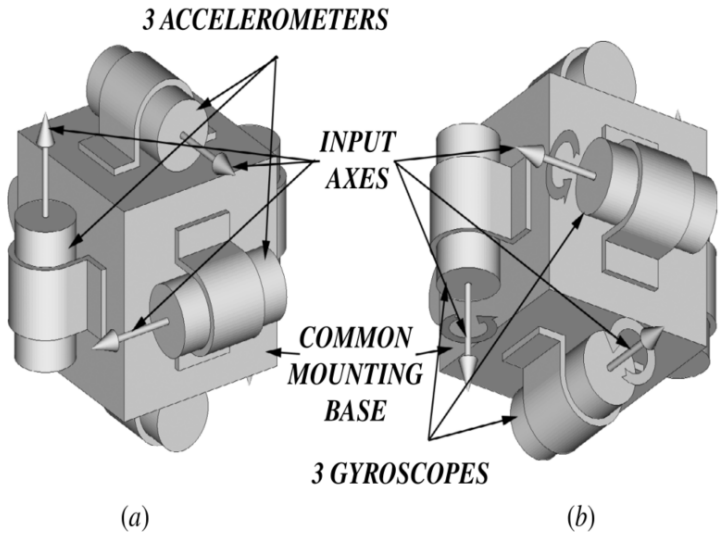

Figure 4.3: Inertial sensor assembly components. Figure from [79].

The specific force measured by the accelerometers, may be integrated in time in order to obtain the body velocity and, after one more integration, the body position, both with respect to an initial condition. However, accelerometers do not sense directly the gravity acceleration **g**, but the reaction to this acceleration, applied by the surface where the body lies. In fact, a 3-axis accelerometer measures the so-called specific force **f**, which is the acceleration of the body comprising the (reaction to the) gravity component

$$\mathbf{f}(t) = \mathbf{a}(t) - \mathbf{g}(t) \tag{4.6}$$

where $\mathbf{a}(t)$ is the total acceleration that determines the body motion in the inertial frame. The motion of the body is extracted by removing the gravity component sensed by the accelerometer from the total acceleration acting on the body.

Gyroscopes measure orientation, traditionally based on the principle of conservation of the angular momentum. The angular orientation of the body can be calculated by integrating the angular rate measurements, provided that an initial orientation of the sensor axis with respect to a reference is given.

A system, where a stable platform is mechanically isolated from the rotations of the

host vehicle is denoted as *gimballed system*. On the other hand, a system where the inertial sensors are mounted directly on the vehicle and move integrally with it, is known as *strapdown* system. Strapdown systems are far more common than gimballed ones, because of the simplicity of their mechanical realization.

4.3.2 The Coriolis theorem

The Coriolis theorem relates the velocity of the body with respect to the Earth measured in an inertial frame $\mathbf{v}^i(t)$ to the velocity expressed in the rotating frame $\mathbf{v}^e(t)$

$$\mathbf{v}^e(t) = \dot{\mathbf{p}}^e(t) = \mathbf{v}^i(t) - \boldsymbol{\omega}_{ie} \times \mathbf{p}(t) \tag{4.7}$$

where the superscript b, i and e indicate quantities expressed in the body, inertial and Earth reference frame, respectively. $\mathbf{v}^e(t)$ is the ground speed, $\mathbf{v}^i(t)$ is the speed with respect to the inertial frame, $\boldsymbol{\omega}_{ie}$ is the turning rate of the ECEF frame with respect to the inertial frame, $\times$ denotes vector cross product and $\mathbf{p}^e(t)$ is the position of the vehicle on the Earth [173]. The acceleration can be obtained as the derivative of (4.7) as [173]:

$$\dot{\mathbf{v}}^e(t) = \ddot{\mathbf{p}}^e(t) - \boldsymbol{\omega}_{ie} \times \mathbf{v}^e(t) - \boldsymbol{\omega}_{ie} \times \left[\boldsymbol{\omega}_{ie} \times \mathbf{p}^i(t)\right] \tag{4.8}$$

where term $\boldsymbol{\omega}_{ie} \times \mathbf{v}^e(t)$ is known as Coriolis acceleration and represents the acceleration caused by the body velocity over the surface of a rotating Earth, while the term $\boldsymbol{\omega}_{ie} \times \left[\boldsymbol{\omega}_{ie} \times \mathbf{p}^i(t) \right]$ defines the centripetal acceleration experienced by the body owing to the rotation of the Earth.

4.3.3 Mechanization equations

The system of equations used to compute the instantaneous position, velocity and attitude, in the selected reference frame, is called *mechanization*. They can be computed in each frame. Hereafter, we consider the ECEF frame. Basically, these equations might be represented by three main steps: body attitude computation, body velocity computation and derivation of the body position.

Attitude computation

The attitude update step uses the angular rate vector expressed in the *e*-frame. it can be obtained as [173]

$$\boldsymbol{\omega}_{eb}^{b}(t) = \boldsymbol{\omega}^{b}(t) - \mathbf{C}_{b}^{e^T}(t)\boldsymbol{\omega}_{ie}^{e}(t) \tag{4.9}$$

where $\boldsymbol{\omega}_{ie}^{e}(t)$ is the Earth rotation rate expressed in body axes and $\mathbf{C}_{b}^{e}(t)$ is the rotation matrix DCM from the body frame to the Earth frame.

The DCM may be calculated from $\boldsymbol{\omega}_{eb}^{b}$ using the relationship [173]

$$\dot{\mathbf{C}}_{b}^{e}(t) = \mathbf{C}_{b}^{e}(t)\boldsymbol{\Omega}_{eb}^{b}(t) \tag{4.10}$$

where $\boldsymbol{\Omega}_{eb}^{b}$ the skew-symmetric matrix derived from $\boldsymbol{\omega}_{eb}^{b}$. Discrete-time propagation of the DCM can be obtained by means of the Taylor approximation as:

$$\mathbf{C}_{b}^{e}[n+1] = \left(\mathbf{I} + T_c\boldsymbol{\Omega}_{eb}^{b}[n]\right)\mathbf{C}_{b}^{e}[n] \tag{4.11}$$

Velocity computation

The body velocity in the *e*-frame, $\mathbf{v}^{e}(t)$, is obtained from integration of the corresponding acceleration $\mathbf{a}^{e}(t)$. However, to obtain the total body acceleration $\mathbf{a}^{e}(t) = \dot{\mathbf{v}}^{e}(t)$ it is necessary to rotate the accelerometer measurement $\mathbf{f}^{b}(t)$ into the proper frame and subtract the components due to gravity, Coriolis effect and centripetal force. It is possible to obtain an equation to describe the velocity variations in time as

$$\dot{\mathbf{v}}^{e}(t) = \mathbf{C}_{b}^{e}(t)\mathbf{f}^{b}(t) - 2\boldsymbol{\Omega}_{ie}^{e}(t)\mathbf{v}^{e}(t) + \mathbf{g}_{l}^{e}(t) \tag{4.12}$$

where where $\mathbf{g}_{l}^{e}(t)$ is the sum of the gravity and of the centripetal acceleration.

Position computation

The position propagation is described by the well known relationship between space and velocity

$$\dot{\mathbf{p}}^{e}(t) = \mathbf{v}^{e}(t) \tag{4.13}$$

where $\mathbf{p}^e(t)$ is the 3-dimensional position of the body in the e-frame.

4.3.4 Noise characterization

The short-term stability of the INS is due to the noise characterizing the accelerometers as well as the gyroscopes. Errors from the inertial sensors are integrated to obtain a position, in case of the accelerometers, and to obtain an updated attitude of the platform, in case of the gyroscopes. These errors cause the navigation solution drifting from the true one.

Errors affecting the inertial sensors can be classified as deterministic and stochastic. Deterministic errors are due to manufacturing and mounting defects, and can be calibrated out from the data. On the other hand, stochastic errors include random noises. The misalignment errors, which are the result of non orthogonalities of the sensor, are part of the deterministic errors. Also the scale factor, which represent the sensibility of the sensor, is a deterministic error. The IMU internal temperature belong to the category of deterministic error, too. As far as the bias is concerned, it can be divided in two categories, such as bias turn-on and bias-drift [152]. The bias-on is considered as a deterministic error. The bias-drift is considered as a stochastic error. Random errors, resulting either from the noise of the sensor itself or to random variations of bias or scale factor over time, are also considered as part of the stochastic error of the sensor.

A suitable estimation of these errors is needed for improving the performance of INS, in order to compensate the input error to the mechanization stage. However, if deterministic errors can be minimized by calibration procedures, see e.g. [56], the stochastic errors need stochastic modeling, which is a challenging task. The estimation of the stochastic model parameters has been already addressed by the research community. [160] analyzed the use of Allance variance method to model the inertial sensors' error terms. [73] targets modeling of the stochastic drift of the MEMS-based gyroscope using a nonlinear system identification technique and comparing with that of higher order Auto-Regressive (AR) stochastic models. A complete overview about some of the stochastic processes, usually used to model the bias-drift, can be found in [152] where the authors

give a complete overview about the random processes that affect the inertial sensors using different techniques, such as autocorrelation, AR, PSD, AV and processes. They also aims at obtaining the parameters of the various stochastic models using experimental data collected in laboratory. Therefore, based on [152], some of the stochastic processes usually used for noise identification and stochastic modeling of inertial sensors errors, are reported in the following.

Autocorrelation

The autocorrelation function can be used for the estimation of the parameters needed for modeling the random errors of the inertial sensors, using the first-order Gauss-Markov (GM) process. It has been used in previous works to analyze the stochastic error of the inertial sensors [136] [73]. The first-order GM can be describes in the time domain as

$$\dot{x}(t) = -\frac{1}{T_c}x + w \tag{4.14}$$

where x is the random process with zero mean, correlation time T_c and driving noise w. Therefore, the parameters needed to implement this process can be extracted from its autocorrelation function, given by

$$R_{xx}(\tau) = \sigma^2 e^{\beta|\tau|} \tag{4.15}$$

where the correlation time is $T_c = 1/\beta$ and σ^2 is the variance of the process at zero time lag ($\tau = 0$).

The importance of the first-order GM process lies in the fact that it can represent bounded uncertainty. As a result, any correlation coefficient at any time lag τ is less or equal to the correlation coefficient at zero time lag $R_{xx}(\tau) \leq R_{xx}(0)$ [71]. On the other hand, it shows some limitation due to the complexity of performing an accurate autocorrelation curve from experimental data. Moreover, when low-cost IMU are used, the shape of the autocorrelation might follow higher order GM processes meaning that first-order GM would not be appropriate to model the bias-drift behavior. A comprehensive discussion about this, can be found in [37]. However, the autocorrelation analysis is

very useful to determine the correlation grade of the underlying random processes that affect the sensors.

In [152], the authors exploit the autocorrelation function to characterize the noise of inertial sensors based on MEMS technology (MicroStrain 3DM-GX3-25 device [2]). Since the obtained autocorrelation functions of the inertial sensors are different from the autocorrelation function of the first-order GM process, they conclude that the assumption that the stochastic error follows a first-order GM process is not valid in most situations for inertial sensors based on MEMS technology.

Autoregressive processes

More accurate modeling of the INS errors can be achieved using AR model. With respect to the autocorrelation technique, that aims at modeling the inertial sensor errors as first-order GM process, AR methods allow to model such errors as higher order GM process. AR models were introduced in [136] and then evaluated in [73], [143]. In [152], the authors estimate the AR model coefficients to the wavelet de-noised static inertial sensor data of MEMS technology (MicroStrain 3DM-GX3-25 device [2]). They consider first and third order AR processes.

Power spectral density

The PSD provides information about the stochastic errors of the inertial sensors from the frequency components. The PSD is related to the autocorrelation function as

$$S_x(jw) = \mathcal{F}\left[R_{xx}(\tau)\right] = \int_{-\infty}^{\infty} R_{xx}(\tau) e^{-jwt} d\tau \tag{4.16}$$

where $S_x(jw)$ is the power spectral density of the process x, as a function of the angular frequency $w = 2\pi f$, $\mathcal{F}[\cdot]$ indicates Fourier transform, $R_{xx}(\tau)$ is the autocorrelation of the process x.

PSD method identifies the noise sources based on the different slopes of the noise terms in a log-log curve. An hypothetical inertial sensor PSD in single-sided is depicted in Figure 4.4.

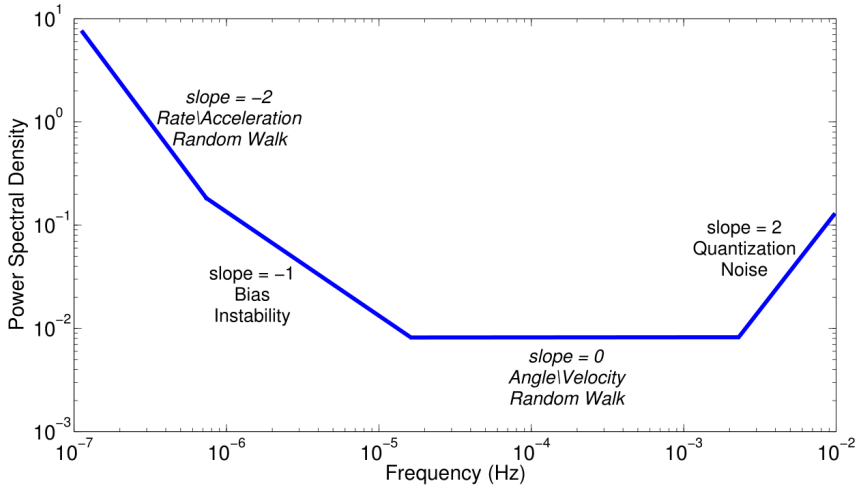

Figure 4.4: Hypothetical PSD in single-sided form of an inertial sensor. Figure from [152].

According to this curve, e.g. a slope of - 1 represents the noise term of the bias instability (B). However, the detailed description of the different noise terms can be found in [160] and [33].

In [152], the authors perform the noise data analysis of inertial sensors based on MEMS technology (MicroStrain 3DM-GX3-25 device [2]), exploiting the PSD method using Welch's method. Basically, comparing the PSDs of acceleromteres and gyroscopes, and the curve in Figure 4.4, they detect different types of noise. As a result, they model the stochastic error of the accelerometers by the sum of velocity random walk (N) with slope 0 and modeled as a white noise, the bias instability (B) with slope -1 modeled as first-order GM process and, finally, the random walk (K) with slope -2 modeled as a random walk process. On the other hand, the stochastic error of the of the gyroscopes is modeled by the sum of angle random walk (N) with slope 0 and modeled as a white noise, the bias instability (B) with slope -1 modeled as first-order GM process.

Allan variance

The Allan variance is a time-domain analysis technique capable to provide information on the types and magnitude of various noise terms in an observed data [23]. In other words, it allows to characterize the different contribution of the error sources to the overall

noise statistics. It has been applied to the modeling of inertial sensors [181], [153].

The idea behind the AV estimation is to consider a long sequence of static data, remove the deterministic bias and then integrate the output of the inertial sensors to obtain the velocity θ. Finally, compute the AV as

$$\sigma^2(T) = \frac{1}{2T^2(N-2n)} \sum_{k=1}^{N-2n} (\theta_{k+2n} - 2\theta_{k+n} + \theta_k)^2 \tag{4.17}$$

where T represents the cluster time, i.e. the time associated with a group of n consecutive observed data samples, N is the length of the data that will be analyzed and θ is the output velocity, in the case of the accelerometers, and output angle, in the case of the gyros; these measurements are made at discrete times from the inertial sensors.

Since the data uncertainty is assumed to be generated by the different noise sources, the covariance can be thus obtained by analyzing the result of the computed AV (4.17). An hypothetical inertial sensor AV log-log curve is depicted in Figure 4.5. Since the AV computation needs a finite number of clusters, it must be pointed out that the accuracy of the AV estimation is a function of the size of these clusters. The bigger the number of independent clusters, the better the estimation accuracy.

In [152], the authors perform the noise data analysis of inertial sensors based on MEMS technology (MicroStrain 3DM-GX3-25 device [2]), exploiting the AV method.

After integrating the acceleration and angular rate, they obtain the instantaneous velocity and angle. Eventually, they obtain the log-log plot of Allan variance standard deviation versus cluster times (T).

Based on the different slopes, the accelerometer error is composed by velocity random walk (N) with slope -1/2, bias instability (B) with slope 0 and acceleration random walk (K) with slope 1/2 and that the dominant noise in short cluster times is the velocity random walk, while the dominant error in long cluster times is the acceleration random walk. On the other hand, the gyroscopes error is composed by two types of noises such as angle random walk N for short cluster times and bias instability B for long cluster times.

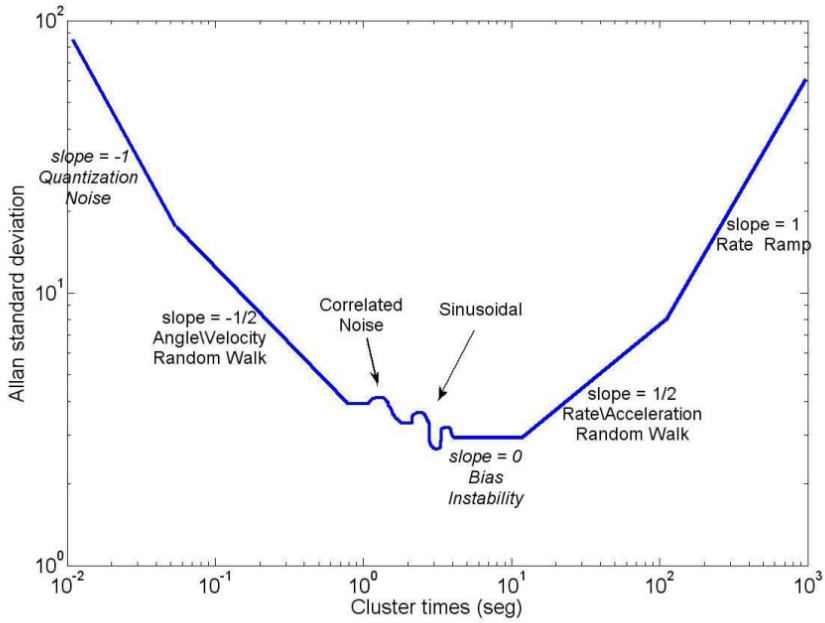

Figure 4.5: Hypothetical AV of an inertial sensor. Figure from [152].

4.4 Visual sensor

Despite INSs are perfect candidate to be integrated with GNSS, due to their complementary nature, the use of a camera as a visual sensors might be exploited to overcome the limitations shown by the INS, especially when MEMS are used (short term drift errors). Visual sensors do not exhibit this kind of errors that rapidly degrade over time, and are insensitive to external sources of errors, such as intentional or non-intentional interference. Moreover, visual measurements obtained from different time epochs are independent and therefore the errors in previous epochs do not affect the measurements from subsequent images. Despite tracking the motion of the features from observed images is a challenge, this concept can be exploited to extract the information about the user motion. However, one of the challenges of the visual-aiding in indoor environments is the shortage of features to be tracked. Following the idea of [38], which developed an outdoor robot navigation system using a special camera configuration, the algorithms used in this thesis have been further developed for indoor use and pedestrian, and furthermore tested for automotive applications. Indeed, we use monocular camera to resolve

the depth, which is obtained adopting a special configuration of the camera, as explained hereafter.

The visual sensor used in this thesis is based on the concepts of *visual gyroscope* and *visual odometer*. These algorithms can be used to obtain the heading change and the translation of the camera between two conscutive images, respectively. Such visual gyroscope and visual odometer were developed by [156] and used in this research to extract the motion of the features in consecutive images. In principle, the motion of the so-called *vanishing points* is tracked, which can be considered as the image point where the lines parallel in the scene appear to intersect. It provides relative measurements of user heading, i.e. change in the attitude estimation. Then, it cannot be used as a standalone system to estimate the heading by it must be integrated with measurements from other sources.

After giving some general concepts about computer vision, relevant in vision-aided for navigation, the remainder of this Section is devoted to the description of *visual gyroscope* and *visual odometer*.

4.4.1 Camera fundamentals and coordinate frames

A very general overview about the fundamentals of camera geometry, in the framework of the computer vision, and about the coordinate frames, is given in this Section. These general principles are derived from [89]. In order to find the relationship between camera frame $\mathbf{X}_{cam}$ and navigation frames $\mathbf{X}_{nav}$, the *pinhole* model is first introduced. Under this model, a point in the camera world with coordinates $\mathbf{X} = (X, Y, Z, 1)^T$ can be mapped onto the point $\mathbf{x} = (fX, fY, Z)^T$ in the image frame. f is the *image plane* or *focal length*. The mapping from world frame $\mathbf{X}$ to image frame $\mathbf{x}$ can be written as

$$\mathbf{x} = \mathbf{P}\mathbf{X} \tag{4.18}$$

where $\mathbf{P}$ is the *camera projection matrix*, that can be written as

$$\mathbf{P} = \mathbf{K}[\mathbf{R}|\mathbf{t}] \tag{4.19}$$

where $\mathbf{K}$ is the *camera calibration matrix* and $\mathbf{t}$ is the translation of the camera origin. Details about the derivation of $\mathbf{P}$, $\mathbf{K}$ and $\mathbf{R}$ can be found in [89]. Assuming that the camera is located at the origin of a Euclidean coordinate system with the principal axis of the camera pointing straight down the Z-axis, (4.18) becomes

$$\mathbf{x} = \mathbf{K}[\mathbf{R}|\mathbf{t}]\mathbf{X}_{cam} \tag{4.20}$$

The relationship between camera frame $\mathbf{X}_{cam}$ and navigation frames $\mathbf{X}_{nav}$, is the following

$$\mathbf{X}_{cam} = \mathbf{R}\mathbf{X}_{nav} + \mathbf{t} \tag{4.21}$$

where $\mathbf{R}$ is the rotation matrix representing the orientation of the camera coordinate frame.

Evaluating the relationship between a point in the 3D space $\mathbf{x}$ in the first view and the point $\mathbf{x}'$ in the second view, it can be written as

$$\mathbf{x}'\mathbf{F}\mathbf{x} = 0 \tag{4.22}$$

where $\mathbf{F}$ is the *fundamental matrix* which has seven degress of freedom. The principles of epipolar geometry needed to better understand the intrinsic projective geometry between two views can be found in [89].

The mapping from an image point $\mathbf{x}$ to an image point $\mathbf{x}'$ is

$$\mathbf{x}' = \mathbf{K}'\mathbf{R}\mathbf{K}^{-1}\mathbf{x} + \mathbf{K}'\mathbf{t}/Z \tag{4.23}$$

where Z is the depth of the point.

4.4.2 Visual gyroscope

The idea behind the *visual gyroscope* is to track the motion of the vanishing points in consecutive images, to monitor the change in the camera attitude. As a result, the camera is used as a visual gyroscope. As already mentioned, this concept was introduced in [156]

and used in this thesis. This algorithm provides relative measurements, i.e. change in the attitude estimation, and not absolute values. Then, it cannot be used as a standalone system to estimate the heading by it must be integrated with measurements from other sources.

The vanishing points, considered as the image point where the lines parallel in the scene appear to intersect, were first identified and located. The Scale Invariant Feature Transform (SIFT) approach [121], [120] was used to extract the features for solving the motion of camera between consecutive images. A part from the SIFT features, all the edges were identified using Canny Edge detector [39] and the straight lines separated from the set of all edges with the Hough Line algorithm [95].

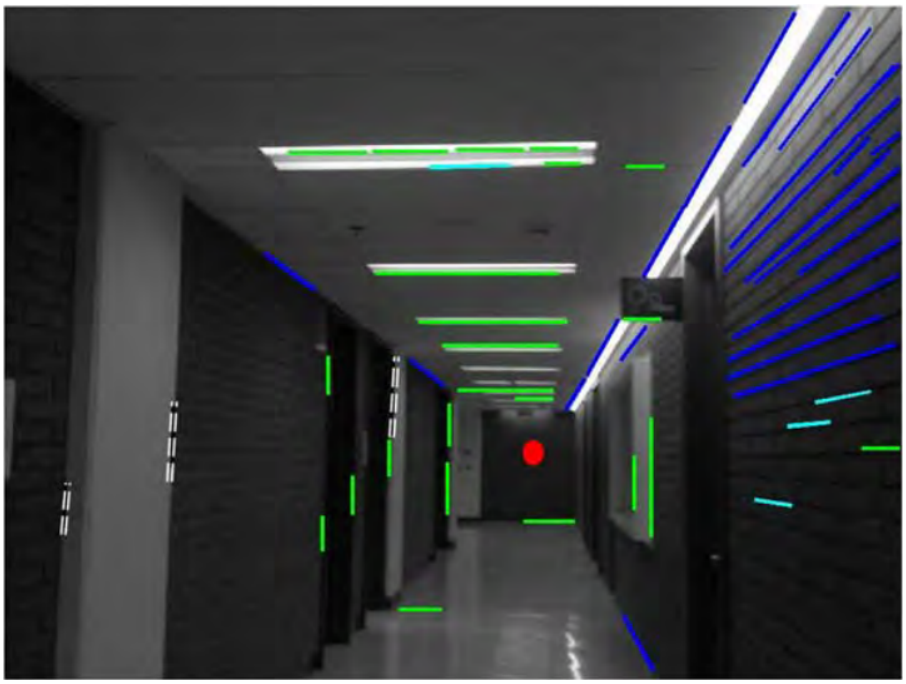

Figure 4.6: Vanishing points representation. Totally vertical or horizontal (green), vertical (white dotted), horizontal (turqoise) and along the direction of propagation (blue). Central vanishing point (red dot). Figure from [156].

In the initial configuration, the central vanishing point $\mathbf{v}_z$ lies at the principal point and the other two vanishing points at infinity on the x and y image axes. Then the location of all the three vanishing points, given by the location matrix $\mathbf{V}$, is linked with

the calibration matrix **K** and the rotation matrix of the camera **R**.

$$\mathbf{V} = \mathbf{KR} \tag{4.24}$$

The *visual gyroscope* provides the roll, pitch and heading when either the horizontal or vertical vanishing point is recognized in addition to the central vanishing point. On the other hand, it does not provide the roll if only the central vanishing point is obtained. The latter was considered within the algorithms used in this thesis so only the central vanishing point was tracked. The logic behind the selection of the central vanishing point is a voting scheme. Any vanishing point candidate is voted for all the lines found. In other words, it is done voting for the intersection points of all lines and correcting the effect of noise with robust estimation using weighted means [97]. Eventually, the one getting most of the votes is selected as the correct one. However, details about the voting scheme are omitted in this thesis and can be found in [156].

The central vanishing point, presented in homogenous coordinates as (x, y,1), where the x and y are the pixel coordinate, can be obtained from (4.24) and written as [156]

$$\mathbf{v}_z = \begin{bmatrix} f_x \sin\theta + u\cos\phi\cos\theta \\ -f_y \sin\phi\cos\theta + \upsilon\cos\phi\cos\theta \\ \cos\phi\cos\theta \end{bmatrix} \tag{4.25}$$

Finally, the heading θ and the pitch ϕ can be obtained from (4.25) as

$$\theta = \arcsin\left(\frac{x-u}{f_x}\right) \tag{4.26}$$

$$\phi = \arcsin\left(\frac{y-\upsilon}{-f_y\cos\theta}\right) \tag{4.27}$$

Error detection

In order to evaluate the accuracy of the estimated vanishing point, the concept of Line Dilution Of Precision (LDOP) is used. It basically consists of a dilution of precision

value demonstrating the geometry of the lines used for calculating the position of the vanishing point. A large LDOP value, leads to large uncertainty of the vanishing point location which can be weighted accordingly into the navigation filter. It is calculated first dividing the frame into four quarters around the estimated vanishing point, and eventually evaluating the geometry of the lines intersecting at the vanishing point itself.

Three different scenarios can be exploited: (*a*) we declare that the vanishing point is correct, thus assigning a minimum LDOP value of $\sqrt{2}$, if lines intersecting at the vanishing point are found from all four sections. (*b*) we declare the line geometry sufficiently accurate, thus assigning a low LDOP value to the estimated vanishing point, if the lines intersecting at the estimated vanishing point are from three of the sections. (*c*) more evaluation of the geometry must be done, if the geometry of lines is reduced, i.e. the lines are found only from two sections or especially only from one. In this case the LDOP evaluation is based on the mutual alignment of the lines using a method proposed in [22]. Details about the concept of LDOP are omitted in this thesis and can be found in [156].

4.4.3 Visual odometer

The *visual odometer* aims at evaluating the translation from consecutive images in order to have relative information about the user position. The goal is to find the unknown depth (Z) of a photographed objects and resolve the scale problem. It is obtained adopting a special configuration of the camera, as shown in Figure 4.7. The height of the camera, h, must be a known parameter so it must be measured before starting navigation. It allows to resolve the distance (Z) of the object.

In order to find the translation of the camera, the mapping from an image point $\mathbf{x}$ to an image point $\mathbf{x}'$, (4.23) is recalled. If the image points in the first ($\mathbf{x}$) and second ($\mathbf{x}'$) image are normalized, (4.23) reduces to

$$\hat{\mathbf{x}}' = \mathbf{R}\hat{\mathbf{x}} + \mathbf{t}/Z \tag{4.28}$$

where $\mathbf{R}$ is the camera rotation and $\mathbf{t} = [t_x, t_y, t_z]$ the translation between the images. $\mathbf{Z}$

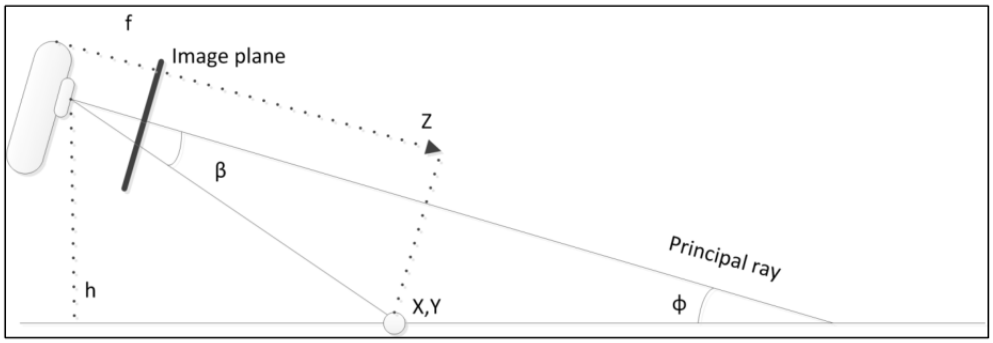

Figure 4.7: Special configuration of the camera with height h and pitch ϕ for resolving the distance Z of the object point (X,Y,Z). Figure from [157].

represents the depth of the object from the camera.

The main challenge is therefore to measure the distance Z from the camera to the object. The object has coordinates (X, Y, Z) and it is projected into image point (x, y, z). ϕ is the pitch of the camera whereas β is the angle between the principal ray of the camera and the ray from the camera to the object using the image point y and the focal length f_y. Following the mathematical derivation in [156], the depth Z of the object is estimated as

$$Z = \frac{h \cos \beta}{\sin(\phi + \beta)} \tag{4.29}$$

X can be used in (4.28) to find the final expression of the translation $\mathbf{t}$.

4.4.4 Noise characterization

In order to characterize the noise affecting the gyroscope accuracy, we report the analysis performed by the author [156] which developed the visual gyroscope algorithm. The AV analysis method [23] is applied to evaluate the camera gyroscope noise level. The Allan variance $\sigma_C^2(t_A)$ [106] for the averaging time t_A is

$$\sigma_C^2(t_A) = \frac{1}{2(N-1)} \sum (\tilde{y}(t_A)_{k+1} - \tilde{y}(t_A)_k) \tag{4.30}$$

where $\tilde{y}(t_A)_k$ is the average value of a bin k containing the heading change and pitch values. The averaging time t_A is the length of a bin and N is the number of bins formed

of the data for the corresponding averaging time.

The variation in heading change and pitch measurements was calculated from the 7555 static images. From the Allan deviation plot in Figure 4.8, it is possible to see how the uncorrelated noise was affecting the visual gyroscope stability for the short integration times. After the deviation reached a minimum value, the rate random walk started to increase the deviation again. The minimum value in the curve, shows the bias instability equal to 0.058 degrees/second for the heading, and 0.045 degrees/second for the pitch. Moreover, since the errors are time invariant, one erroneous measurement does not necessarily introduce drift in the propagated heading value if it is identified by error detection.

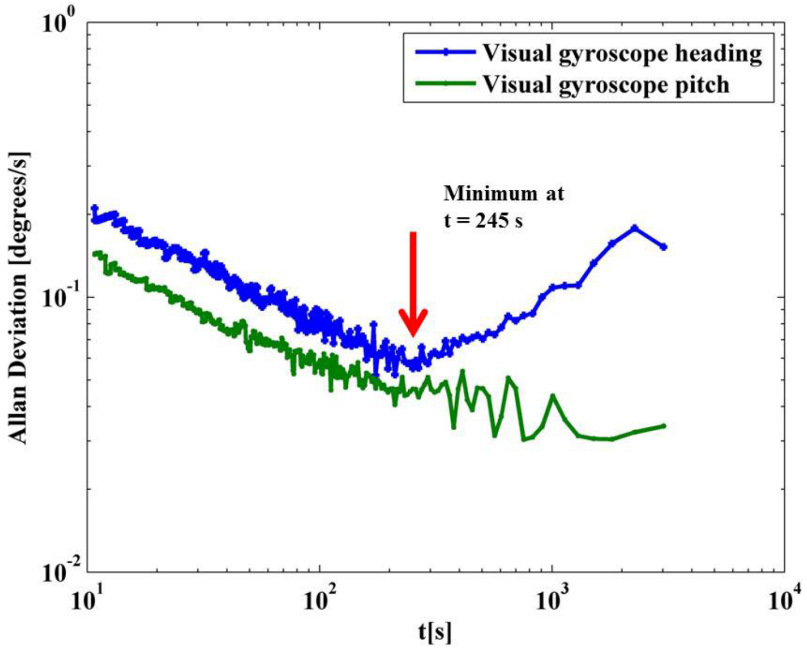

Figure 4.8: Allan deviation plot showing the noise in the visual gyroscope. Figure from [156].

Details about the noise characterization of the visual gyroscope are omitted in this thesis. However, a rigorous accuracy analysis for estimating parameters of geometric models from noisy data is given in [102], where the authors used various techniques for the parameter estimation for vision applications. It includes deep explanations and proofs

about the theorems used for the estimation.

4.5 Odometer

An *odometer* provides information about the curvilinear distance traveled by a vehicle. Such a distance is obtained by measuring the number of full and fractional rotations of the vehicle's wheels [162], [14]. Typically, an odometer is an electronic device that outputs an integer number of pulses for each revolution of the wheel. The number of pulses generated during a time slot are eventually converted to an estimate of the traveled vehicle distance, during that time slot, by multiplying the number of pulses by an odometer scale factor. This scale factor generally depends on the radius of the vehicle's wheel and therefore it is not constant provided that a wheel's radius can change with tire pressure, temperature, tread wear, and the vehicle's speed. Beside these variations in the scale factor, there are several sources of random errors affecting the odometer output, e.g. wheel slips, uneven road surfaces or skidding. An empirical evaluation of data that quantify the change in odometer scale factor versus tire pressure and vehicle speed is presented in [114] while a more complete overview about both systematic and non-systematic errors is given in [40].

However, in this thesis we use the term odometer to identify the sensor providing the velocity components of the vehicle. This information, that is typically given by *velocity encoders* observing the rotation rates of the wheels, is fed to the navigation filter, in addition to the data coming from the other sensors.

Chapter 5

Multi-sensor integration

As widely discussed in Chapter 4, each sensor that can be used for positioning, exhibits strengths and weaknesses based on the own nature. Coupling sensors that have complementary characteristics, consistently enhances the performance of the navigation integrated system in terms of positioning accuracy, reliability and continuity of the position. The integration of GNSS and external sensors with complementary characteristics, is therefore the key for overcoming the weaknesses and enhancing the strengths of each sensors. Such an integration can be performed using different fusion filters and according to different strategies, that differ in the degree of integration of the systems.

After discussing the most commonly used filters to combine information from sensors of different nature, this Chapter gives an overview about the different strategies that can be used for the data fusion. Loose, tight and ultra-tight integration algorithms are thus introduced addressing a generic multi-sensor GNSS receiver. Each of these integration strategies are therefore described in detail addressing a specific subset of sensors, chosen within this thesis, i.e. INS, visual sensor and odometer, as external sensors to be coupled with GNSS.

5.1 Navigation filter

The mathematical operator employed to combine information from different sensors is called *navigation filter*, hereafter. Essentially, it is characterized by a model, that describes the process and measurement dynamics of the navigation system, together with a proper description of the process and measurement noise statistics. A survey of the information fusion technologies used in current in-car navigation systems is presented in [162], where the most common filters used to combine the information from the various sources are presented.

Since non-linear processes and measurement models generally are used to describe vehicle dynamics, non-linear filtering methods must be employed. One of the most used non-linear filtering approach is the EKF [154], [174], [132] (described in Appendix A), due to its simplicity, which transforms the non-linear filtering problem into a linear problem, by linearizing the navigation equations around the current navigation solution. Unfortunately, when the measurements are characterized by high non-linear nature, such a linearization process can affect the accuracy of the obtained solution. In this case, enhanced performance can be obtained by using more refined non-linear filtering approaches. Unscented Kalman Filter (UKF) can be used for this purpose [161], [100]. It assumes that the probability density of the state vector is Gaussian, and this density is sampled at a number of carefully chosen points to approximate the multidimensional integrals required. Particle filter might be also used within this context [53], [86], [41]. It can be seen as genetic-type Monte Carlo methods, that use weighted samples to generate approximations of the probability density function. However, the intrinsic weakness of these non-linear filtering approaches is the computational complexity of the filter, that grows exponentially with the dimension of the state vector being estimated [53].

Therefore, the choice of the filter algorithm is driven by a trade-off between an adequate description of the system and a sufficient simplicity for the filtering algorithm to become computationally feasible. In other words, it comes from a balance between computational complexity, robustness against modeling errors, and accuracy of the algorithm. Since EKF offers a good compromise between these aspects, it is the non-linear filtering

approach used in this thesis to fuse the sensors' information.

5.2 Integration strategies

Depending on the level of information exchanged between GNSS and the other components in the integrated system, they can be integrated according to different strategies, commonly referred as [146] *uncoupled*, *loose*, *tight* and *ultra-tight* (or *deep*) integration. These solutions basically differ in the degree of integration of the systems, i.e. for the nature of the information extracted from the systems and used in the hybridization process, as well as for the architecture of the interactions between the systems. The terms Loosely Coupled (LC), Tightly Coupled (TC) and Ultra-Tightly Coupled (U-TC) are used hereafter to refer to *loose*, *tight* and *ultra-tight* approach, respectively.

Considering GNSS/INS integrated systems, the *uncoupled* approach is characterized by two distinct solutions. Typically the GNSS solution is used to correct (or reset) the INS solution, but without estimating the causes of the sensor drift (as happens in the other integration approaches). It is not considered in this thesis.

LC systems integrate position and velocity, measured from the GNSS receiver and from the external sensors. Compared with TC and U-TC integrated systems, they are relatively easy to implement. On the other hand, TC systems are characterized by the use of raw GNSS observables, such as pseudorange and Doppler measurements, to be coupled with the INS observations. In this case, the position is computed by the navigation filter, which gathers the information from GNSS as well as from the external sensors. As a result, the system is able to compute the position even if the number of GNSS measurements is insufficient for a standalone solution, i.e. equal to 4. Finally, U-TC systems are the deepest level of integration since the GNSS tracking module is embedded within the integration filter. Within this integration scheme, the updates are used to aid the GNSS receiver NCOs tracking loops.

As far as the integration filter is concerned, these strategies share in principle the same basic state-space model of the involved quantities. Minor differences are introduced in the number of the involved states and in the forcing functions models; on the other hand,

substantial differences determine the three observation models, which lead to substantially different integration strategies.

The high-level representation of GNSS receiver, coupled with other sensors according to LC, TC and U-TC integration strategies is reported in Figure 5.1. In such a representation, the branch addressing GNSS processing is depicted on the left side, whereas the other sensors (INS, barometer, visual sensor, etc.) are depicted on the right side.

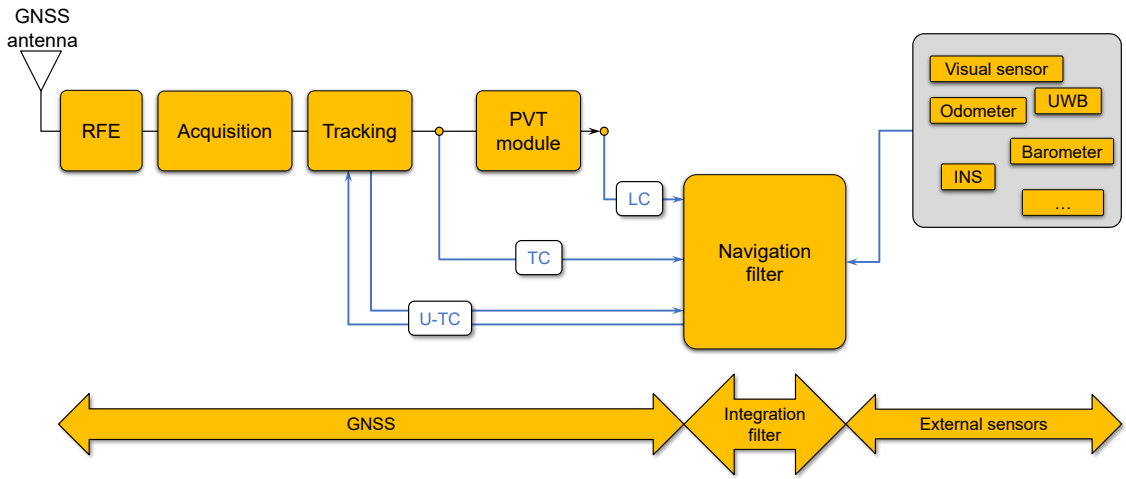

Figure 5.1: Architecture of a multi-sensor LC, TC and U-TC GNSS receiver.

5.3 Loose integration

A LC integration system uses the position and velocity measured from the GNSS receiver to compute the corrections, that are consecutively applied to the trajectory estimated by the external sensors. The loose integration of GNSS and other sensors for positioning has been addressed by the GNSS research community during the last years. In particular, the loose integration of GNSS and INS has been extensively studied and consolidated during the last decades, in fact details and real implementations can be found in [146], [64], [92], [65] and [165].

Within this LC architecture, the navigation solution of the two subsystems is blended. This type of integration is relatively easy to implement since the access to low level processing observables is not required and then any commercial-of-the-shelf receiver can

be used. Although its simplicity, it has some drawbacks. Since the position and velocity estimates from the GNSS receiver are correlated in space and time and with a structure most likely unknown to the information fusion algorithm designer, the correct statistics on the estimation error are not available for the navigation filter, leading to suboptimal performance [162]. Moreover, the navigation solution can be estimated only when the GNSS receiver has enough satellite in view for computing the navigation solution.

The architecture of a LC GNSS receiver is shown in Figure 5.2 where GNSS data are fused with measurements from INS, visual sensor and odometer. It computes the corrections necessary to refine the INS-based trajectory meanwhile estimating the position and velocity of the navigation unit. The biases that affect the accelerometers and the gyroscopes are estimated by the navigation filter and given as a feedback to INS.

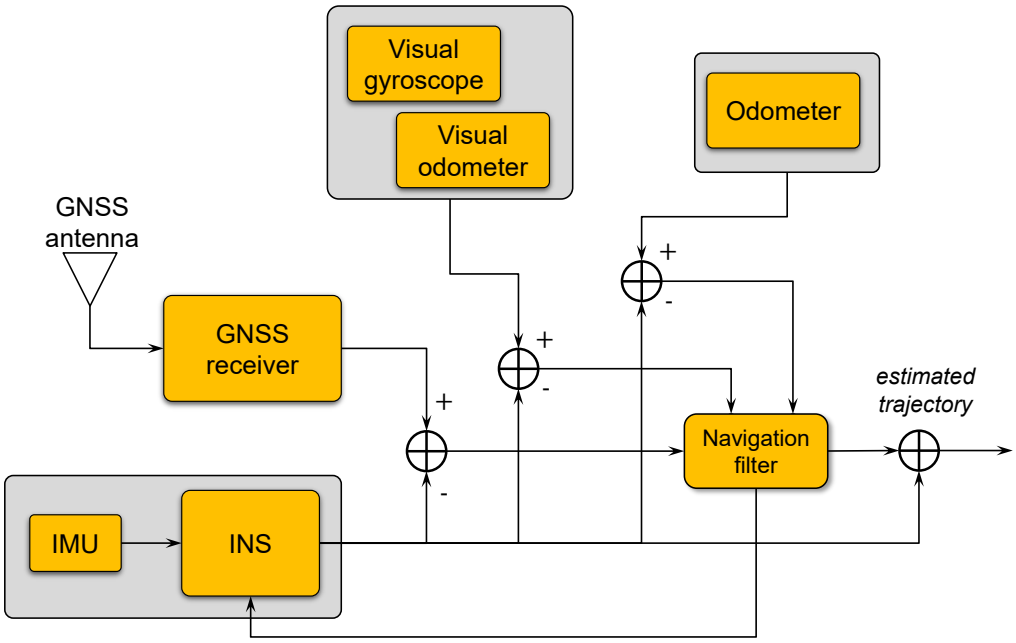

Figure 5.2: Architecture of a multi-sensor GNSS receiver LC with INS, visual sensor and odometer.

The details of the navigation filter, implemented according to an EKF scheme, used within the architecture of the multi-sensor LC GNSS receiver reported in Figure 5.2, are presented in the following.

State-space model

The definition of the state-space model needed to implement a loosely integrated system is shown hereafter. The model equations are written in the continuous-time domain. The structure adopted for the set of the system states (*incremental states*) is the following:

$$\Delta\mathbf{x}(t) = \left[\Delta\mathbf{p}^e(t)^T,\ \Delta\mathbf{v}^e(t)^T,\ \Delta\boldsymbol{\psi}^e(t)^T,\ \mathbf{b}_a^b(t)^T, \mathbf{b}_g^b(t)^T\right]^T \in \mathbb{R}^{15,1} \tag{5.1}$$

where the superscripts ^{e,b} indicates *Earth frame* and *body frame* respectively. The state vector store the following components:

$\Delta\mathbf{p}^e(t) \in \mathbb{R}^{3,1}$ is the *corrections vector* to be applied to the *nominal body position* at the time instant t, expressed in the Earth frame;

$\Delta\mathbf{v}^e(t) \in \mathbb{R}^{3,1}$ is the *corrections vector* to be applied to the *nominal body velocity* at the time instant t, expressed in the Earth frame;

$\Delta\boldsymbol{\psi}^e(t) \in \mathbb{R}^{3,1}$ is the vector of misalignment angles along each axis (*attitude corrections*) at the time instant t, expressed in the Earth frame;

$\mathbf{b}_a^b(t) \in \mathbb{R}^{3,1}$ is the vector of the biases of the accelerometers at the time instant t, expressed in the body frame;

$\mathbf{b}_g^b(t) \in \mathbb{R}^{3,1}$ is the vector of the biases of the gyroscopes at the time instant t, expressed in the body frame;

State transition matrix

In order to define the state transition matrix $\mathbf{\Phi}[n]$ of the discrete-time state-space model, the discrete-time of the state-transition model is:

$$\Delta\mathbf{p}^e[n+1] = \Delta\mathbf{p}^e[n] + T_c\Delta\mathbf{v}^e[n] \tag{5.2}$$

$$\begin{aligned}\Delta\mathbf{v}^e[n+1] = \mathbf{N}^e\Delta\mathbf{p}^e[n] + \left(\mathbf{I}_3 - 2T_c\mathbf{\Omega}^e_{ie}\right)\Delta\mathbf{v}^e[n] + \\ - T_c\mathbf{F}^e[n]\Delta\boldsymbol{\psi}^e[n] + T_c\mathbf{C}^e_b[n]\mathbf{b}^b_a[n] \qquad +T_c\mathbf{C}^e_b[n]\boldsymbol{\eta}_a[n]\end{aligned} \tag{5.3}$$

$$\Delta\boldsymbol{\psi}^e[n+1] = \left(\mathbf{I}_3 - T_c\mathbf{\Omega}^e_{ie}\right)\Delta\boldsymbol{\psi}^e[n] - T_c\mathbf{C}^e_b[n]\mathbf{b}^b_g[n] \qquad -T_c\mathbf{C}^e_b[n]\boldsymbol{\eta}_g[n] \tag{5.4}$$

$$\mathbf{b}^b_a[n+1] = \left(\mathbf{I}_3 + T_c\mathbf{D}_a\right)\mathbf{b}^b_a[n] \qquad +T_c\boldsymbol{\eta}_{aa}[n] \tag{5.5}$$

$$\mathbf{b}^b_g[n+1] = \left(\mathbf{I}_3 + T_c\mathbf{D}_g\right)\mathbf{b}^b_g[n] \qquad +T_c\boldsymbol{\eta}_{gg}[n] \tag{5.6}$$

where:

- T_c is the sampling interval
- $\mathbf{N}^e$ is the tensor of gravity gradients [146]
- $\mathbf{\Omega}^e_{ie}$ is the Earth rotation rate
- $\mathbf{F}^e$ is the skew symmetric matrix of the accelerometers measurements
- $\mathbf{C}^e_b$ is the rotation matrix from the body frame to the Earth frame
- $\boldsymbol{\eta}_a$ is a driving noise term acting on the accelerometers in the body frame
- $\boldsymbol{\eta}_g$ is a driving noise term acting on the gyroscopes in the body frame
- $\mathbf{D}$ a is the time-constant diagonal matrix that defines a first-state Gauss-Markov model
- $\boldsymbol{\eta}_{aa}$ is the driving noise for the accelerometers biases
- $\boldsymbol{\eta}_{gg}$ is the driving noise for the gyroscopes biases

so that the discrete-time state-space model is written as:

$$\Delta\mathbf{x}[n+1] = \mathbf{\Phi}[n]\Delta\mathbf{x}[n] + \mathbf{\Gamma}[n]\boldsymbol{\eta}[n], \tag{5.7}$$

where:

$$\boldsymbol{\eta}[n] = \left[\boldsymbol{\eta}_a(nT_c)^T,\ \boldsymbol{\eta}_g(nT_c)^T,\ \boldsymbol{\eta}_{aa}(nT_c)^T,\ \boldsymbol{\eta}_{gg}(nT_c)^T\right]^T \in \mathbb{R}^{12,1} \tag{5.8}$$

$$\mathbf{\Phi}[n] = \begin{bmatrix} \mathbf{I}_3 & T_c\mathbf{I}_3 & \mathbf{0}_3 & \mathbf{0}_3 & \mathbf{0}_3 \\ \mathbf{N}^e & \mathbf{I}_3 - 2T_c\mathbf{\Omega}_{ie}^e & -T_c\mathbf{F}^e[n] & T_c\mathbf{C}_b^e[n] & \mathbf{0}_3 \\ \mathbf{0}_3 & \mathbf{0}_3 & \mathbf{I}_3 - T_c\mathbf{\Omega}_{ie}^e & \mathbf{0}_3 & -T_c\mathbf{C}_b^e[n] \\ \mathbf{0}_3 & \mathbf{0}_3 & \mathbf{0}_3 & \mathbf{I}_3 + T_c\mathbf{D}_a & \mathbf{0}_3 \\ \mathbf{0}_3 & \mathbf{0}_3 & \mathbf{0}_3 & \mathbf{0}_3 & \mathbf{I}_3 + T_c\mathbf{D}_g \end{bmatrix} \in \mathbb{R}^{15,15} \tag{5.9}$$

$$\mathbf{\Gamma}[n] = \begin{bmatrix} \mathbf{0}_3 & \mathbf{0}_3 & \mathbf{0}_3 & \mathbf{0}_3 \\ T_c\mathbf{C}_b^e[n] & \mathbf{0}_3 & \mathbf{0}_3 & \mathbf{0}_3 \\ \mathbf{0}_3 & -T_c\mathbf{C}_b^e[n] & \mathbf{0} & \mathbf{0} \\ \mathbf{0}_3 & \mathbf{0}_3 & T_c\mathbf{I}_3 & \mathbf{0}_3 \\ \mathbf{0}_3 & \mathbf{0}_3 & \mathbf{0}_3 & T_c\mathbf{I}_3 \end{bmatrix} \in \mathbb{R}^{15,12} \tag{5.10}$$

Note that the process noise is defined as $\mathbf{w}[n] = \mathbf{\Gamma}[n]\boldsymbol{\eta}[n]$.

Measurement equation

The incremental observation vector can be written as follows:

$$\Delta\mathbf{z}[n] = \begin{bmatrix} \Delta\mathbf{z}_{GNSS}[n] \\ \Delta\mathbf{z}_{ext}[n] \end{bmatrix} \in \mathbb{R}^{15,1} \tag{5.11}$$

where $\Delta\mathbf{z}_{GNSS}[n]$ is defined as

$$\Delta\mathbf{z}_{GNSS}[n] = \mathbf{z}[n] - \check{\mathbf{z}}[n] \in \mathbb{R}^{6,1} \tag{5.12}$$

where

- $\mathbf{z}[n] = \left[\mathbf{p}^e[n]^T, \mathbf{v}^e[n]^T\right]^T \in \mathbb{R}^{6,1}$ is the vector of the position $\mathbf{p}^e[n]$ and velocity $\mathbf{v}^e[n]$, estimated by GNSS, at the time instant n;
- $\check{\mathbf{z}}[n] = \left[\check{\mathbf{p}}^e[n]^T, \check{\mathbf{v}}^e[n]^T\right]^T \in \mathbb{R}^{6,1}$ is the vector of the position $\check{\mathbf{p}}^e[n]$ and velocity $\check{\mathbf{v}}^e[n]$, estimated by the INS, at time n.

$\Delta\mathbf{z}_{ext}[n]$ is defined as

$$\Delta\mathbf{z}_{ext}[n] = \bar{\mathbf{\Theta}}[n] - \check{\mathbf{\Theta}}[n] \in \mathbb{R}^{9,1} \tag{5.13}$$

where the vectors $\bar{\mathbf{\Theta}}[n]$ and $\check{\mathbf{\Theta}}[n]$ are:

$$\bar{\mathbf{\Theta}}[n] = \left[\bar{\boldsymbol{\psi}}^e_{vis}[n]^T,\ \bar{\mathbf{v}}^e_{vis}[n]^T,\ \bar{\mathbf{v}}^e_{odo}[n]^T\right]^T \in \mathbb{R}^{9,1} \tag{5.14}$$

$$\check{\mathbf{\Theta}}[n] = \left[\check{\boldsymbol{\psi}}^e[n]^T,\ \check{\mathbf{v}}^e[n]^T,\ \check{\mathbf{v}}^e[n]^T\right]^T \in \mathbb{R}^{9,1} \tag{5.15}$$

where

- $\bar{\boldsymbol{\psi}}^e_{vis}[n]$ is the vector of attitude estimated by the visual gyroscope;
- $\bar{\mathbf{v}}^e_{vis}[n]$ is the vector of velocity estimated by the visual odometer;
- $\bar{\mathbf{v}}^e_{odo}[n]$ is the vector of velocity estimated by the odometer;
- $\check{\boldsymbol{\psi}}^e[n]$ is the vector of attitude estimated by the INS;
- $\check{\mathbf{v}}^e[n]$ is the vector of velocity estimated by the INS;

The predicted incremental observation $\Delta\mathbf{z}^-[n]$ relative to the state space model is obtained from the a-priori incremental state $\Delta\mathbf{x}^-[n] = \mathbf{\Phi}[n]\Delta\mathbf{x}[n-1]$ as

$$\Delta\mathbf{z}^-[n] = \mathbf{H}[n]\Delta\mathbf{x}^-[n] \tag{5.16}$$

where the observation matrix $\mathbf{H}[n]$ is defined as

$$\mathbf{H}[n] = \begin{bmatrix} \mathbf{H}_{GNSS}[n] \\ \mathbf{H}_{ext}[n] \end{bmatrix} \in \mathbb{R}^{15,15} \tag{5.17}$$

where the observation matrix $\mathbf{H}_{GNSS}[n]$ is constant in time and equal to:

$$\mathbf{H}_{GNSS} = \begin{bmatrix} \mathbf{I}_3 & \mathbf{0}_3 & \mathbf{0}_3 & \mathbf{0}_{3\times6} \\ \mathbf{0}_3 & \mathbf{I}_3 & \mathbf{0}_3 & \mathbf{0}_{3\times6} \end{bmatrix} \in \mathbb{R}^{6,15} \tag{5.18}$$

The additional component $\mathbf{H}_{ext}[n]$ is related to the external sensors and it can be written as

$$\mathbf{H}_{ext}[n] = \begin{bmatrix} \mathbf{H}_{vis}[n] \\ \mathbf{H}_{odo}[n] \end{bmatrix} \in \mathbb{R}^{9,15} \tag{5.19}$$

where $\mathbf{H}_{vis}[n]$ can be written as

$$\mathbf{H}_{vis}[n] = \begin{bmatrix} \mathbf{0}_3 & \mathbf{0}_3 & \mathbf{I}_3 & \mathbf{0}_3 & \mathbf{0}_3 \\ \mathbf{D}_{pos}[n] & \mathbf{I}_3 & \mathbf{0}_3 & \mathbf{0}_3 & \mathbf{0}_3 \end{bmatrix} \in \mathbb{R}^{6,15} \tag{5.20}$$

and $\mathbf{D}_{pos}[n]$ [156] is equal to

$$\mathbf{D}_{pos}[n] = \begin{bmatrix} \Delta \boldsymbol{v}_x[n] cos\left(\theta[n]\right) Tc & 0 & 0 \\ 0 & \Delta \boldsymbol{v}_y[n] sin\left(\theta[n]\right) Tc & 0 \\ 0 & 0 & \Delta \boldsymbol{v}_z[n] Tc \end{bmatrix} \in \mathbb{R}^{3,3} \tag{5.21}$$

where

- $\theta[n]$ is the yaw estimated by the INS
- $\Delta \boldsymbol{v}^e[n] = \bar{\mathbf{v}}^e[n] - \check{\mathbf{v}}^e_{vis}[n]$ is the difference between the velocity estimated by the INS and the visual odometer, expressed in the Earth frame.

$\mathbf{H}_{odo}[n]$ can be written as

$$\mathbf{H}_{odo}[n] = \begin{bmatrix} \mathbf{0}_3 & -\mathbf{I}_3 & -\grave{\mathbf{v}}^e_{INS}[n] & \mathbf{0}_3 & \mathbf{0}_3 \end{bmatrix} \in \mathbb{R}^{3,15} \tag{5.22}$$

where $\grave{\mathbf{v}}^e_{INS}[n]$ is the skew matrix of the velocity $\bar{\mathbf{v}}^e_{INS}$ estimated by the INS, expressed in the Earth frame.

Finally, the measurement noise covariance matrix $\mathbf{R}[n]$ can be written as

$$\mathbf{R}[n] = \begin{bmatrix} \mathbf{R}_{GNSS}[n] & \\ & \mathbf{R}_{ext}[n] \end{bmatrix} \in \mathbb{R}^{15,15} \tag{5.23}$$

where the component $\mathbf{R}_{ext}[n]$ include the variances of the measurements calculated by the visual gyroscope $\boldsymbol{\psi}_{vis}$, visual odometer $\mathbf{v}_{vis}$ and odometer $\mathbf{v}_{odo}$, such as

$$\mathbf{R}_{ext}[n] = diag\left(\sigma^2_{\psi_{vis_x}}, \sigma^2_{\psi_{vis_y}}, \sigma^2_{\psi_{vis_z}}, \sigma^2_{v_{vis_x}}, \sigma^2_{v_{vis_y}}, \sigma^2_{v_{vis_z}}, \sigma^2_{v_{odo_x}}, \sigma^2_{v_{odo_y}}, \sigma^2_{v_{odo_z}}\right) \in \mathbb{R}^{9,9} \tag{5.24}$$

5.4 Tight integration

The TC integration algorithms use pseudorange and pseudorange-rates (i.e. Doppler) measurements, as extracted by the GNSS receiver, and coupled with the observations provided by the external sensors. TC integration has been studied in the last decade by the GNSS community to augment GNSS standalone receivers by using sensors from different nature. Implementations of of this approach can be found in [146], [64], [127], [26], [158], [172].

One advantage offered by TC approaches, with respect to LC, is that the basic GNSS observations are not as correlated as the position and velocity solutions calculated in the GNSS receiver and therefore better statistics can be known leading to higher accuracy of the integrated system [21]. Another advantage is that it allows continuous navigation even if the number of GNSS measurements is lower than the ones required by the GNSS standalone solution, i.e. equal to 4. Moreover, it usually provides better performance in terms of accuracy, continuity of the position solution and robustness in signal degraded environments, with respect to LC. However, the larger size of the state vector requires more computational time and it requires access to the raw GNSS measurements.

The architecture of a TC GNSS receiver is shown in Figure 5.3 where GNSS pseudoranges and Doppler are fused with data coming INS, visual sensor and odometer. Within this structure, the error estimates by the navigation filter, are used to correct the

INS derived position, velocity and attitude using GNSS measurements as external aiding. Basically, the INS measurements are used to predict the nominal position, velocity and attitude, that are eventually employed to predict the pseudoranges and the pseudorange-rates of all the visible satellites.

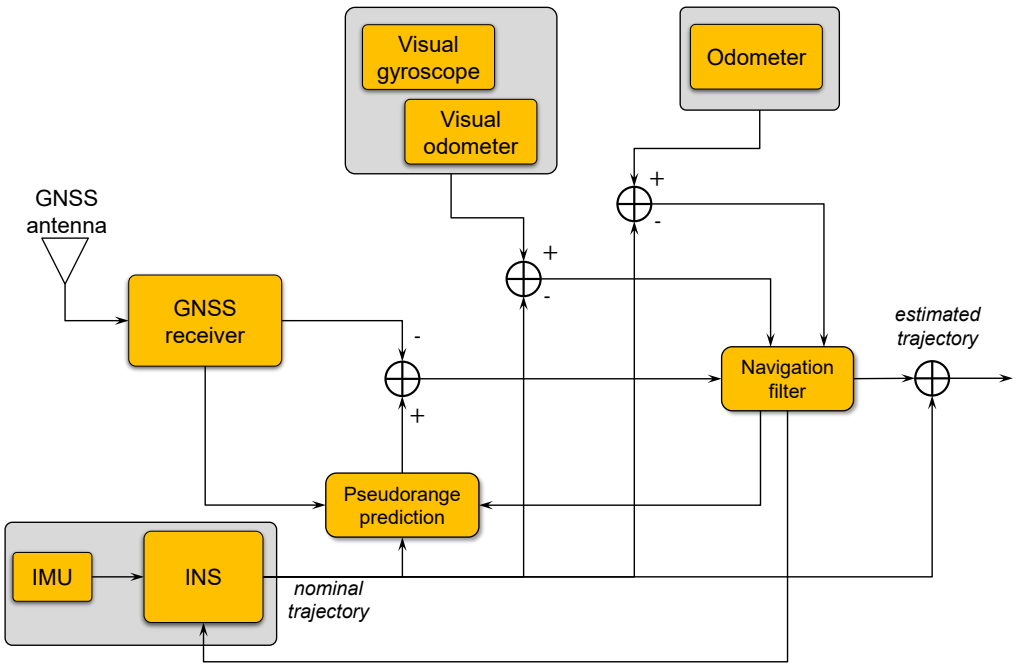

Figure 5.3: Architecture of a multi-sensor GNSS receiver TC with INS, visual sensor and odometer.

The details of the navigation filter, implemented according to an EKF scheme, used within the architecture of the multi-sensor TC GNSS receiver reported in Figure 5.3, are presented in the following.

State-space model

The set of the system states (*incremental states*) is the following:

$$\Delta\mathbf{x}(t) = \left[\Delta\mathbf{p}^e(t)^T, \Delta\mathbf{v}^e(t)^T, \Delta\boldsymbol{\psi}^e(t)^T, \mathbf{b}_a^b(t)^T, \mathbf{b}_g^b(t)^T, \Delta\boldsymbol{\tau}(t)^T, \Delta v_\tau(t)\right]^T \in \mathbb{R}^{18,1} \quad (5.25)$$

It can be easily noticed that the state vector (5.25) for tightly integrated systems is identical to (5.1), previously set for the loosely integrated system, plus two additional components:

- $\Delta\boldsymbol{\tau}(t) \in \mathbb{R}^{2,1}$ is the receiver clock bias for GPS and Galileo expressed in meters;
- $\Delta v_\tau(t) \in \mathbb{R}^{1,1}$ is the receiver clock drift expressed in meters per second.

State transition matrix

The TC integrated system is characterized by the same transition matrix of the LC integrated system plus two more line to characterize the clock bias and drift. The discrete time domain equations are defined as:

$$\Delta\tau[n+1] = \Delta\tau[n] + \Delta v_\tau[n] T_c \tag{5.26}$$

$$\Delta v_\tau[n+1] = \Delta v_\tau[n] + \upsilon_\tau T_c \tag{5.27}$$

Thus, the state transition matrix $\boldsymbol{\Phi}[n]$ can be defined as:

$$\boldsymbol{\Phi}[n] = \begin{bmatrix} \mathbf{I}_3 & T_c\mathbf{I}_3 & \mathbf{0}_3 & \mathbf{0}_3 & \mathbf{0}_3 & \mathbf{0}_{3\times2} & \mathbf{0}_{3\times1} \\ \mathbf{N}^e & \mathbf{I}_3 - 2T_c\boldsymbol{\Omega}^e_{ie} & -T_c\mathbf{F}^e[n] & T_c\mathbf{C}^e_b[n] & \mathbf{0}_3 & \mathbf{0}_{3\times2} & \mathbf{0}_{3\times1} \\ \mathbf{0}_3 & \mathbf{0}_3 & \mathbf{I}_3 - T_c\boldsymbol{\Omega}^e_{ie} & \mathbf{0} & -T_c\mathbf{C}^e_b[n] & \mathbf{0}_{3\times2} & \mathbf{0}_{3\times1} \\ \mathbf{0}_3 & \mathbf{0}_3 & \mathbf{0}_3 & \mathbf{I}_3 + T_c\mathbf{D}_a & \mathbf{0}_3 & \mathbf{0}_{3\times2} & \mathbf{0}_{3\times1} \\ \mathbf{0}_3 & \mathbf{0}_3 & \mathbf{0}_3 & \mathbf{0}_3 & \mathbf{I}_3 + T_c\mathbf{D}_g & \mathbf{0}_{3\times2} & \mathbf{0}_{3\times1} \\ \mathbf{0}_{2\times3} & \mathbf{0}_{2\times3} & \mathbf{0}_{2\times3} & \mathbf{0}_{2\times3} & \mathbf{0}_{2\times3} & \mathbf{I}_2 & \mathbf{T_c}_{2\times1} \\ \mathbf{0}_{1\times3} & \mathbf{0}_{1\times3} & \mathbf{0}_{1\times3} & \mathbf{0}_{1\times3} & \mathbf{0}_{1\times3} & \mathbf{0}_{1\times2} & 1 \end{bmatrix} \tag{5.28}$$

where $\boldsymbol{\Phi}[n] \in \mathbb{R}^{18,18}$, and

$$\boldsymbol{\Gamma}[n] = \begin{bmatrix} \mathbf{0}_3 & \mathbf{0}_3 & \mathbf{0}_3 & \mathbf{0}_3 & \mathbf{0}_{3\times2} & \mathbf{0}_{3\times1} \\ T_c\mathbf{C}^e_b[n] & \mathbf{0}_3 & \mathbf{0}_3 & \mathbf{0}_3 & \mathbf{0}_{3\times2} & \mathbf{0}_{3\times1} \\ \mathbf{0}_3 & -T_c\mathbf{C}^e_b[n] & \mathbf{0}_3 & \mathbf{0}_3 & \mathbf{0}_{3\times2} & \mathbf{0}_{3\times1} \\ \mathbf{0}_3 & \mathbf{0}_3 & T_c\mathbf{I}_3 & \mathbf{0}_3 & \mathbf{0}_{3\times2} & \mathbf{0}_{3\times1} \\ \mathbf{0}_3 & \mathbf{0}_3 & \mathbf{0}_3 & T_c\mathbf{I}_3 & \mathbf{0}_{3\times2} & \mathbf{0}_{3\times1} \\ \mathbf{0}_{2\times3} & \mathbf{0}_{2\times3} & \mathbf{0}_{2\times3} & \mathbf{0}_{2\times3} & \mathbf{I}_2 & \mathbf{0}_{2\times1} \\ \mathbf{0}_{1\times3} & \mathbf{0}_{1\times3} & \mathbf{0}_{1\times3} & \mathbf{0}_{1\times3} & \mathbf{0}_{1\times2} & T_c \end{bmatrix} \in \mathbb{R}^{18,15} \tag{5.29}$$

with the definition of the model noise vector is

$$\boldsymbol{\eta}[n] = \left[\boldsymbol{\eta}_a[n]^T,\ \boldsymbol{\eta}_g[n]^T,\ \boldsymbol{\eta}_{aa}[n]^T,\ \boldsymbol{\eta}_{gg}[n]^T,\ \boldsymbol{\tau}[n]^T,\ \upsilon_\tau[n]\right]^T \in \mathbb{R}^{15,1} \tag{5.30}$$

Measurement equation

The incremental observation vector $\Delta\mathbf{z}[n]$ can be written as

$$\Delta\mathbf{z}[n] = \begin{bmatrix} \Delta\mathbf{z}_{GNSS}[n] \\ \Delta\mathbf{z}_{ext}[n] \end{bmatrix} \in \mathbb{R}^{2N_{sat}+9,1} \tag{5.31}$$

where the component $\Delta\mathbf{z}_{ext}[n]$ was defined in (5.13) and the component $\Delta\mathbf{z}_{GNSS}[n]$ is defined as

$$\Delta\mathbf{z}_{GNSS}[n] = \boldsymbol{\zeta}[n] - \check{\boldsymbol{\zeta}}[n] \tag{5.32}$$

where

- $\boldsymbol{\zeta}[n] = \left[\boldsymbol{\rho}[n]^T,\ \mathbf{r}[n]^T\right]^T \in \mathbb{R}^{2N_{sat},1}$ is the vector of the pseudoranges $\boldsymbol{\rho}[n]$ and pseudorange-rates $\mathbf{r}[n]$ (i.e Doppler measurements), measured by GNSS, at the time instant n;
- $\check{\boldsymbol{\zeta}}[n] = \left[\check{\boldsymbol{\rho}}[n]^T,\ \check{\mathbf{r}}[n]^T\right]^T \in \mathbb{R}^{2N_{sat},1}$ is the nominal pseudorange and pseudorange-rate vector.

The predicted incremental observation dependent from the state-space model only is written from the a-priori state $\Delta\mathbf{x}^-[n] = \boldsymbol{\Phi}[n]\Delta\mathbf{x}[n-1]$ as follows:

$$\Delta\mathbf{z}^-[n] = \mathbf{H}[n]\Delta\mathbf{x}^-[n] \tag{5.33}$$

where the observation matrix $\mathbf{H}[n]$ is defined as

$$\mathbf{H}[n] = \begin{bmatrix} \mathbf{H}_{GNSS}[n] \\ \mathbf{H}_{ext}[n] \end{bmatrix} \in \mathbb{R}^{2N_{sat}+9,18} \tag{5.34}$$

The components $\mathbf{H}_{GNSS}[n]$ is equal to

$$\mathbf{H}_{GNSS}[n] = \begin{bmatrix} -\mathbf{u}_e[n] & \mathbf{0}_{N_{sat}\times 3} & \mathbf{0}_{N_{sat}\times 3} & \mathbf{0}_{N_{sat}\times 3} & \mathbf{0}_{N_{sat}\times 3} & \mathbf{1}_{N_{sat}\times 2} & \mathbf{0}_{N_{sat}\times 1} \\ \mathbf{0}_{N_{sat}\times 3} & -\mathbf{u}_e[n] & \mathbf{0}_{N_{sat}\times 3} & \mathbf{0}_{N_{sat}\times 3} & \mathbf{0}_{N_{sat}\times 3} & \mathbf{0}_{N_{sat}\times 2} & \mathbf{0}_{N_{sat}\times 1} \end{bmatrix} \in \mathbb{R}^{2N_{sat},18} \tag{5.35}$$

where $\mathbf{u}_e[n]$ is the line-of-sight vector from the receiver to the satellite. $\mathbf{H}_{ext}[n]$ (5.19) is composed by the components $\mathbf{H}_{vis}[n]$ and $\mathbf{H}_{odo}[n]$, respectively equal to

$$\mathbf{H}_{vis}[n] = \begin{bmatrix} \mathbf{0}_3 & \mathbf{0}_3 & \mathbf{I}_3 & \mathbf{0}_3 & \mathbf{0}_3 & \mathbf{0}_{3\times 2} & \mathbf{0}_{3\times 1} \\ \mathbf{D}_{pos}[n] & \mathbf{I}_3 & \mathbf{0}_3 & \mathbf{0}_3 & \mathbf{0}_3 & \mathbf{0}_{3\times 2} & \mathbf{0}_{3\times 1} \end{bmatrix} \in \mathbb{R}^{6,18} \tag{5.36}$$

$$\mathbf{H}_{odo}[n] = \begin{bmatrix} \mathbf{0}_3 & -\mathbf{I}_3 & -\grave{\mathbf{v}}^e_{INS}[n] & \mathbf{0}_3 & \mathbf{0}_3 & \mathbf{0}_{3\times 2} & \mathbf{0}_{3\times 1} \end{bmatrix} \in \mathbb{R}^{3,18} \tag{5.37}$$

where $\mathbf{D}_{pos}[n]$ was defined in (5.21) and $\grave{\mathbf{v}}^e_{INS}[n]$ was defined in (5.22).

Measurement noise covariance matrix

Finally, the measurement noise covariance matrix $\mathbf{R}[n]$ can be written as

$$\mathbf{R}[n] = \begin{bmatrix} \mathbf{R}_{GNSS}[n] & \\ & \mathbf{R}_{ext}[n] \end{bmatrix} \in \mathbb{R}^{2N_{sat}+9,2N_{sat}+9} \tag{5.38}$$

where the component $\mathbf{R}_{ext}[n]$ was defined in (5.24) and the component $\mathbf{R}_{GNSS}[n]$ which can be written as

$$\mathbf{R}_{GNSS}[n] = \begin{bmatrix} \mathbf{R}_\rho[n] & \\ & \mathbf{R}_r[n] \end{bmatrix} \in \mathbb{R}^{2N_{sat},2N_{sat}} \tag{5.39}$$

$\mathbf{R}_\rho[n]$ contains the variances of the pseudoranges whereas $\mathbf{R}_r[n]$ contains the variance of the pseudorange rates observations.

$$\mathbf{R}_\rho[n] = \begin{bmatrix} \sigma^2_{\rho_1} & & \\ & \ddots & \\ & & \sigma^2_{\rho_{N_{sat}}} \end{bmatrix} \in \mathbb{R}^{N_{sat},N_{sat}} \tag{5.40}$$

$$\mathbf{R}_r[n] = \begin{bmatrix} \sigma^2_{r_1} & & \\ & \ddots & \\ & & \sigma^2_{r_{N_{sat}}} \end{bmatrix} \in \mathbb{R}^{N_{sat},N_{sat}} \tag{5.41}$$

Considering a satellite j, $\sigma^2_{\rho_j}[n]$ and $\sigma^2_{r_j}[n]$ can be calculated according to [110]:

$$\sigma^2_{\rho_j}[n] = a + b \cdot 10^{\frac{-C/N0}{10}} \tag{5.42}$$

$$\sigma^2_{r_j}[n] = c + d \cdot 10^{\frac{-C/N0}{10}} \tag{5.43}$$

where the constants a, b, c and d are defined in Table 5.1 for lightly degraded signal environments and heavily degraded signal environments. It is worth noting that these two signal degradation categories are dictated by a qualitative classification, in fact it is not possible to have an analytic definition about lightly and heavily degraded signal environments. In practice, urban canyons can be an example of heavily signal degraded environments since the GNSS signals are typically attenuated, blocked or reflected by high buildings and other objects in the line of sight between the user and the satellite. On the other hand, sub-urban scenarios (e.g. highway) can be classified as lightly degraded signal environments.

Table 5.1: Coefficients for pseudoranges and pseudorange-rates variance calculation [110].

	Lightly degraded signal environments	**Heavily degraded signal environments**
$a\ (m^2)$	10	500
$b\ (m^2Hz)$	150^2	10^6
$c\ \left(\frac{m^2}{s^2}\right)$	0.01	0.001
$d\ \left(\frac{m^2}{s^2}Hz\right)$	25	40

5.5 Ultra-tight integration

U-TC integration differs from LC and TC mainly because it is the deepest level of integration between GNSS and the external sensors. Within this structure, the GNSS tracking module is embedded within the navigation filter. The GNSS updates are basically used to calibrate the INS, while the estimates of the navigation filter are used to aid the GNSS receiver NCOs tracking loops. While LC and TC are quite consolidated in the scientific literature, the benefits of U-TC, especially in presence of different sensors with different features, have still to be investigated, due to its high complexity. However, the most relevant implementations can be found in [82], [141], [142], [147], [148], [139], [85], [182] and [27].

U-TC implementation is very close to the concept of vector-tracking GNSS receiver, introduced in Section 3.6. The difference lies in the fact that in U-TC implementation, the navigation filter is aided by the INS, thus making the estimation of code and carrier frequencies more robust. As in the case of vector-tracking receiver, U-TC can sustain tracking of GNSS signals with low C/N_0 provided that the estimation of precise carrier phase measurements is not required. This enhances the robustness of the overall system in signals degraded conditions, e.g. jamming. From this discussion, we might consider U-TC integration as a fusion between TC integration and a vector tracking GNSS receiver. However, the main drawback with respect to TC integration algorithm is that it requires modification to the conventional GNSS firmware since it requires access to the tracking stage of the GNSS receiver. Also, the computational burden is increased.

The architecture of an U-TC GNSS receiver is shown in Figure 5.4. The tracking errors for a specific channel are estimated by the *channel filter*. Such a filter includes either DLL and PLL loop filters in case of scalar-based tracking or a KF in case of KF-based tracking. The advantaged and disadvantages of using the two approaches were discussed in Section 3.4.3. Following the discussion about coherent and non-coherent KF tracking-based architectures reported in Section 3.4.3 and Section 3.6, a non-coherent approach is considered within this representation.

The details of the navigation filter, implemented according to an EKF scheme, used

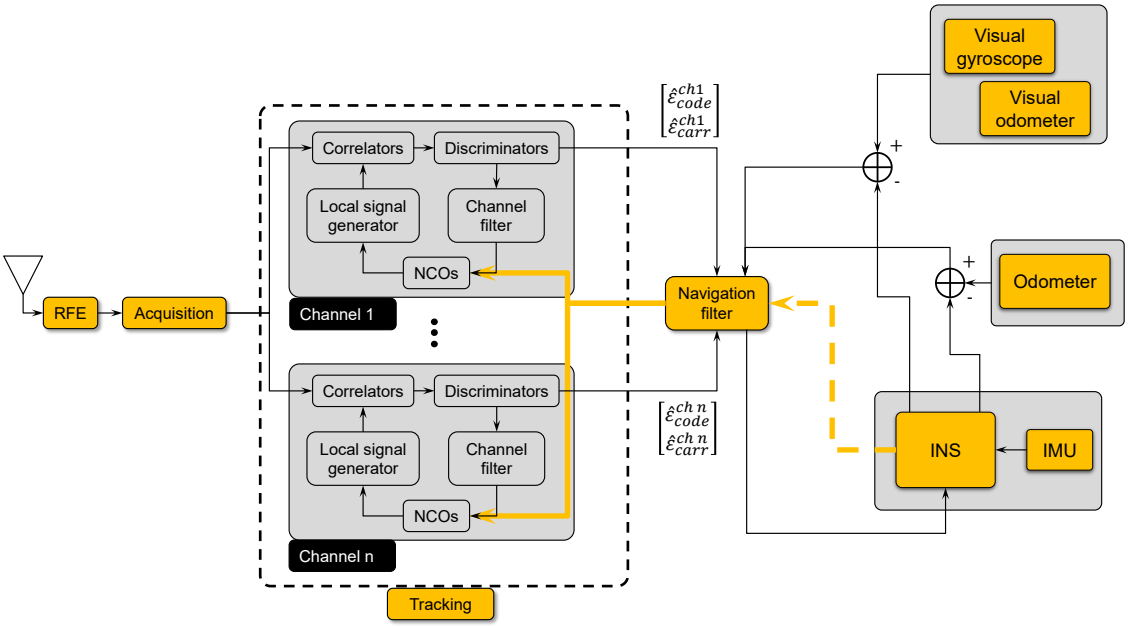

Figure 5.4: Architecture of a multi-sensor GNSS receiver U-TC with INS, visual sensor and odometer.

within the architecture of the multi-sensor U-TC GNSS receiver reported in Figure 5.4, are presented in the following.

State-space model

The vector of incremental states of the centralized EKF is the same as the one introduced for the tight integration architecture in (5.25).

State transition matrix

As a consequence, the same state transition matrix $\mathbf{\Phi}[n]$ and input matrix $\mathbf{\Gamma}[n]$ respectively reported in (5.28) and (5.29) are applied in the state equation of the ultra-tightly coupled KF.

Measurement equation

The main difference between U-TC and TC lies basically in the observation models of GNSS. Recalling the incremental observation vector $\Delta\mathbf{z}[n]$ defined in (5.31), in case

of TC, $\Delta\mathbf{z}_{GNSS}[n]$ is given by the difference between pre-corrected GNSS measured pseudoranges and pseudorange rates computed by INS. In case of U-TC it is given by the pseudorange and pseudorange rate residuals produced in each tracking channel through an ad-hoc *discrimination function*, for the code and carrier tracking error respectively, i.e.,

$$\Delta\mathbf{z}_{GNSS}[n] = \left[\tilde{\boldsymbol{\varepsilon}}_{\text{code}}[n]^T, \tilde{\boldsymbol{\varepsilon}}_{\text{carr}}[n]^T\right]^T \in \mathbb{R}^{2N_{sat},1} \tag{5.44}$$

where $\tilde{\boldsymbol{\varepsilon}}_{\bullet}[n]$ is the vector gathering all the outputs of either the code or carrier discrimination functions at the time instant n, properly scaled and corrected to directly express pseudorange and pseudorange rate errors. As a consequence, the observation matrix used to compute the innovation vector can be identical to the one written in (5.34).

Measurement noise covariance matrix

As far as the measurement noise covariance matrix $\mathbf{R}[n]$ is concerned, it was defined in (5.38) and it is composed by the component $\mathbf{R}_{ext}[n]$ (5.24) and the component $\mathbf{R}_{GNSS}[n]$. $\mathbf{R}_{GNSS}[n]$ contains the components $\mathbf{R}_{\rho}[n]$ (5.40) and $\mathbf{R}_{r}[n]$ (5.41). Considering a satellite j, $\sigma^2_{\rho_j}[n]$ and $\sigma^2_{r_j}[n]$ are function of C/N_0, and equal to [159]:

$$\sigma^2_{\rho_j}[n] = \left(\frac{c}{f_{code}}\right)^2 \frac{d}{4T_c(C/N0)_j}\left[1 + \frac{2}{(2-d)\,(C/N0)_j T_c}\right] \tag{5.45}$$

$$\sigma^2_{r_j}[n] = \left(\frac{c}{2\pi f_{carr} T_c}\right)^2 \frac{2}{T_c(C/N0)_j}\left[1 + \frac{1}{(C/N0)_j T_c}\right] \tag{5.46}$$

where f_{code} is the code frequency, expressed in Hz; c is the speed of light, expressed in m/s; d is the chip spacing, expressed in $chip$; T_c is the sampling interval, expressed in s; $(C/N0)_j$ is the C/N_0 of the satellite j, expressed in dB/Hz; f_{carr} is the carrier frequency of the signal, expressed in Hz.

NCOs update

What in this architecture mainly differs with respect to the tight integration, discussed in Section 5.4, is represented by the feedbacks from the navigation filter to the NCOs.

These feedbacks are computed from the prediction of the code rate and Doppler frequency derived from the inertial system corrected through the bias estimates of the EKF, as shown by the block diagram in Figure 5.4. The code and carrier frequency are therefore updated following the explanation introduced in Section 3.6 for the vector-tracking receiver. In particular, code frequency is (3.27) and carrier frequency is (3.28).

Chapter 6

The record and replay approach

The persistent growth of applications and services based on GNSS, together with the advent of new satellite navigation systems, is of paramount interest for different areas of the GNSS research community. Among such different areas, security aspects are certainly critical since GNSS signals are extremely weak and thus vulnerable to non intentional or intentional RFI. Moreover, since GNSS receivers are expected to operate in environments more and more challenging, there might be the need to develop customized positioning algorithms specifically tailored to the user's requirements. For instance, by processing the signals broadcast by the modern satellite navigation systems and eventually fusing it with the information coming from different sensors. The performance assessment of the positioning unit, by means of different receiver configurations and architectures, thus become essential for the development process of smart transportation that exploits the ITS technology.

Capturing real world signal environments with high fidelity, and then faithfully replaying it in a controlled environment might be useful for addressing some of these challenges. Not only it may act as a basis for the creation of synthetic but realistic scenarios – useful for assessing the impact of impairments such as RFI – but it also grants the principle of repeatability since the test can be repeated as many times as desired under exactly the same known conditions.

The R&R concept is presented and discussed in this Chapter. It starts discussing the

general principles of R&R and the advantages offered by the recording and replaying of the raw samples of the GNSS signal. After presenting the technical details of the playback system, the use of such an approach is mainly discussed for two applications: the performance assessment of a GBPT and the creation of synthetic scenarios based on data collected in a real environment. Eventually, the results of real data replay – related to two different cases – are presented as follows. First, in Section 6.5 for the GNSS receiver performance assessment in different operational environments. Finally, in Section 6.6 the effectiveness of the method is discussed assessing the impact of two types of interfering signals, such as CW and WB, on GNSS signals affected by ionospheric scintillations recorded in equatorial region.

6.1 Principles of record and replay

The concept of recording digital samples of the GNSS signal and then replay them in a lab controlled environment, recreating the original scenario, is a topic already addressed by the GNSS community and it is gaining much attention in recent years.

The block scheme of a R&R system for GNSS signals is depicted in Figure 6.1. It is possible to distinguish between the recording system, which consists of a RFE already presented in Section 3.2, and the playback system. The latter, which consists of a Vector Signal Generator (VSG), works as an inverted RFE. It basically re-constructs the signal $\hat{y}_{RF}(t)$, which is a replica of the received GNSS signal, as in $y_{RF}(t)$ (3.6), starting from its samples at IF, as in $y_{IF}[n]$ (3.10). However, the operations performed by the replay system will be described in detail in Section 6.2.

Design and implementation of the R&R approach are available in the literature. In [29], the authors present a detailed description of the design of a system capable of replaying narrowband GNSS IF signals. They also compare the performance of a replayed data set with its live counterpart with regards to position, timing, and Signal-to-Noise Ratio (SNR). In [87], the author focuses on the setup of the hardware components and assesses the performance of a commercial receiver in terms of signal strength and position. In [90], the design challenges of a system able to R&R GNSS signals for

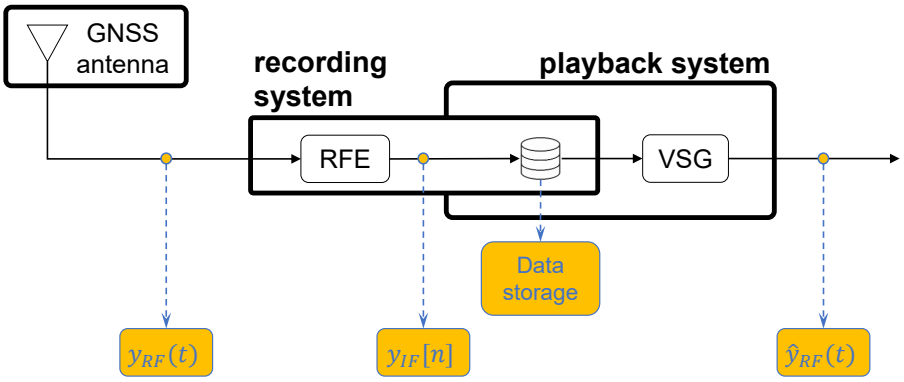

Figure 6.1: R&R system for GNSS signals. Block scheme.

multiple constellations and frequency bands are presented. In [44] the authors described the use of the R&R approach for testing different receivers, related to vehicular data collections, discussing also the repeatability of such a method.

Among the advantages offered by the recording of the raw samples of the signal, it enables the possibility of capturing a specific event or scenario from the real world for deeper and refined analyses. Some specific events may be rare and the analysis in real-time might not provide sufficient information. In this case more processing would be needed with respect to what it is possible to do when the event is detected.

On the other hand, the availability of the raw samples of the signal allows the replay of recorded data as many times as desired under exactly the same known conditions. This, in turn, enables the possibility to feed the signal to different devices under test to assess their performance in the desired scenario. Indeed, the R&R approach offers high repeatability, although the use of replayed scenarios embeds the limitation that they cannot be changed once the data are collected. Moreover, it has the significant advantage of being very close to the real world, so it offers high realism.

The storage of the raw samples of the GNSS signal, nonetheless, offers other advantages. For instance, the possibility to use a software receiver enables access to the complete receiver chain and to intermediate measures as well as the possibility to use different configurations of the receiver. This, in turn, can offer tools to develop new algorithms specifically tailored to the user's requirements.

Nevertheless, the design of a proper R&R systems, requires the tuning of the different

parameters of the systems to grant the right trade off between the fidelity of the recorded scenario to the real environment and an affordable level of complexity, as discussed in the following Sections.

6.1.1 The bottleneck of data storage and the quantization trade-off

As far as the storage of the samples is concerned, it requires data repository of large dimension. In case the collected data have to be transferred, large bandwidth data connections are also required. Lately, proper standards for the data description and exchange are also being defined. Considerably, the Institute of Navigation is developing a specification for standardized metadata, which would accurately and unambiguously describe the digitized data. With the objective to promote interoperability, the adoption of such a metadata standard will be used both by the data collection hardware and the software-defined radio receiver [84, 67].

Looking at the GNSS RFE architecture in Figure 3.1, the availability of the signal samples $y_{IF}[n]$ (3.10) allows for a recording of the GNSS signals that embed the characteristics of the environment. The fidelity of the recorded signal to the physical one, and in turn the size of the data collected, is affected by the two main parameters:

- the *sampling frequency* f_s of the ADC;
- the *number of bits* n_b necessary for the representation of the digital signal.

In detail, the choice of f_s is driven by the bandwidth not only of the GNSS signal but also by other "out-of GNSS band" events that might need to be represented in the saved data log, e.g. interference. On the other hand, the choice of the number of bits n_b used by the quantization process is driven by the desired dynamic resolution of the recorded signal. A proper setting of f_s and n_b is needed to preserve the information on the specific environment, assuring the fidelity of the recorded scenario with respect to the real one. Note that a too-small n_b limits the fidelity of the replayed scenario, sometimes introducing artifacts in the results. However, an optimum working point between IF recording quality and data volume has to be found with the goal to do not mask the meaningful features of the collected signals, thus preserving the information on the specific environment.

The amount of Bytes required for the data storage is equal to:

$$S = f_s \cdot N_{\text{bands}} \cdot N_s \cdot Q \cdot T \tag{6.1}$$

where:

- f_s is expressed in samples per second;
- N_{bands} is the number of frequency bands considered;
- N_s is the number of samples per instant which is equal to 1 in case of real samples and equal to 2 in case of concatenated I and Q samples, as explained in Section 3.4;
- Q is the number of Bytes per samples;
- T is the total time considered, expressed in seconds.

The storage memory requirement for a range of sampling frequencies and different quantization levels is shown in Figure 6.2, in case of concatenated I and Q samples. Note that the requirement of a signal sampled by using n_b equal to either 1, 2, or 4 would be the same as that of a signal sampled by using n_b equal to 8, by using 1-byte coding. As an example, a data-grabber acquiring the L1 GNSS bandwidth sampled at $f_s = 10$ MHz and $n_b = 16$ requires 40 Mbyte/s. Thus, 30 minutes of raw data amount to about $72GB$.

$$\begin{aligned} S &= f_s \cdot N_{\text{bands}} \cdot N_s \cdot Q \cdot T \\ &= \left(10 \cdot 10^6\right) \cdot 1 \cdot 2 \cdot (16/8) \cdot 1800 = 72GB \end{aligned} \tag{6.2}$$

6.2 Playback system

The playback system is considered as a dual system with respect to the recording system, shown in Figure 3.1 in case of GNSS signals. Essentially, it reconstructs and modulates the signals from the recorded digital scenario at IF to the analog signal at RF. In other words, it generates the signal $\hat{y}_{RF}(t)$, which is a replica of the GNSS signal $y_{RF}(t)$, as in (3.6), starting from its digital samples at IF $y_{IF}[n]$, as in (3.10).

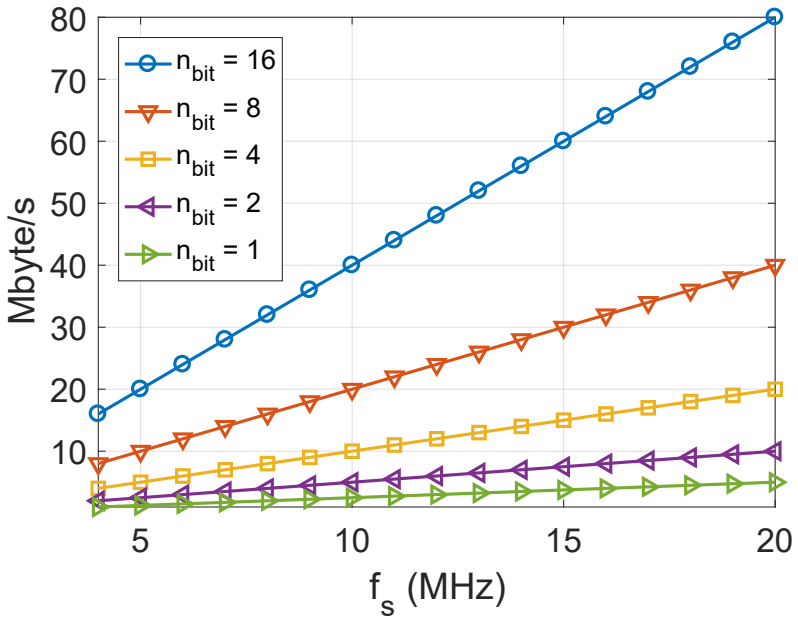

Figure 6.2: Memory requirement for a range of sampling frequencies and different quantization levels.

The full operational chain of the playback system is depicted in Figure 6.3. The block scheme highlights the duality of such a system with respect to the RFE, depicted in Figure 3.1. The GNSS signal at IF, $y_{IF}[n]$, is converted from digital to analog by a Digital-Analog Converter (DAC) and filtering stage.

The signal $\hat{y}_{IF}(t)$ is then modulated to the original RF by the LO using signal mixing frequencies from LOs. Considering only one component of the signal i, only one satellite j and neglecting the Doppler frequency shift f_d and the code delay τ, then the signal $\hat{s}_{mix}(t)$ can be written as:

$$\begin{aligned}\hat{s}_{mix}(t) &= \underbrace{x y_{IF}(t)}_{\text{IF signal}} \cdot \underbrace{2\cos(2\pi f_{LO} t)}_{\text{LO}} \\ &= \sqrt{2P}c(t)\bar{c}(t)d(t)\cos(2\pi \underbrace{(f_{IF} + f_{LO})}_{\text{RF}} t + \varphi) + \\ &\quad \sqrt{2P}c(t)\bar{c}(t)d(t)\cos(2\pi(f_{IF} - f_{LO})t + \varphi) + \eta(t)\end{aligned} \tag{6.3}$$

where f_{LO} term is the local oscillator frequency, which depends on the overall frequency plan and on the desired IF. It is chosen in order to obtain ($f_{IF} = f_{RF} - f_{LO}$). The other terms P_T, $c(t)$, $\bar{c}(t)$, $d(t)$, φ and $\eta(t)$ were introduced in (2.5) and (3.6).

The signal $\hat{s}_{mix}(t)$, at the mixer output, contains two different terms with: one with frequency centered at ($f_{IF} + f_{LO} = f_{RF}$) and the other one with frequency centered at ($f_{IF} - f_{LO}$). Since only the term at RF is desired, the higher order harmonics are filtered out. At the end of the band-pass filtering process, the component $\hat{y}_{RF}(t)$ can be written as:

$$\hat{y}_{RF}(t) = \sqrt{2P}c(t)\bar{c}(t)d(t)\cos(2\pi f_{RF}t + \varphi) \tag{6.4}$$

Depending on the power of the generated signal, an attenuation stage may be needed to emulate the power level received at the output of an active antenna. The signal at the output signal $\hat{y}_{RF}(t)$ in (6.4) can be finally broadcast by the playback system. Note that, an high-quality external reference clock may be needed to avoid introducing spurious components to the signal.

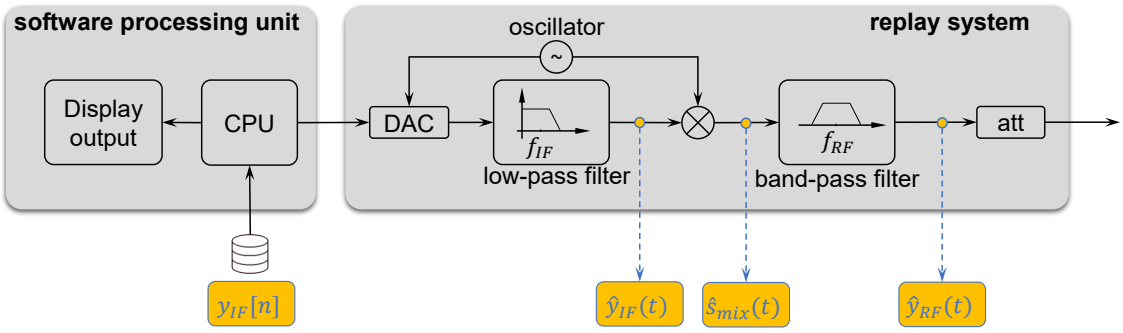

Figure 6.3: Software processing unit and GNSS replay system.

As an example, the comparison between the recorded (blue) and replayed (orange) signals, considering the real data recording and replaying presented in Section 6.5, is shown in Figure 6.4. The plot in the frequency domain is shown in the left whereas the histogram of the samples are shown in the right part of the Figure. The two signals exhibit a very similar frequency contents, as it can be seen by the spectra, as well as the same Gaussian shape of the histograms.

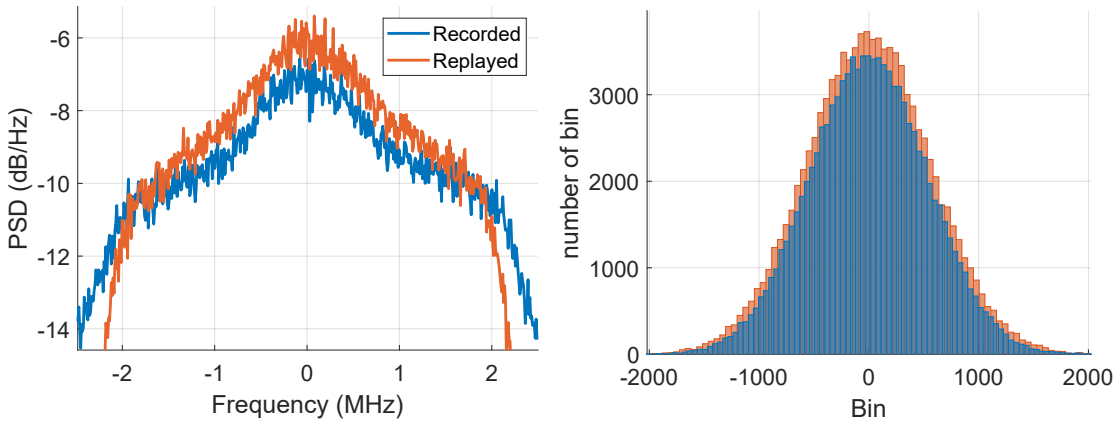

Figure 6.4: PSD (left) and histogram (right) of the recorded (blue) and replayed (orange) signals.

6.3 Record and replay for GBPT performance assessment

Since the R&R approach can potentially exhibit very high realism and repeatability, it can be an efficient solution for assessing the performance of a positioning terminal, thus offering a valid alternative to the classical approaches generally proposed, i.e. *laboratory tests* and *field tests*.

Before introducing how these approaches can be exploited for the performance assessment of a GBPT, it is important to recall the whole process-flow which has to be followed, regardless to the chosen approach. It might be represented by the main steps summarized in Figure 6.5. The first step is the definition of the scenario by means of trajectories and environmental conditions. Once the GBPT is installed on board of the vehicle, the test can be executed and positioning data are saved. Both a reference trajectory (ground truth) as well as the desired GBPT outputs are recorded. Such data are used to compute the errors to assess the metrics that define the GBPT performance.

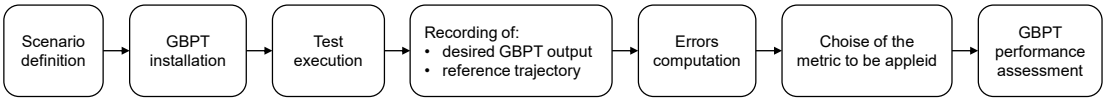

Figure 6.5: GBPT performance assessment.

6.3.1 Test procedures

The three approaches, generally proposed for the GBPT performance assessment, are the *laboratory tests*, *field tests* and the *R&R tests*.

The *laboratory tests* foresee the use of Radio Frequency Constellation Simulatorss (RFCSs) to define the scenario in a controlled and repeatable way. Several parameters, such as the pre-defined trajectory, the satellite geometry, the simulation of the errors (e.g., ionosphere, troposphere, multipath), and the power signal level, are under the user's control. The appropriate RF output is thus determined by using mathematical models. The laboratory tests are performed in a dedicated suitable area, usually an anechoic chamber or via a cable directly connecting the simulator to the GNSS antenna. During the execution of the test, the desired measurements are recorded by the GBPT under test and then compared to the reference trajectory, perfectly known from the mathematical model adopted by the RFCS. This method requires a sensitive amount of resources, especially if dynamic tests have to be performed. An overview of this approach for automotive testing is given in [25], where the authors presented a methodology to evaluate the position availability of automotive-grade GPS receivers utilizing a multichannel satellite signal simulator in a controlled laboratory environment.

The *field tests* rely on the use of specific test vehicles for accommodating the GBPT under test as well as the Reference Trajectory Measurement System (RTMeS), which is used to establish the true position referred to as the ground truth. As an example, the features and applications of the Vehicle for Experimental Research on Trajectories (VERT) are described in detail in [140]. After the definition of the scenario in terms of trajectories and on-board equipment installations, the test could be executed and the measurements from the GBPT and from the RTMeS are recorded. These are finally compared and thus the performance assessment of the GBPT under test can be performed.

The *R&R tests* can be considered as a combined solution between *laboratory tests* and *field tests*. Within this context, it is possible to identify two phases, such as the live operations (*record*) and the operations performed in a controlled lab environment (*replay*). During the live operations, the recording system is in charge of storing the raw GNSS of the signal as well as data from non-GNSS sensors, in case the output of other

sensors is of interest. It is worth noting that in this case it is important to grant the time tagging of the samples by a common stable clock. The signal captured from the antenna, is also fed to the RTMeS which estimates the ground truth. On the other hand, during the operations performed in the laboratory, the recorded data are replayed and the generated signal can be fed into the GBPT under test. Output positioning data are compared to the reference trajectory, and eventually used to compute the errors for the GBPT performance assessment.

A typical system architecture of the R&R system architecture for the GBPT performance assessment is reported in Figure 6.6 where the operations expected to be live-performed on-board the test vehicle are shown in the left part, while the ones carried out in the lab at a later stage are shown in the right part.

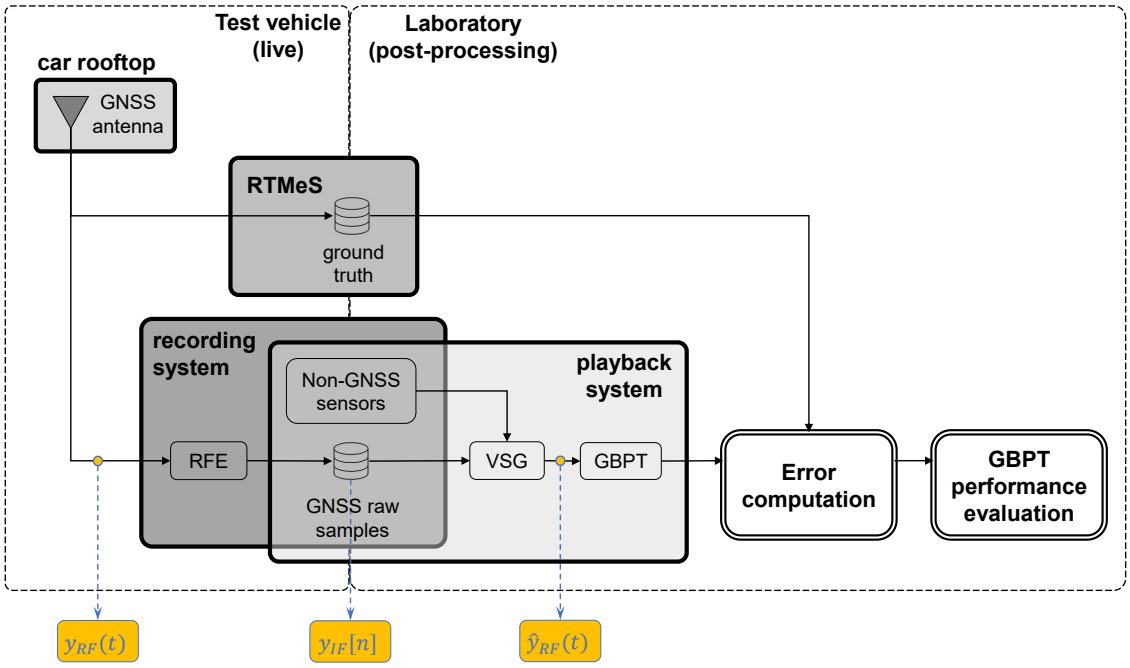

Figure 6.6: R&R system architecture for GBPT performance testing.

6.3.2 Test procedures comparison

Depending on the specific requirements and constraints, the different approaches proposed for the GBPT performance assessment present advantages and drawbacks,

as summarized in Table 6.1. However, they all are valid tools for testing since the characteristics of one device cannot replace the functionality of another.

Table 6.1: Advantages and drawbacks of the approaches for GBPT testing.

	Lab tests	**Field tests**	**R&R tests**
Cost	low	high	medium
Realism	low	high	high
Complexity	medium	high	medium
Repeatability	high	low	high
Controllability	high	low	medium
Valid for Hybrid	partially	yes	yes

Among the advantages offered by the lab tests is that the user has the ability to define different scenarios and repeat the tests as many times as desired, under exactly the same known conditions. Lab tests can account for unusual situations that otherwise would demand massive field campaigns to be recorded. For instance, intensive atmospheric effects, satellite clock drift and errors, orbit and ephemeris errors and other phenomena that can be modeled thanks to the high controllability offered by these lab tests. However, the major problem associated with such tests is that it is very difficult to model the signal degradation in the case of constrained environment scenarios such as the urban environment, so they ultimately offer low realism. Another drawback is that the hybridization of GNSS and other positioning sensors may be simulated only up to a certain level.

On the other hand, field tests present high realism because they allow the investigation of conditions that are difficult to simulate. Another advantage is that they are suitable for testing hybridized GBPT. However, they present the limitation that the environments are usually time-varying and so exhibit low repeatability.

Since a properly designed R&R approach offers high realism, it can be used for performance assessment. However, to have a stable and reliable statistic of the results, long data collections may be necessary. Furthermore, in order to obtain unbiased parameter statistics such as mean and standard deviation of the position, the results have to be averaged over a sufficient number of "consistent" scenarios.

As in the case of the lab tests, this approach might exhibit some limitations when

hybridized GBPTs are concerned. It is not straightforward to synchronously replay the GNSS signal and the other signals coming from other sensors. However, new capabilities are offered by the GNSS chipset manufacturers to record multiple sensor data inputs coherently with the GNSS signals and then replay them, increasing the level of playback realism. For instance, [3, 4] produce very sophisticated systems meeting such requirements. However, in some cases (e.g., if hybrid GNSS solutions have to be tested), the time series of the measurement of the other sensors do not need to be replayed, and only the GNSS scenario can be modified (e.g., adding interference), thus testing the robustness of the hybrid receiver.

6.4 Record and replay for the creation of synthetic scenarios

Since the R&R approach exhibits high flexibility and realism, the data samples can also act as a basis for the creation of synthetic – but realistic – scenarios adding impairments to a faithful reconstruction of the real received signal, as for example in the case of RFI, which can, in many cases, be modeled as an additive component to the received signal.

Instead of using models that are often over-simple, the RFI can be added to the replayed signal by mixing them in a lab environment. In this case, the parameters of the interfering signals are under the user's control, thus allowing a parametric assessment of the performance with respect to the nature and features of the interfering source that is synthetically created.

Furthers advantages offered by such an approach might be appreciated as far as malicious intentional interference is concerned. For instance, the interference produced by jammers could be safely injected onto GNSS pre-recorded data in order to evaluate its impact on the receiver performance.

The block scheme of a generic system which might be used to add impairments to the pre-recorded GNSS data is depicted in Figure 6.7. In the figure it is visible how the replay can be performed as many times as needed injecting the desired interference in

order to create the database of synthetic scenarios.

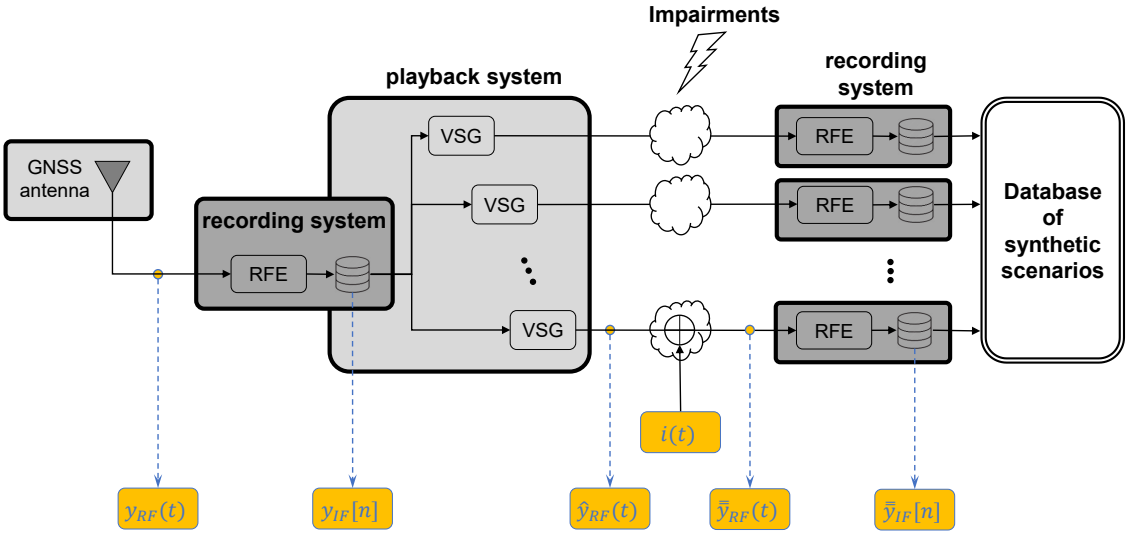

Figure 6.7: Adding impairments to the GNSS pre-recorded data. Block scheme.

In particular the following operations are performed:

- the GNSS signal $y_{RF}(t)$ is captured by the antenna and fed to the recording system,
- the RFE down-converts and samples $y_{RF}(t)$ creating $y_{IF}[n]$,
- $y_{IF}[n]$ is played back by the VSG generating $\hat{y}_{RF}(t)$,
- $\hat{y}_{RF}(t)$ is mixed with an additive interfering component $i(t)$ at RF generating the interfered signal $\bar{\bar{y}}_{RF}(t)$,

$$\bar{\bar{y}}_{RF}(t) = \hat{y}_{RF}(t) + i(t) \tag{6.5}$$

- $\bar{\bar{y}}_{RF}(t)$ is fed to the recording system which down-converts and samples the signal, creating $\bar{\bar{y}}_{RF}[n]$,
- $\bar{\bar{y}}_{RF}[n]$ is finally stored on a storage unit and added to the database of synthetic scenarios.

6.5 Real data replay: GNSS receiver performance assessment in harsh scenarios

This Section reports the results obtained by exploiting the R&R approach for assessing the performance of the GBPT. It is worth noting that, with respect to the positioning terminal depicted in Figure 1.1, the performance assessment is focused only on the GNSS module. The different sensors, which might be involved within the GBPT architecture, are thus not considered.

Nonetheless, the choice of considering the GNSS module only within the GBPT, is not restrictive since the GNSS sensor is the only one able to provide the absolute position of the vehicle, which is the basis for the overall positioning procedure.

USRP hardware [5] was used in order to build a flexible, low complexity and low cost system. Since it allows GPPs or Digital Signal Processorss (DSPs) to function as high bandwidth communication device, it is extremely versatile and flexible in terms of configuration parameters. USRP has gained much attention in recent years and widely exploited for GNSS SDR applications in several research projects [145, 50]. USRP can also be used as modulating device, allowing to replay the GNSS scenario recreating the analogue signals at RF from the stored baseband digital data. The variety of commercial devices able to record a range of additional signals, synchronised to the GNSS input, increasing the level of playback realism, [3, 4] are thus not considered within the performance assessment presented in this Section.

Data were recorded from vehicular data collections, within the city center of Helsinki, Finland, on November 15-16, 2016. Among the generic user environments described in [6], a qualitative classification between urban and suburban environments was performed. A snapshot of the data collected is shown in Figure 6.8 for urban (top) and suburban (bottom) environments. In particular, the former has a duration of approximately 4200 s and a path length of about 20 km whereas the latter has a duration of about 1000 s and a path length of about 21 km.

The advantages and disadvantages of the use of the R&R approach are highlighted for these two different operational environments.

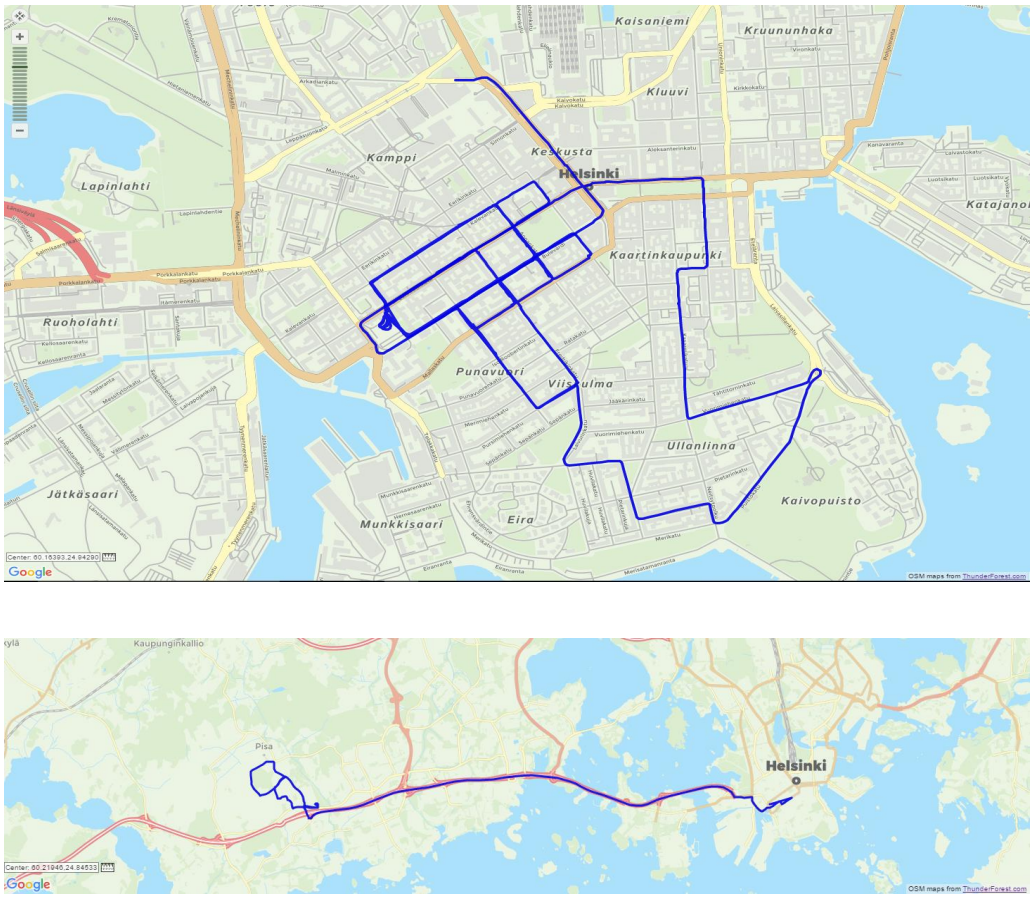

Figure 6.8: Datasets shown in Google Maps. Urban (top) and suburban (bottom) environments.

6.5.1 System Setup

The setup of the R&R system is shown in Figure 6.9. During the live operations performed on-board the test vehicle, the signal $y_{RF}(t)$ was first captured by the active Novatel OEM GNSS antenna (placed on the vehicle rooftop), and thus it was split among three branches. The power supply for the recording system was provided by an external battery whereas the reference receiver was powered directly from the car battery. On the other side, the playback operations were carried out in the laboratory in a post-processing stage.

The first branch included an RTMeS given by the dual frequency Novatel SPAN-CPT system receiver [7] calculating the ground truth. It is a compact, single-enclosure GNSS

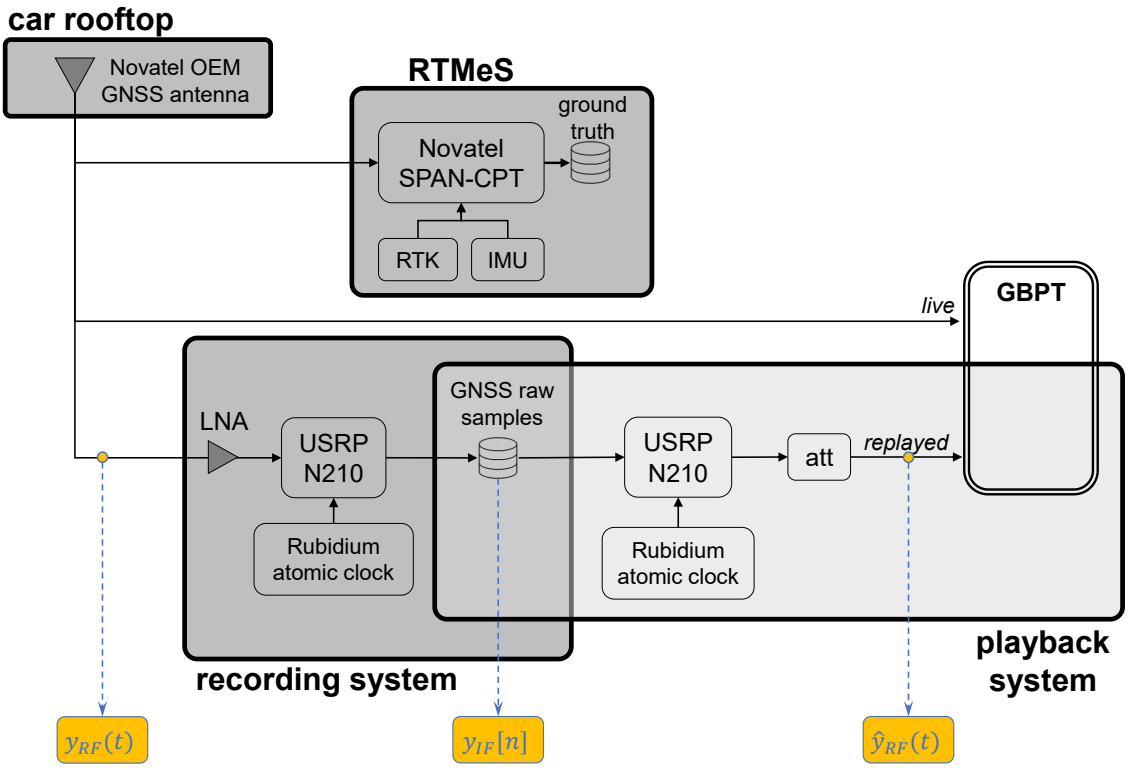

Figure 6.9: R&R system setup adopted for assessing the performance of a GBPT.

receiver with a tactical-grade Honeywell HG1700 IMU. The final accuracy was improved by exploiting the RTK corrections download from the FinnRef network. FinnRef is a nationwide network of permanent GNSS stations in Finland, providing publicly available differential GNSS corrections, but also RTK corrections for scientific use.

As depicted in Figure 6.9, the second branch included the GBPT under test, which was a consumer-grade GNSS receiver – namely, a uBlox M8T [8].

The third branch was the recording system. Within this block, the signal $y_{RF}(t)$ was first amplified by the LNA, which provided a 30 dB gain, and then it was fed to the RFE, a USRP N210 [5]. The latter was synchronized to a Rubidium frequency standard to control the ADC in order to have a very accurate and stable sampling frequency. Considering a trade-off between signal quality and available data storage resources, the USRP was configured by using the parameters listed in Table 6.2. By using these configuration parameters, 60 min of raw data amounted to approximately 72 GB.

The playback system is shown in the right part of Figure 6.9. It depicts the setup used

Table 6.2: USRP N210 configuration parameters.

Configuration parameter	**Value**
f_{if}	0 Hz (baseband)
f_s	5 MHz
Sampling Type	I and Q
Quantization	16 bits
Interface	Ethernet
Reference	Rubidium

in the laboratory to play back the binary samples stored on the disk, recorded during the data collections. The RFE used to reproduce the RF signal was the USRP N210, which was the same as the one used for recording the data setting the configuration parameters, listed in Table 6.2. It first converted the recorded samples $y_{IF}[n]$ to analog through the DAC. After a low-pass filtering stage, the samples were converted back to RF, and finally, band-pass filtered. $\hat{y}_{RF}(t)$ was finally attenuated to emulate the power received at the output of an active antenna and thus it was fed to the GBPT under test.

6.5.2 Analysis of the recorded GNSS raw samples

In order to study the dynamic range of the recorded signal, the GNSS raw samples of the signal, $y_{IF}[n]$, were analyzed in the time/frequency domain prior to being fed to the playback system. The analysis in the time domain is shown in the top-left panel of Figure 6.10, where the PSD of the signal is shown in the bottom panel. Since the AGC was not present within the RFE architecture, the gain provided by the RFE itself was manually adjusted in order to trigger 12 bits of the ADC, out of its maximum resolution of 14 bits.

The histogram, highlighting the Gaussian shape of the bins, shows its distribution over 12 bits where the output values were placed between -2048 and +2048. This design choice was twofold: on the one hand, it allows the recorded signal to be represented with a very high resolution, which might be needed to catch all the features of constrained environments. On the other hand, in the case of signal impairments such as RFI which requires higher signal power levels, it gives the possibility of enlarging the dynamic of the signal, as 2 bits are still available within the ADC. Note that this design choice also

has an important role in the playback operations – namely when the recorded signal is converted back to RF and fed to a GNSS receiver, provided that the GNSS receivers are designed to receive signals within a certain power level.

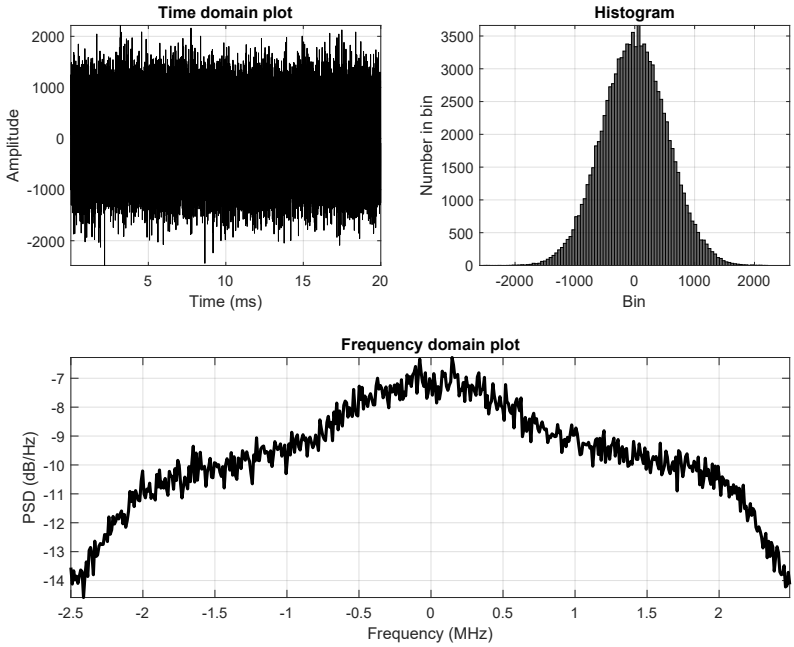

Figure 6.10: Analysis of the collected GNSS raw samples in time domain (top-left), histogram of the samples (top-right) and frequency domain (bottom).

6.5.3 Performance Assessment

The statistical characterization of the HPE related to the live and replayed trajectories is plotted in Figure 6.11 respectively, by the continuous and dashed lines. Moreover, the blue and orange lines are related respectively to the suburban and urban environments. The CDFs of the HPE are plotted in Figure 6.11 (left).

The 50^{th}, 75^{th}, 95^{th} percentiles, and the mean value of the HPEs are plotted in Figure 6.11 (right). As expected, the error on the final accuracy was larger in the case of harsh scenarios, as can be seen in the plot by comparing the continuous blue and orange lines. Such environments present several challenges to GNSS signal reception, such as blockage and reflection of the signals by buildings or trees.

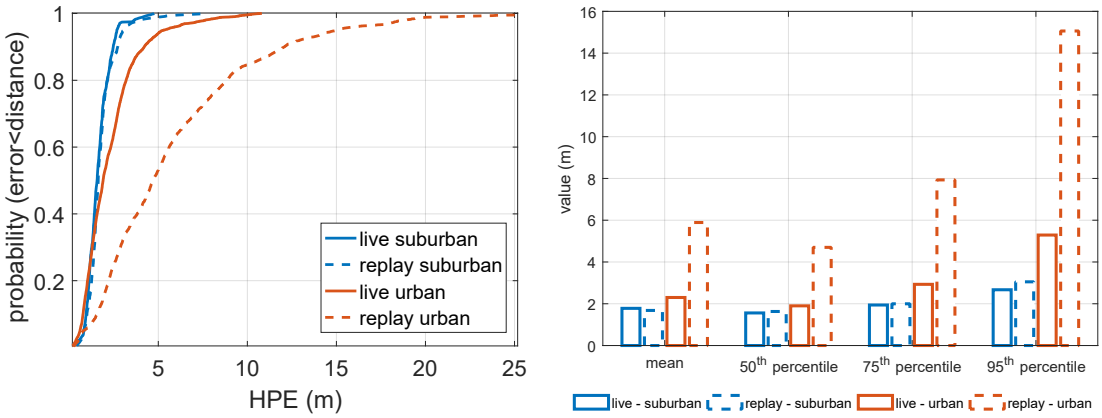

Figure 6.11: Statistical characterization of the HPE. CDFs (left) and additional metrics (right).

On the other hand, the comparison between continuous and dashed curves, which states the fidelity of the reproduced environment with respect to the real one, led to different results in suburban and urban environments. Considering for example the 95^{th} percentile as a metric, in suburban environments they exhibited a difference of about 40 cm. This can be acceptable since it might be due to some additional noise introduced during the replay operation. On the other hand, in the urban environment they exhibited a difference of about 10 m. One of the causes of such a fidelity loss could be the signal phase noise induced by the sampling and down/up converting reference oscillator, which impacts twice in the R&R chain, and has a larger impact in the case of the harsh urban environment with respect to the suburban one. This issue is deeply analyzed and discussed further in Section 6.5.4.

6.5.4 Analysis of the discrepancies for the urban environment case

Among the benefits of collecting the raw signal samples, as already discussed in Section 6.1, the possibility to perform deeper analysis of the signals was exploited here to analyze the discrepancy between the recorded and the replayed trajectories in the urban environment. Among the data collected during the test campaign presented in Figure 6.8, a dataset captured in the city center of Helsinki was chosen as a test case. It has a duration of about 600 s.

In order to assess the fidelity of the live signal with respect to the one generated by the playback system, they were analyzed and compared by means of the IF raw samples. Essentially, the RF signal generated by the playback system, i.e. $\hat{y}_{RF}(t)$, was down-converted to IF and the raw samples, i.e. $\hat{y}_{IF}[n]$, were eventually saved. Finally, $y_{IF}[n]$ and $\hat{y}_{IF}[n]$ were compared. The system setup is shown in Figure 6.12.

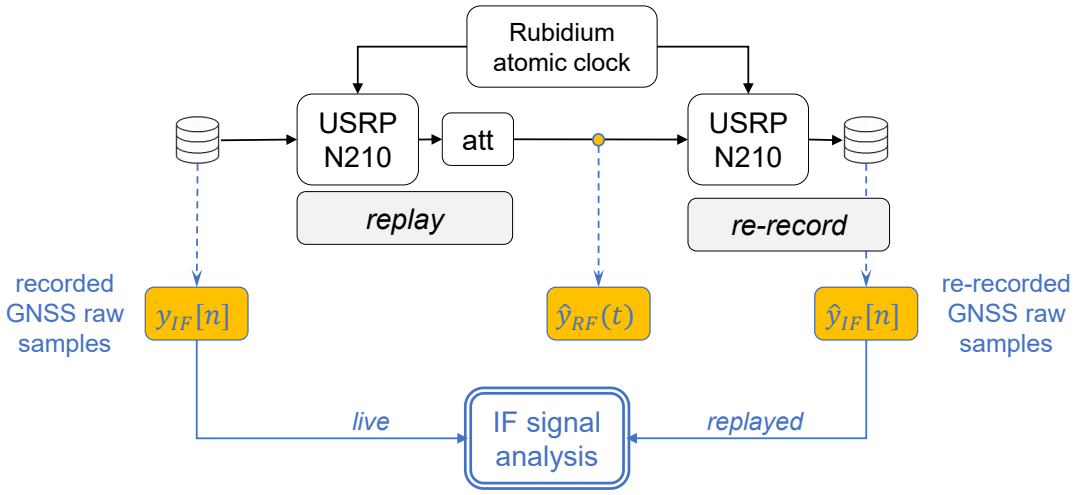

Figure 6.12: Test case for the urban environment. System setup.

As a first analysis, the two signals were analyzed in the time–frequency domain. The spectrogram of the recorded GNSS raw samples $y_{IF}[n]$ is shown in Figure 6.13 (left), where the power spectral density is color-coded. It highlights the presence of strong interference components located at about +2 and −0.4 MHz with respect to the central frequency. In order to evaluate how the recording and playback systems behaved under such strong impairments, the spectrogram of the re-recorded GNSS raw samples $\hat{y}_{IF}[n]$ was computed, as shown in Figure 6.13 (middle). The difference between the two spectrograms, shown in Figure 6.13 (right), states that the two signals had the same time–frequency components, meaning that the playback system faithfully reproduced the RF signal. This was true except for the highest frequencies attenuated by the RFE filter, as well as in the time interval from 352 to 355 s.

In order to investigate this mismatch, a snapshot of the two signal samples was taken at three different time instants. The histogram and the PSD are shown, respectively, in the top and bottom panels of Figure 6.14 for the recorded (blue) and re-recorded (orange)

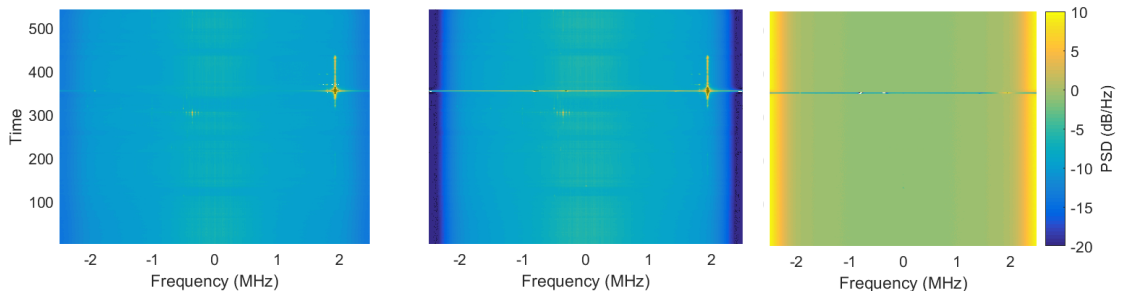

Figure 6.13: Test case for the urban environment. Spectrogram of the recorded (left) and re-recorded (middle) GNSS raw samples. Difference between the two spectrograms (right).

signal samples. It is possible to distinguish three cases, as follows:

- Case I, Figure 6.14 (left): nominal conditions and faithful RF signal reconstruction. Histogram (top) and PSD (bottom) were computed at second 155. We can define this situation as nominal conditions due to the absence of interference components within the signal. Therefore, in nominal conditions the histogram of the live and replayed signal samples had the same Gaussian shape. In addition, the two signals exhibited identical spectra.

- Case II, Figure 6.14 (middle): presence of RFI and faithful RF signal reconstruction. Histogram (top) and PSD (bottom) were computed at second 351. In that time instant, some interference components were present and located at approximately 2 MHz away from the central frequency. In correspondence of these points, the histogram of the signal samples did not have a Gaussian shape, as it should be in nominal conditions. However, the live and replayed histograms had the same shape. In addition, the two signals exhibited identical spectra, showing the capability of the system to collect and replay the full spectral information, even in non-nominal cases.

- Case III, Figure 6.14 (right): presence of RFI and wrong RF signal reconstruction. Histogram (top) and PSD (bottom) were computed at second 353. In that time instant, some strong interference components, located approximately 2 MHz away

from the central frequency, threatened the data collection system, since the RFE went into saturation.

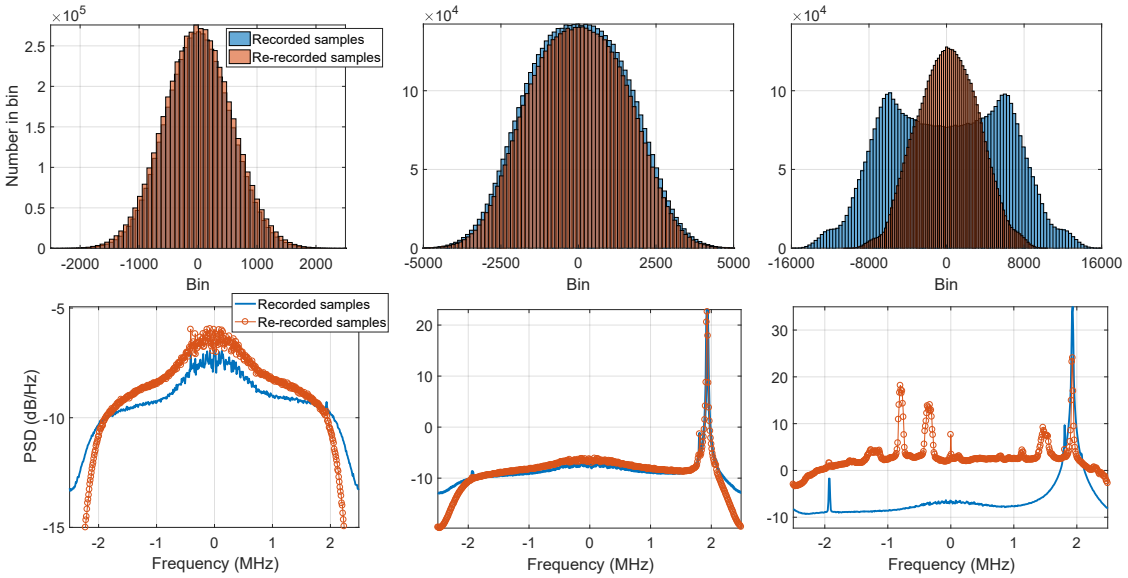

Figure 6.14: Test case for the urban environment. Histograms (top) and PSDs (bottom) of the recorded and re-recorded GNSS raw samples at seconds 155 (left), 351 (middle), and 353 (right).

As stated by the analysis of the live and replayed signals at IF, the playback system was able to faithfully re-generate the RF signal except for the time interval when the RFE went into saturation. Therefore, by feeding the two signals to the GBPT under test and comparing the HPEs, one would expect a similar behavior. In other words, the two curves should match for all the signal durations except for the time interval when the RFE went into saturation, which in this specific case was from 352 to 355 s.

The experiment was conducted by using different levels of attenuation for the re-generated RF signal before feeding it to the GBPT. The resulting HPEs are plotted in Figure 6.15 (left). Regardless of the different attenuation levels, the HPE of the replayed signal (dashed curve) was larger than the HPE of the live signal (solid curve). As a summary, it is possible to state that in constrained environments, despite the recorded and replayed signals having the same time and frequency behavior, they did not provide the same HPE when fed to the GBPT under test. In other words, in such harsh scenarios, the R&R system was not capable of fully reproducing the detailed recorded environment,

despite the good matching of the time and frequency representations. This is also visible from the C/N_0 estimation in Figure 6.15 (right), which shows the difference of the C/N_0 values between the live and replayed signals, for all the different levels of attenuation.

The receiver reacted in a different way to the recorded data with respect to the live operation. It has to be remarked that in harsh environments the receiver is forced to react to the variability of the environment, performing a number of operations for the management of the channels, the re-acquisition of the signals, and the logic for the allocation of the resources. Such operations are based on the monitoring of some parameters and according to a rationale that is unknown to the user. The values of the monitored unknown parameters may be slightly different in the replayed signal with respect to the real case, causing the receiver to behave in a different way when the signal is far from the nominal conditions (e.g., presence of interference, distortion of the Gaussian statistics, etc.), as shown in Figure 6.14.

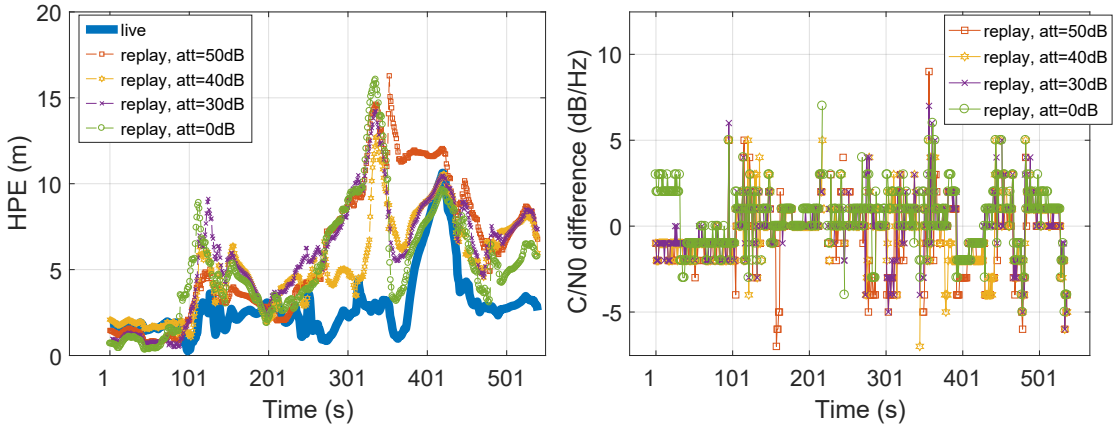

Figure 6.15: Test case for the urban environment. Different attenuation levels for the replayed signal. HPE over time (left) and C/N_0 (right) difference between live and replay signals for PRN 22.

The results show that the R&R approach should be used carefully when the recorded signal is far from the GNSS nominal condition, and it is hard to check the fidelity of the replayed signal in terms of metrics that take into account features that are important drivers for the receiver logic, but are unknown to the testing user who treats the receiver as a “black box”.

6.6 Real data replay: interference effect on GNSS signals affected by ionospheric scintillations

Another real application of the R&R approach is reported in this Section. As theoretically anticipated in Section 6.4, it was used here for adding two types of interfering signals, on GNSS data already affected by ionospheric scintillations. More precisely, following the of different types of interfering signal reported in Section 2.3.2, CW and WB interference are considered. Eventually, the impact of such interfering signals on the calculation of ionospheric scintillation indices is evaluated. Data were recorded in the monitoring station named Presidente Prudente, Brasil, (coordinates: 22° 07′ 19″ S, 51° 24′ 25″ W) on March 25, 2015.

6.6.1 System setup

The block diagram of the setup is shown in Figure 6.16. The USRP N210 [5] was used to record the digital samples of the GNSS signal as well as to playback them.

During the recording operations, the GNSS signal $y_{RF}(t)$ was first captured by the antenna. An RF power splitter was then used to distribute the signal between a professional ISMR, used as a benchmark, and the recording module. At this point, it was amplified by an LNA of 30 dB. The RFE, USRP N210 [5], was synchronized to a Rubidium atomic clock, providing a very accurate and stable reference to the ADC.

On the other hand, during the playback operations to inject the interference, the USRP was used to up-convert the pre-recorded IF signal $y_{IF}[n]$ back to RF obtaining $\hat{y}_{RF}(t)$. At this point, it was combined at RF level with the interfering signal $i(t)$ generated by an hardware signal generator. In particular, two types of interfering signals were considered. First, a narrow-band interference $i_{CW}(t)$ in the form of a CW, which has a small spectral occupation with respect to the GNSS signal bandwidth and appears as a single tone in the frequency domain. Then, a WB interference $i_{WB}(t)$ in the form of wideband noise, which has a spectral occupation comparable with respect to the GNSS signal bandwidth. In both cases, the interfering signals were injected between minutes 11 and 44, as shown

in Figure 6.17.

The combined signals, respectively $\bar{\bar{y}}_{RF,CW}(t)$ and $\bar{\bar{y}}_{RF,WB}(t)$ were then recorded back to IF by a second USRP and finally $\bar{\bar{y}}_{RF,CW}[n]$ and $\bar{\bar{y}}_{RF,WB}[n]$ were saved on a storage unit.

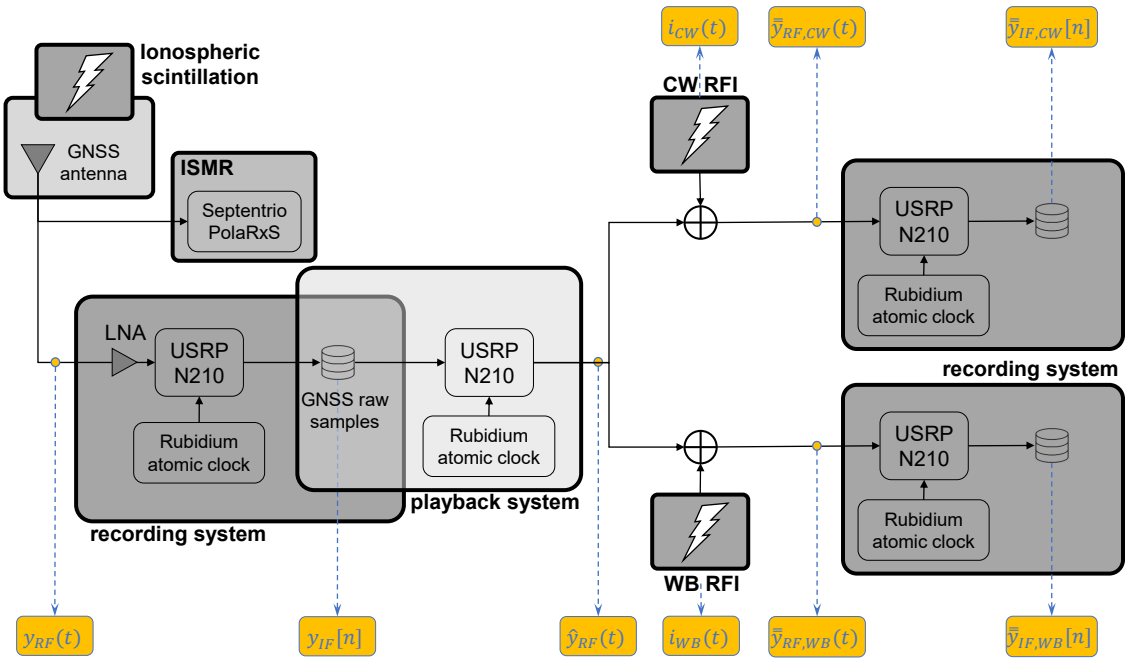

Figure 6.16: R&R technique used to inject CW/WB RFI onto the pre-recorded GNSS data. Block diagram.

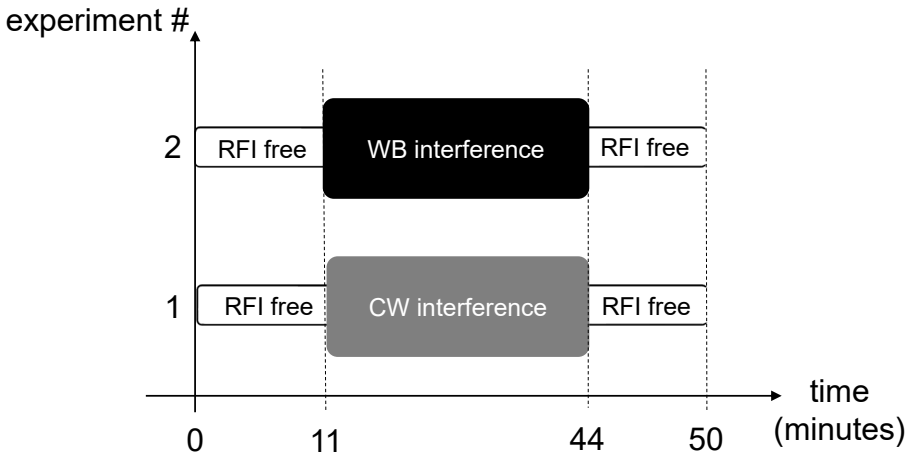

Figure 6.17: Experiment performed in the lab to inject CW and WB interference onto the pre-recorded GNSS data.

$$\bar{\bar{y}}_{RF,CW}(t) = \hat{y}_{RF,CW}(t) + i_{CW}(t) \tag{6.6}$$

$$\bar{\bar{y}}_{RF,WB}(t) = \hat{y}_{RF,WB}(t) + i_{WB}(t) \tag{6.7}$$

6.6.2 Interference impact analysis

The power spectral density of the signals, in case of RFI free, CW and WB interference, is shown in Figure 6.18. The spectrum related to CW RFI exhibits a spike with a power of about 40 dB with respect to the nominal power of the RFI free signal. The offset is equal to -3 KHz from the IF central frequency which in this case is equal to 0 Hz. On the other hand, the spectrum related to WB RFI might be considered as wideband noise over the whole spectrum increasing the power of about 10 dB.

It is worth noting that the power levels of the interference signals were never sufficient to completely blind the GNSS receiver. They were rather set to a level where the interference may cause some impairments in the measurements but its presence could actually go undetected. Indeed, failing to detect the presence of interference may cause mistaking any of its effects, for example on the estimation of scintillation indices as being originated from ionospheric activity.

Figure 6.19 (left) reports the C/N_0 as estimated by the software receiver in the three different situations: interference free scenario (blue), CW RFI (orange) and WB RFI (yellow). As expected, in the interference-free portions of the signal (before minute 11 and after minute 44) the three estimates perfectly overlap. Once the interference is injected, it is possible to see the impact of the interfering signal in the estimation of the C/N_0. WB interference constantly impacts the performance of the estimator for the whole duration of the impairment, behaving as additional thermal noise. On the contrary, CW narrow band interference induces a time dependent effect, because of the relative overlapping of CW central frequency and CA code spectral components [57]. The latter presents stronger C/N_0 drops, but concentrated in limited time slots.

Figure 6.19 (right) reports the $S4$. While in the interference-free case (blue line)

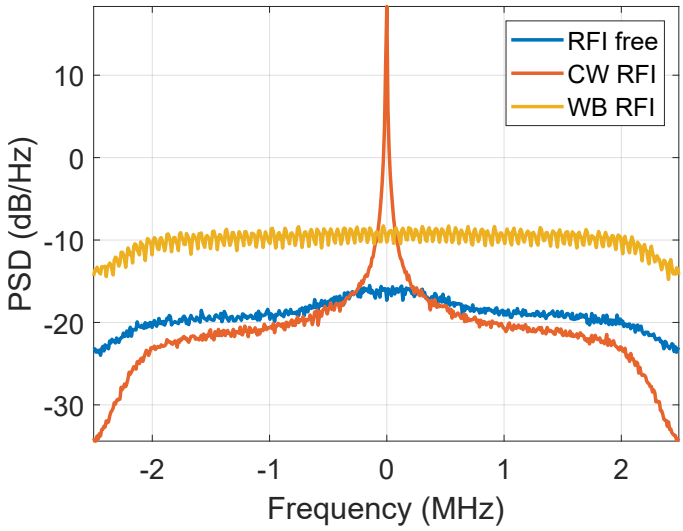

Figure 6.18: Estimation of PSD for different interfering signals.

no scintillation activity is detected ($S4 < 0.4$), artificial signal impairments fool the tracking and scintillation monitoring stage of the receiver. WB interference behaves as additional noise, slightly increasing the noise level in the $S4$ estimation (yellow line). On the contrary, CW interference induces a strong outlier (orange line), which could be wrongly interpreted as scintillation.

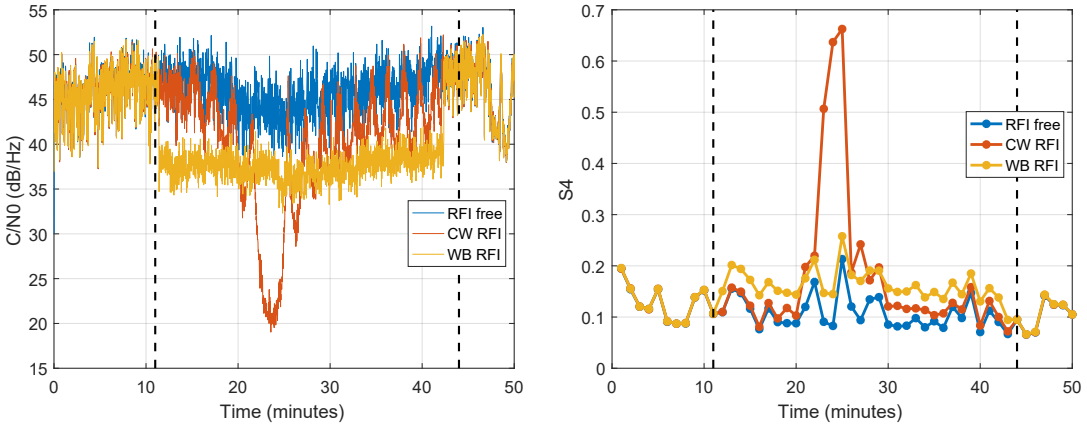

Figure 6.19: Estimation of the C/N_0 (left) and S4 (right) under CW and WB RFI for PRN 25. Black bars encase the period of time when interference is present.

6.6.3 Quantization trade-off

In order to evaluate the impact of the number of quantization bits on the assessment of the scintillation indices, the original signal (originally stored with a 16 bits resolution) was down-converted respectively to 8, 4, 2 and 1 bit. Eventually, the scintillation indices related to such configurations, were compared with the data recorded using a Septentrio PolaRxS ISMR.

The plot in Figure 6.20 shows the $S4$ and σ_ϕ indices of GPS PRN 1, as computed by the Septentrio receiver and by the software receiver on the raw data. The figure clearly shows how, decreasing the number of quantization bits, the loss with respect to the reference value is negligible. Even just using a single quantization bit the difference in the $S4$ value is less than 0.1. All replayed results are consistent with those obtained from the original recorded file, for all satellites. The noise level is increased when using 1 bit, slightly overestimating the value of $S4$.

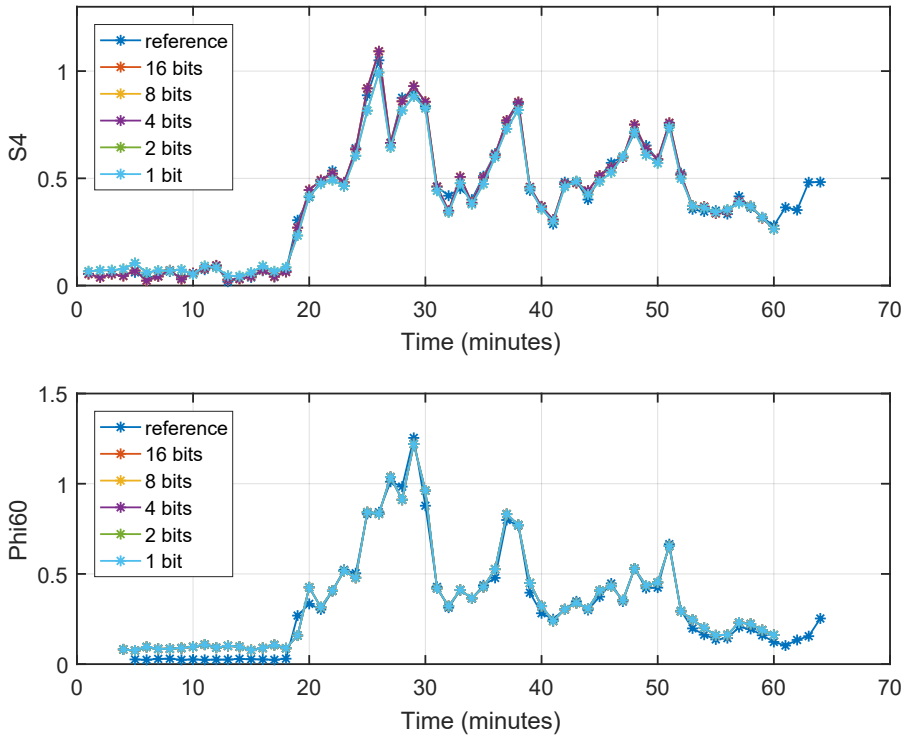

Figure 6.20: Comparison of the value of the scintillation indices for different quantization levels.

Thus, looking at this result, it seems straightforward to choose a 1-bit quantization level for SDR monitoring stations, in order to save in storage mass. However, the limitation of such an extreme choice is that most of the information is lost during the non linear quantization process. Indeed, a larger number of quantization bits is needed to preserve the fidelity of the original scenario. The data collected can be, of course, post processed, but there is not much room for the application of advanced signal processing algorithms that either could highlight a less global information such as the $S4$ is (averaged over long time windows) or could make the data usable to re-play realistic scenarios.

6.7 Conclusions

The R&R concept was presented in this chapter discussing its advantages and disadvantages together with its strengths and weaknesses. In particular, the use of such an approach was discussed for the performance assessment of a GNSS receiver as well as for the creation of synthetic scenarios adding impairments to the received signal. As a first conclusion, it is possible to state that the R&R approach is a reliable and powerful method but it might carefully used.

As far as the injection of impairments to the received signal is concerned, it is worth noting that, in case of impairments that naturally need multiplicative models to be properly represented, e.g. ionospheric phenomena such as ionospheric scintillations, the R&R is not suitable. In this case, mathematical models are needed to simulate the presence of such impairments to the signal. On the other hand, if the impairment itself can be modeled as an additive component to the received signal, e.g. RFI, thus the R&R could be an efficient solution, as shown by the results of the real data replay in Section 6.6.

However, despite the impairment to be injected can be modeled as an additive component to the received signal, but it contains strong non-linearities, e.g. an RFI component with a power too high with respect to the nominal power of the GNSS signal, the R&R approach might not be suitable to properly add such an impairment to the recorded signal. In this case, proper models able to model and simulate such strong non-linearities would be needed.

Another important aspect that has to be taken into account for a faithful injection of the desired impairment, is that all the significant spectral components of the impairment itself must lie within the narrow bandwidth of the RFE, which is achieved tuning the f_s as discussed in Section 6.1.1. This issue was not encountered within the results presented in Section 6.6 since the CW RFI had a very small bandwidth occupation, equal to 3 kHz with respect the RFE bandwidth equal to 5 MHz. On the other hand, the WB RFI behaved as additional noise slightly increasing the noise level over the whole bandwidth.

Finally, another aspect highlighted by the real data replay, in particular in Section 6.5, is that when the signal to be recorded is far from the nominal conditions (meaning that it contains strong linearities due to the presence of interference, distortion of the Gaussian statistics, etc.), the recording system might be threatened due to the saturation of the RFE. As a result, it might not be able to faithfully re-generate the RF signal.

Chapter 7

Performance assessment of multi-sensor integration

This Chapter includes the performance assessment of the multi-sensor navigation system, addressing TC and U-TC architectures of the hybridized receiver. The performance is assessed in different scenarios, characterized by different GNSS signal conditions, and described in the first part of this Chapter, discussing also the criteria behind the choice of these meaningful scenarios. The general principles of TC and U-TC integration algorithms were described in Chapter 5, while details about their implementation are discussed in this Chapter, before introducing the performance assessment. Therefore, the results of a GNSS standalone system are first presented to demonstrate the lack of accuracy of the solution in a signal degraded environment. Afterwards, comparisons with GNSS/INS integrated system are proposed to assess the improvement associated by fusing GNSS and INS. The choice of considering this system, before analyzing the multi-sensor integration, is made for reasons of comparison with a state of the art integrated navigation systems. Finally, the performance of the multi-sensor integration system is assessed, considering GNSS, INS, visual sensor and odometer, to evaluate the improvement associated with the increased number of sensors.

7.1 Methodology for performance assessment

Before introducing the different scenarios used for the performance assessment, an important consideration must be given about the reason of selecting only some meaningful scenarios. It is dictated by the complexity of having an exhaustive and fair performance assessment in all the possible conditions. In other words, the variability of many parameters such as the environmental conditions (satellite visibility, presence of multipath, etc.), the different number of sensors involved within the integrated system, the architecture of the GNSS module, to cite only few of them, lead the process of measuring and quantifying the performance metrics very complex.

Therefore, relative comparisons among meaningful scenarios are proposed, which are chosen as follows. The first considered scenario (***CaseA***) is characterized by good satellite visibility conditions, chosen for the performance assessment in an environment characterized by nominal condition of the GNSS signal. It might be considered our benchmark since it is well known that in such environments, GNSS receivers exhibit already good performance, in terms of positioning accuracy. Therefore, in contrast to *CaseA*, the second scenario (***CaseB***) is characterized by signal degraded environments since data were collected in an urban area known to be affected by severe multipath and unintentional RF interference sources in the GNSS bandwidths. This scenario is chosen to evaluate the real benefits of multi-sensor integration in such harsh environments where the standalone GNSS receiver might exhibit poor performance.

7.1.1 Open sky (Case A)

CaseA refers to a scenario characterized by nominal conditions of the GNSS signals since they are not blocked by high buildings and they are not affected by severe multipath. The data collection was performed on May 19, 2017 on a parking within the campus of Politecnico di Torino, Italy. A snapshot of the described environment is illustrated in Figure 7.1. Such a test was characterized by a duration of about 5 minutes.

Figure 7.1: *CaseA*. Test case for open sky. Torino, Italy. Image from Google Earth.

System setup

The system setup used for recording the data is shown in Figure 7.2 showing the kart where the sensors were mounted. The GNSS recording system consisted of a USRP B210 [9], synchronized to a Rubidium frequency standard, and used to record the digital samples of the GNSS signal. It was configured by using the parameters listed in Table 7.1. GNSS navigation data were logged by a consumer-grade receiver [10] and its velocity components were eventually exploited for emulating the odometer. A consumer-grade MEMS IMU XSens MTi-G-700 [11] was logging the specific forces and the angular measurements. The camera used for visual sensor measurements was a GoPro Hero5 Session [12]. The power supply for the recording system was provided by an external battery.

7.1.2 Harsh environment (Case B)

CaseB refers to a scenario characterized by signal degraded environments. Data were collected in a urban scenario in an area known to be affected by severe unintentional RF

Figure 7.2: *CaseA*. Kart used during the data collection.

Table 7.1: USRP B210 configuration parameters.

Configuration parameter	**Value**
f_{if}	0 Hz (baseband)
f_s	10 MHz
Sampling Type	I and Q
Quantization	16 bits
Interface	Ethernet
Reference	Rubidium

interference sources in the GNSS bandwidths. In terms of dynamics, a vehicular case was considered. The data collection was performed on March 2, 2018 in Helsinki, Finland. The vehicle started from a parking, selected because it provided excellent GNSS satellite visibility, with a static initialization period of about 10 minutes. Then it was driven on roads in urban canyons of the downtown area of Helsinki. In this context, GNSS signals were either blocked or affected by severe multipath as the scenario was characterized by high buildings, very narrow streets and trees. A snapshot of the described environment is illustrated in Figure 7.3. Such a test was characterized by a duration of about 10 minutes.

Vehicle speeds varied from 0 to about 40 km/h. Vehicle dynamics were somewhat limited due to the traffic jam present within the city center.

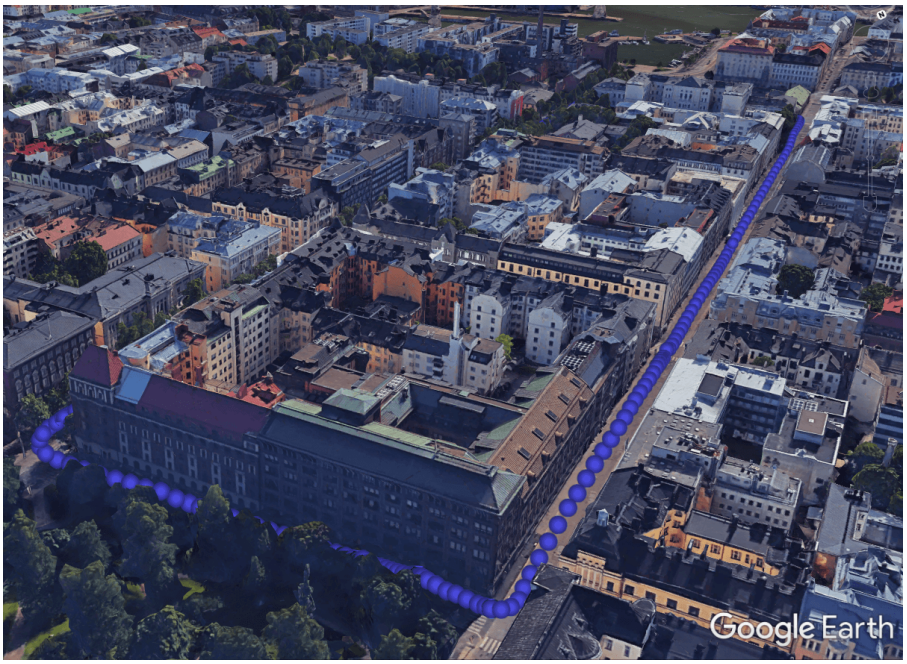

Figure 7.3: *CaseB*. Test case for harsh environment. Helsinki downtown. Image from Google Earth.

System setup

The system setup used for recording the data is shown in Figure 7.4. The reference trajectory was logged by the dual frequency Novatel SPAN-CPT system receiver [7]. It is a compact, single-enclosure GNSS receiver with a tactical-grade Honeywell HG1700 IMU. The final accuracy was improved by exploiting the RTK corrections download from the FinnRef network. FinnRef is a nationwide network of permanent GNSS stations in Finland, providing publicly available differential GNSS corrections, but also RTK corrections for scientific use. The GNSS recording system consisted of a USRP B210 [9], synchronized to a Rubidium frequency standard, and used to record the digital samples of the GNSS signal. It was configured by using the parameters listed in Table 7.1. The consumer-grade receiver uBlox M8-T [8] was used to log GNSS observables. The branch

containing the external sensors, consisted of a consumer-grade MEMS IMU XSens MTi-G-700 [11], that was logging the specific forces and the angular measurements. A GoPro Hero5 Session [12] has been as a visual sensor. The odometer was emulated by exploiting the velocity components from the Novatel SPAN-CPT system receiver [7]. The power supply for the recording system was provided by an external battery whereas the reference receiver was powered directly from the car battery.

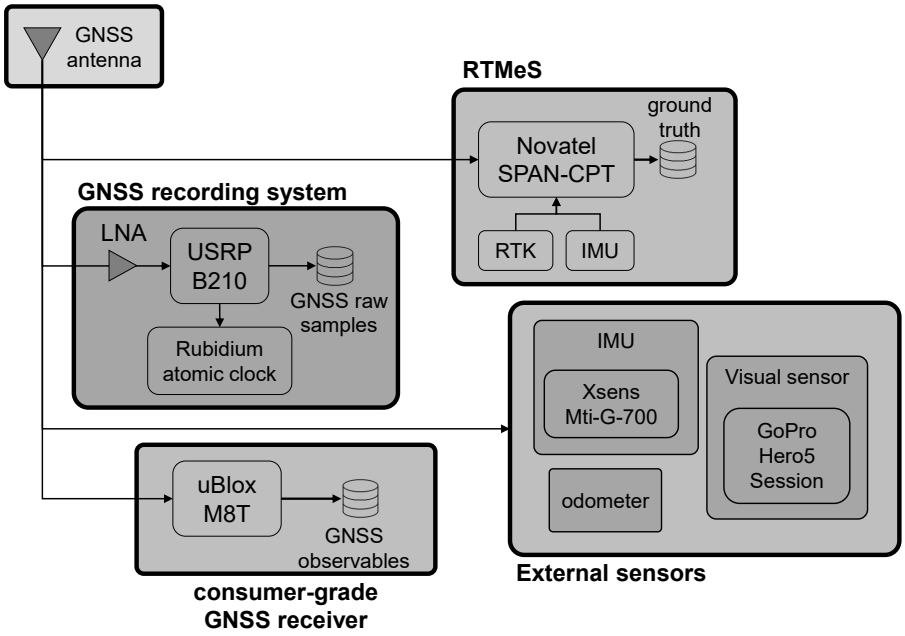

Figure 7.4: *CaseB*. System setup used for recording real data during the data collection.

7.2 Multi-sensor TC integration setup

The navigation filter for multi-sensor TC integration, developed within this research, is an error state EKF. The equation characterizing the EKF are reported in Section 5.4. It gathers GNSS data, such as GPS and Galileo, as well as data given by the INS, the visual sensor and the odometer. The error estimates are used to correct the INS derived position, velocity and attitude using GNSS measurements as external aiding. The block diagram of the whole navigation system is shown in Figure 7.5.

The update rates are listed in Table 7.2 for *CaseA* (and all the relative jammed

instances) and for *CaseB*. An update rate of 50 Hz was chosen for the navigation filter. On the other hand, the update rates of the sensors were given by the characteristic of the sensors themselves. In particular, GNSS observables were provided by the software receiver [164] for *CaseA* (thus choosing a rate as high as the one chosen for the navigation filter, i.e. 50 Hz) and by the consumer-grade GNSS receiver [8] for *CaseB* (thus exploiting its output rate, i.e. 1 Hz).

Due to a particular configuration of the camera, visual sensor provided data with a rate of 1.42 Hz (for *CaseA*) and 10 Hz (for *CaseB*). As the odometer was emulated exploiting the velocity components from [7] (for *CaseA*) and [10] (for *CaseB*), the choice of its update rate was dictated by the one of such navigation data, i.e. 1 Hz. It is worth noting that, since both *CaseA* and *CaseB* were not characterized by particularly high dynamic (vehicle speeds varied from 0 to about 1 m/s for *CaseA* and from 0 to about 12 m/s for *CaseB*), these values are enough to account for realistic dynamics of the motion of a vehicle.

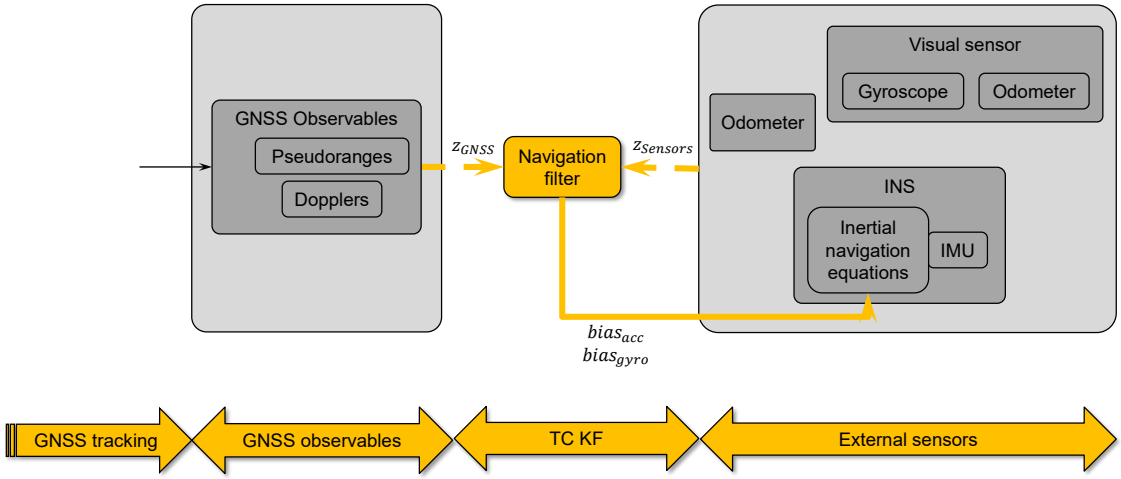

Figure 7.5: Block diagram of the proposed multi-sensor TC GNSS receiver.

Measurements exclusion strategy

The GNSS measurements are included within the incremental observation vector $\Delta\mathbf{z}_{GNSS}[n]$ based on their quality that, in turn, relates to the satellite elevation, presence of multipath and other impairments, and is generally measured by the C/N_0. Since the

Table 7.2: Update rates for TC integration.

	Update rate (Hz)	
	CaseA	*CaseB*
Navigation filter	50	50
GNSS observables	50	1
INS	400	400
Visual sensor	1.42	10
Odometer	1	1

presence of multipath is more likely to affect satellites with low elevations, two masks are considered to exclude satellites with elevations lower than 10° and a satellite showing C/N_0 lower than 38 dB-Hz.

7.3 Multi-sensor U-TC integration setup

As the main part of this research, the software for implementing the multi-sensor U-TC integration strategy, has been written within the software-defined multi-GNSS receiver platform, named as FGI-GSRx3 [164]. The navigation filter is an error state EKF, described in Section 5.5. According to the U-TC approach, it accepts the GNSS inputs from the signal tracking channels, which in this case processes GPS and Galileo signals. The other input is given by data logged from the INS, the visual sensor and the odometer. On the other hand, the navigation filter outputs the corrections for the INS and the predicted pseudoranges and pseudorange-rates for updating the NCOs. The block diagram of the whole system is shown in Figure 7.6.

The update rates are listed in Table 7.3 for *CaseA* (and all the relative jammed instances) and for *CaseB*. An update rate of 50 Hz was chosen for the navigation filter. On the other hand, the update rates of the sensors were given by the characteristic of the sensors themselves. In particular, GPS and Galileo signals were processed using a coherent integration time equal to 1 ms and 4 ms, respectively (and so their update rate equal to 1 kHz and 250 Hz).

Due to a particular configuration of the camera, visual sensor provided data with a rate

of 1.42 Hz (for *CaseA*) and 10 Hz (for *CaseB*). As the odometer was emulated exploiting the velocity components from [7] (for *CaseA*) and [10] (for *CaseB*), the choice of its update rate was dictated by the one of such navigation data, i.e. 1 Hz. It is worth noting that, since both *CaseA* and *CaseB* were not characterized by particularly high dynamic (vehicle speeds varied from 0 to about 1 m/s for *CaseA* and from 0 to about 12 m/s for *CaseB*), these values are enough to account for realistic dynamics of the motion of a vehicle.

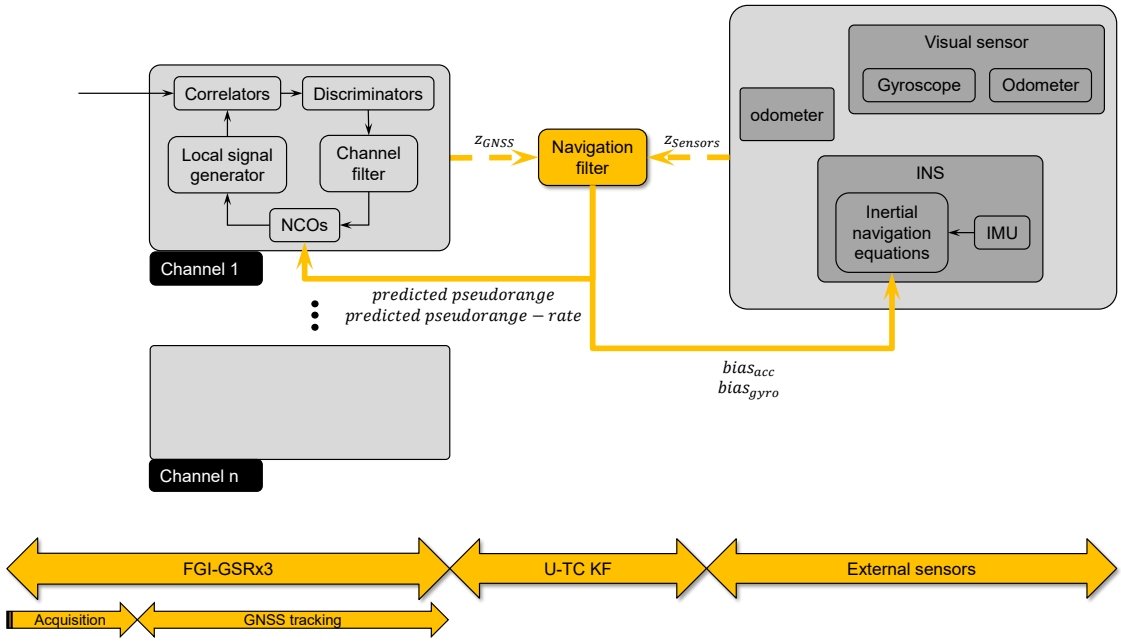

Figure 7.6: Block diagram of the proposed multi-sensor U-TC GNSS receiver.

Table 7.3: Update rates for U-TC integration.

	Update rate (Hz)	
	CaseA	*CaseB*
Navigation filter	50	50
GNSS tracking (GPS)	1000	1000
GNSS tracking (Galileo)	250	250
INS	400	400
Visual sensor	1.42	10
Odometer	1	1

As far as the GNSS measurements are concerned as input to the navigation filter, a non coherent approach is used. The difference between coherent and non coherent integration strategies, as explained in Section 3.4.3, is that the former utilizes the correlators outputs as measurements for the KF whereas the latter uses the output from the discriminator functions. Although a coherent approach would not introduce any non-linearity to the measurements, thus increasing the performance of the KF estimation, it relies on the ability to predict the GNSS carrier phase based on the INS output. Nevertheless, it is feasible only under circumstances where the GNSS signal is received with high C/N_0 in order to be able to track the carrier phase variations.

Since the purpose of this work is to assess the performance of the navigation system in weak signal condition and highly constrained interference environments, where carrier-phase precision was not required, the use of non coherent integration is the optimum integration architecture. Moreover, the low-cost MEMS IMU, used in our system, does not allow the ability to predict the GNSS carrier phase based on the INS output.

As far as the measurement equation is concerned, the component $\Delta\mathbf{z}_{GNSS}[n]$ (5.44) has been chosen according to an hybrid solution between the TC and U-TC approach. Recalling the $\Delta\mathbf{z}_{GNSS}[n]$ of TC in (5.32), it is given by the difference between pre-corrected GNSS measured pseudoranges and pseudorange-rates computed by GNSS and INS. On the other hand, the $\Delta\mathbf{z}_{GNSS}[n]$ of U-TC in (5.44) is given by the pseudorange and pseudorange-rate residuals produced in each tracking channel through an ad-hoc *discrimination function*, for the code and carrier tracking error respectively. In this case we chose as hybrid approach in the sense that $\Delta\mathbf{z}_{GNSS}[n]$ includes the pseudorange residuals $\tilde{\boldsymbol{\varepsilon}}_{\text{code}}[n]$ produced by the code discriminators and the difference between pre-corrected GNSS measured pseudorange-rates $\mathbf{r}[n]$ and $\check{\mathbf{r}}[n]$ computed by GNSS and INS. Thus, $\Delta\mathbf{z}_{GNSS}[n]$ can be written as

$$\Delta\mathbf{z}_{GNSS}[n] = \left[\tilde{\boldsymbol{\varepsilon}}_{\text{code}}[n]^T,\ \left[\mathbf{r}[n]^T - \check{\mathbf{r}}[n]^T\right]\right]^T \in \mathbb{R}^{2N_{sat},1} \tag{7.1}$$

Measurements exclusion strategy

The GNSS measurements are included within the incremental observation vector $\Delta\mathbf{z}_{GNSS}[n]$ based on a strategy, which depends on the variance of the phase error estimate. A specific measurement is included when such a variance estimate is below a threshold th_{GNSS}

$$th_{GNSS} = 6\ \sigma^2_{\hat{\theta}}|_{C/N0=35dB/Hz} \tag{7.2}$$

where $\sigma^2_{\hat{\theta}}$ is the variance of the phase error estimate, that can be written as [130]:

$$\sigma^2_{\hat{\theta}} = 2\sigma^2_{\eta_\theta} B_\theta T_D \tag{7.3}$$

where T_D is the integration time, expressed in s, $\sigma^2_{\eta_\theta}$ and B_θ are respectively the noise variance of PLL and the noise equivalent bandwidth for second order-loop [130], that can be written as:

$$\sigma^2_{\eta_\theta} = \frac{1}{2\dfrac{C/N0}{N_0}T_D}\ rad^2 \tag{7.4}$$

$$B_\theta = \frac{\omega_N}{8\zeta}\left(4\zeta^2 + 1\right) \tag{7.5}$$

where ω_N is the undamped natural frequency and ζ is the damping ratio.

As an example, $\sigma^2_{\hat{\theta}}$ is reported in Figure 7.7 for *CaseA*. The C/N_0 is plotted in Figure 7.8 in order to see how they are correlated. In this case, the GNSS measurement of channel 2 is not considered within the $\Delta\mathbf{z}_{GNSS}[n]$ when it exceeds the threshold. In this interval a drop of the C/N_0 can be observed.

7.4 Performance of GNSS standalone receiver

The navigation results of the GNSS standalone system are reported in the first part of our performance assessment. They can be considered as a benchmark for assessing the improvement associated with the integration of external sensors with respect to a GNSS standalone solution. Moreover, *CaseA* and *CaseB* are selected to assess the performance of such a system in different operational environments and to demonstrate

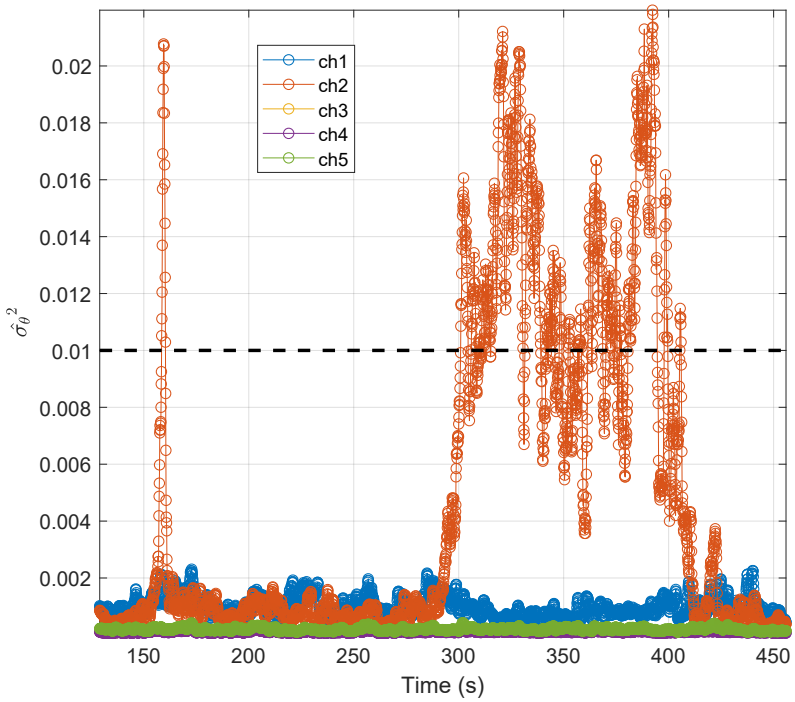

Figure 7.7: Variance of phase error estimate for *CaseA*.

the lack of accuracy of the solution in a signal degraded environment. LS algorithm was implemented using the pseudoranges from the GNSS software receiver [164] for *CaseA* and from the consumer-grade receiver [8] for *CaseB*. The statistical assessment of the position solution accuracy is summarized in Table 7.4.

	CaseA	***CaseB***
$\text{HPE}_{mean}(m)$	9.73	29.01
$\text{HPE}_{max}(m)$	64.30	152.83
$\text{HPE}_{50^{th}percentile}(m)$	6.74	20.04
$\text{HPE}_{75^{th}percentile}(m)$	11.00	38.85
$\text{HPE}_{95^{th}percentile}(m)$	31.28	107.12
Vel_X RMS Error (m/s)	0.18	1.79
Vel_Y RMS Error (m/s)	0.10	1.07
Vel_Z RMS Error (m/s)	0.20	1.31
Position provision (%)	100	96.02

Table 7.4: GNSS standalone. Position errors for *CaseA* and *CaseB*.

The position solutions for *CaseA* are reported respectively in Figure 7.9 and Figure

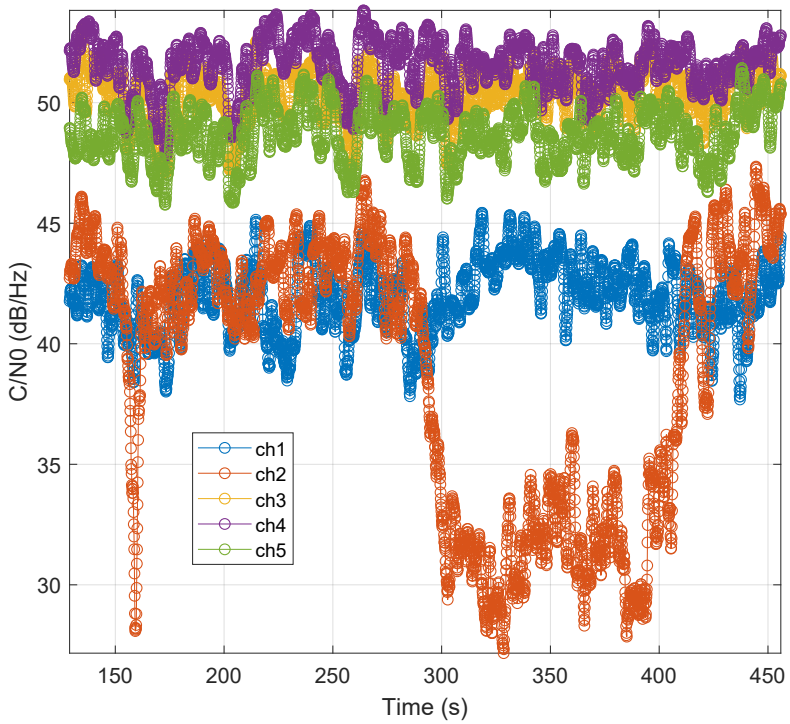

Figure 7.8: C/N_0 for *CaseA*.

7.10 showing the $2D$ trajectory and the HPE plotted over time. The same plots are reported in Figure 7.11 and Figure 7.12 for *CaseB*. The first consideration that can be drawn is about the poor performance exhibited by the GNSS standalone system in both scenarios, as expected. E.g. the 95^{th} percentile of the HPE is equal to 31.28 m and 107.12 m for *CaseA* and *CaseB*, respectively. The larger values of *CaseB* are due to the degraded GNSS signal conditions embedded in that scenario.

Since *CaseA* is characterized good satellite visibility, the number of available satellites is equal or greater than 4 for all the dataset duration. The receiver is then able to provide navigation solution. On the other hand, considering *CaseB*, the low satellite visibility due to the harsh conditions, forces the receiver to do not provide position solution 96.02% of the time. These results highlight how the performance position accuracy of standalone GNSS positioning can be seriously threatened in case of bad signal condition or low number of available satellites. The integration with other sensors is therefore needed and addressed in the remainder of this Chapter.

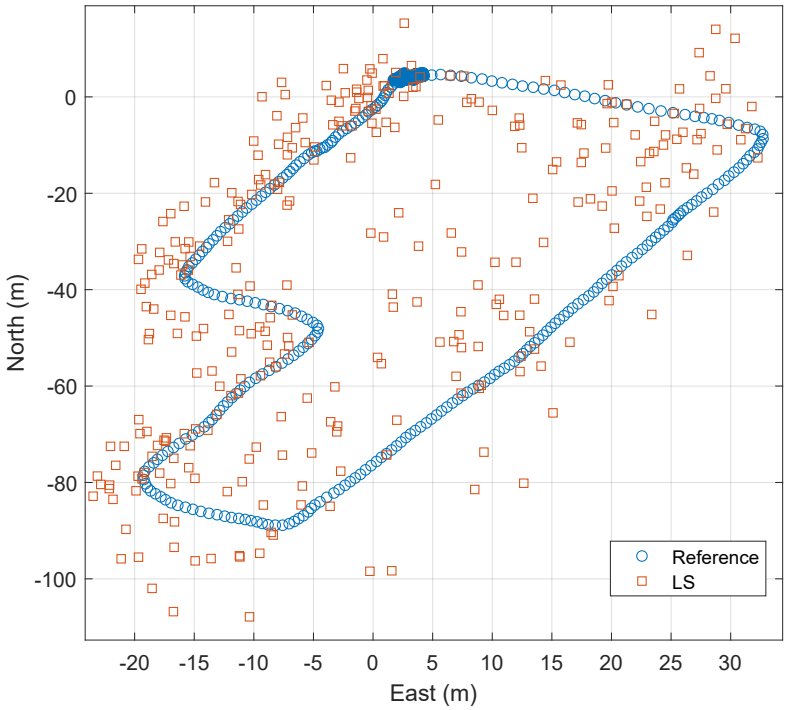

Figure 7.9: GNSS standalone results (orange) for *CaseA* and reference trajectory (blue). $2D$ trajectories.

7.5 Performance of GNSS/INS integration

Before considering the multi-sensor integration algorithms, the performance of the integrated GNSS and INS system is assessed here. Such a system, considered as the state of the art integrated navigation system, can be considered as a bridge in our performance assessment for the comparison with GNSS standalone as well as with multi-sensor integration. Table 7.5 reports the statistical assessment.

As far as the integration of GNSS and INS is concerned, a significant reduction of the HPE can be observed with respect to the GNSS standalone system. This is true for both TC and U-TC integration strategies. In fact comparing the values of Table 7.4 and Table 7.5 it is possible to see how the mean value of HPE, its maximum value and the reported percentiles are decreased. For instance, considering the 95^{th} percentile of the HPE, it is notably decreased from 31.28 m (GNSS-only) to 2.91 m (TC) to 3.73 m (U-TC).

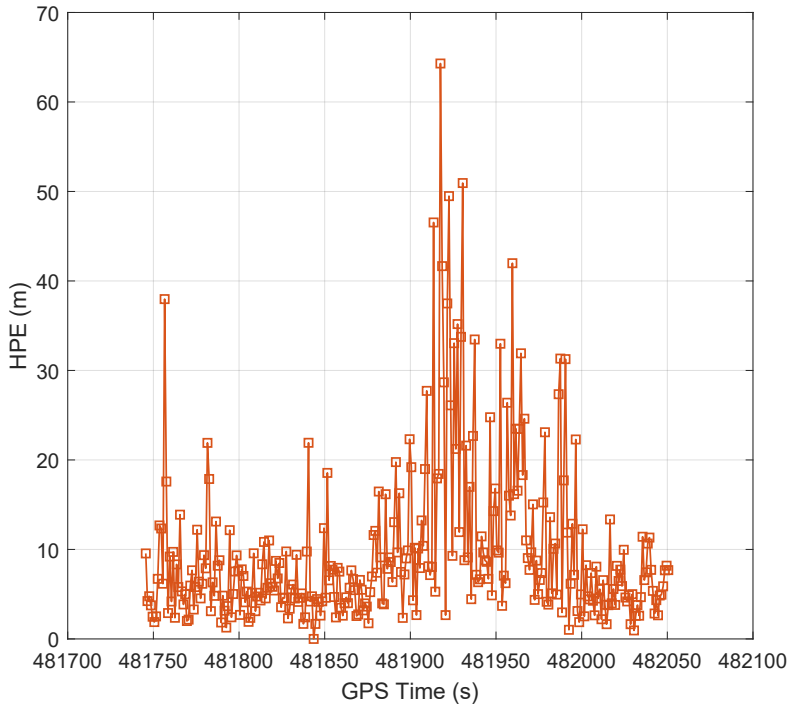

Figure 7.10: GNSS standalone results (orange) for *CaseA* and reference trajectory (blue). HPE over time.

	CaseA		***CaseB***	
	TC	**U-TC**	**TC**	**U-TC**
$\text{HPE}_{mean}(m)$	1.11	2.10	15.06	2.98
$\text{HPE}_{max}(m)$	21.56	3.91	288.73	16.28
$\text{HPE}_{50^{th}percentile}(m)$	0.73	2.12	4.87	2.26
$\text{HPE}_{75^{th}percentile}(m)$	1.05	2.83	9.53	4.51
$\text{HPE}_{95^{th}percentile}(m)$	2.91	3.73	58.24	7.77
Vel_X RMS Error (m/s)	0.18	0.18	2.28	0.34
Vel_Y RMS Error (m/s)	0.08	0.07	1.37	0.28
Vel_Z RMS Error (m/s)	0.18	0.18	0.45	0.23
Position provision (%)	100	100	100	49.97

Table 7.5: GNSS/INS TC and U-TC integration. Position errors for *CaseA* and *CaseB*.

Considering *CaseA*, the position solutions are plotted in Figure 7.13 where the reference trajectory is depicted in blue while the TC and U-TC solutions are depicted in yellow and green respectively. The HPE values are plotted over time in Figure 7.14. Looking at these results, it is possible to state that the performance of TC and U-TC are

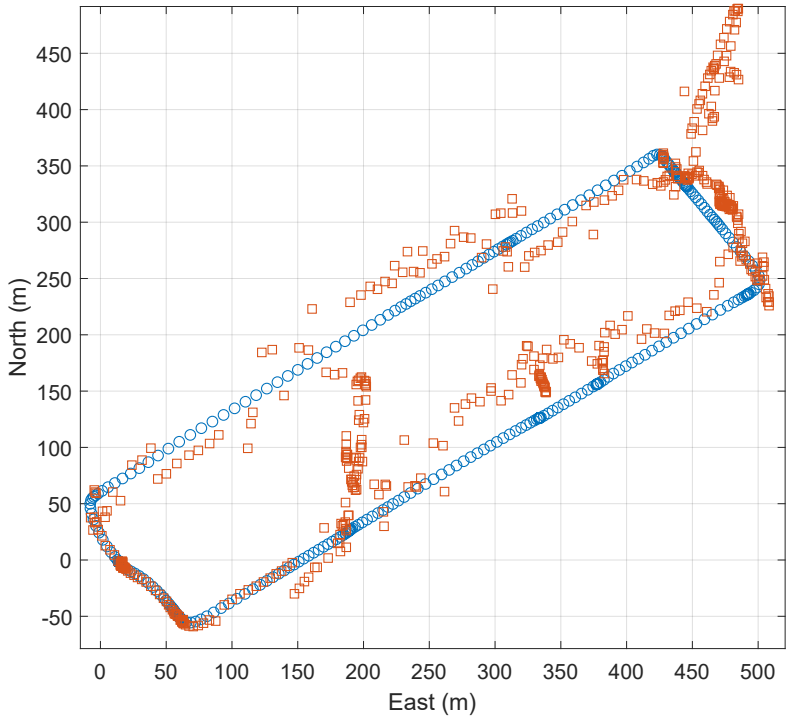

Figure 7.11: GNSS standalone results (orange) for *CaseB* and reference trajectory (blue). $2D$ trajectories.

in the same order of magnitude. This was expected since *CaseA* is characterized by open sky conditions and then it is not possible to appreciate the real benefits of U-TC with respect to TC. As a result, it is possible to state that the TC integration is already an excellent solution in case of nominal condition of the GNSS signal. In this case the high complexity of the U-TC algorithm is not justified. This aspect is however investigated in the remainder of the Chapter when *CaseB* is involved. Another aspect that comes out from the HPE analysis, is the large value of the maximum value of HPE in case of TC. It is due to a transient of the navigation filter in the beginning of the estimation introducing a bias into the position estimation. The integrated system is able to provide a navigation solution 100% of the time.

On the other hand, considering the performance assessment for *CaseB*, the position solutions are reported in Figure 7.15 where the reference trajectory is depicted in blue while the TC and U-TC solutions are depicted in yellow and green, respectively. The HPE values are plotted over time in Figure 7.16. The integration of GNSS and INS shows

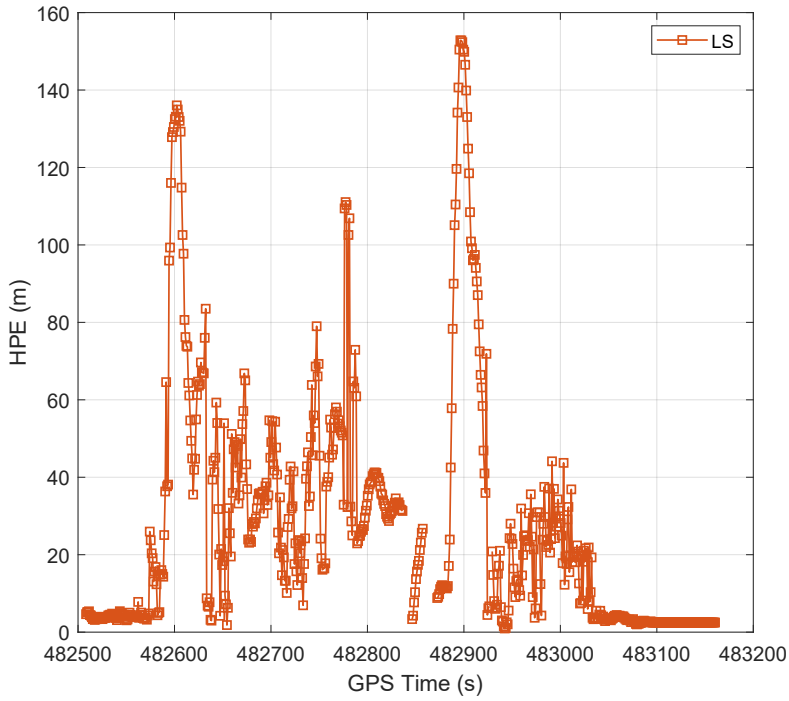

Figure 7.12: GNSS standalone results (orange) for *CaseB* and reference trajectory (blue). HPE over time.

a substantial improvement for what concern the mean value of the HPE and the reported percentiles. For instance, considering the 95^{th} percentile, it is decreased from 107.12 m (GNSS-only) to 58.24 m (TC) to 7.77 m (U-TC). Therefore, in contrast to *CaseA*, the benefits of U-TC with respect to TC are more evident highlighting the benefits of U-TC in degraded signal conditions. However, the TC shows a performance degradation, with respect to GNSS-only, on the maximum value of the HPE and on the error in the velocity component in the x axis. It can also be seen on Figure 7.16 where the yellow trajectory (TC) starts to drift making the estimation of the maximum error very large. This degradation makes such a value increasing from 152.03 m (GNSS-only) to 288.73 m (TC). This is due to different reasons: the very low number of available satellites, correlated with the low quality of the IMU that made the velocity to drift, as shown in Figure 7.17. The velocity estimated by the TC system is depicted in blue, in addition to the one estimated by the reference system, depicted in green. Also the number of available satellites is visible, plotted in orange. From the plot, it is possible to see how

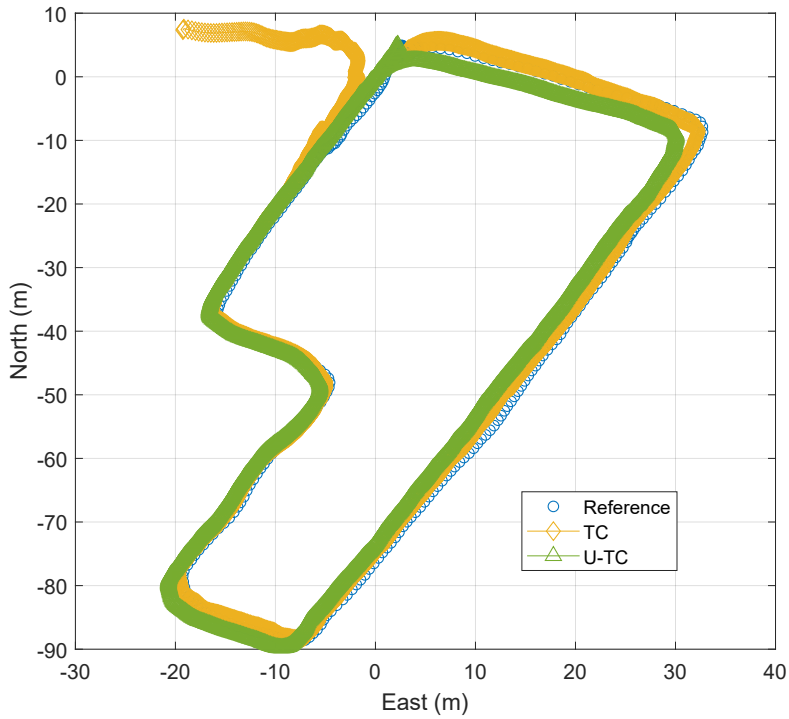

Figure 7.13: GNSS/INS TC (yellow) and U-TC (green) integration for *CaseA*. 2*D* trajectory.

the velocity started drifting in correspondence to the black bar, due to the number of satellites equal to 2. This corresponds to the point where the HPE started increasing. The benefit of the U-TC integration might be appreciated in this case since it is able to correctly estimate the velocity even with a low number of satellites. In that case, the maximum value of the HPE is considerably decreased to 16.28 m.

Considering again *CaseB* in case of TC, the integrated system is able to give a navigation solution 100% of the time with respect to GNSS-only where the same value was equal to 96.02%. However, it shows a degradation in case of U-TC (49.97%). As it happened for TC, it was due to the very low number of available satellites, correlated with the low quality of the IMU, that made the velocity drifting. The difference with respect to TC lies on the different logic of the GNSS receivers providing the data. In case of TC, the GNSS data were given by a consumer-grade GNSS receiver [8], which typically are forced to react to the variability of the environment, performing the re-acquisition of the signals. On the other hand, in case of U-TC, the GNSS data were given by the GNSS

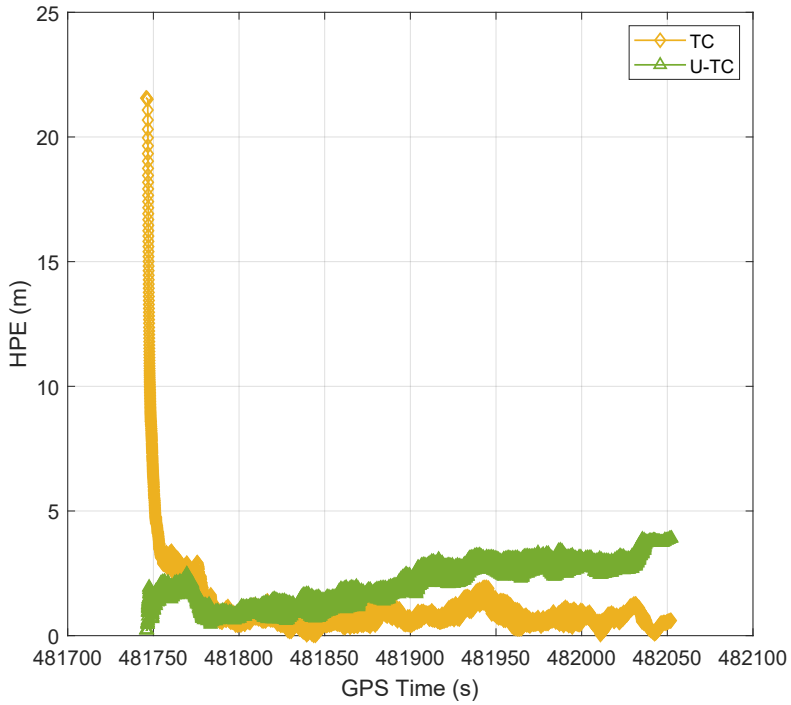

Figure 7.14: GNSS/INS TC (yellow) and U-TC (green) integration for *CaseA*. HPE over time.

software receiver [164] which did not have such a mechanism of re-acquisition. This problem was overcome by performing multi-sensor integration that made the estimation of the velocity and of the yaw more stable in such critical situation, as illustrated in the next Chapter.

7.6 Performance of multi-sensor integration

TC and U-TC multi-sensor systems are finally analyzed for *CaseA* and *CaseB* to assess the improvement associated with the increased number of sensors with respect to the GNSS/INS integrated system. GNSS, INS, visual sensor and odometer are then part of the integrated system. The statistical assessment of the position solution is reported in Table 7.6.

Looking at the performance assessment of *CaseA*, it is possible to see that the multi-sensor integration does not bring considerable improvement with respect to the GNSS/INS

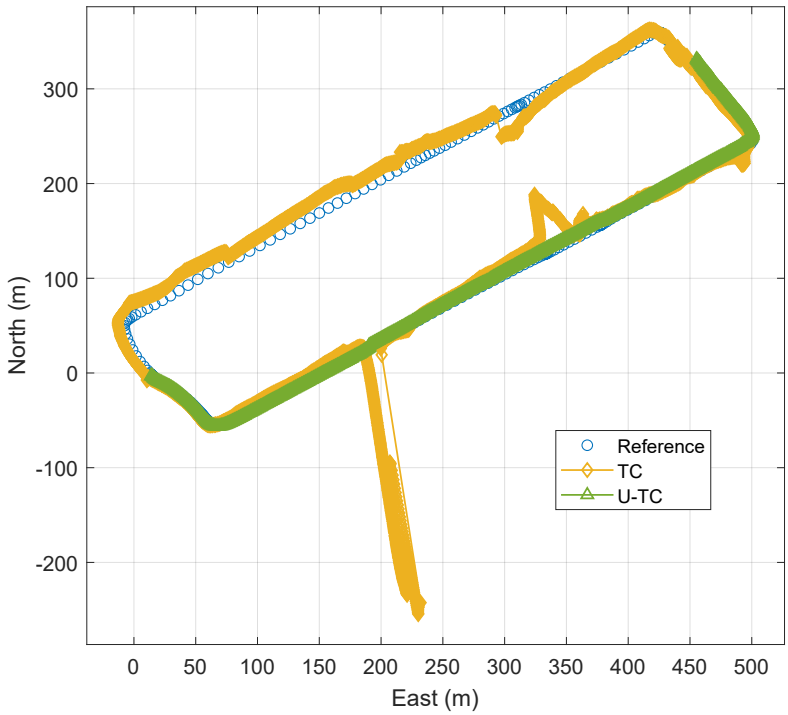

Figure 7.15: GNSS/INS TC (yellow) and U-TC (green) integration for *CaseB*. 2*D* trajectory.

	CaseA		***CaseB***	
	TC	**U-TC**	**TC**	**U-TC**
$\text{HPE}_{mean}(m)$	2.37	2.59	6.88	6.04
$\text{HPE}_{max}(m)$	21.56	4.62	22.46	10.8
$\text{HPE}_{50^{th}percentile}(m)$	2.27	2.93	5.4	6.66
$\text{HPE}_{75^{th}percentile}(m)$	3.10	3.76	9.21	8.61
$\text{HPE}_{95^{th}percentile}(m)$	4.13	4.22	13.92	9.09
Vel_X RMS Error (m/s)	0.19	0.19	0.28	0.27
Vel_Y RMS Error (m/s)	0.08	0.08	0.24	0.25
Vel_Z RMS Error (m/s)	0.18	0.18	0.29	0.29
Position provision (%)	100	100	100	100

Table 7.6: Multi-sensor TC and U-TC integration. Position errors for *CaseA* and *CaseB*.

system. It can be seen comparing the HPE values of Table 7.5 and the ones of Table 7.6. Since *CaseA* is characterized by open sky conditions, the integration of GNSS and INS provided already good results in terms of positioning accuracy. The position solutions are reported in Figure 7.18 where TC and U-TC are depicted in yellow and green respectively.

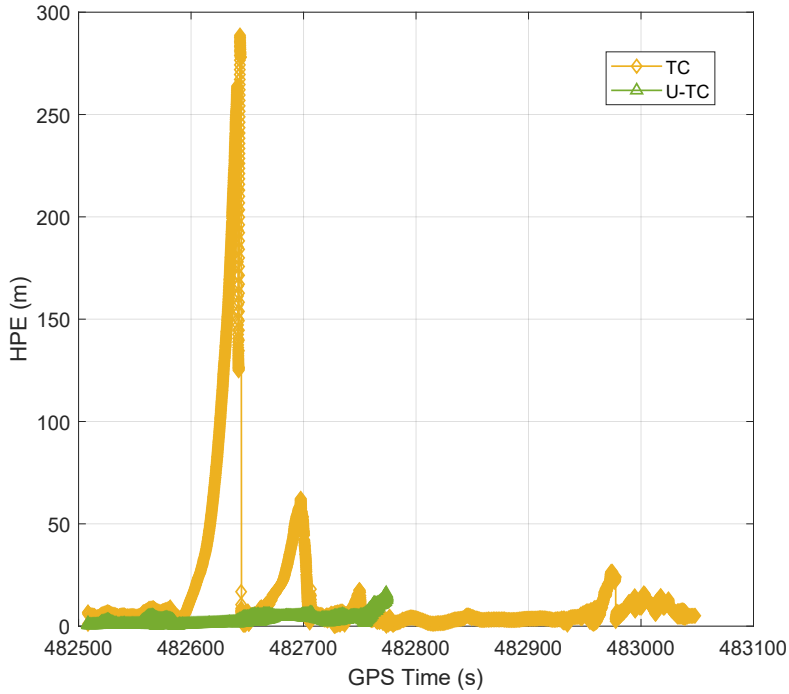

Figure 7.16: GNSS/INS TC (yellow) and U-TC (green) integration for *CaseB*. HPE over time.

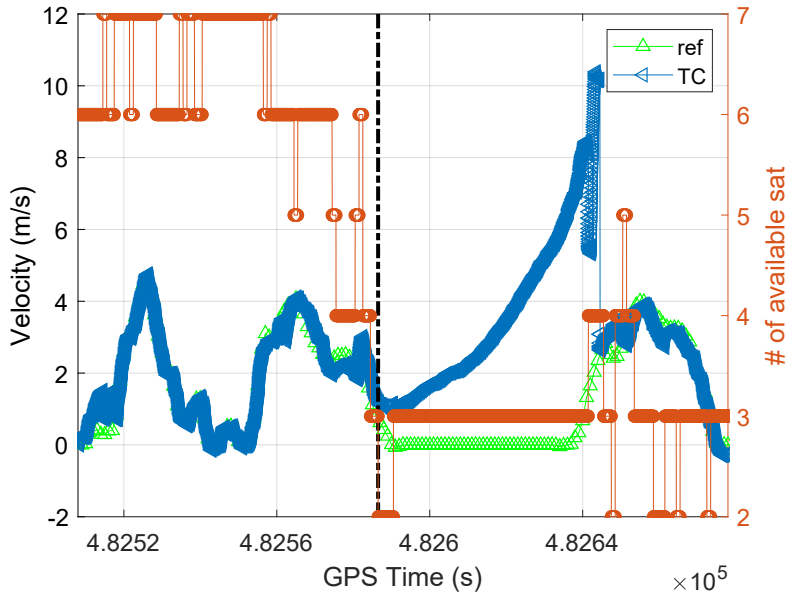

Figure 7.17: *CaseB*. Zoom to the point where the TC started drifting. Velocity estimated by the reference system (green) and by the TC (blue). Number of available satellites (orange).

The reference trajectory is depicted in blue. The HPE is plotted over time in Figure 7.19.

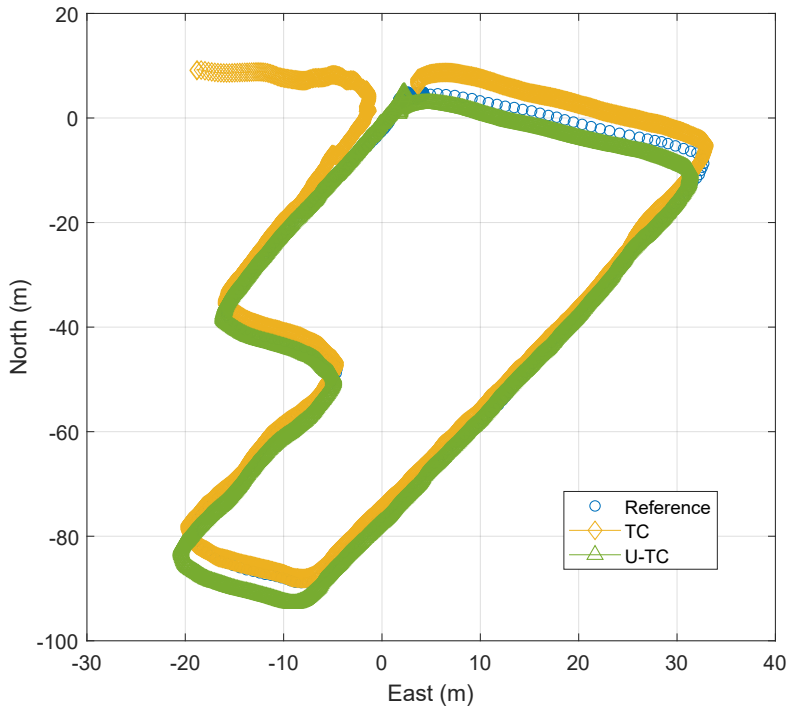

Figure 7.18: Multi-sensor TC (yellow) and U-TC (green) integration for *CaseA*. 2*D* trajectory.

Different considerations can be made for *CaseB* where the benefits of multi-sensor are evident. The position solutions are reported in Figure 7.20 where TC and U-TC are depicted in yellow and green respectively. The reference trajectory is depicted in blue. The HPE is plotted over time in Figure 7.21. Considering first the TC integration and considering the maximum value of HPE, it is reduced from 288.73 m (TC) to 22.46 m (U-TC). Also the mean value and the reported percentiles of HPE are reduced. E.g. the 95^{th} percentile is reduced from 58.24 m (TC) to 13.92 m (U-TC). Considering U-TC, the main advantage of multi-sensor integration, with respect to the GNSS/INS, lies on the continuity of the position solution. In fact, the integrated system in able to give a navigation solution 100% of the time (the same value was equal to 49.97% for GNSS/INS). The comparison between the HPE values of the multi-sensor U-TC and GNSS/INS U-TC, is not fair in this case since it is correlated with the different values of availability showed by the two systems. The HPE statistics of the GNSS/INS system

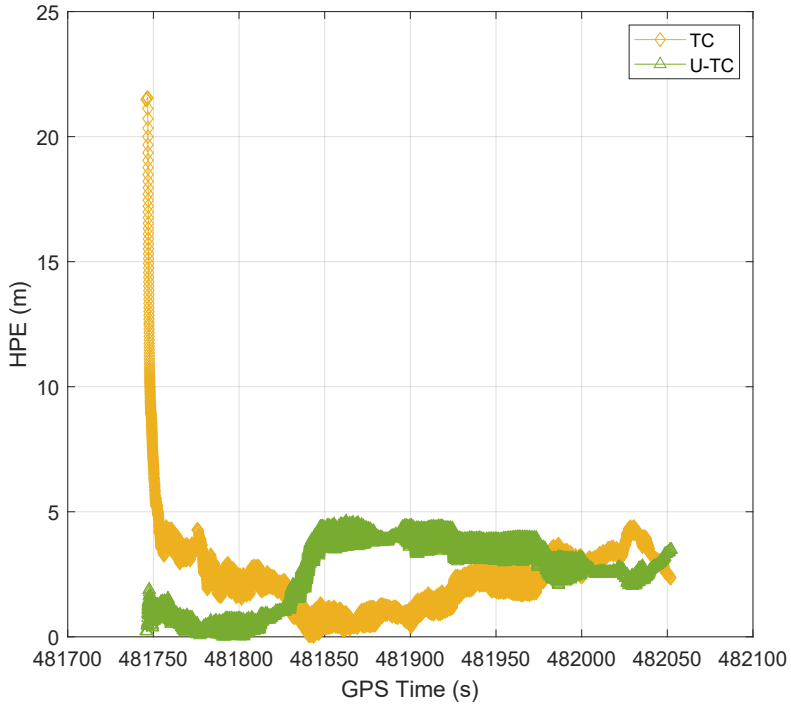

Figure 7.19: Multi-sensor TC (yellow) and U-TC (green) integration for *CaseA*. HPE over time.

were calculated over half trajectory with respect to the one related to the multi-sensor system.

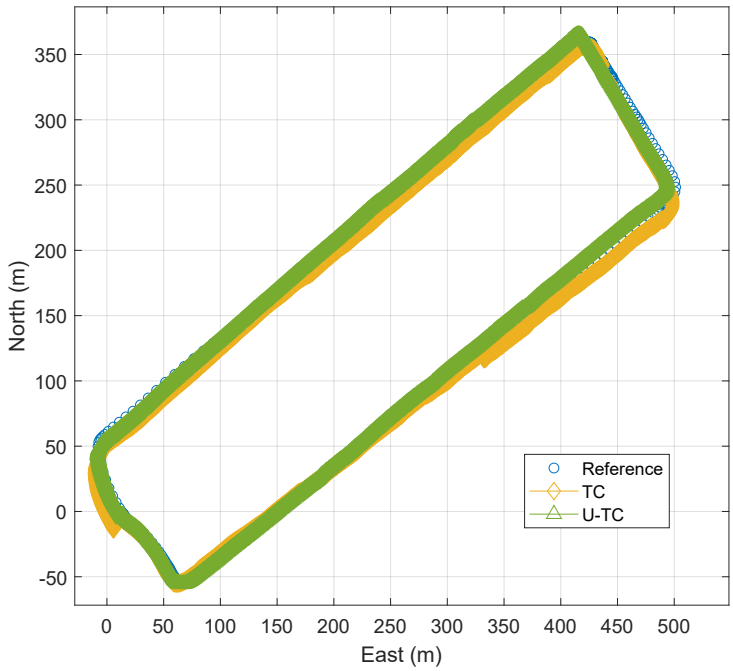

Figure 7.20: Multi-sensor TC (yellow) and U-TC (green) integration for *CaseB*. 2*D* trajectory.

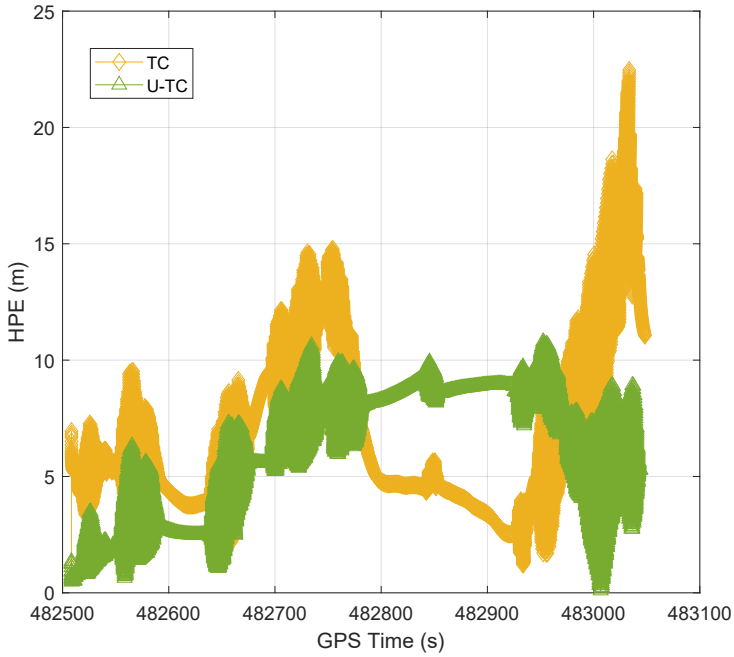

Figure 7.21: Multi-sensor TC (yellow) and U-TC (green) integration for *CaseB*. HPE over time.

Chapter 8

Performance assessment of multi-sensor integration in jamming environments

This Chapter aims at assessing the performance of the multi-sensor TC and U-TC integration algorithms, in scenarios characterized by the presence of intentional interference, jamming, in the GNSS L1 bandwidth. The choice of these scenarios allows to evaluate the advantages of multi-sensor integrated systems, with respect to a GNSS standalone solution, in scenarios where the presence of jamming might threat the operations of the receiver. Furthermore, comparisons between different integration strategies, i.e. TC and U-TC, are provided to assess and quantify the performance improvement of using the multi-sensor architecture with respect to the strength of the jamming signal. The scenarios were artificially generated using the R&R approach, injecting jamming signals with different power strengths into the pre-recorded GNSS data *CaseA*. These meaningful scenarios were chosen to be representative of different operational environments, as explained in Chapter 7, since it is fairly impossible to have an exhaustive performance assessment in all the possible conditions. For this reason, relative comparisons are proposed.

This Chapter first gives an overview about the scenarios chosen for the performance assessment and how they were artificially generated. Then, before assessing the performance of the multi-sensor integrated systems, GNSS standalone solution and GNSS/INS

integrated systems are considered and their performance are assessed in all the jammed scenarios.

8.1 Test scenarios setup

In order to create realistic jammed scenarios, the R&R approach was exploited, as described in Section 6.4. This methodology puts together the benefits of having a realistic scenario as a a baseline and the possibility to have under control the interference power level. In particular, starting from the original GNSS scenario *CaseA*, the jamming signals were injected with different power strengths. Therefore, for sake of clarity, the scenarios are denoted as ***CaseA-jamLight***, ***CaseA-jamMedium*** and ***CaseA-jamStrong***.

The setup used to inject the jamming signals into the pre-recorded GNSS data, is depicted in Figure 8.1. With respect to the whole system setup described in Section 7.1.1, only the GNSS part is considered. The USRP B210 [9] was used to record the digital samples of the GNSS signal as well as to playback them, set according to the parameters listed in Table 7.1. The signal $y_{IF}[n]$, as in (3.10), was up-converted back to RF, obtaining a good replica, $\hat{y}_{RF}(t)$, as in (6.4), thanks to the choice of the parameters that grants the fidelity of the scenario during the recording phase, and then combined with the interfering jamming signal $i(t)$. As a result, the interfered signal $\bar{\bar{y}}_{RF}(t)$, as in (6.5), was fed to the recording system, creating the digital version $\bar{\bar{y}}_{RF}[n]$ and stored on a memory.

In order to emulate jamming signals with different signal strengths, the power emitted by the jammer was controlled using a variable hardware attenuator. Three different scenario datasets were created, each characterized by different level of attenuation. As it is possible to see in Figure 8.2, such an interfering signal was injected only in the time interval between $t_{jam,start}$ and the end of the experiment. It is worth noting that the assessment of the positioning performance will be computed only within this time interval. A picture of the experiment carried out in the laboratory is reported Figure 8.3.

The power spectral density of the received signals, for all the experiments, is shown in Figure 8.4. The C/N_0 as estimated by the GNSS software receiver, considering GPS

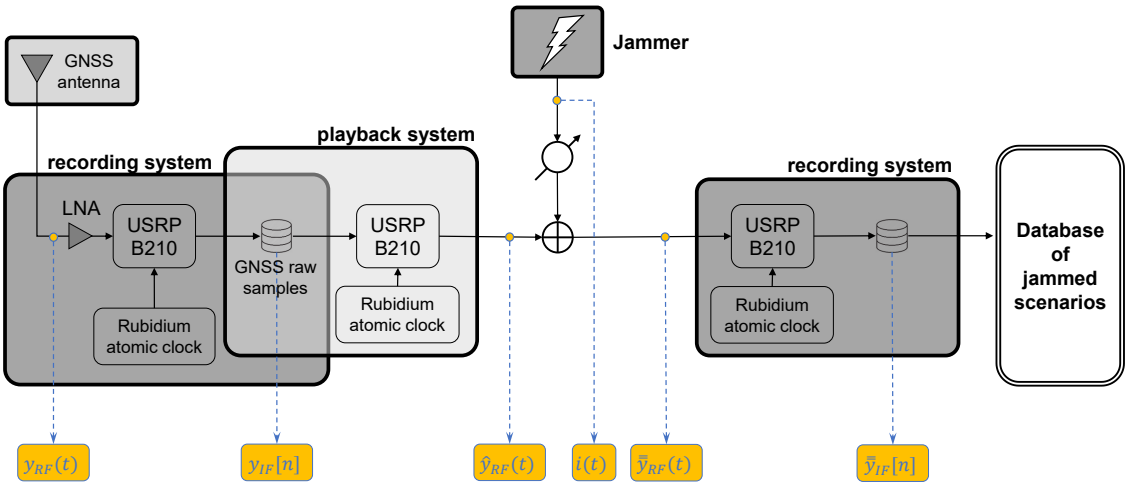

Figure 8.1: Interfered signal $\bar{\hat{y}}_{RF}(t)$ obtained mixing $i(t)$ and $\hat{y}_{RF}(t)$. Block diagram.

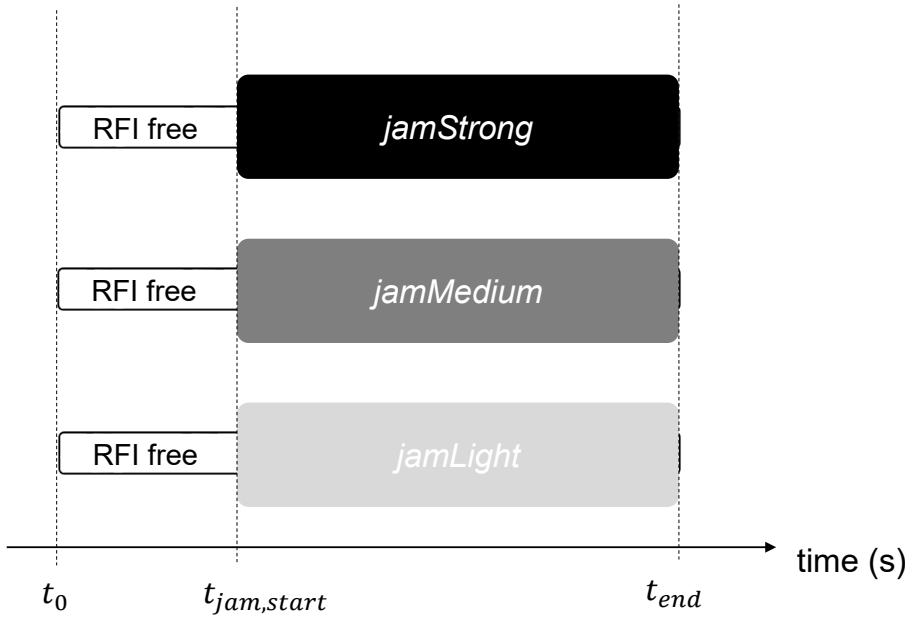

Figure 8.2: Experiments performed in the lab to inject jamming onto the pre-recorded GNSS data.

PRN31, is shown in Figure 8.5. In the interference-free portion of the signal, the four estimated perfectly overlap, and this is an implicit proof that the replay and new recording phase have not significantly altered the information of the originally recorded signal. Once the interference was injected, it is possible to see the impact of the interfering signal on the measured C/N_0. Considering the experiment in which the GNSS signal

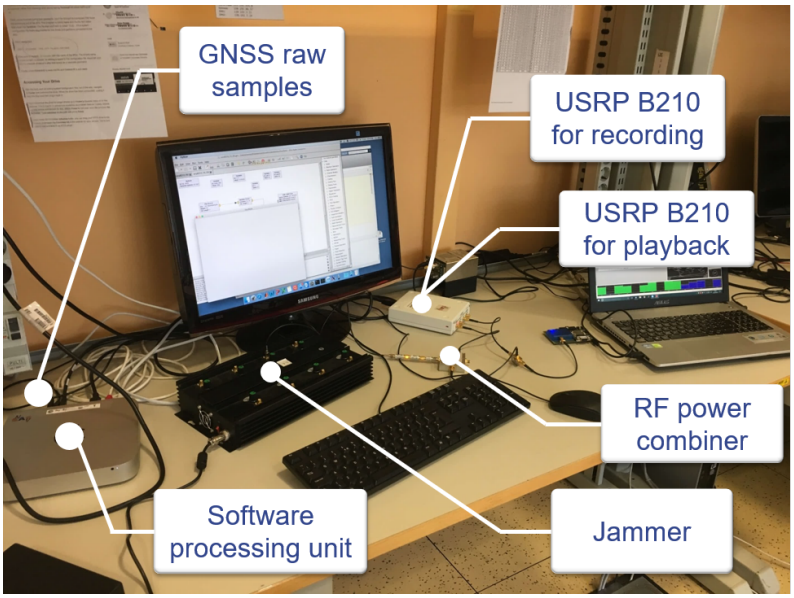

Figure 8.3: Picture of the real setup used to inject jamming onto the pre-recorded GNSS data.

was affected by jamming signal with the strongest power (purple line), it is possible to observe a drop of the C/N_0 of about 20 dB-Hz.

8.2 Performance of GNSS standalone receiver

Before assessing the performance of the integrated systems, the GNSS standalone system is considered in this Section as a benchmark to quantify the real benefits of multi-sensor integration in different constrained environments.

The LS algorithm uses the pseudoranges from the GNSS software receiver [164] to compute the position. As soon as the power of the jamming increases, the GNSS standalone system is not able to give any position solution as it can be seen by the HPE values reported in Table 8.1.

Looking at the position solutions reported in Figure 8.6 as well as the HPE plotted over time in Figure 8.7, in the *jamLight* (yellow) case the HPE values are higher than the ones of *jamFree* (orange), as expected due the presence of the jammer, but the receiver is still able to provide navigation solution. For higher values of the jamming power, no

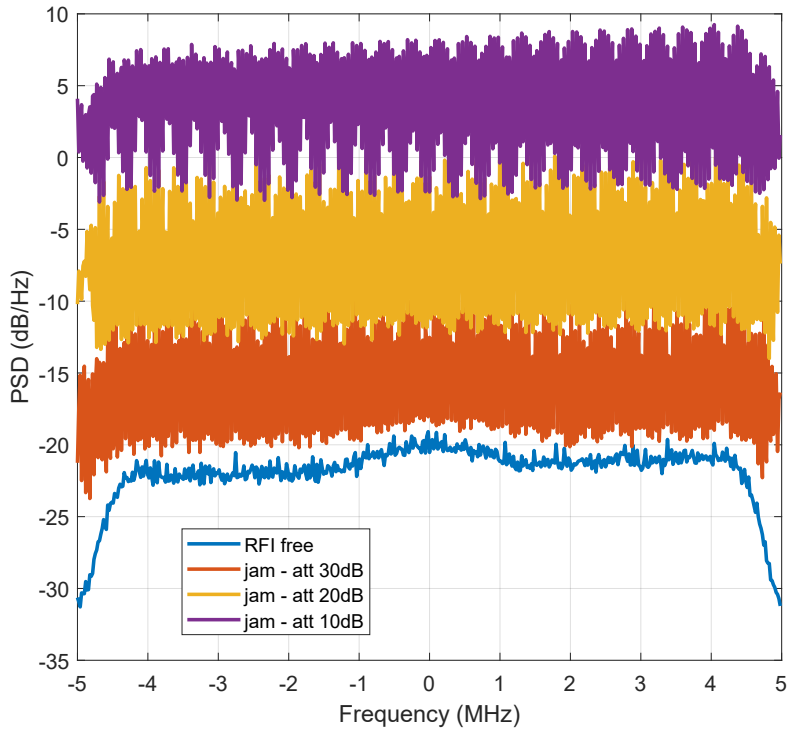

Figure 8.4: Estimation of PSD for different jamming signal strengths.

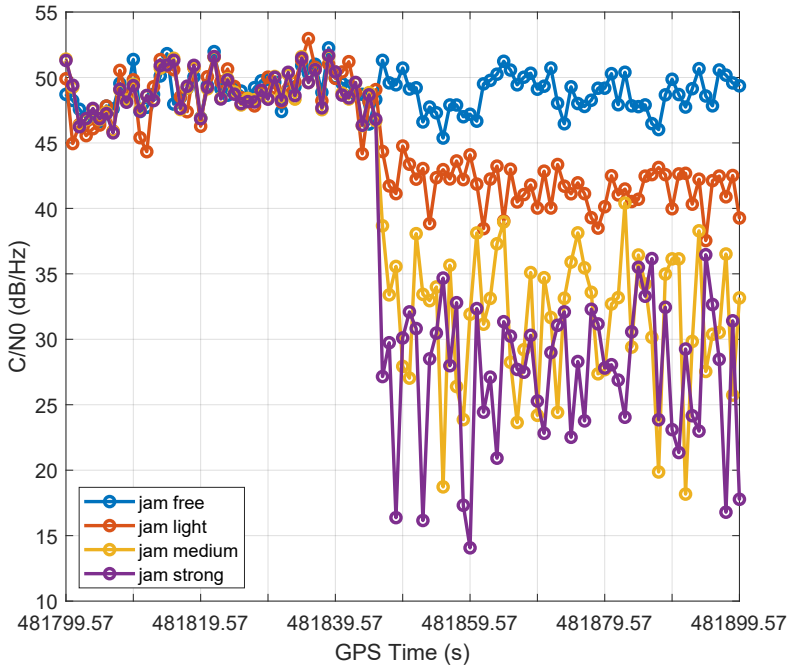

Figure 8.5: Estimation of C/N_0 for different jamming signal strengths.

solution can be provided by the receiver as summarized in Table 8.1. Considering the 95^{th} percentile of the HPE, it is increased from 32.14 m (*jamFree*) to 66.67 m (*jamLight*). Also the estimation of the Root Mean Square (RMS) error of the z component is increased from 0.17 m/s (*jamFree*) to 5.62 m/s (*jamLight*). Figure 8.7 shows also how the HPE reaches values up to 147.76 m in case of jamming environments.

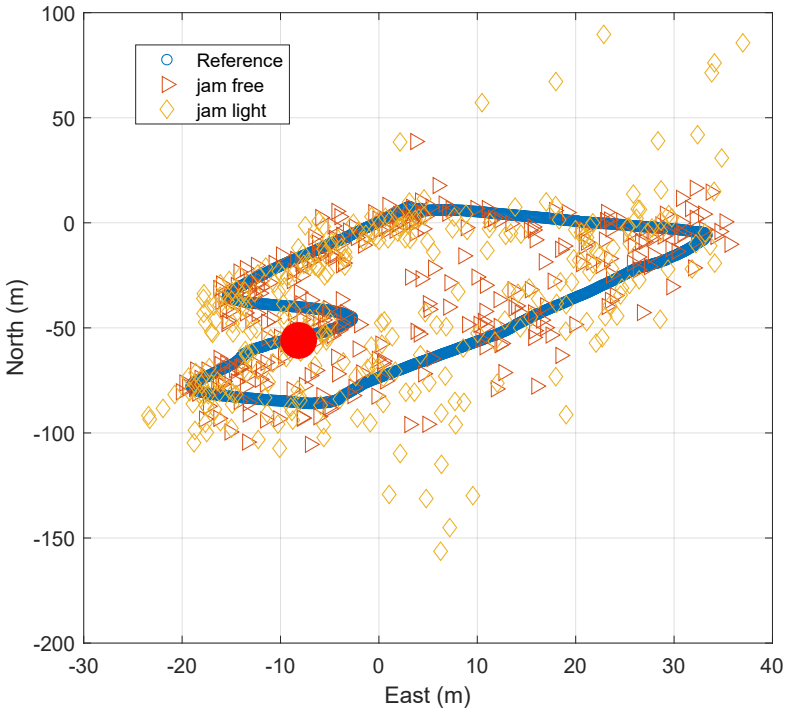

Figure 8.6: GNSS-only solution. 2D trajectory.

8.3 Performance of GNSS/INS integration

The lack of navigation solution exhibited by the GNSS standalone system in case of *jamMedium* and *jamStrong* scenarios, shows how the performance position accuracy can be seriously threatened by the presence of in-band interference. The integration of GNSS and INS is therefore addressed in this Section considering TC and U-TC integration strategies. GNSS/INS system is considered here, before addressing multi-sensor system, to have a benchmark referred to the state of the art and to assess the improvement when adding multiple sensors. The statistical assessment of the position solution accuracy is

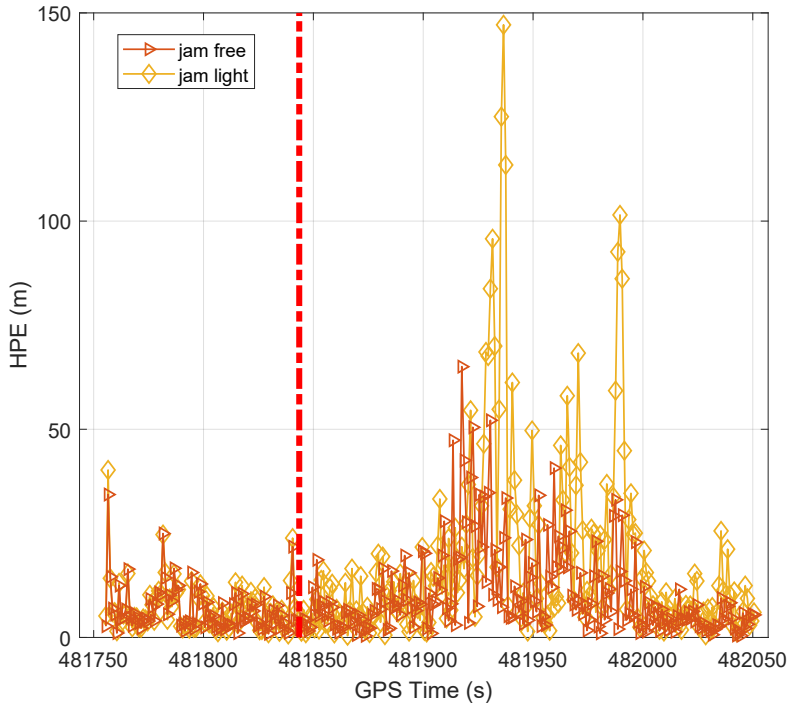

Figure 8.7: GNSS-only solution. HPE over time. The red bar corresponds to the time when the jamming signals were injected.

	Jam free	**Jam light**	**Jam medium**	**Jam strong**
$\text{HPE}_{mean}(m)$	10.82	18.03	-	-
$\text{HPE}_{max}(m)$	63.35	147.76	-	-
$\text{HPE}_{50^{th}percentile}(m)$	8.35	12.03	-	-
$\text{HPE}_{75^{th}percentile}(m)$	11.99	19.77	-	-
$\text{HPE}_{95^{th}percentile}(m)$	32.14	66.67	-	-
Vel_X RMS Error (m/s)	0.14	1.16	-	-
Vel_Y RMS Error (m/s)	0.09	0.73	-	-
Vel_Z RMS Error (m/s)	0.17	5.62	-	-
Position provision (%)	100	100	0	0

Table 8.1: Positioning performance assessment of GNSS-only.

shown in Figure 8.9 where the red dot highlights the point where the jamming signal was injected. The numerical evaluation is reported in Table 8.2.

As in the case of GNSS standalone system, also the TC integration is able to give a position solution only for *jamLight*, among the jammed scenarios. This is due to the fact

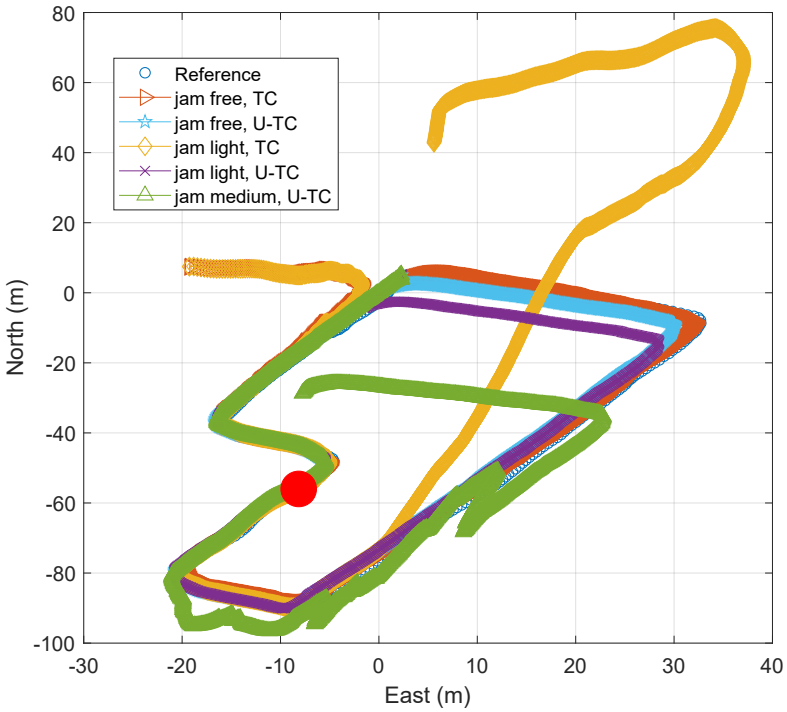

Figure 8.8: TC and U-TC GNSS/INS integration. $2D$ trajectory.

	Jam free		**Jam light**		**Jam medium**		**Jam strong**	
	TC	**U-TC**	**TC**	**U-TC**	**TC**	**U-TC**	**TC**	**U-TC**
$\text{HPE}_{mean}(m)$	0.74	2.52	32.85	4.94	-	18.07	-	-
$\text{HPE}_{max}(m)$	1.96	3.91	80.81	9.47	-	34.40	-	-
$\text{HPE}_{50^{th}percentile}(m)$	0.67	2.69	40.81	4.92	-	18.01	-	-
$\text{HPE}_{75^{th}percentile}(m)$	0.91	2.96	57.22	7.44	-	29.32	-	-
$\text{HPE}_{95^{th}percentile}(m)$	1.39	3.77	74.71	9.17	-	33.52	-	-
Vel_X RMS Error (m/s)	0.15	0.15	0.19	0.15	-	0.60	-	-
Vel_Y RMS Error (m/s)	0.07	0.07	0.13	0.07	-	0.20	-	-
Vel_Z RMS Error (m/s)	0.15	0.16	1.50	0.17	-	0.77	-	-
Position provision (%)	100	100	100	100	0	100	0	0

Table 8.2: Positioning performance assessment of TC and U-TC GNSS/INS integration.

that the GNSS observables, to be fused with the other sensors information, cannot be provided to the central navigation filter in (5.31), due to the presence of jamming heavily corrupting the GNSS signal. However, the HPE performance assessment, together with the velocity estimation, show a significant deterioration with respect to *jamFree*. It means that the TC integration is not robust against jamming, as expected. For instance,

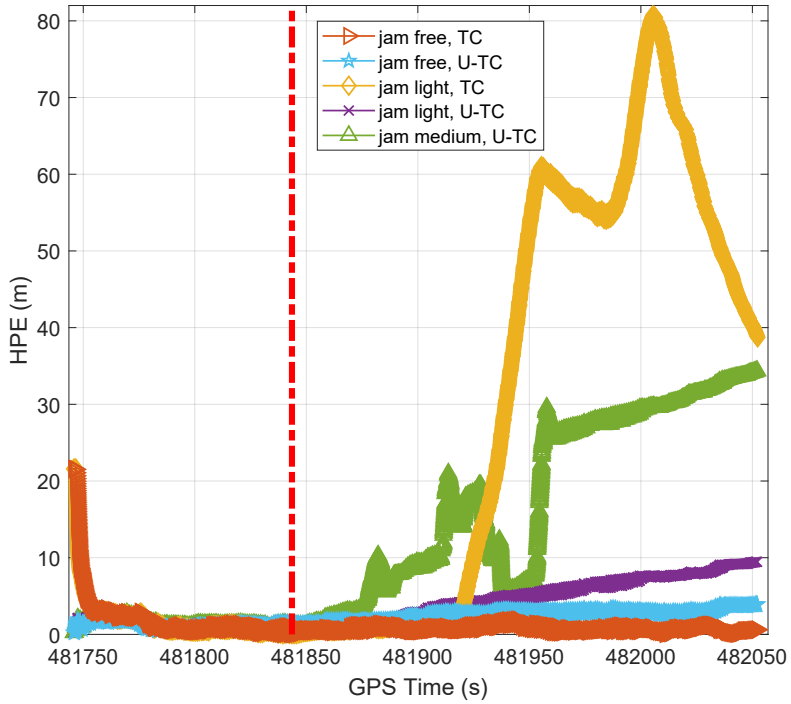

Figure 8.9: TC and U-TC GNSS/INS integration. HPE over time. The red bar corresponds to the time when the jamming signals were injected.

considering the mean value of the HPE, it is increased from 0.74 m (TC *jamFree*) to 32.85 m (TC *jamLight*). The RMS error on the x component of the velocity it is increased from 0.15 m/s (TC *jamFree*) to 1.50 m/s (TC *jamLight*).

The HPE of TC *jamLight* (yellow curve) shows a value of about 0.5 m in the interference-free portion of the signal. Once the jamming is injected, it slowly starts increasing for the first 80 s, and reaching a value of 2 m, and then it dramatically increases. This because the jamming forces the tracking loops of the GNSS receivers to loose the lock.

On the other hand, analyzing the performance of the U-TC integration, two main aspects can be noticed. The first one is that, as soon as the power of the jamming increases, U-TC is the only system allowing navigation. Despite the positioning performance of *jamMedium* are worse with respect to *jamLight*, as expected, the 95% of the HPE values are below 33.52 m. It can also be seen by the green trajectory in Figure 8.8.

The second aspect is that the benefits of U-TC with respect to TC increase as the

power strength of the jamming signal increases. Considering the 95^{th} percentile of the HPE, in case of *jamFree*, it is equal to 1.39 m (TC *jamFree*) and 3.77 m (U-TC *jamFree*). Considering *jamLight*, it is equal to 74.71 m (U-TC *jamLight*) and 9.17 m (U-TC *jamLight*).

8.4 Performance of multi-sensor integration

The GNSS/INS integrated system analyzed in the previous Section, shows some limitations when GNSS signal is affected by severe jamming interference in the GNSS bandwidths. In fact, it is not able to give any position solution in case of *jamStrong*. Therefore, the positioning performance of the multi-sensor system is evaluated in this Section to exploit the improvement with respect to the GNSS/INS integrated system. Another important aspect is to see how such an improvement is correlated with the jamming signal strength. The sensors fused in the navigation system are GNSS, INS, visual sensor and odometer.

Analyzing the statistical HPE in Table 8.3, the first remark is that U-TC multi-sensor integration is the only strategy capable to give a position solution in strongly degraded GNSS signal environments for the 100% of the simulation time, even if with different accuracy performance along the track. It can be seen also by the HPE of U-TC *jamStrong* (black curve) in Figure 8.11. It shows a value of about 0.5 m in the interference-free portion of the signal. As expected, it starts increasing once the jamming is injected, with the same rate as *jamLight* and *jamMedium* and for about 130 s. Finally, it starts increasing reaching the maximum value of HPE equal to 18.04 m.

As far as the U-TC integration is concerned, the results highlight how the benefits of multi-sensor, with respect to the GNSS/INS integration, increases as the power strength of the jamming increases. Despite the position performance is remarkably improved in case of both *jamMedium* and *jamLight*, the improvement is more consistent in case of jamming *jamMedium*. In fact the 95^{th} percentile of the HPE is improved from 9.17 m (GNSS/INS) to 3.85 m (multi-sensor) for *jamLight* and from 33.52 m (GNSS/INS) to 4.55 m (multi-sensor) for *jamMedium*.

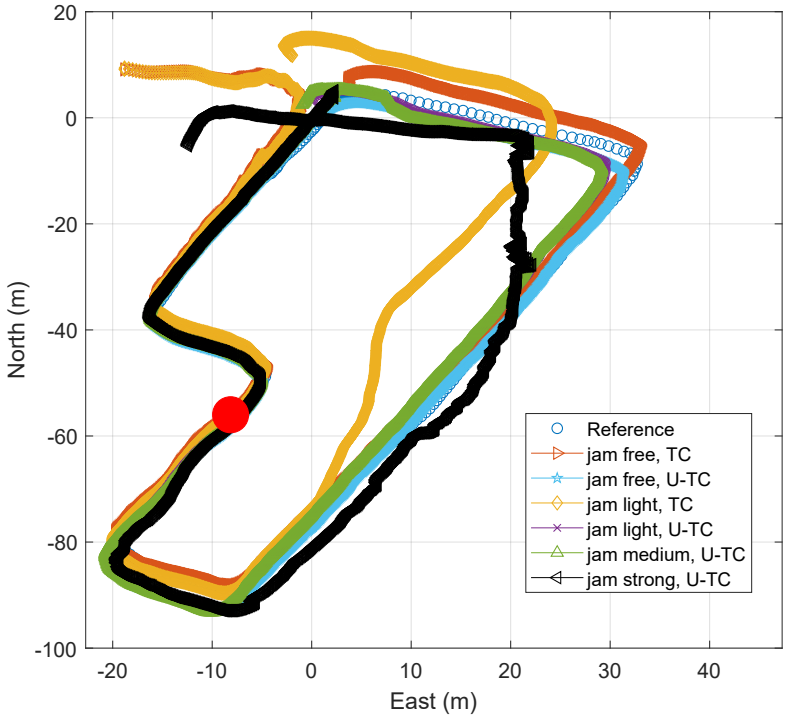

Figure 8.10: TC and U-TC multi-sensor integration. $2D$ trajectory.

	Jam free		**Jam light**		**Jam medium**		**Jam strong**	
	TC	**U-TC**	**TC**	**U-TC**	**TC**	**U-TC**	**TC**	**U-TC**
$\text{HPE}_{mean}(m)$	2.09	3.40	7.05	3.32	-	3.98	-	6.78
$\text{HPE}_{max}(m)$	4.45	4.62	14.86	4.17	-	5.04	-	18.04
$\text{HPE}_{50^{th}percentile}(m)$	2.21	3.51	9.39	3.30	-	3.97	-	4.08
$\text{HPE}_{75^{th}percentile}(m)$	3.00	3.91	11.65	3.57	-	4.17	-	10.42
$\text{HPE}_{95^{th}percentile}(m)$	3.88	4.28	13.76	3.85	-	4.55	-	17.19
Vel_X RMS Error (m/s)	0.16	0.16	0.16	0.16	-	0.17	-	0.17
Vel_Y RMS Error (m/s)	0.09	0.08	0.15	0.08	-	0.09	-	0.13
Vel_Z RMS Error (m/s)	0.16	0.16	0.20	0.16	-	0.16	-	0.17
Position provision (%)	100	100	100	100	0	100	0	100

Table 8.3: Positioning performance assessment of TC and U-TC multi-sensor integration.

The same can be said about the TC integration. In fact, the benefits of multi-sensor with respect to the GNSS/INS integration are consistent in case of *jamLight*. The 95^{th} percentile of the HPE, it is decreased from 74.71 m (GNSS/INS *jamLight*) to 13.76 m (multi-sensor *jamLight*). On the other hand, for *jamFree*, the multi-sensor integration

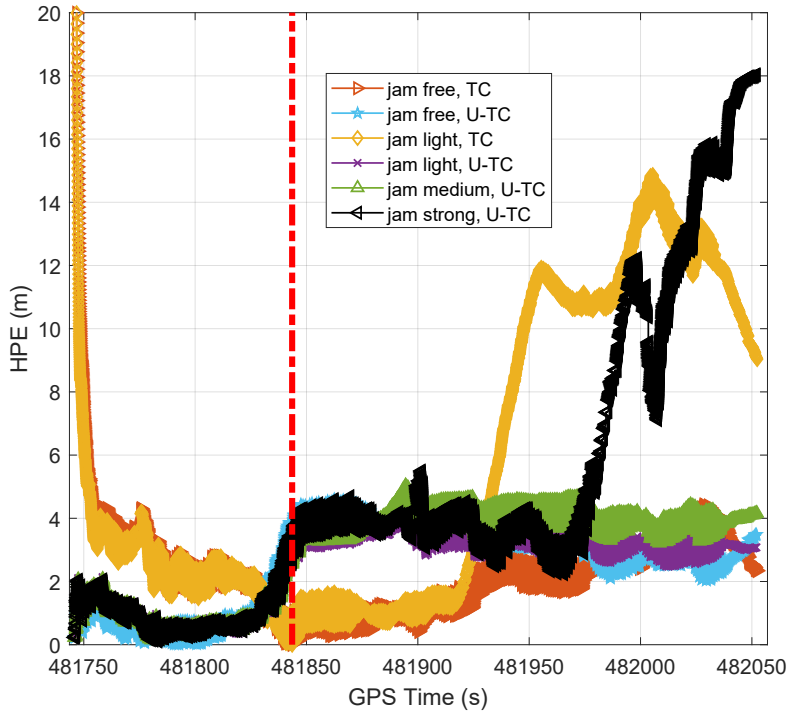

Figure 8.11: TC and U-TC multi-sensor integration. HPE over time. The red bar corresponds to the time when the jamming signals were injected.

does not show any improvements with respect to the GNSS/INS integration. This was already found out and commented in Chapter 7.

Chapter 9

Conclusions

In this thesis, we assessed the performance of multi-sensor navigation systems mainly addressing two different architectures of the hybridized receiver, i.e. tight and ultra tight integration. The performance was assessed in different scenarios, with the aim to show its feasibility and applicability with respect to different classes of ITS services. Within this context, one relevant document addressing the user needs and requirements for the road segment, was proposed by the Global Navigation Satellite Systems Agency (GSA) [83] with the aim to provide a reference for the European GNSS Programmes and for the automotive community. Based on the specific applications, different requirements are listed in this document addressing accuracy, availability, integrity, authentication and robustness to the interference. Another document is [175], that proposed some reference values for classes of transportation services. These values are reported in Table 9.1 and they bound the errors that are acceptable to the system. In other words, according to this classification, a specific system is considered available when the positioning errors given by the navigation unit are below that reference value, for the 95% of the time.

Therefore, following the classes of services reported in Table 9.1, the integrated navigation algorithms developed in this thesis are statistically analyzed, considering the CDF of the HPE in the different operational environments. It has to be anticipated that neither the TC nor U-TC algorithm are able to match the requirements of the *Class*1 and *Class*2 services, that would require sensors of different nature, such as, for example,

Table 9.1: Accuracy reference values for transport services [175].

Acceptable values	**Service name**	**Class**
0.1 meters (95%)	automated highway lane control	1
1 meters (95%)	collision avoidance restraint deployment intelligent speed adaptation	2
5 meters (95%)	in-car navigation urban traffic control emergency call road user charging	3
25 meters (95%)	trip travel information fleet management stolen vehicle recovery dynamic route guidance	4

radars for collision avoidance, or different uses of the visual information. However, these kind of sensors and relative processing algorithm were not in the scope of this study, which has been GNSS oriented. Nevertheless, applications of *Class*3 and of *Class*4 have been the target of this study, and the following remarks will show what kind of architecture is needed to design a positioning unit able to match the requirements.

9.1 Performance vs. requirements

Considering first *CaseA*, which is a scenario characterized by good satellite visibility conditions and thus by almost nominal conditions of the GNSS signal, all the navigation units meet the requirements of the services belonging to both *class*3 and *class*4. Figure 9.1, in fact, reports CDFs of the HPE for the different navigation units.

The requirement is not met by the GNSS standalone system for which the HPE is below 5 meters only for about the 40% of the cases but it may be able to be used for the *Class*4 services, even if the 95% availability is barely reached. It means that none of the above mentioned services can be provided by a GNSS standalone system and then highlights the need of smart integration of GNSS and external sensors.

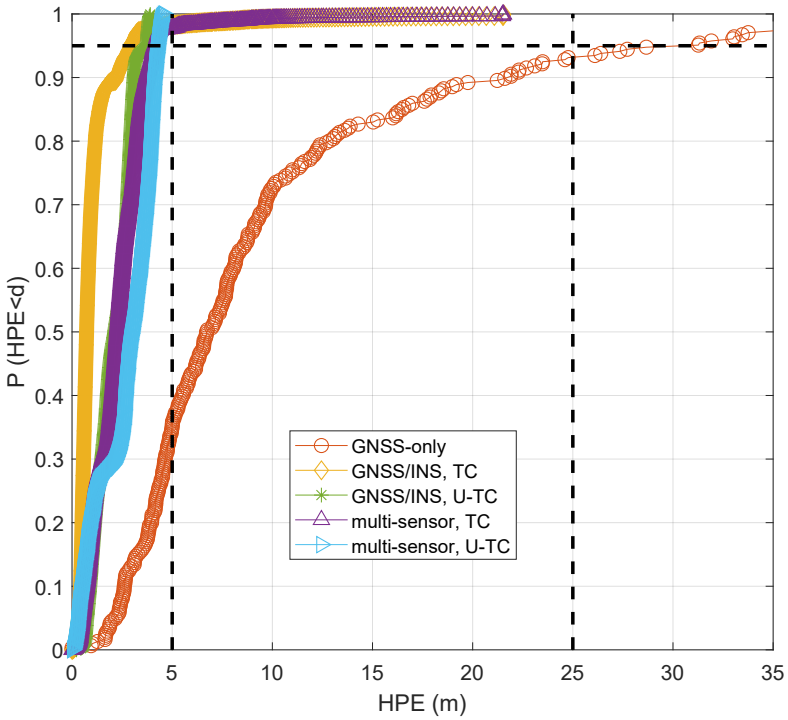

Figure 9.1: CDFs for *CaseA*.

The performance assessment carried out for *CaseB*, in contrast to *CaseA*, is related to a scenario characterized by signal degraded environments, where data were collected in an urban area, known to be an harsh environment for GNSS systems. The CDFs of the HPE are reported in Figure 9.2. Again, the performance improvements behind the use of integrated systems, with respect to the GNSS standalone system, are clearly visible comparing the orange curve against the others. In particular, the U-TC integration shows the best performance, in comparison with TC, highlighting the benefits of using such an integration strategy in degraded signal environments. As far as the number of sensors fused in the navigation unit is concerned, the benefits of multi-sensor system can be seen in TC integration comparing yellow and purple curves. However, looking at the requirements for *Class*4 services, the HPE is below the 25 meter for the 95% of the cases only when multisensors are considered, while the U-TC is able to match the requirement with just the INS as well as with multisensors. As for the *Class*3 services, the GNSS/INS U-TC seems to be the only one able to get close to a full matching with the

requirements. However, such a comparison is misleading because they refer to different values of solution availability, as shown in Figure 9.3. In fact as it can be seen in Figure 7.15 for a large part of time the positioning unit is not able to provide any output, thus making this kind of integration useless, and the good performance stemming from Figure 9.2 are just due to the fact that when the scenario is not so critical the error is mostly below 5 meters. However the architecture is weak, and subject to easy loss of lock leading to a lack of position solutions.

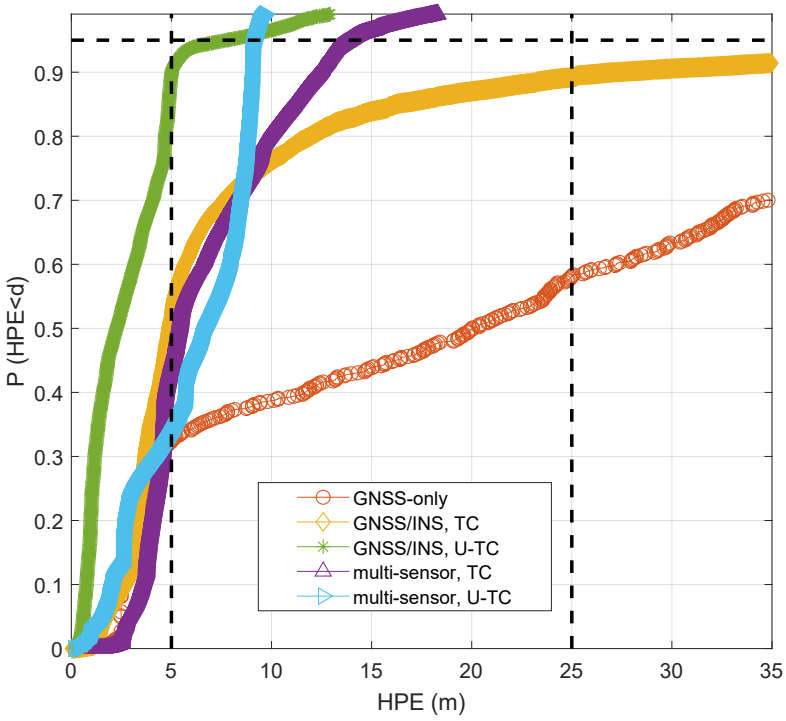

Figure 9.2: CDFs for *CaseB*.

Different conclusions can be drawn considering scenarios characterized by the presence of jamming interference corrupting the GNSS signal. In fact, it is possible to analyze the CDFs of the HPE related to the scenarios *jamLight*, *jamMedium* and *jamStrong*, each affected by jamming signals with different power strengths and reported in Figure 9.4, Figure 9.5 and Figure 9.6, respectively. The most significant outcome is related to the real benefit of using U-TC integration with respect to TC in jammed scenarios and the fact that such a benefit increases as the power of the jamming signals increases. In fact, U-TC is the only system capable to guarantee a navigation solution 100% of the time.

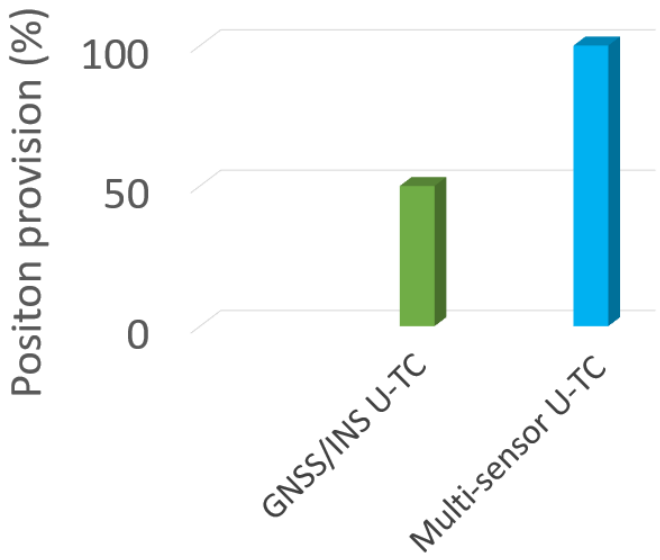

Figure 9.3: *class4* availability for *CaseB*.

Moreover, it is the only system capable to meet the requirements of services belonging to *class*3, unless in *jamStrong* scenario where it guarantees availability of services of *class*4. The advantages of using multi-sensor, with respect to GNSS/INS integrated system, is visible for all the jammed scenarios and for both the integration strategies TC and U-TC.

9.1.1 Estimation of code and carrier frequencies in jammed scenarios

Although the U-TC integration algorithm developed in this thesis exhibits high complexity and computational capability, it is capable of tracking GNSS signals under very weak signal conditions, as shown by the statistical analysis of the HPE in jammed scenarios. It lies in the key point of the U-TC integration, which is the estimation of code and carrier frequencies by the NCOs driven by the navigation filter.

In fact, looking at the variances of code and carrier frequencies estimation of Galileo PRN18, reported in Table 9.2 and plotted in Figure 9.7 and in Figure 9.8, respectively, it is possible to see that U-TC integration estimates both code and carrier frequency with lower uncertainty with respect to the scalar tracking loops of the GNSS standalone

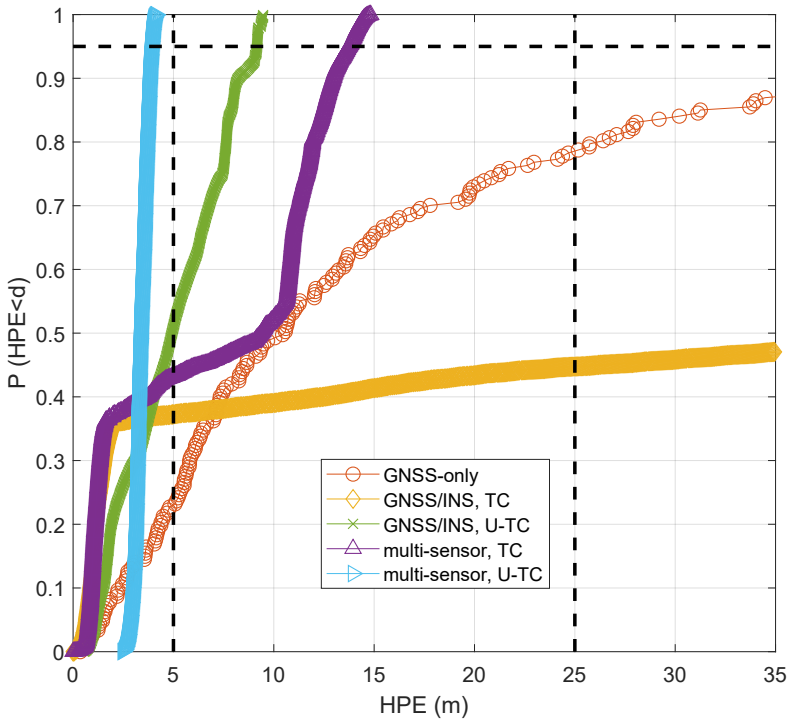

Figure 9.4: CDFs for *jamLight*.

receiver. It is due to the fact that the estimation of the frequencies is based on a PVT feedback that leverages on a Kalman filter approach. Comparing code and carrier NCOs within the jammed scenarios, it is possible to see how the code NCO is more robust than the carrier NCO. It is due to the higher robustness shown by the DLL with respect to the PLL in terms of capability of keeping the lock under weak signal conditions.

Evaluating the performance of the carrier NCO, it is possible to see how the uncertainty of the frequency estimation increases as the power of the jamming signal increases. In particular, the variance of *jamLight* is slightly increased with respect to the *jamFree* scenario. The same trend can be observed looking at *jamMedium* with respect to *jamLight*. On the contrary, in case of *jamStrong*, we observe a remarkable increment of the error in the frequency estimation (four orders of magnitude higher). Since the frequency estimation is strongly dependent on the accuracy of the PVT, such estimation experiences an high variance error due to the poor quality of the PVT in case of *jamStrong*. However, the U-TC system is able to correctly track both the code and carrier frequencies in this

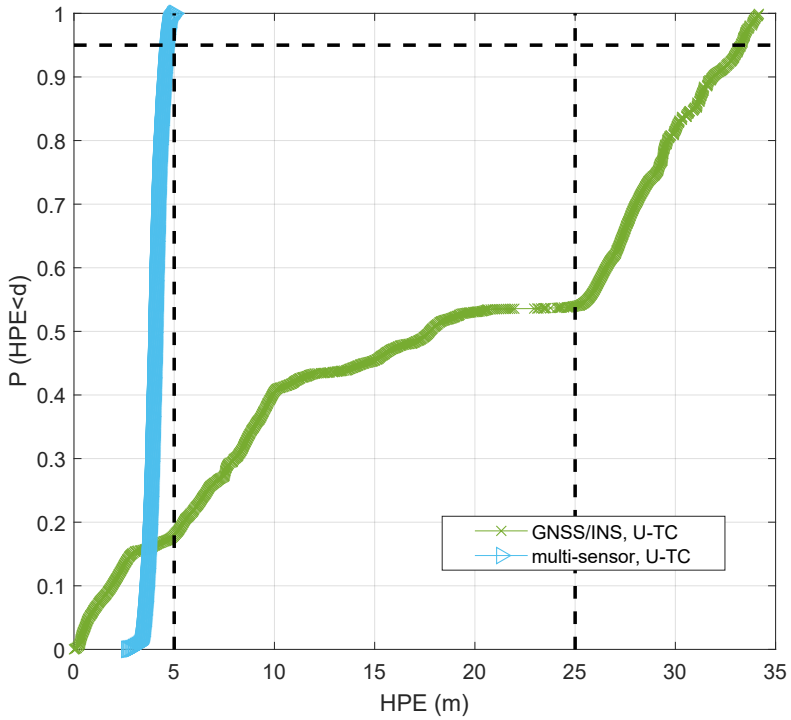

Figure 9.5: CDFs for *jamMedium*

very challenging environment.

	$\sigma^2_{f_{code}}$ (Hz)	$\sigma^2_{f_{carr}}$ (Hz)
GNSS-only, scalar	0.0116	0.0323
jam free, U-TC	0.0071	0.0017
jam light, U-TC	0.0071	0.0022
jam medium, U-TC	0.0071	0.0035
jam strong, U-TC	0.0074	55.0670

Table 9.2: Variances of code and carrier frequencies *jamFree*, *jamLight*, *jamMedium* and *jamStrong* scenarios for Galileo PRN18.

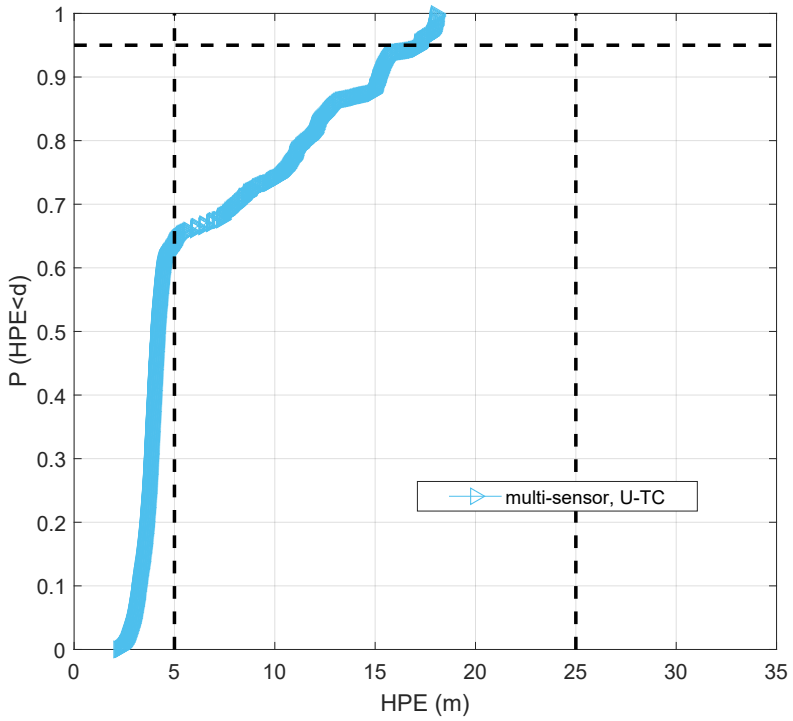

Figure 9.6: CDFs for *jamStrong*.

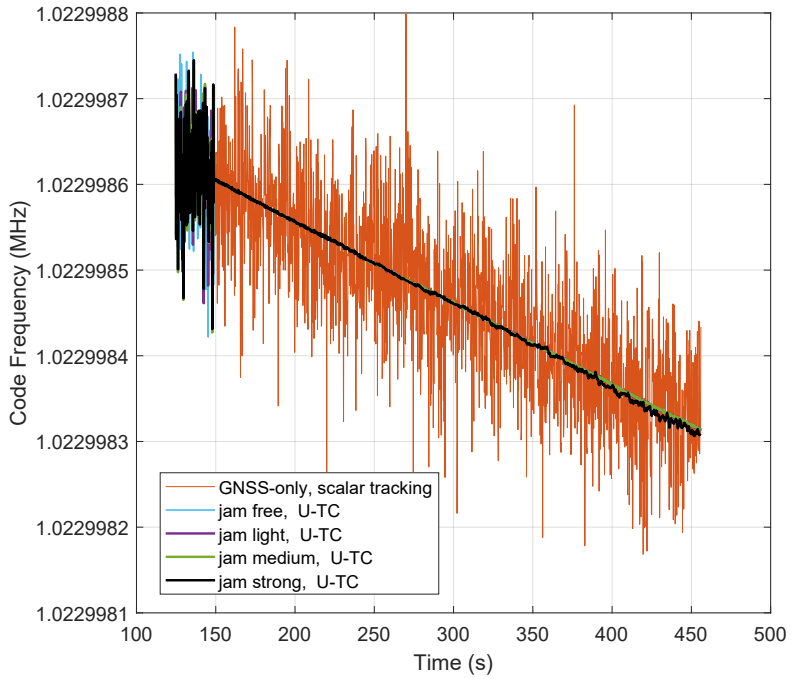

Figure 9.7: Code frequency estimated by the multi-sensor U-TC integration system of Galileo PRN18.

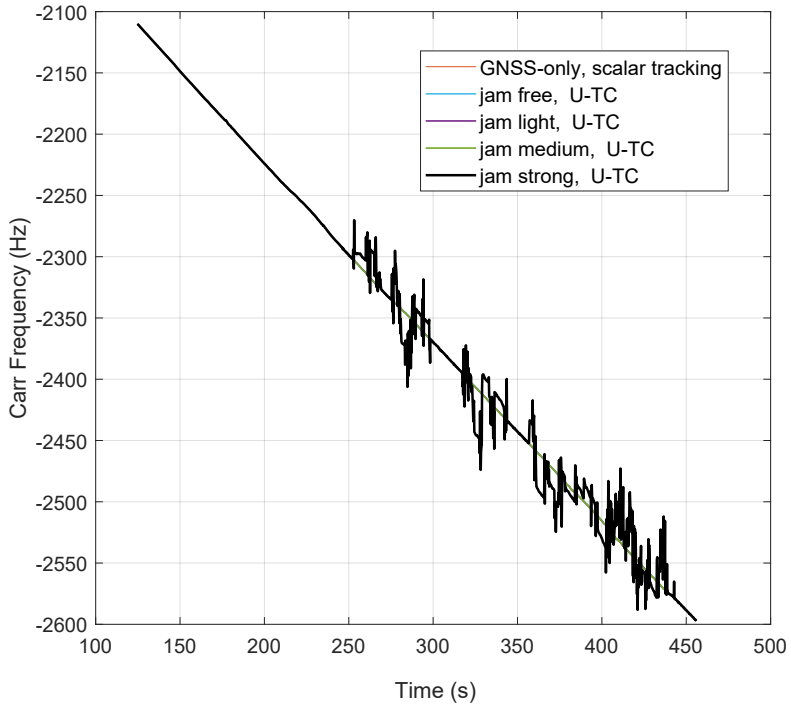

Figure 9.8: Carrier frequency estimated by the multi-sensor U-TC integration system of Galileo PRN18.

9.2 Future activities

The work of this thesis analyzed the benefits of U-TC integration and the use of INS, vision sensors and odometer to match the requirements of several services in the ITS domain. However, it also highlighted new research path to follow to further improve the integrated systems.

Future activities could address the improvement of the position performance of the developed integration algorithms, with the aim to enable the ITS services of *class*1 and *class*2, listed above. In order to go toward this direction, future development of the GNSS processing chain will have to take into account the new signals broadcast by the new satellite systems on multiple frequency bands, including the modern European Galileo system and the Chinese BeiDou. It is know in fact that multifrequency GNSS receiver can provide better quality measurements, thus improving the GNSS contributions to the integrated systems. Nevertheless, it has to be highlighted how, changing the statistical nature of the error of the measurement error, the procedure for the optimisation of the Kalman parameters should be as well revised.

Furthermore, the great number of sensors available nowadays, e.g. LiDAR, UWB, modern thermal cameras, could be exploited in the fusion algorithm. Among the additional sources of information that can be fused, it is worth mentioning the recent results obtained by cooperative techniques that allows to have estimation of the baseline between vehicles, just using GNSS measurements [171, 129, 128]. This is another key factor to enhance the intelligence of the navigation unit of each actor involved in the framework of smart cities and smart mobility.

As far as the integration algorithm is concerned, the classical KF-based integration techniques, used in this thesis, could look toward different implementations, such as particle filters, able to handle any non-linearity and any distributions of the driving measurements noises, outperforming in some cases KF-based methods. Also, non-linear integration modules based on Artificial Intelligence (AI) could be exploited, either as a complete replacement for KF or for its augmentation. These techniques are generally platform-independent systems thus do not requiring detailed knowledge of the integrated

sensors and technologies, unlike KF that requires accurate stochastic models of fused sensors.

Besides the above mentioned new research paths, to be followed for enhancing the multi-sensor integrated systems performance, future activities could address more advanced use of the R&R approach for the GBPT performance assessment. Since this method exhibited some limitations attempting to record/replay scenarios where GNSS signals were far from the nominal conditions (e.g. urban scenarios), it would be beneficial to develop a methodology capable to grant fidelity to a realistic scenario regardless to the quality of the GNSS signals, i.e. both lightly and heavily signal degraded environments. Higher sampling frequency of the ADC as well as higher number of bits, necessary for the representation of the digital signal, could be exploited within the recording system, to preserve the information on the specific environment, assuring the fidelity of the recorded scenario with respect to the real one. It would allow to faithfully record GNSS signals as well as other "out-of GNSS band" events that might need to be represented in the saved data log. Moreover, further investigations about the capability to synchronously record/replay GNSS signals and the other signals coming from other sensors, are still needed.

Appendix A

Estimation

Estimation is the process of estimating an unknown state from a set of process measurements. The relationship between the two, can be expressed through the *state equation* and the *measurement equation*:

$$\dot{\mathbf{x}}(t) = \mathbf{f}(\mathbf{x}(t)) + \mathbf{w}(t) \tag{A.1}$$

$$\mathbf{z}(t) = \mathbf{h}(\mathbf{x}(t)) + \boldsymbol{\nu}(t) \tag{A.2}$$

where $\mathbf{x}(t)$ is the *state vector*, $\mathbf{w}(t)$ is the *process noise*, $\mathbf{z}(t)$ is the *measurement vector*, $\boldsymbol{\nu}(t)$ is the *measurement noise* and $\mathbf{f}$ and $\mathbf{h}$ are two known linear or non-linear functions.

Assuming a linear model, (A.1) and (A.2) have the following form:

$$\dot{\mathbf{x}}(t) = \mathbf{F}(t)\mathbf{x}(t) + \mathbf{w}(t) \tag{A.3}$$

$$\mathbf{z}(t) = \mathbf{H}(t)\mathbf{x}(t) + \boldsymbol{\nu}(t) \tag{A.4}$$

where $\mathbf{F}(t)$ is the *continuous-time state transition matrix* and $\mathbf{H}(t)$ is the linear relationship between the states and the observations (*measurement matrix* or *observation matrix*).

Least Squares

In LS the state vector estimation is based purely on the measurements. The discrete version of the *measurement vector*(A.4), dropping the time instant $[n]$ hereafter for simplicity, can be written as:

$$\mathbf{z} = \mathbf{H}\mathbf{x} + \boldsymbol{\nu} \tag{A.5}$$

The estimate of the state vector can be obtained as:

The goal of the LS is to estimate $\hat{\mathbf{x}}$ minimizing the weighted sum of the squares of the difference $(\mathbf{z} - \mathbf{H}\hat{\mathbf{x}})$. The cost function J can be defined:

$$J = (\mathbf{z} - \mathbf{H}\hat{\mathbf{x}})^T \mathbf{W} (\mathbf{z} - \mathbf{H}\hat{\mathbf{x}}) \tag{A.6}$$

where W is the weighting function. The solution consists of setting to zero the derivative of the cost function J and solving for $\hat{\mathbf{x}}$. It is given by:

$$\hat{\mathbf{x}} = (\mathbf{H}^T \mathbf{W} \mathbf{H})^{-1} \mathbf{H}^T \mathbf{W} \mathbf{z} \tag{A.7}$$

Its estimated covariance matrix is:

$$\mathbf{C}_{\hat{\mathbf{x}}} = (\mathbf{H}^T \mathbf{W} \mathbf{H})^{-1} \mathbf{H}^T \mathbf{W} \mathbf{C}_{\mathbf{z}} \mathbf{W} \mathbf{H} (\mathbf{H}^T \mathbf{W} \mathbf{H})^{-1} \tag{A.8}$$

where C_z is the covariane matrix of the measurement vector. The weighting matrix can be set as the inverse of the measurement covariance matrix as:

$$\mathbf{W} = \mathbf{C}_{\mathbf{z}}{}^{-1} \tag{A.9}$$

In this case, the estimated covariance matrix (A.8) becomes:

$$\mathbf{C}_{\hat{\mathbf{x}}} = (\mathbf{H}^T \mathbf{W} \mathbf{H})^{-1} = (\mathbf{H}^T \mathbf{C}_{\mathbf{z}}{}^{-1} \mathbf{H})^{-1} \tag{A.10}$$

Kalman filter

The KF is a set of mathematical equations that estimate in a recursive way the state of a system, minimizing the mean of the squared error. The pronciples of the KF are presented in this Section, using the notation of [66] (and for the rest of the thesis). With respect to LS, it takes into consideration the noisy nature of the measurements. Considering the discrete time version of the system in (A.3) and (A.4), the *discrete-time state-space equation* corresponds to:

$$\mathbf{x}[n+1] = \mathbf{\Phi}[n]\mathbf{x}[n] + \mathbf{w}[n], \tag{A.11}$$

where T_c is the chosen *sampling interval*, $\mathbf{\Phi}[n]$ is the *state transition matrix* and $\mathbf{w}[n]$ is the process noise which is supposed to be a zero-mean white Gaussian with covariance $\mathbf{Q}[n]$, defined by:

$$\mathbb{E}\left\{\mathbf{w}[n]\mathbf{w}[i]^T\right\} = \begin{cases} \mathbf{Q}[n] & n = i \\ \mathbf{0} & n \neq i \end{cases} \tag{A.12}$$

The *measurement vector* can be written as:

$$\mathbf{z}[n] = \mathbf{H}[n]\mathbf{x}[n] + \boldsymbol{\nu}[n], \tag{A.13}$$

where $\mathbf{H}[n]$ is the *observation matrix* and $\boldsymbol{\nu}[n]$ is an additive noise component, which is supposed to be a zero-mean white Gaussian process, with covariance $\mathbf{R}[n]$, defined by:

$$\mathbb{E}\left\{\boldsymbol{\nu}[n]\boldsymbol{\nu}[i]^T\right\} = \begin{cases} \mathbf{R}[n] & n = i \\ \mathbf{0} & n \neq i \end{cases} \tag{A.14}$$

Recursive estimation

In the KF approach, the state variables are estimated by means of a recursive iterative process, based on two steps: *prediction* and *update*. During the *prediction* step, a predicted estimate $\widehat{\mathbf{x}}^{-}[n+1]$ is obtained by applying the state transition matrix. On the other hand, during the *update* step, a contribute is determined from the measurement vector.

The predicted state estimation is called a *priori* estimate $\widehat{\mathbf{x}}^{-}[n]$ and the updated state estimate a posteriori $\mathbf{x}[n]$. The measurement $\mathbf{z}[n]$ is used to update the state as:

$$\widehat{\mathbf{x}}[n] = \widehat{\mathbf{x}}^{-}[n] + \mathbf{K}[n](\mathbf{z}[n] - \mathbf{H}[n]\widehat{\mathbf{x}}^{-}[n]) \tag{A.15}$$

where the term $\boldsymbol{\alpha}[n] = (\mathbf{z}[n] - \mathbf{H}[n]\widehat{\mathbf{x}}^{-}[n])$ is called *innovation* or *residual* and $\mathbf{K}[n]$ is the *Kalman gain*, computed as:

$$\mathbf{K}[n] = \mathbf{P}^{-}[n]\mathbf{H}[n]^{T}(\mathbf{H}[n]\mathbf{P}^{-}[n]\mathbf{H}[n]^{T} + \mathbf{R}[n])^{-1} \tag{A.16}$$

The objective of the Kalman gain is to minimize the mean squared state error $\mathbb{E}\left\{\mathbf{e}[n]^{H}\mathbf{e}[n]\right\}$ where the errors of a priori and a posteriori state estimate can be defined as:

$$\mathbf{e}^{-}[n] = \mathbf{x}[n] - \widehat{\mathbf{x}}^{-}[n] \tag{A.17}$$

$$\mathbf{e}[n] = \mathbf{x}[n] - \widehat{\mathbf{x}}[n] \tag{A.18}$$

The *a-priori error covariance matrix* of $\mathbf{e}^{-}[n]$ and the *a-posteriori error covariance matrix* of $\mathbf{e}[n]$, are defined respectively as:

$$\mathbf{P}^{-}[n] = \mathbb{E}\left\{\mathbf{e}^{-}[n]\mathbf{e}^{-}[n]^{T}\right\} \tag{A.19}$$

$$\mathbf{P}[n] = \mathbb{E}\left\{\mathbf{e}[n]\mathbf{e}[n]^{T}\right\} \tag{A.20}$$

The KF is initialized by setting values for the initial state $\mathbf{x}[0]$ and initial state error covariance $\mathbf{P}[0]$. The algorithm then recursively predicts the state as:

$$\widehat{\mathbf{x}}^{-}[n] = \boldsymbol{\Phi}[n-1]\widehat{\mathbf{x}}[n-1] \tag{A.21}$$

$$\mathbf{P}^{-}[n] = \boldsymbol{\Phi}[n-1]\mathbf{P}[n-1]\boldsymbol{\Phi}^{T}[n-1] + \mathbf{Q}[n-1] \tag{A.22}$$

and updates the state estimate and state error covariance when the measurement is obtained

incorporating the new Kalman $\mathbf{K}[n]$ gain computed using (A.16) as:

$$\widehat{\mathbf{x}}[n] = \widehat{\mathbf{x}}^{-}[n] + \mathbf{K}[n](\mathbf{z}[n] - \mathbf{H}[n]\widehat{\mathbf{x}}^{-}[n]) \tag{A.23}$$

$$\mathbf{P}[n] = [\mathbf{I} - \mathbf{K}[n]\mathbf{H}[n]]\mathbf{P}^{-}[n] \tag{A.24}$$

Details about the derivation of the KF equations can be found in [101], [37] and [71]. The pictorial representation is given in Figure A.1 [37].

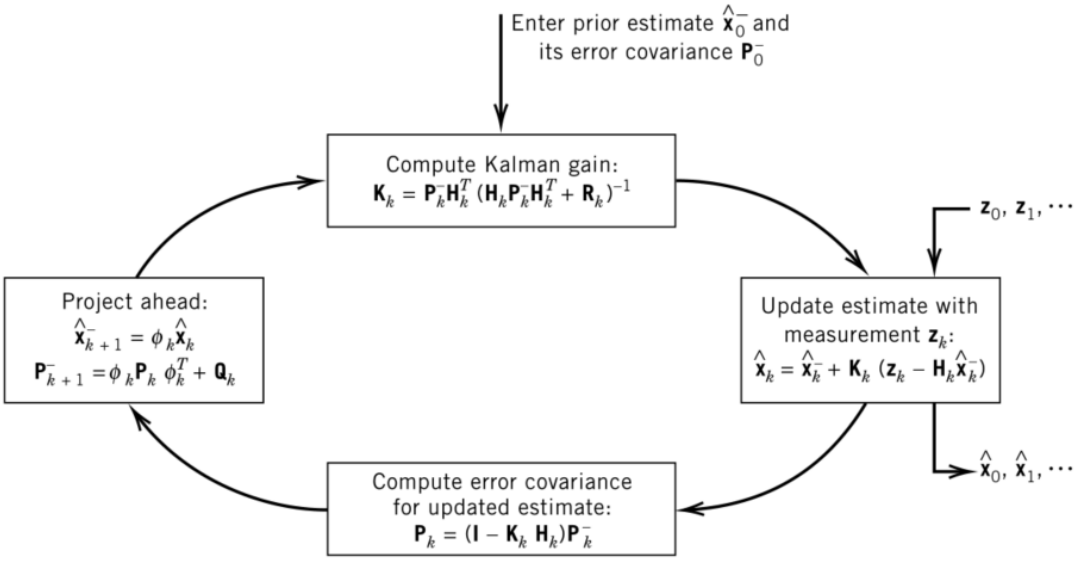

Figure A.1: Pictorial representaiton of the KF. Taken from [37].

Extended Kalman filter

The KF allows to estimate the state when both the functions **f** and **h** in (A.1) and (A.2) are linear. Therefore, to solve non-linear problem, i.e. when at least one between the functions **f** and **h** are not linear, it is necessary to use an extension of KF called EKF.

This implies the approximation of the non-linear equations (A.1) and (A.2) by a first order Taylor series computed around a *nominal trajectory* $\breve{\mathbf{x}}(t)$. It can be defined as the time-series of the parameters contained in the state vector. In other words, it has to be intended as a known trajectory that represents an approximation of the real trajectory.

The actual state vector can then be expressed as:

$$\mathbf{x}[n] = \check{\mathbf{x}}[n] + \Delta\mathbf{x}[n] \tag{A.25}$$

where $\Delta\mathbf{x}[n]$ is the *increment* between the nominal and the actual trajectory.

If the states are well estimated, the perturbation remains sufficiently small to satisfy the linearization assumptions. The EKF usually operates in a closed-loop mode. It means that, every time the state vector $\Delta\mathbf{x}[n]$ is updated, it is used to correct the nominal state. The state vector is thus reset to a null vector. Therefore, the state vector prediction (A.21) is no longer necessary and only the covariance propagation must be performed in the prediction step.

However, the EKF exhibit poor performance when the state and measurement models are highly non-linear. UKF is an alternative to the EKF that provides superior performance at an equivalent computational complexity. It addresses the approximation issues of the EKF in which the KF states are propagated through the "first-order" linearization of the nonlinear system. This simple approximation can generate large error on the states estimates when the system is highly nonlinear.

Appendix B

Performance metrics

The performance of the GBPT can be characterized with respect to different features, quantified by a corresponding metric. In turn, each performance feature of the terminal is quantified by a corresponding metric. In the road application domain, the most relevant performance features are *availability*, *accuracy*, and *integrity*.

The ***availability*** is the percentage of time during which the system can be used for the required function in a given scenario [149]. An example of a relevant metric for the availability feature is the number of epochs with a position output divided by the total number of epochs for a given operational scenario.

The ***accuracy*** can be measured by the error between the position provided by the positioning terminal, when this position is available, and the user's "true" position, generally estimated by a reference measurement system. This error, which is a random variable, is fully characterized by its CDF. In $2D$, the error is called HPE. Some relevant metrics for HPE are the 50^{th}, 75^{th}, and 95^{th} percentiles.

The ***integrity*** is a measurement of the confidence the user can have in the position supplied by the system. For civil aviation, it is expressed in the form of a probability (or risk) of failure over the period during which the positioning service is provided [149]. However, the applicability of the aviation-born integrity to other transportation fields is not straightforward due to the limitation of the urban contexts. Some "local integrity" concepts, suitable to automotive applications in urban scenarios, have already

been proposed [125].

A summary of the metrics for the performance characterization of the positioning terminal was proposed by the CEN-CENELEC standardization organization to [13]. However, in this work the statistical assessment of the GBPT performance evaluation was carried out by considering the horizontal accuracy only (i.e., HPE), defined as follows:

$$HPE = \sqrt{(x^{rx}_{East} - x^{ref}_{East})^2 + (y^{rx}_{North} - y^{ref}_{North})^2}, \tag{B.1}$$

where:

- x^{rx}_{East} and x^{ref}_{East} are the east coordinates estimated respectively by the receiver under test and the reference receiver, at a specific time instant;
- y^{rx}_{North} and y^{ref}_{North} are the north coordinates estimated respectively by the receiver under test and the reference receiver, at a specific time instant.

Bibliography

[1] Esa. Navipedia. Available online: https://gssc.esa.int/navipedia/index.php/GNSS_signal (accessed on May 2019).

[2] 3DM-GX3-25 Technical Product Overview.

[3] LabSat 3 Wideband. Available online: https://www.labsat.co.uk/index.php/en/products/labsat-3-wideband (accessed on May 2019).

[4] Spirent GSS6425. Available online: https://www.spirent.com/Products/GSS6425 (accessed on May 2019).

[5] USRP N-210. Available online: https://www.ettus.com/product/details/UN210-KIT (accessed on May 2019).

[6] ETSI TS 103 246-5: Satellite Earth Stations and Systems (SES), GNSS based location systems, Performance Test Specification. Available online: http://www.etsi.org/deliver/etsi_ts/103200_103299/10324605/01.01.01_60/ts_10324605v010101p.pdf (accessed on May 2019).

[7] Novatel SPAN Inertial navigation System. Available online: http://www.novatel.com/products/span-gnss-inertial-systems/ (accessed on May 2019).

[8] ublox NEO/LEA-M8T. Available online: https://www.u-blox.com/en/product/neolea-m8t (accessed on May 2019).

[9] USRP B-210. Available online: https://www.ettus.com/product/details/UB210-KIT (accessed on May 2019).

[10] ublox M8QCAM. Available online: https://www.u-blox.com/en/product/evk-m8xcam (accessed on May 2019).

[11] Xsense MTi-G-710. Available online: https://www.xsens.com/products/mti-g-710/ (accessed on May 2019).

[12] GoPro Hero5 Session. Available online: https://it.shop.gopro.com/EMEA/cameras/ (accessed on May 2019).

[13] European Committee for Standardization—European Committee for Electrotechnical Standardization (CEN-CENELEC) EN 16803-1. *Space—Use of GNSS-Based Positioning for Road Intelligent Transport Systems (ITS). Part 1: Definitions and System Engineering Procedures for the Establishment and Assessment of Performances*; European Committee for Standardization: Brussels, Belgium, 2016.

[14] E. Abbott and D. Powell. "Land-vehicle navigation using GPS". In: *Proceedings of the IEEE* 87.1 (1999), pp. 145–162.

[15] M. H. Afzal, V. Renaudin, and G. Lachapelle. "Magnetic field based heading estimation for pedestrian navigation environments". In: *2011 International Conference on Indoor Positioning and Indoor Navigation*. IEEE. 2011, pp. 1–10.

[16] European GNSS Agency. "GNSS Market Report". In: 5 (2017). URL: https://www.gsa.europa.eu/system/files/reports/gnss_mr_2017.pdf.

[17] European GNSS Agency. "GNSS User Technology Report". In: 2 (2018). URL: https://www.gsa.europa.eu/system/files/reports/gnss_user_tech_report_2018.pdf.

[18] S. Aikawa, S. Yamamoto, and M. Morimoto. "WLAN Finger Print Localization using Deep Learning". In: *2018 IEEE Asia-Pacific Conference on Antennas and Propagation (APCAP)*. IEEE. 2018, pp. 541–542.

[19] D. M. Akos. "A software radio approach to global navigation satellite system receiver design". PhD thesis. Ohio University, 1997.

[20] D. M. Akos. "Who's afraid of the spoofer? GPS/GNSS spoofing detection via automatic gain control (AGC)". In: *Navigation: Journal of the Institute of Navigation* 59.4 (2012), pp. 281–290.

[21] S. Alban et al. "Performance analysis and architectures for INS-aided GPS tracking loops". In: *Proceedings of the Institute of Navigation National Technical Meeting*. Institute of Navigation. 2003, pp. 611–622.

[22] F. Alizadeh-Shabdiz and M. A. Heidari. *Method of determining position in a hybrid positioning system using a dilution of precision metric*. US Patent 8,279,114. 2012.

[23] D. W. Allan. "Statistics of atomic frequency standards". In: *Proceedings of the IEEE* 54.2 (1966), pp. 221–230.

[24] M. Alloulah and M. Hazas. "An efficient CDMA core for indoor acoustic position sensing". In: *2010 International Conference on Indoor Positioning and Indoor Navigation*. IEEE. 2010, pp. 1–5.

[25] D.N. Aloi, M. Alsliety, and D.M. Akos. "A methodology for the evaluation of a GPS receiver performance in telematics applications". In: *IEEE Transactions on Instrumentation and Measurement* 56.1 (2007), pp. 11–24.

[26] A. Angrisano. "GNSS/INS Integration Methods". PhD thesis. University of Calgary, 2010.

[27] B. M. Aumayer. "Ultra-tightly Coupled Vision/GNSS for Automotive Applications". PhD thesis. University of Calgary, 2016.

[28] J.A. Avila-Rodriguez et al. "The MBOC modulation: the final touch to the Galileo frequency and signal plan". In: (2006).

[29] S. Backen, D.M. Akos, and S.G. Wilson. "RF replay system for narrowband GNSS IF signals". In: *IEEE Transactions on Aerospace and Electronic Systems* 47.1 (2011), pp. 586–595.

[30] T. Bailey and H. Durrant-Whyte. "Simultaneous localization and mapping (SLAM): Part II". In: *IEEE Robotics & Automation Magazine* 13.3 (2006), pp. 108–117.

[31] U. Becker et al. *COST Action TU1302. SaPPART Guidelines: Assessment of positioning performance in ITS applications*. Techniques et méthodes, TMI 3. 2018.

[32] D. Benson. "Interference benefits of a vector delay lock loop (VDLL) GPS receiver". In: *Proceedings of the 63rd Annual Meeting of the Institute of Navigation*. 2007, pp. 749–756.

[33] ISS Board. "IEEE standard specification format guide and test procedure for single-axis interferometric fiber optic gyros". In: *IEEE Std* (1998), pp. 952–1997.

[34] D. Borio. "A statistical theory for GNSS signal acquisition". PhD thesis. Politecnico di Torino, 2008.

[35] K. Borre et al. *A software-defined GPS and Galileo receiver: a single-frequency approach*. Springer, 2007.

[36] M. Bosse et al. "Simultaneous localization and map building in large-scale cyclic environments using the Atlas framework". In: *The International Journal of Robotics Research* 23.12 (2004), pp. 1113–1139.

[37] R. G. Brown and P. Y. C. Hwang. *Introduction to random signals and applied kalman filtering*. Wiley, 1997.

[38] J. Campbell et al. "A robust visual odometry and precipice detection system using consumer-grade monocular vision". In: *Proceedings of the 2005 IEEE International Conference on robotics and automation*. IEEE. 2005, pp. 3421–3427.

[39] J. Canny. "A computational approach to edge detection". In: *Readings in computer vision*. Elsevier, 1987, pp. 184–203.

[40] C. R. Carlson, J. C. Gerdes, and J. D. Powell. "Error Sources When Land Vehicle Dead Reckoning with Differential Wheelspeeds". In: *Navigation* 51.1 (2004), pp. 13–27.

[41] F. Caron et al. “Particle filtering for multisensor data fusion with switching observation models: Application to land vehicle positioning”. In: *IEEE transactions on Signal Processing* 55.6 (2007), pp. 2703–2719.

[42] M. J. Caruso. *Applications of magnetoresistive sensors in navigation systems*. Tech. rep. SAE Technical Paper, 1997.

[43] G. Cheng. “Accurate TOA-based UWB localization system in coal mine based on WSN”. In: *Physics Procedia* 24 (2012), pp. 534–540.

[44] T. Chu et al. “GNSS Receiver evaluation: Record-and-playback test methods”. In: *GPS World* 21.1 (2010), pp. 28–34.

[45] C. Cristodaro, F. Dovis, and L. Ruotsalainen. “Benefits and Limitations of the Record and Replay Approach for GNSS Receiver Performance Assessment in Harsh Scenarios”. In: *Sensors* 18.7 (2018), p. 2189.

[46] C. Cristodaro, F. Dovis, and L. Ruotsalainen. “The record and replay approach for GNSS receiver performance assessment in road environment”. In: *Proceedings of the 2017 International Technical Meeting of The Institute of Navigation*. 2017, pp. 1369–1375.

[47] C. Cristodaro, L. Ruotsalainen, and F. Dovis. “GNSS/INS/Visual Deeply Coupled Integration: Preliminary Investigation on Dynamic Jammed Datasets”. In: *Proceedings of the 31th International Technical Meeting of The Satellite Division of the Institute of Navigation (ION GNSS+ 2018)*. 2018, pp. 3088–3097.

[48] C. Cristodaro et al. “Design of a Configurable Monitoring Station for Scintillations by Means of a GNSS Software Radio Receiver”. In: *IEEE Geoscience and Remote Sensing Letters* 15.3 (2018), pp. 325–329.

[49] C. Cristodaro et al. “GNSS receiver performance in urban environment: Challenges and test approaches for automotive applications”. In: *2017 Electrical and Electronic Technologies for Automotive*. IEEE. 2017, pp. 1–6.

[50] J.T. Curran et al. “Developing a Multi-Frequency for GNSS-Based Scintillation Monitoring Receiver”. In: *Proceedings of the 27th International Technical Meeting of The Satellite Division of the Institute of Navigation (ION GNSS+ 2014)*. 2014, pp. 1142–1152.

[51] J.T. Curran et al. “Innovation: The continued evolution of the GNSS software-defined radio”. In: *GPS World* 29.1 (2018), pp. 43–49.

[52] P. Dabove et al. “Indoor positioning using Ultra-wide band (UWB) technologies: Positioning accuracies and sensors’ performances”. In: *2018 IEEE/ION Position, Location and Navigation Symposium (PLANS)*. IEEE. 2018, pp. 175–184.

[53] F. Daum. “Nonlinear filters: beyond the Kalman filter”. In: *IEEE Aerospace and Electronic Systems Magazine* 20.8 (2005), pp. 57–69.

[54] G. Deak, K. Curran, and J. Condell. “A survey of active and passive indoor localisation systems”. In: *Computer Communications* 35.16 (2012), pp. 1939–1954.

[55] L. Deambrogio and C. Macabiau. “Vector tracking aiding for carrier phase estimation in the presence of ionospheric scintillation”. In: *ION ITM 2013, International Technical Meeting of The Institute of Navigation*. 2013, pp–333.

[56] M. El-Diasty and S. Pagiatakis. “Calibration and stochastic modelling of inertial navigation sensor errors”. In: *Journal of Global Positioning Systems* 7.2 (2008), pp. 170–182.

[57] F. Dovis. *GNSS Interference Threats and Countermeasures*. Artech House, 2015.

[58] F. Dovis, P. Mulassano, and F. Dominici. “Overview of Global Navigation Satellite Systems”. In: Sept. 2011, pp. 923–974.

[59] F. Dovis et al. “Recent Trends in Interference Mitigation and Spoofing Detection”. In: *International Journal of Embedded and Real-Time Communication Systems (IJERTCS)* 3.3 (2012), pp. 1–17.

[60] H. Durrant-Whyte and T. Bailey. “Simultaneous localization and mapping: part I”. In: *IEEE robotics & automation magazine* 13.2 (2006), pp. 99–110.

[61] European Commission. *Implementing Decision (EU) 2017/224 of 8 February 2017 setting out the technical and operational specifications allowing the commercial service offered by the system established under the Galileo programme to fulfil the function referred to in Article 2(4)(c) of Regulation (EU) No 1285/2013 of the European Parliament and of the Council*. Available at: `http://data.europa.eu/eli/dec_impl/2017/224/oj` (accessed on May 2019). 2017.

[62] European Commission website. *Galileo goes live!, Press release, Brussels*. Available at: `http://europa.eu/rapid/press-release_IP-16-4366_en.htm` (accessed on May 2019). 2016.

[63] European Union. *European GNSS (Galileo) Open Service Signal-In-Space Interface Control Document, OS SIS ICD, Issue 1.3*. Available at: `https://www.gsc-europa.eu/system/files/galileo_documents/Galileo-OS-SIS-ICD.pdf` (accessed on May 2019). 2016.

[64] G. Falco, M. Pini, and G. Marucco. "Loose and tight GNSS/INS integrations: Comparison of performance assessed in real urban scenarios". In: *Sensors* 17.2 (2017), p. 255.

[65] G. Falco et al. "Performance Analysis of Constrained Loosely Coupled GPS/INS Integration Solutions". In: *Sensors* 12.11 (2012), pp. 15983–16007.

[66] E. Falletti and G. Falco. "Kalman Filter-based Approaches for Positioning: Integrating Global Positioning with Inertial Sensors". In: *Handbook of Position Location: Theory, Practice, and Advances, Second Edition* (2018), pp. 763–838.

[67] A. Favenza, N. Linty, and F. Dovis. "Exploiting standardized metadata for GNSS SDR remote processing: A case study". In: *Proceedings of the 29th International Technical Meeting of The Satellite Division of the Institute of Navigation (ION GNSS+ 2016)*. Portlnad, Oregon (USA), 2016, pp. 77–85.

[68] D. Fernandez et al. "Fusion of WLAN and GNSS observables for positioning in urban areas: The position ambiguity". In: *2011 IEEE Symposium on Computers and Communications (ISCC)*. IEEE. 2011, pp. 748–751.

[69] J. Gao, M. G. Petovello, and M. E. Cannon. "Development of Precise GPS/INS/Wheel Speed Sensor/Yaw Rate Sensor Integrated Vehicular Positioning System". In: 2006.

[70] Y. Gao et al. "INS/GPS/LiDAR integrated navigation system for urban and indoor environments using hybrid scan matching algorithm". In: *Sensors* 15.9 (2015), pp. 23286–23302.

[71] A. Gelb. *Applied optimal estimation*. MIT press, 1974.

[72] J. Georgy, A. Noureldin, and C. Goodall. "Vehicle navigator using a mixture particle filter for inertial sensors/odometer/map data/GPS integration". In: *IEEE Transactions on Consumer Electronics* 58.2 (2012), pp. 544–552.

[73] J. Georgy et al. "Modeling the Stochastic Drift of a MEMS-Based Gyroscope in Gyro/Odometer/GPS Integrated Navigation". In: *IEEE Transactions on Intelligent Transportation Systems* 11.4 (2010), pp. 856–872.

[74] Global Positioning System Directorate, System Engineering and Integration. *Interface Specification, NAVSTAR GPS Space Segment / Navigation User Segment Interfaces, IS-GPS-200 Rev. H, IRN003*. Available at: `http://www.gps.gov/technical/icwg/IRN-IS-200H-001+002+003_rollup.pdf` (accessed on May 2019). 2016.

[75] Global Positioning System Directorate, System Engineering and Integration. *Interface Specification, NAVSTAR GPS Space Segment / User Segment L1C Interfaces, IS-GPS-800 Rev. D*. Available at: `http://www.gps.gov/technical/icwg/IS-GPS-800D.pdf` (accessed on May 2019). 2014.

[76] Global Positioning System Directorate, System Engineering and Integration. *Interface Specification, NAVSTAR GPS Space Segment / User Segment L5 Interfaces, IS-GPS-705 Rev. D*. Available at: `http://www.gps.gov/technical/icwg/IS-GPS-705D.pdf` (accessed on May 2019). 2014.

[77] S. Goel et al. “Cooperative Localization of Unmanned Aerial Vehicles Using GNSS, MEMS Inertial, and UWB Sensors”. In: *Journal of Surveying Engineering* 143.4 (2017), p. 04017007.

[78] D. Goward. “Mass GPS Spoofing Attack in Black Sea”. In: *The Maritime Executive* (2017).

[79] M. S. Grewal, L. R. Weill, and A. P. Andrews. *Global positioning systems, inertial navigation, and integration*. John Wiley, 2007.

[80] SBAS Ionospheric Working Group et al. *Effect of ionospheric scintillations on GNSS—A white paper*. 2010.

[81] P. D. Groves. *Principles of GNSS, inertial, and multisensor integrated navigation systems*. Artech house, 2013.

[82] P.D. Groves, C.J. Mather, and A.A. Macaulay. “Demonstration of non-coherent deep INS/GPS integration for optimised signal-to-noise performance”. In: *Proceedings of the 20th International Technical Meeting of The Satellite Division of the Institute of Navigation (ION GNSS 2007)*. Vol. 3. 2007, pp. 2627–2638.

[83] GSA. *GSA Report on Road User Needs and Requirements 233537*. Tech. rep. 2018.

[84] S. Gunawardena and T. Pany. “GNSS SDR Metadata Standard Working Group Report”. In: *Proceedings of the 28th International Technical Meeting of The Satellite Division of the Institute of Navigation (ION GNSS+ 2015)*. 2015, pp. 3218–3221.

[85] D. Gustafson, J. Dowdle, and K. Flueckiger. “A deeply integrated adaptive GPS-based navigator with extended range code tracking”. In: *IEEE 2000. Position Location and Navigation Symposium*. IEEE. 2000, pp. 118–124.

[86] F. Gustafsson et al. “Particle filters for positioning, navigation, and tracking”. In: *IEEE Transactions on signal processing* 50.2 (2002), pp. 425–437.

[87] D. Hall. “Record, Replay, Rewind: Testing GNSS Receivers with Record and Playback Techniques”. In: *GPS World* (2010).

[88] H. J. von der Hardt et al. “A method of mobile robot localisation by fusion of odometric and magnetometric data”. In: *International Journal of Advanced Manufacturing Technology 9(1)*. 1994, pp. 65–69.

[89] R. Hartley and A. Zisserman. *Multiple view geometry in computer vision*. Cambridge university press, 2003.

[90] S. Hickling and T. Haddrell. “Recording and replay of GNSS RF signals for multiple constellations and frequency bands”. In: *Proceedings of the 26th International Technical Meeting of The Satellite Division of the Institute of Navigation (ION GNSS+ 2013)*. Nashville, Tennessee (USA), 2013, pp. 1907–1918.

[91] C. Hide, T. Moore, and T. Botterill. “Low cost IMU, GPS and camera integration for handheld indoor positioning”. In: *Proceedings of the 24th International Technical Meeting of The Satellite Division of the Institute of Navigation (ION GNSS 2011)*. 2001, p. 1378.

[92] C. Hide, T. Moore, and M. Smith. “Adaptive Kalman filtering for low-cost INS/GPS”. In: *The Journal of Navigation* 56.1 (2003), pp. 143–152.

[93] G. M. Hoang et al. “Cooperative localization in GNSS-aided VANETs with accurate IR-UWB range measurements”. In: *2016 13th Workshop on Positioning, Navigation and Communications (WPNC)*. IEEE. 2016, pp. 1–6.

[94] C. Holzmann and M. Hochgatterer. “Measuring distance with mobile phones using single-camera stereo vision”. In: *2012 32nd International Conference on Distributed Computing Systems Workshops*. IEEE. 2012, pp. 88–93.

[95] P. V. C. Hough. *Method and means for recognizing complex patterns*. Tech. rep. 1962.

[96] H. Hurskainen et al. “Multicore software-defined radio architecture for GNSS receiver signal processing”. In: *EURASIP Journal on Embedded Systems* 2009.1 (2009), p. 543720.

[97] Jepson, A. and Fleet, D. *Foundations of Computer Vision, Robust estimation*. Lecture notes. Available at: `http://www.cs.toronto.edu/~fleet/courses/2503/fall11/Handouts/robustEstimation.pdf` (accessed on May 2019). 2009.

[98] Y. Jiao et al. "Characterization of high-latitude ionospheric scintillation of GPS signals". In: *Radio Science* 48.6 (2013), pp. 698–708.

[99] R. Jirawimut et al. "Visual odometer for pedestrian navigation". In: *IEEE Transactions on Instrumentation and Measurement* 52.4 (2003), pp. 1166–1173.

[100] D. J. Jwo and C. N. Lai. "Unscented Kalman filter with nonlinear dynamic process modeling for GPS navigation". In: *GPS solutions* 12.4 (2008), pp. 249–260.

[101] R. E. Kalman. "A new approach to linear filtering and prediction problems". In: *Journal of basic Engineering* 82.1 (1960), pp. 35–45.

[102] K. Kanatani. "Statistical analysis of geometric computation". In: *CVGIP: Image Understanding* 59.3 (1994), pp. 286–306.

[103] E. Kaplan and C. Hegarty. *Understanding GPS: Principles and Applications*. Artech house, 2005.

[104] J. K. Kim et al. "Experimental studies of autonomous driving of a vehicle on the road using LiDAR and DGPS". In: *2015 15th International Conference on Control, Automation and Systems (ICCAS)*. IEEE. 2015, pp. 1366–1369.

[105] P. M. Kintner, B. M. Ledvina, and E. R. De Paula. "GPS and ionospheric scintillations". In: *Space weather* 5.9 (2007).

[106] M. Kirkko-Jaakkola, J. Collin, and J. Takala. "Bias prediction for MEMS gyroscopes". In: *IEEE Sensors Journal* 12.6 (2012), pp. 2157–2163.

[107] B. M. Kitt et al. "Monocular visual odometry using a planar road model to solve scale ambiguity". In: (2011).

[108] S. Knauth et al. "The iloc+ ultrasound indoor localization system for aal applications at evaal 2012". In: *International Competition on Evaluating AAL Systems through Competitive Benchmarking*. Springer. 2012, pp. 83–94.

[109] A. Kushki, K. N. Plataniotis, and A. N. Venetsanopoulos. *WLAN positioning systems: principles and applications in location-based services*. Cambridge University Press, 2012.

[110] H. Kuusniemi. "User-level reliability and quality monitoring in satellite-based personal navigation". PhD thesis. Tampere University of Technology, 2005.

[111] M. Lashley and D. M. Bevly. "Comparison of traditional tracking loops and vector based tracking loops for weak GPS signals". In: *Proceedings of the 2008 National Technical Meeting of The Institute of Navigation*. 2008, pp. 310–316.

[112] T. Lemaire and S. Lacroix. "Monocular-vision based SLAM using line segments". In: *Proceedings 2007 IEEE International Conference on Robotics and Automation*. IEEE. 2007, pp. 2791–2796.

[113] H. Leppakoski, J. Collin, and J. Takala. "Pedestrian navigation based on inertial sensors, indoor map, and WLAN signals". In: *Journal of Signal Processing Systems* 71.3 (2013), pp. 287–296.

[114] T. W. Lezniak, R. W. Lewis, and R. A. McMillen. "A dead reckoning/map correlation system for automatic vehicle tracking". In: *IEEE Transactions on Vehicular Technology* 26.1 (1977), pp. 47–60.

[115] N. Linty, F. Dovis, and L. Alfonsi. "Software-defined radio technology for GNSS scintillation analysis: bring Antarctica to the lab". In: *GPS Solutions* 22.4 (2018), p. 96.

[116] N. Linty et al. "Ionospheric scintillation threats to GNSS in polar regions: the DemoGRAPE case study in Antarctica". In: *European Navigation Conference (ENC)*. IEEE. 2016, pp. 1–7.

[117] N. Linty et al. "Monitoring Ionosphere Over Antarctica by Means of a GNSS Signal Acquisition System and a Software Radio Receiver". In: *Proceedings of the 29th International Technical Meeting of The Satellite Division of the Institute of Navigation (ION GNSS+ 2016)*. Monterey, California (USA), 2016, pp. 549–555.

[118] N. Linty et al. “The Software Defined Radio Approach to Ionosphere Monitoring Using GNSS: Multiple Receivers at the Price Of One”. In: *XXXIV SCAR Open Science Conference 2016 ’Antarctica in the Global Earth System: From the Poles to the Tropics’ - Abstract Book*. Cambridge, 2016. ISBN: 978-0-948277-32-0.

[119] L. Lo Presti et al. “Software defined radio technology for GNSS receivers”. In: *IEEE Metrology for Aerospace (MetroAeroSpace)*. IEEE. 2014, pp. 314–319.

[120] D. G. Lowe. “Distinctive image features from scale-invariant keypoints”. In: *International journal of computer vision* 60.2 (2004), pp. 91–110.

[121] D. G. Lowe. “Object recognition from local scale-invariant features”. In: *iccv*. IEEE. 1999, p. 1150.

[122] Z. Lu and K. Hu Z.and Uchimura. “SLAM estimation in dynamic outdoor environments: A review”. In: *International Conference on Intelligent Robotics and Applications*. Springer. 2009, pp. 255–267.

[123] V. Lucas-Sabola et al. “Efficiency analysis of Cloud GNSS signal processing for IoT applications”. In: *Proceedings of the 30th International Technical Meeting of The Satellite Division of the Institute of Navigation (ION GNSS+ 2017)*. 2017, pp. 3843–3852.

[124] G. MacGougan, K. O’Keefe, and R. Klukas. “Tightly-coupled GPS/UWB integration”. In: *The Journal of Navigation* 63.1 (2010), pp. 1–22.

[125] D. Margaria and E. Falletti. “The Local Integrity Approach for Urban Contexts: Definition and Vehicular Experimental Assessment”. In: *Sensors* 16.2 (2016), p. 154.

[126] R. Mautz. “Overview of current indoor positioning systems”. In: *Geodezija ir kartografija* 35.1 (2009), pp. 18–22.

[127] I. Miller and M. Campbell. “Sensitivity analysis of a tightly-coupled GPS/INS system for autonomous navigation”. In: *IEEE Transactions on Aerospace and Electronic Systems* 48.2 (2012), pp. 1115–1135.

[128] A. Minetto, C. Cristodaro, and F. Dovis. "A collaborative method for GNSS-based inter-agent range estimation and hybrid positioning algorithm in harsh environment". In: *Proceedings of the 30th International Technical Meeting of The Satellite Division of the Institute of Navigation (ION GNSS+ 2017)*. 2017, pp. 3784–3795.

[129] A. Minetto, C. Cristodaro, and F. Dovis. "A collaborative method for positioning based on GNSS inter agent range estimation". In: *2017 25th European Signal Processing Conference (EUSIPCO)*. IEEE. 2017, pp. 2714–2718.

[130] P. Misra and P. Enge. *Global positioning system: signals, measurements, and performance*. Ganga-Jamuna Press, 2006.

[131] J. Mitola. "The software radio architecture". In: *IEEE Communications magazine* 33.5 (1995), pp. 26–38.

[132] A. H. Mohamed and K. P. Schwarz. "Adaptive Kalman filtering for INS/GPS". In: *Journal of geodesy* 73.4 (1999), pp. 193–203.

[133] A. Molino et al. "N-GENE GNSS software receiver for acquisition and tracking algorithms validation". In: *2009 17th European Signal Processing Conference*. IEEE. 2009, pp. 2171–2175.

[134] Mo. Mostafa et al. "Radar and visual odometry integrated system aided navigation for UAVS in GNSS denied environment". In: *Sensors* 18.9 (2018), p. 2776.

[135] B. Motella, M. Pini, and F. Dovis. "Investigation on the effect of strong out-of-band signals on global navigation satellite systems receivers". In: *GPS Solutions* 12.2 (2008), pp. 77–86.

[136] S. Nassar et al. "Modeling inertial sensor errors using autoregressive (AR) models". In: *Navigation* 51.4 (2004), pp. 259–268.

[137] N. Nourani-Vatani, J. Roberts, and M. V. Srinivasan. "Practical visual odometry for car-like vehicles". In: *2009 IEEE International Conference on Robotics and Automation*. IEEE. 2009, pp. 3551–3557.

[138] C. O'Driscoll and G. Lachapelle. "Comparison of traditional and Kalman filter based tracking architectures". In: *Proceedings of European navigation conference*. 2009, pp. 3–6.

[139] E. J. Ohlmeyer. "Analysis of an ultra-tightly coupled GPS/INS system in jamming". In: *2006 IEEE/ION Position, Location, And Navigation Symposium*. IEEE. 2006, pp. 44–53.

[140] M. Ortiz et al. "From Lab to Road Test: Using a reference vehicle for solving GNSS localization challenges". In: *Inside GNSS* 8.5 (2013), 19p.

[141] T. Pany and B. Eissfeller. "Use of a vector delay lock loop receiver for GNSS signal power analysis in bad signal conditions". In: *2006 IEEE/ION Position, Location, And Navigation Symposium*. IEEE. 2006, pp. 893–903.

[142] T. Pany, R. Kaniuth, and B Eissfeller. "Deep Integration of Navigation Solution and Signal Processing". In: *Proc. ION-ITM-2005, Long Beach, California* (), pp. 1095–1102.

[143] M. Park and Y. Gao. "Error and performance analysis of MEMS-based inertial sensors with a low-cost GPS receiver". In: *Sensors* 8.4 (2008), pp. 2240–2261.

[144] B. W. Parkinson et al. *Global positioning system: Theory and applications, Volume II*. American Institute of Aeronautics and Astronautics, 1996.

[145] S. Peng and Y. Morton. "A USRP2-based reconfigurable multi-constellation multi-frequency GNSS software receiver front end". In: *GPS Solutions* 17.1 (2013), pp. 89–102.

[146] M. G. Petovello. "Real-time integration of a tactical-grade IMU and GPS for high-accuracy positioning and navigation". PhD thesis. University of Calgary, 2003.

[147] M. Petovello, C. O'Driscoll, and G. Lachapelle. "Weak Signal Carrier Tracking of Weak Using Using Coherent Integration with an Ultra-Tight GNSS/IMU Receiver". In: *Proceedings of European Navigation Conference, Toulouse*. 2008.

[148] M.G. Petovello and G. Lachapelle. "Comparison of vector-based software receiver implementations with application to ultra-tight GPS/INS integration". In: *Proceedings of ION GNSS*. Vol. 6. 2006.

[149] F. Peyret. "Standardization of performances of GNSS-based positioning terminals for ITS applications at CEN/CENELEC/TC5". In: *ITS WorId Congress*. Japan, 2013.

[150] M. L. Psiaki. "Smoother-based GPS signal tracking in a software receiver". In: *Proceedings of ION GPS*. Vol. 2001. 2001, pp. 2900–2913.

[151] M. L. Psiaki and T. E. Humphreys. "GNSS spoofing and detection". In: *Proceedings of the IEEE* 104.6 (2016), pp. 1258–1270.

[152] A. Quinchia et al. "A comparison between different error modeling of MEMS applied to GPS/INS integrated systems". In: *Sensors* 13.8 (2013), pp. 9549–9588.

[153] R. Ramalingam, G. Anitha, and J. Shanmugam. "Microelectromechnical systems inertial measurement unit error modelling and error analysis for low-cost strapdown inertial navigation system". In: *Defence Science Journal* 59.6 (2009), pp. 650–658.

[154] S. Rezaei and R. Sengupta. "Kalman filter-based integration of DGPS and vehicle sensors for localization". In: *IEEE Transactions on Control Systems Technology* 15.6 (2007), pp. 1080–1088.

[155] R. Romero et al. "On the use and performance of new Galileo signals for ionospheric scintillation monitoring over Antarctica". In: *Proceedings of the 2017 International Technical Meeting of The Institute of Navigation*. 2017, pp. 989–997.

[156] L. Ruotsalainen. "Vision-Aided Pedestrian Navigation for Challenging GNSS Environments, vol. 151". PhD thesis. Publications of the Finnish Geodetic Institute, Masala, Finland, 2013.

[157] L. Ruotsalainen. "Visual gyroscope and odometer for pedestrian indoor navigation with a smartphone". In: *Proceedings of the ION GNSS*. 2012, pp. 17–21.

[158] M. Schreiber et al. “Vehicle localization with tightly coupled GNSS and visual odometry”. In: *2016 IEEE Intelligent Vehicles Symposium (IV)*. IEEE. 2016, pp. 858–863.

[159] D. Serant et al. “Field test performance assessment of GNSS/INS ultra-tight coupling scheme targeted to mass-market applications”. In: *6th ESA Workshop on Satellite Navigation Technologies and European Workshop on GNSS Signals and Signal Processing,(NAVITEC), 2012*. IEEE. 2012, pp. 1–8.

[160] N. El-Sheimy, H. Hou, and X. Niu. “Analysis and modeling of inertial sensors using Allan variance”. In: *IEEE Transactions on instrumentation and measurement* 57.1 (2008), pp. 140–149.

[161] E. H. Shin and N. El-Sheimy. “Unscented Kalman Filter and Attitude Errors of Low-Cost Inertial Navigation Systems”. In: *Navigation* 54.1 (2007), pp. 1–9.

[162] I. Skog and P. Handel. “In-car positioning and navigation technologies—A survey”. In: *IEEE Transactions on Intelligent Transportation Systems* 10.1 (2009), pp. 4–21.

[163] P. Smith, I. D. Reid, and A. J. Davison. “Real-time monocular SLAM with straight lines”. In: (2006).

[164] S. Soderholm et al. “A multi-GNSS software-defined receiver: design, implementation, and performance benefits”. In: *Annals of Telecommunications* 71.7-8 (2016), pp. 399–410.

[165] A. Solimeno. “Low-cost INS/GPS data fusion with extended Kalman filter for airborne applications”. In: (2007).

[166] A. Soloviev, S. Gunawardena, and F. van Graas. “Deeply Integrated GPS/Low-Cost IMU for Low CNR Signal Processing: Concept Description and In-Flight Demonstration”. In: *Navigation* 55.1 (2008), pp. 1–13.

[167] M. Spangenberg, V. Calmettes, and J. Y. Tourneref. “Fusion of GPS, INS and odometric data for automotive navigation”. In: *2007 15th European Signal Processing Conference*. 2007, pp. 886–890.

[168] J. J. Spilker and B. W. Parkinson. “Fundamentals of signal tracking theory”. In: *Progress in Astronautics and Aeronautics* 163 (1996), pp. 245–328.

[169] A. Stelzer, M. Jahn, and S. Scheiblhofer. “Precise distance measurement with cooperative FMCW radar units”. In: *2008 IEEE Radio and Wireless Symposium*. IEEE. 2008, pp. 771–774.

[170] C. Stöber et al. “ipexSR: A real-time multi-frequency software GNSS receiver”. In: *Proceedings ELMAR-2010*. IEEE. 2010, pp. 407–416.

[171] M. Tahir et al. “On the Accuracy of Inter-Vehicular Range Measurements Using GNSS Observables in a Cooperative Framework”. In: *IEEE Transactions on Intelligent Transportation Systems* 99 (2018), pp. 1–10.

[172] Z. Tao and P. Bonnifait. “Tightly coupling GPS with lane markings for autonomous vehicle navigation”. In: *17th International IEEE Conference on Intelligent Transportation Systems (ITSC)*. IEEE. 2014, pp. 439–444.

[173] D. Titterton, J. L. Weston, and J. Weston. *Strapdown inertial navigation technology*. Vol. 17. IET, 2004.

[174] R. Toledo-Moreo et al. “High-integrity IMM-EKF-based road vehicle navigation with low-cost GPS/SBAS/INS”. In: *IEEE Transactions on Intelligent Transportation Systems* 8.3 (2007), pp. 491–511.

[175] COST Action TU1302. “SaPPART White Paper-Better Use of Global Navigation Satellite Systems for Safer and Greener Transport”. In: (2015). URL: `https://infoscience.epfl.ch/record/212763/files/White-Paper_SaPPART_sept15.pdf`.

[176] N. Vagle, A. Broumandan, and G. Lachapelle. “Multiantenna GNSS and Inertial Sensors/Odometer Coupling for Robust Vehicular Navigation”. In: *IEEE Internet of Things Journal* 5.6 (2018), pp. 4816–4828.

[177] A. J. Van Dierendonck, J. Klobuchar, and Q. Hua. “Ionospheric scintillation monitoring using commercial single frequency C/A code receivers”. In: *proceedings of ION GPS*. Vol. 93. 1993, pp. 1333–1342.

[178] K. Wesson, D. Shepard, and T. Humphreys. "Straight talk on anti-spoofing". In: *Gps World* 23.1 (2012), pp. 32–39.

[179] M. Wildemeersch et al. "Impact study of unintentional interference on GNSS receivers". In: *EC Joint Research Centre Scientific and Technical Reports, Institute for the Protection and Security of the Citizen, European Union* (2010).

[180] J. H. Won, T. Pany, and G. Hein. "GNSS software defined radio". In: *Inside GNSS* 1.5 (2006), pp. 48–56.

[181] X. Zhang et al. "Allan variance analysis on error characters of MEMS inertial sensors for an FPGA-based GPS/INS system". In: *Proceedings of the International Symposium on GPS/GNNS*. 2008, pp. 127–133.

[182] S. Zhao and D. Akos. "An open source GPS/GNSS vector tracking loop-implementation, filter tuning, and results". In: *Proceedings of the 2011 International Technical Meeting of The Institute of Navigation*. 2011, pp. 1293–1305.

[183] H. Zhou et al. "StructSLAM: Visual SLAM with building structure lines". In: *IEEE Transactions on Vehicular Technology* 64.4 (2015), pp. 1364–1375.

This Ph.D. thesis has been typeset by means of the TEX-system facilities. The typesetting engine was pdfLATEX. The document class was `toptesi`, by Claudio Beccari, with option `tipotesi =scudo`. This class is available in every up-to-date and complete TEX-system installation.